A New Approach to Neutron Spectrometry with Multi-Element Scintillators

By

Nafisah Khan

A Thesis Submitted in Partial Fulfillment

of the Requirements for the Degree of Doctor of Philosophy

in

Nuclear Engineering

Faculty of Energy Systems and Nuclear Science

University of Ontario Institute of Technology

Oshawa, Ontario, Canada

Dedicated to my parents

Abstract

The combined effects of the nuclear industrial renaissance, the events of 9/11, and the Fukushima disaster have had a significant impact on the research and development of radiation detection instrumentation. Notably, there is ample worldwide scientific research effort into a better understanding of the material properties and nuclear interactions with a view to support the improvement of radiation detection and measurement. These improvements are spurred by the heightened security requirements that entail the monitoring of contraband material including explosives in transit, and the need to enhance occupational safety as well as environmental radiation protection in respect to nuclear power generation. Moreover, the regulatory authorities require routinely employed radiation detection and measuring devices in nuclear installations to meet the revised standard specifications in terms of their design and performance.

Currently, there is no neutron dosimeter/spectrometer that can meet the requirements in terms of size and performance. In particular, the requirements for high sensitivity, spectroscopic features, and determination of operational quantities to enable radiation protection decision making have resulted in a closer examination of the basic physics of the radiation interactions in detector materials.

Neutron dosimetry is regarded as the last frontier in radiation protection. Due to the large span of neutron energy and the strong energy dependence of the dose to fluence coefficient, neutron dosimetry requires the knowledge of the neutron spectra for any accurate neutron dose quantification. As a result, spectrometry is a precursor to determine dosimetry quantities and spectrometers are therefore vital to determine and characterize radiation fields present to individuals as they provide information about the radiation intensity and energy spectra. However, current spectrometers have many drawbacks and limitations in different aspects. From one side, fast spectrometry currently uses the scattering process on hydrogen rich materials and uses complicated unfolding techniques to extract the energy spectra. From another side, neutron fields are inherently mixed with a gamma component and therefore, it is paramount to distinguish each component since their contribution to the dose equivalent is weighted

differently. More specifically, the challenge becomes more profound with neutrons in the energy range between 10 keV and few MeV. These challenges are mainly due to:

- The drastic change in the dose-to-fluence conversion coefficient that increases by a factor of 40;
- The low sensitivity of the neutron sensors used in neutron spectroscopy (low cross section);
- The poor resolution of the detectors, which makes accurate neutron spectrometry difficult to achieve.

However, by exploiting new developments and high sensitivity scintillators, in this thesis, a new approach has been adopted using different nuclear reaction processes with different contents of scintillating material. More specifically, two nuclear reactions, i.e. (n,α) and (n,p), on two different elements have been used to carry out neutron spectrometry.

In addition, this thesis aims to investigate the spectrometric properties of scintillating materials as a first step to establish a platform for developing a neutron spectrometer/dosimeter.

In terms of methodology, the thesis has taken an empirical approach in studying potential sensors that can be used for neutron spectrometry. Four scintillators have been explored and studied. Each scintillator corresponds to a particular energy region. The first part of the thesis consists of extensive Monte Carlo calculations to optimize the sensor's isotope contents, while the second part consists of conducting a series of experiments using three main facilities, namely an AmBe source of 120 mCi, a neutron generator of 2.5 MeV neutrons at the University of Ontario Institute of Technology, a KN Van De Graaff accelerator at McMaster University, and gamma ray sources with different energies. All sensors have been used in conjunction with a miniature data acquisition system that consists of a multi-channel analyzer, mounted on a photomultiplier, and controlled by software to operate, control and analyze the output data. The time characteristics of the output pulse, such as integration time and rising time, have been optimized for each sensor.

The thesis presents a thorough literature review, a comprehensive methodology of the study, a description of the used facilities and the results of the simulation data with four different sensors along with the experimental work carried out at the aforementioned facilities. The response

functions of each scintillator to a given radiation type and energy has been analyzed and discussed. Furthermore, the sensor's potential for use in neutron spectrometry/dosimetry has been assessed for future work.

Acknowledgments

First and foremost, I am grateful to God for His many blessings. It is by His grace, love, and mercy, that I am able to achieve anything.

I would like to thank my supervisor, Dr. Rachid Machrafi, for his guidance and his passionate and judicious encouragements that motivates me to achieve research excellence.

I would like to thank the Natural Sciences and Engineering Research Council of Canada for their funding support to aid in carrying out this research.

I would like to thank my parents and siblings for their unconditional love, continuous support, and encouragement throughout all of my years of studies.

Table of Contents

List of Tables

List of Figures

List of Appendix Figures

Nomenclature

Greek Symbols

α : Alpha particle

β : Beta particle

γ : Gamma-ray

μ: Micro

ρ: Density

δ_s: Intrinsic resolution

δ_p: Photoelectron statistics

ν: Variance

ϵ_{abs}: Absolute efficiency

ϵ_{int}: Intrinsic efficiency

τ: Decay time

Φ: Particle fluence

Ψ: Energy fluence

$\bar{\varepsilon}$: Energy imparted by ionizing radiation

ϕ: Fluence

ε: Efficiency

English Symbols

E_n: Neutron energy

E_{max}: Maximum energy

E_{min}: Minimum energy

M: Particle mass

E_{e^-} : Electron energy

E_{e^+} : Positron energy

E_γ: Incident photon energy

$E_{\gamma\prime}$: Scattered photon energy

E_b: Binding energy

Z: Atomic number

R: Range of particle

A: Atomic weight

T: Kinetic energy

m: Rest mass of particle

c: Speed of light

w_i: Weight fraction

L: Number of elements

E_R: Energy resolution

E_0: Peak centroid

N: Number of particles

I: Instantaneous emission intensity

I_0: Initial emission intensity

t: Time

A_c: Cross-sectional area

K: Kerma

$\bar{E}_{tr}$: Energy imparted in a medium

D: Absorbed dose

k: Kerma factor

H: Dose equivalent

Q: Quality factor

$\bar{Q}$: Mean quality factor

M: Detector reading

R_Φ: Fluence response function

O: Output signal

S: Sensitivity

Y: Signal influence

r: Distance

E_{th}: Threshold energy

E': Critical energy

n: Nano

m: Milli

c: Centi

k: Kilo

M: Mega

G: Giga

Abbreviations

UOIT: University of Ontario Institute of Technology

LET: Linear Energy Transfer

FWHM: Full width at half maximum

NCRP: National Council on Radiation Protection

ICRP: International Commission on Radiation Protection

NRC: Nuclear Regulatory Commission

BSS: Bonner Sphere Spectrometer

BSE: Bonner Sphere Extension

ROSPEC: Rotating Spectrometer

SSS: Simple Scintillation Spectrometer

NE: Nuclear Enterprise Limited

PWR: Pressurized Water Reactor

BWR: Boiling Water Reactor

GCR: Gas Cooled Reactor

PSI: Paul Scherer Institute

RENT: Reactor Neutron Therapy

LiI:Eu: Europium activated Lithium Iodide

CLYC: Cs_2LiYCl_6:Ce

MCNPX: Monte Carlo N-Particle eXtended Code

VISED: Visual Editor

FORTRAN: Formula Translation

EJ: Eljen Technology

AmBe: Americium Beryllium

PuBe: Plutonium Beryllium

PMT: Photomultiplier Tube

MCA: Multi-channel Analyzer

DAQ: Data Acquisition System

RMD: Radiation Monitoring Devices Inc.

CVL: Core-to-valence Luminescence

STE: Self-Trapped Exciton

UV: Ultraviolet

PC: Personal Computer

ADC: Analog-to-digital Convertor

SCA: Single Channel Analyzer

FPGA: Field Programmable Gate Array

DSP: Digital Signal Processor

USB: Universal Serial Bus

GEB: Gaussian Energy Broadening

ENDF: Evaluated Nuclear Data File

eV: Electron Volt

MeeV: Megalectron Volt electrion equivalent

GEE: Gamma Equivalent Energy

Introduction

Neutron monitoring devices are mandated in nuclear facilities where neutron radiation is of concern. From a radiation protection point of view, it is critical to monitor an individual's exposure when working where radiation is present [1-2]. Radiation instruments, in general, and neutron instruments in particular, are deployed in areas of radiation protection, inspection, homeland security, nuclear energy safety and monitoring, and facilities for neutron radiotherapy study. Recently, the disaster of Fukushima in Japan, the events of 9/11, and the nuclear industrial renaissance has significantly impacted the research and development of such instruments. There is ample worldwide scientific research and ongoing efforts into a better understanding of the material properties and nuclear interactions to support the improvement of radiation detection and measurement. These improvements are spurred by the heightened security requirements that entail the monitoring of contraband material including explosives in transit, and the need to enhance occupational safety as well as environmental radiation protection in respect to nuclear power generation. Regulatory authorities require routinely employed radiation detection and measuring devices in nuclear installations to meet the revised standard specifications in terms of their design and performance.

Radiation protection devices are particularly deficient when it comes to neutrons. In the past, passive personal dosimeters have been used in all different types of radiation facilities, but due to their drawbacks of strong energy dependence and high detection threshold, active personal dosimeters have become favourable [3]. Reviews on the current status and need for electronic personal dosimeters and spectrometers has been described in [4-6].

Currently, there is no neutron dosimeter/spectrometer that can meet the requirements in terms of size and performance. In particular, the requirements for high sensitivity, spectroscopic features, and determination of operational quantities to enable radiation protection decision making have resulted in a closer examination of the basic physics of the radiation interactions in detector materials.

Due to the recent developments and requirements in interdiction and inspection technologies, as well as extensive use of radiation devices in decommissioning and nuclear waste management,

the magnitude of dose and dose rate has increased. As such, the demand of improved radiation equipment has increased accordingly.

Neutron radiation is a major component of the radiation fields around nuclear facilities and due to their high LET, their contribution to the dose equivalent is significant. Therefore, the detection of neutrons is vital since they can penetrate far through matter and deposit a lot of their energy through secondary particles, making them detrimental to the health of individuals. To control this risk, it is important to have systems that are capable of detecting their presence.

Neutron dosimetry is regarded as the last frontier in radiation protection. It requires the knowledge of the neutron spectra for any accurate neutron dose quantification. As a result, spectrometry is a precursor to determine dosimetry quantities, and spectrometers are therefore vital to determine and characterize radiation fields present to individuals as they provide information about the radiation intensity and energy spectra.

The main challenge with neutron radiation is firstly due to the wide range of energies (from a fraction eV to million of eV) and secondly, the strong dependence of the neutron dose on the neutron energy. For instance, the conversion factor of the dose to fluence drastically changes from a value of ~10 $pSv \cdot cm^2$ in the low neutron energy range to more than ~500 $pSv \cdot cm^2$ for energies beyond 1 MeV. This is not the case with gamma radiation, since its energy ranges within an energy interval of few keV to ~3 MeV.

In practice, another major challenge with neutron spectroscopy is the presence of interfering gamma radiation in mixed fields where the capability of discrimination of a neutron spectrometer is crucial. It is therefore paramount to distinguish each component since their contribution to the dose equivalent is weighted differently. Thus, it is not surprising that the requirement and specification established by regulatory bodies emphasizes the need for good neutron-gamma discrimination as a criterion for a good neutron spectrometer.

Current neutron spectrometers have many drawbacks and limitations in different aspects. Most neutron sensors are limited due to their detection efficiency and energy dependence. Presently, the detection of neutrons employs detectors with a high thermal neutron response (i.e. Boron, Helium, Lithium), embedded in a thermalizing medium. This technology is well established and has some advantages such as reasonable detection efficiency and good discrimination against

gamma-rays. This approach however, does not provide any information on the neutron energy and is therefore unable to serve for an accurate dosimetry quantity determination. From another side, due to the poor energy resolution of the detectors, it is difficult to accurately extract the incident energy information to obtain the energy spectra, thereby making spectrometry challenging to achieve.

Another method presently used for fast spectrometry is using hydrogen rich materials as sensors that use the neutron scattering process on ^{1}H. The drawback with this method is that the energy transferred to the proton highly depends on the scattered angle. As a result, a distribution of energies from the proton is observed and complicated unfolding techniques are required to determine the incident neutron energy. Also, using ^{3}He gas for detection is becoming more and scarcer due to the current worldwide shortage. So, there is a need to seek out other sensors.

The observed limitations in neutron devices are mainly due to the physical properties of the sensors and intrinsic qualities of the detectors themselves [7]. Although for the last decades, the engineering of radiation instrumentation has drastically progressed in electronics as well as in software and signal processing. In literature, except for a couple of new sensors that are not commercially available [58-62], there are no indications of new sensor technology that can have a significant impact on fast neutron detection.

Despite the considerably resourced civilian and military research efforts in developing a desired spectrometer to fulfill and overcome the aforementioned challenges, recent evaluation of existing neutron spectrometers have pointed out many deficiencies and limitations.

To monitor individuals in radiation fields, the dose equivalent is a relevant quantity to measure since it reflects the biological effects of different types of ionizing radiation. This quantity can be obtained by knowing the neutron fluence and neutron fluence-to-dose conversion factor which is generally updated constantly. The neutron fluence can be calculated from the detector response in a given field, and by knowing the energy spectra, dosimetric quantities can be determined. An ideal spectrometer should have a high efficiency in detecting neutrons in a large range of energies. Most spectrometers do not have very good energy resolution, and as a result, precise energies can be difficult to determine. This means that the correct dose will also be difficult to obtain. Currently, there is no single device that is capable of offering good resolution. Therefore,

a combination of mathematical models along with empirical data can reduce the gap between a desired neutron device for neutron dosimetry and the physical limitations of current neutron sensors.

Radiation fields where dosimeters are employed are generally not very intense and usually multidirectional; have a large energy range from thermal energies to hundreds of MeVs; and interference from gamma-rays is prevalent. Therefore, for dosimetric purposes, an acceptable neutron spectrometer can be developed by combining two neutron sensors in a single unit and along with mathematical algorithms; one can extract the dosimetric quantities. In addition, with the recent development of new scintillating materials, there is hope that the use of the optical properties of these materials that incorporate different elements in their content can change the way of dealing with neutron spectrometry. For instance, when investigating the properties of newer crystals that contains different elements, it was found that when neutrons interact with the sensor, two different reactions take place: one with ^{6}Li through an (n,α) reaction while the second with ^{35}Cl through an (n,p) reaction. It is worth mentioning that this crystal has been mainly developed for thermal neutron detection. The first reaction occurs with thermal neutrons with an energy release of 4.78 MeV, while the second reaction produces a proton peak, the position of which depends on the neutron energy. Therefore, by exploiting the presence of different constituents in a single sensor, one can detect, not only different particles, but also carry out high performance neutron spectroscopy. As a result, one single sensor can serve as a neutron spectrometer in a large neutron energy range with better resolution and good discrimination against gamma radiation. These types of sensors, using these fundamental nuclear reactions, presents a breakthrough that can revolutionize the challenges faced over the last two decades in neutron detection in general, and neutron spectrometry in particular. To overcome the sensitivity problem that is governed by a combination of the area and detection efficiency, which in turn is related to the constituents and density of the sensor, the key to investigate is to optimize the concentration of different constituents in the sensor for a desired response. It has been noted that traditionally the way of detecting neutrons in a wide energy range has been based on multiple sensors combined in a single detection unit.

Motivation of Thesis

In this context, the motivation of this thesis stems from the heightened security requirements, improvements in occupational safety, and revised standard specifications related to radiation detection and measurement devices. Recent events like Fukushima in Japan, the events of 9/11, and the nuclear industrial renaissance have placed a significant demand to enhance radiation instrumentation. Much research effort is therefore needed to understand the materials currently used for neutron detection, and to explore the potential use of other materials. Neutron devices must meet the requirements of design and performance established by regulatory bodies. Current detector technology regarding neutron spectrometry and dosimetry has many drawbacks and limitations. Significant work must be done to explore the possibilities and develop new options to ensure that these devices meet the requirements.

Objective of Thesis

The objective of this thesis is to investigate the spectrometric properties of scintillating materials as a first step to establish a platform for developing a neutron spectrometer/dosimeter. More specifically:

1. Investigate different neutron sensors that can be used to carry out neutron spectrometry; the first for thermal and epithermal energy regions, and the second for the fast energy region.
2. Investigate the possibility of using a single neutron sensor with different neutron sensitive elements to exploit different neutron reactions.

Novelty and Contribution

With the lack of any neutron spectrometric system that can accurately and sensitively measures the neutron spectra, an investigation was embarked on with newly developed sensors. To our knowledge, this attempt is:

- The first work done in neutron spectrometry using dual neutron absorption reactions;
- The first series of experiments conducted with a scintillator from the elpasolite family;

- The first effort to combine simulation and experimental work to analyze the nature of peaks on the pulse height spectra obtained with the elpasolite family.

It is worth mentioning that the LiI:Eu scintillator was used in this work for comparing different low energy neutron detectors.

Approach

This thesis has taken an empirical approach in studying potential sensors that can be used for neutron spectrometry. Different scintillators, for a particular energy region, have been explored and studied. The first part of the thesis consists of extensive Monte Carlo calculations to investigate the detector response functions to a given radiation type, and to optimize the sensor's isotope contents not only for higher sensitivity but also for good discrimination. The second part consists of conducting a series of experiments using three main facilities, namely an AmBe source of 120 mCi, a D-D neutron generator of 2.5 MeV neutrons at the University of Ontario Institute of Technology, a KN Van De Graaff accelerator at McMaster University, and gamma-ray sources with different energies. All sensors have been used in conjunction with a miniature data acquisition system that consists of a multi-channel analyzer, mounted on a photomultiplier and controlled by software to operate, control and analyze the output data. The time characteristics of the output signals (pulse) such as integration time and rising time have been optimized for each sensor to obtain the desired response.

Outline of Thesis

The thesis consists of an introduction, four chapters, a conclusion, recommendations, a list of publications and references, and appendices. Chapter 1 presents a detailed background on the fundamental theories of neutron and gamma radiation interaction and detection. Chapter 2 gives a thorough literature review of neutron detectors and spectrometers/dosimeters. Chapter 3 describes a detailed and comprehensive methodology of the study using simulations and experiments. Chapter 4 gives the simulation and experimental results and analysis with an inter-comparison of detectors. The conclusion summarizes the main findings of the sensors' potential

for use in neutron spectrometry/dosimetry. Lastly, recommendations are discussed giving some future possibilities.

Chapter 1: Background on Neutron and Gamma Radiation Interaction and Detection

1.1 Radiation Interactions with Matter

The study of nuclear interactions is fundamental in the field of nuclear engineering. It is therefore imperative to study how radiation interacts with matter. Firstly, it is essential to focus on the fundamental particles that affect the design of nuclear systems and facilities. On the atomic and nuclear level, these include the electron, proton, neutron, photon, and neutrino. Atomic radiations that originate from the orbital electron system of the atom are photons (x-rays, ultraviolet and visible radiations) and electrons. Nuclear radiations from radioactive materials are alpha particles, beta particles (electrons and positrons) accompanied by neutrinos and gamma-rays. These are sometimes associated with atomic radiations, produced by interactions of the excited nucleus or nuclear radiations with the orbital electron system i.e. x-rays accompanying *K*-electron capture by the nucleus; and internal conversion electrons associated with gamma-ray emission. Photons, nucleons, and heavy ions are the common (lighter) products of nuclear reactions at intermediate energies (< 100 MeV).

For the purpose of this thesis, the focal point is neutral radiation, neutrons and gamma-rays that comprises a mixed radiation field commonly found in nuclear facilities. Charged particle radiation is included as a result of the process in which these types of radiation interact with matter.

1.1.1 Gamma-ray Interactions with Matter

Gamma rays are electromagnetic radiation that travel at the speed of light and have zero mass and charge. They interact with matter through various mechanisms, however concerning radiation detection, primarily through three mechanisms: photoelectric effect, Compton scattering, and pair production. Through each of these mechanisms, the gamma ray energy is transferred to electron energy. The probability of interaction depends on the gamma ray energy, and the electron density of the material which is determined by its atomic number, Z.

1.1.1.1 Photoelectric Effect

The photoelectric effect occurs at low photon energies with highly dense materials. The interaction occurs with the photon and an electron. Consequently, the photon is fully absorbed and all of its energy is transferred to the atomic electron, known as a photoelectron, and is ejected from the atom. The kinetic energy of the photoelectron can be determined as the difference between the incident photon energy and the binding energy of the electron,

$$E_{e^-} = E_\gamma - E_b \tag{1}$$

where, E_{e^-} is the electron energy, E_γ is the incident photon energy, and E_b is the binding energy of the electron. Since there must be enough energy to eject the electron from the atom, this mode of interaction must occur at distinct photon energies.

The photoelectric mode is predominant for photons of fairly low energy and even more so if the absorbing medium is of high atomic Z number. A rough approximation for the probability of the photoelectric process can be given as,

$$\tau \cong constant \times \frac{Z^n}{{E_\gamma}^{3.5}} \tag{2}$$

where the exponent n is between 4 and 5 depending on the gamma-ray energy of interest.

1.1.1.2 Compton Scattering

Compton scattering occurs at medium photon energies with moderately dense materials. This interaction occurs between the photon and atomic electron. The incident gamma-ray is inelastically scattered at an angle, θ, from its original direction. Only part of the energy of the incident photon is transferred to the electron. The amount of energy transferred depends on the angle of scattering and therefore, the electron energy can range from zero to a large amount of the photon energy. The kinetic energy of the electron can be determined as the difference between the incident photon energy and scattered photon energy,

$$E_{e^-} = E_\gamma - E_{\gamma'} \tag{3}$$

where E_γ is the scattered photon energy. From the conservation of energy and momentum, the energy of the scattered photon as a function of the scattered angle can be calculated as,

$$E_{\gamma'} = \frac{E_\gamma}{1 + \frac{E_\gamma}{m_0 c^2}(1 - cos\ \theta)} \tag{4}$$

where $m_0 c^2$ is the rest-mass energy of the electron, 0.511 MeV. At 0°, the scattered photon is maximum whereas the electron energy is minimum, and at 180°, the scattered photon is minimum whereas the electron energy is maximum. The probability of Compton scattering per atom depends on the number of electrons available, therefore it increases linearly with Z. For radioisotopes of typical photon energies, this is the predominant mode of interaction.

1.1.1.3 Pair Production

Pair production occurs at high photon energies with low density materials. It can only occur if the incident photon energy is equaled to or exceeds double the rest-mass energy of an electron, 1.022 MeV. This interaction occurs between the photon and the electric field of the nucleus. The photon disappears and its energy is converted into an electron-positron pair. From the conservation of energy, the kinetic energy of the electron and positron are given by,

$$E_{e^-} + E_{e^+} = E_\gamma - (m_0 c^2)_{e^-} - (m_0 c^2)_{e^+} = E_\gamma - 1.022\ MeV \tag{5}$$

where E_{e^-} and E_{e^+} are the energies of the electron and positron. For photon energies in the ranges of several MeV, this is the predominant mode of interaction.

Figure 1 shows the regions where certain photon interactions with matter dominate.

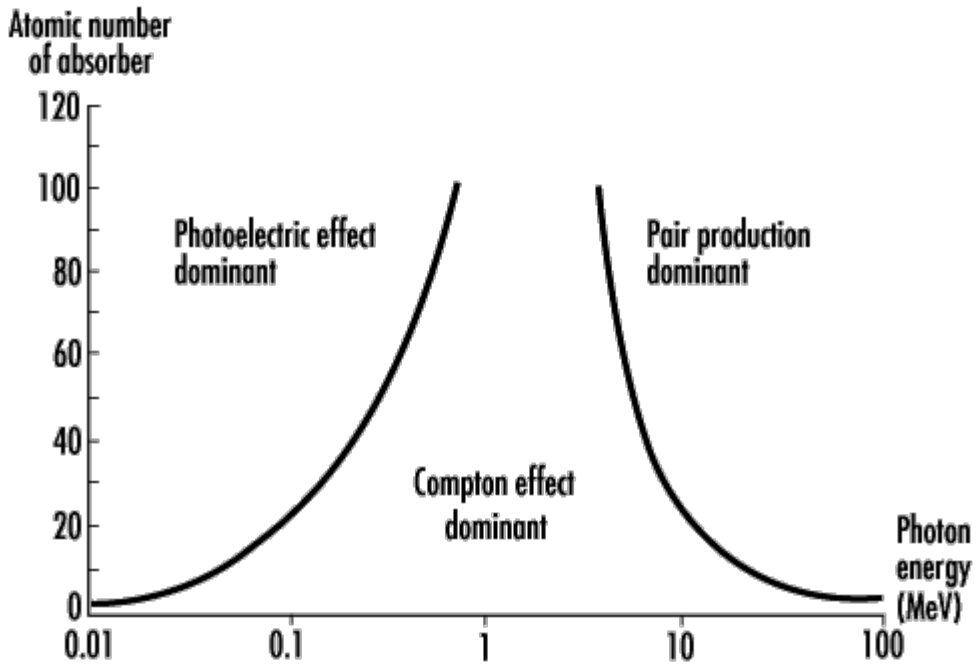

Figure 1: Importance of photon interactions with matter as a function of photon energy [9]

1.1.2 Neutron Interactions with Matter

Neutrons are found in the nucleus of an atom, along with protons. They have a mass but do not carry a charge. Due to being neutral, they do not interact with the electric field of the atom, therefore only interacting by nuclear forces. This enables them to travel some distance through matter without any interaction. Since they interact via nuclear forces, they have a higher cross section of interaction around the nucleus than charged particles. Neutron interactions can be divided into two categories: scattering and absorption. The scattering reactions are called elastic scattering and inelastic scattering. The absorption reactions are called transmutation, radiative capture, and fission. In a scattering process, the number of neutrons and protons in the nucleus is unchanged, only the energy and momentum of the neutron changes. In an absorption process, a neutron is captured and a variety of emissions are possible. Their probability of interaction depends heavily on the neutron energy and the structure of nucleus.

1.1.2.1 Elastic Scattering (n,n)

Elastic scattering is when the total kinetic energy of the colliding particles is conserved. A neutron collides with a nucleus similar to a billiard ball collision. Some energy from the neutron is transferred to the nucleus, which is then scattered at some angle. The amount of energy transferred depends on how 'hard' the hit was. The total kinetic energy is distributed between the neutron and nucleus. This is known as an (n,n) reaction. This mode of interaction is most effective with low Z materials for slowing down neutrons, like hydrogen.

1.1.2.2 Inelastic Scattering (n, nγ)

Inelastic scattering is when the total kinetic energy of the colliding particles is not conserved. A neutron collides with a nucleus and can be absorbed by creating a compound nucleus, leaving it in an excited state. It de-excites by emitting a neutron of lower energy. The remaining energy from the nucleus is released in the form of a gamma-ray photon. This is known as an (n, nγ) reaction. This mode of interaction is common with very high energy neutrons and high Z materials.

1.1.2.3 Transmutation (n, p) (n, α)

Transmutation is when the nucleus of one element is transformed into another element by nuclear reactions. The neutron interacts with the nucleus of the absorbing material forming a compound nucleus. The result is an emission of a heavy charged particle, like a proton or alpha particle, thus resulting in a different element. If a proton is emitted, the atomic number of the element decreases by one unit. If an alpha particle is emitted, the element has one less neutron and two less protons. These are known as (n,p) and (n,α) reactions. An example of an (n,α) reaction is,

$$ {}^{1}_{0}n + {}^{10}_{5}B \rightarrow {}^{7}_{3}Li + {}^{4}_{2}He \qquad (6) $$

where the ^{10}B nucleus absorbs the neutron and becomes ^{7}Li, emitting an alpha particle.

An example of an (n,p) reaction is,

$$^{1}_{0}n + {}^{16}_{8}O \rightarrow {}^{16}_{7}N + {}^{1}_{1}p \quad (7)$$

where the ^{16}O nucleus absorbs the neutron and becomes ^{16}N, emitting a proton. The above reactions are mainly used in all sensors investigated in this thesis.

1.1.2.4 Radiative Capture (n, γ)

Radiative capture is one of the most common neutron reactions. The neutron is absorbed by the nucleus and goes into an excited state. It de-excites by emitting a gamma-ray photon. As a result, the isotopic composition of the element changes due to the addition of a neutron. The nucleus has rearranged its internal structure, releasing a gamma-ray photon. This is known as an (n,γ) reaction. An example of this reaction is,

$$^{1}_{0}n + {}^{12}_{6}C \rightarrow {}^{13}_{6}C + \gamma \quad (8)$$

where the ^{12}C nucleus absorbs the neutron and becomes ^{13}C emitting a gamma-ray photon. The resulting isotope may or may not be stable. In this case, ^{13}C is a stable nuclide. Another example is if ^{2}H absorbs a neutron, it becomes ^{3}H (tritium), which is unstable. This reaction is given by,

$$^{1}_{0}n + {}^{2}_{1}H \rightarrow {}^{3}_{1}H + \gamma. \quad (9)$$

1.1.2.5 Neutral (n, xn)

A neutral type of reaction is where the neutron interacts with the nucleus and emits one or more neutrons. In this way, the nucleus is ridding itself of excess neutrons. It can emit from one to x number of neutrons.

1.1.2.6 Fission (n, f)

Nuclear fission is probably the most important reaction that can occur with neutrons. A thermal neutron interacts with a heavy nucleus taking it into an excited state. Quickly after, the nucleus

will split into fragments and 2-3 neutrons and gamma-ray photons are emitted. There can be various fission fragments produced in this process. This is known as an (n,f) reaction. This reaction is what generates heat in a thermal nuclear reactor via the fission of ^{235}U with thermal neutrons.

1.1.2.7 Neutron Cross Sections

Cross section is the measure of probability for a reaction to occur between two particles. It is measured in the dimensions of area, either in barns or cm^2. The most common types of reaction cross sections are absorption, scattering, and fission. At the level of nucleus, this quantity is called microscopic cross section which reflects the probability for the neutron to interact with a single nucleus.

Realistically, a neutron will not interact with a single nucleus, but rather with a sample of several nuclei. Thus, the macroscopic cross section has been introduced which is a measure of the probability for the neutron to interact with several nuclei in a bulk of material.

1.1.3 Charged Particles Emitted in n-Reaction

Since the detection mechanism used in this work uses secondary charged particles, it is worthwhile to briefly mention the range of different charge particles.

As charged particle moves through matter, they lose their kinetic energy. It does so by interacting with the atoms of the material. This material is called an absorber. The energy of the particle is therefore reduced throughout the absorber. The range of a charged particle depends on the type of particle, the energy, and the absorber material. However, range is an averaged quantity, which means that a particle with the same energy traveling through the same absorber may not necessarily have the same range. It also depends at what point in the absorber the interaction has taken place. For instance, if the interaction took place near the beginning of the material, it is more likely to deposit its entire energy in the absorber, given the absorber's thickness is sufficient for the range of the particle. However, if the interaction took place near the end of the absorber, it is more likely that it would not deposit its entire energy in the absorber,

again depending on the particle's range. As such, the range is important to know to determine the thickness of a material needed in order to stop the particle. It is measured as a distance in m or kg/m^2. They can be related as [111],

$$R\left(\frac{kg}{m^2}\right) = [R(m)][\rho(kg/m^3] \tag{10}$$

where ρ is the density of the material. Charged particles are classified in two categories, light charged particles i.e. electrons and negatrons and heavy charged particles i.e. protons, alphas and heavy ions.

1.1.3.1 Range of Electrons

For electrons in the energy range of 0.3 keV to 30 MeV, the following equation can be used to calculate the range [111],

$$R\left(\frac{kg}{m^2}\right) = a_1\left(\frac{\ln[1 + a_2(\gamma - 1)]}{a_2} - \frac{a_3(\gamma - 1)}{1 + a_4(\gamma - 1)^{a_5}}\right) \tag{11}$$

where,

$$a_1 = \frac{2.335A}{Z^{1.209}} \tag{12}$$

$$a_2 = 1.78\ x\ 10^{-4}Z \tag{13}$$

$$a_3 = 0.9891 - (3.01\ x\ 10^{-4}Z) \tag{14}$$

$$a_4 = 1.468 - (1.180\ x\ 10^{-2}Z) \tag{15}$$

$$a_5 = \frac{1.232}{Z^{0.109}} \tag{16}$$

$$\gamma = \frac{(T + mc^2)}{mc^2} \tag{17}$$

Z is the atomic number of the material, *A* is the atomic weight, *T* is the kinetic energy of the electron, *m* is the rest-mass energy of the particle, and *c* is the speed of light.

For mixtures or compounds of the absorber material, the atomic number and weight can be calculated as [111],

$$Z_{ef} = \sum_{i}^{L} w_i Z_i \tag{18}$$

$$A_{ef} = Z_{ef} \left(\sum_{i}^{L} w_i \frac{Z_i}{A_i} \right)^{-1} \tag{19}$$

where w_i is the weight fraction of the element with atomic number Z_i and the atomic weight A_i.

1.1.3.2 Range of Heavy Charged Particles: Alpha Particle

The range of an alpha particle can be determined if its range in another material is known. For example, if the range of an alpha particle in air or silicon is known, its range in any other material can be determined. For silicon, using the Bragg-Kleeman rule, the range in any other material can be calculated by [111],

$$\frac{R_1}{R_2} = \frac{\rho_2}{\rho_1} \sqrt{\frac{A_1}{A_2}} \tag{20}$$

where ρ_i and A_i are the density and atomic weight of the material i.

If the material is a compound, the effective atomic weight can be calculated by [111],

$$\sqrt{A_{ef}} = \left(\sum_{i=1}^{L} \frac{w_i}{\sqrt{A_i}} \right)^{-1} \tag{21}$$

where L is the number of elements.

1.2 Neutron and Gamma-ray Detection

For radiation protection, the radiation field must be known in order to properly assess the radiological hazard present. This is done by characterizing the radiation field itself. However, radiation cannot be detected directly. In other words, the presence of radiation cannot be determined by using the human senses; sight, smell, touch, taste and hearing. As a result, it must be indirectly detected. As previously discussed, radiation interacts with matter by different means. These interactions and their effects can be used to determine the presence of radiation.

A single particle or quantum of radiation will undergo some interaction in a solid, liquid, or gaseous medium. In the case of neutral radiation, a significant interaction must occur in the detector in order for the radiation to be quantified. In doing so, the secondary charged particles produced deposits its energy in the medium. Depending on the type of detector, these charged particles either ionize or excite the medium producing a flow of secondary charges. Through signal processing, this information is transmitted using electronics to some readout circuitry. The result is energy deposition events that can be displayed through a spectrum of counts versus channel. These events are proportional to the radiation that interacted with the detector media hereby giving direct information about the radiation field. A basis schematic of this process using a scintillation detector can be seen in Fig. 2.

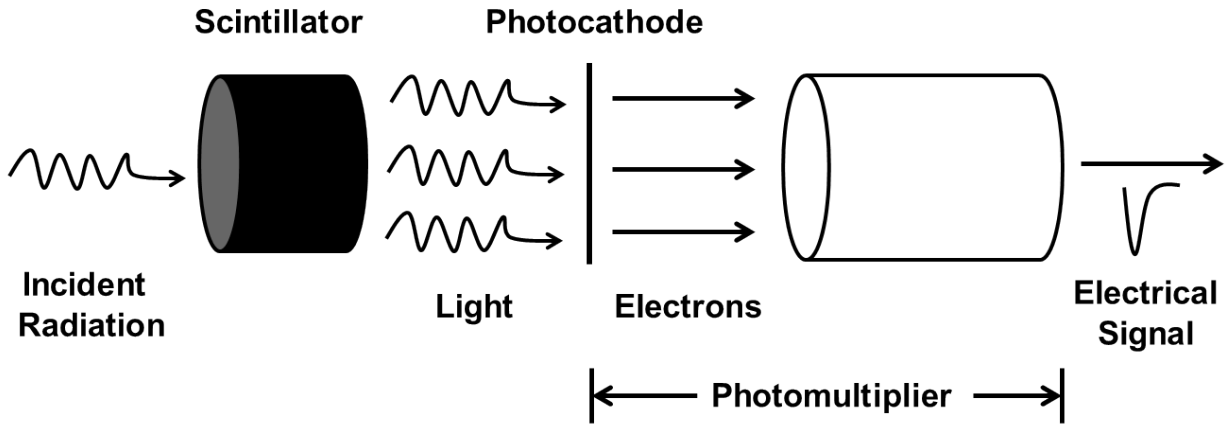

Figure 2: Scintillation Detection Mechanism

The most common types of counters used are:

a) The gas ionization counter in which the particle passes through. Across the chamber a relatively small electric field is applied. The primary ions produced are collected at the electrodes and the ionization charge is measured.

b) The gas proportional counter which is a similar system but with an increased applied electric field so that the primary ions are accelerated and produce secondary ions, which are also accelerated producing further secondary multiplication before collection at the electrodes. The secondary ionization pulse is proportional to the primary ionization.

c) The Geiger-Muller counter in which the field applied across the gas is further increased so that the production of a single ion-pair in the chamber is sufficient to cause a large ionization current pulse to pass, whose magnitude is independent of the primary ionization.

d) The liquid ionization counter similar in principle to the gas counters, in which the application of an electric field across a suitable liquid results in a similar acceleration and collection of primary or secondary ions formed by the passage of an ionizing particle.

e) The solid ionization counter in which the electrons and holes generated by the passage of an ionizing particle through a suitable semiconducting solid (i.e. germanium, silicon, gallium arsenide) are collected under the action of an applied field, which may be enhanced by an internal field, as in the *p*-*n* junction detector.

f) The Cerenkov counter in which the Cerenkov radiation produced in a transparent solid or liquid medium, by an incident ionizing particle whose velocity exceeds the velocity of light in the medium is detected by a photomultiplier.

g) The scintillation counter in which the fluorescence emission produced in a suitable solid, liquid or gas by an ionizing particle is detected by a photomultiplier or other light-sensitive device or in its original form, by eye.

Counters may be employed in numerous ways: as simple detectors recording all ionizing particles passing through their sensitive volume; as ratemeters recording the radiation flux; as

spectrometers yielding information about the energies and relative intensities of the ionizing radiations; as particle discriminators differentiating between different types of radiation; as timing devices recording prompt of delayed coincidences between related ionizing particles; as particle selectors choosing ionizing particles or events which satisfy certain energy, temporal and/or spatial criteria. It is in the last role that they are normally used in conjunction with track visualization chambers.

The most versatile instrument is the scintillation counter. In its various forms it may be used in all the functions enumerated, as a detector, ratemeter, spectrometer, particle discriminator, timing device, and particle selector; and it is suitable for the detection and measurement of the complete range of particles listed above. No other single nuclear instrument approaches its range of application, flexibility, and its adaptability, but then the scintillation counter is not a single instrument, but the generic name for the family of instruments based on the same general physical principles.

1.2.1 Gamma-ray Detection

Gamma-rays or photons for that matter are a type of neutral radiation in that they carry no charge. Since they are indirectly ionizing, in order for a photon to be picked up by a detector, it must undergo a reaction that produces secondary charges particles. Irrespective of the type of interaction, electrons are always produced. This simplifies the detection process because the focus is only on how electrons excite the atoms in the medium. If a mono-energetic source of gamma-rays, for example ^{137}Cs interact with a scintillation detector, the ideal spectrum where only a single photoelectric peak is observed is given in Fig. 3.

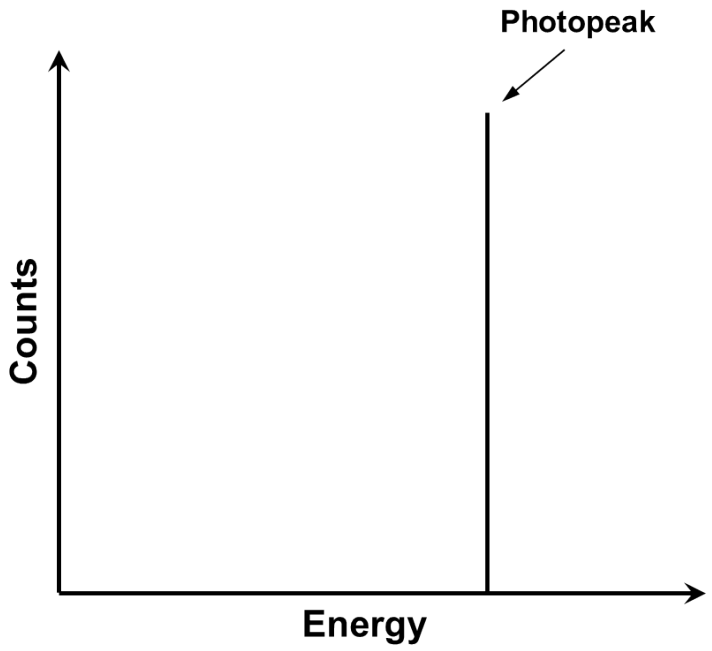

Figure 3: Ideal gamma-ray spectrum with photo-peak

If a gamma-ray undergoes Compton scattering, only partial energy is deposited depending on the angle to which is was scattered. The maximum energy deposited is at the Compton edge when the gamma-ray is scattered at 180° and the minimum energy is at 0°. The resulting ideal spectrum including both Compton scattering and the photoelectric effect is seen in Fig. 4.

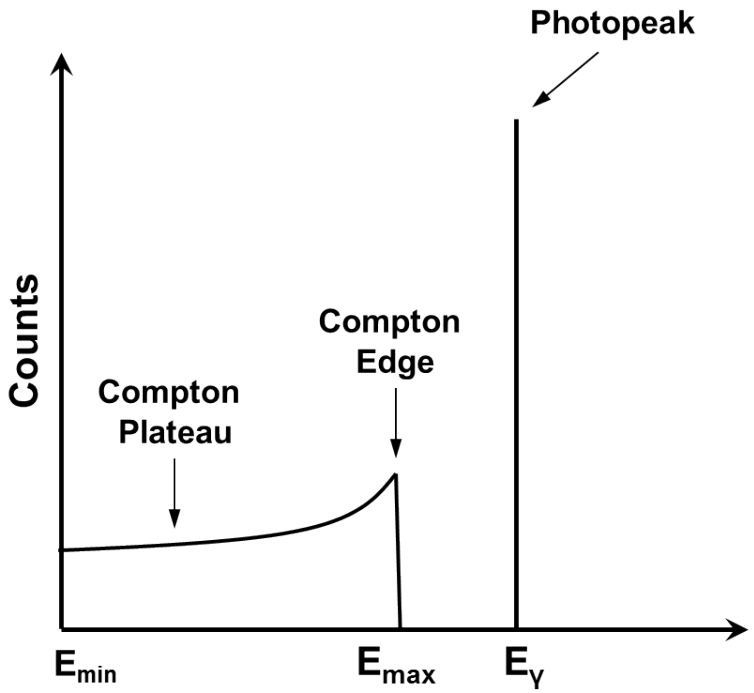

Figure 4: Ideal gamma-ray spectrum with photo-peak and Compton scattering

A typical gamma-ray spectrum for one gamma-ray energy can be seen in Fig. 5.

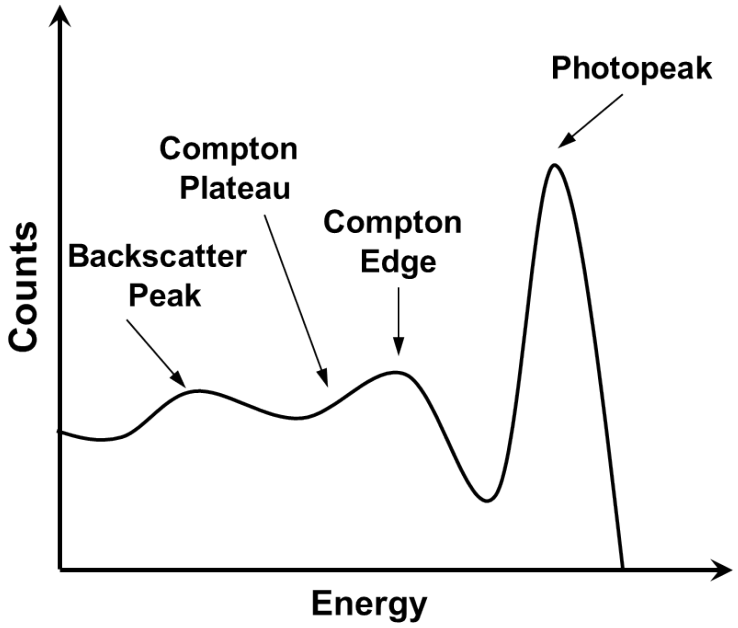

Figure 5: Typical gamma-ray spectrum

In order to reliably measure the detector's response to a known number of counts, it must be properly calibrated. Different gamma-ray sources are used for this purpose. Table 1 outlines the most common energies used.

Table 1: Gamma-ray energies used for calibration

Radioactive Isotope	Decay mode	Daughter	Gamma-ray energy (MeV)
^{60}Co	β^-	^{60}Ni	1.332 1.172
^{137}Cs	β^-	^{137}Ba	0.032 (X) 0.662
^{22}Na	β^+	^{22}Ne	0.511 (A) 1.274

When the daughter is highly ionized, it emits a characteristic x-ray as denoted by X, as in the case of ^{137}Ba. When a source emits positrons, they usually annihilate with electrons producing two gamma-rays of energy 0.511 MeV, equal to the rest mass energy of the electron, as in the case of ^{22}Na. An example of a decay scheme is given for ^{22}Na in Fig. 6.

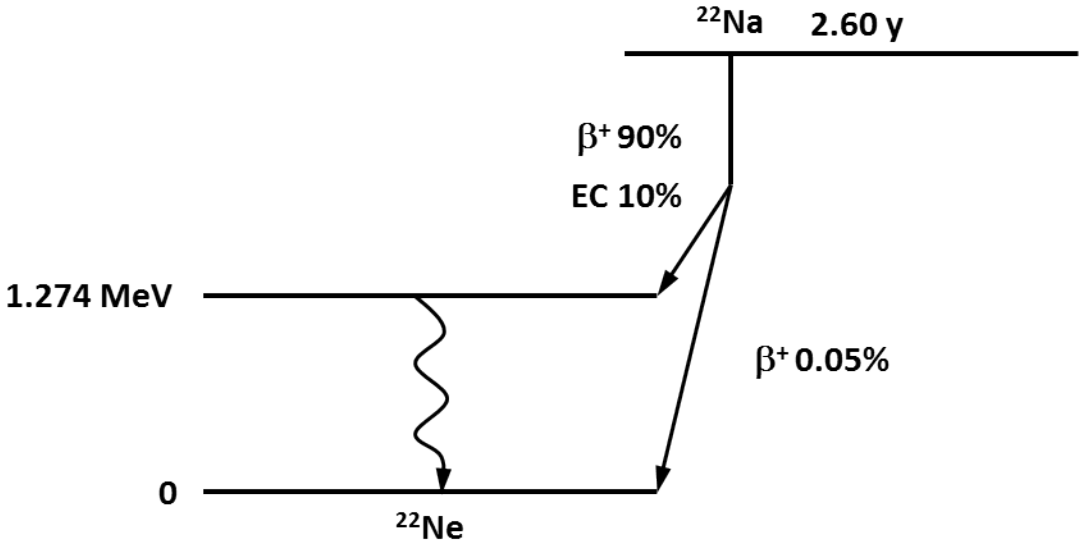

Figure 6: ^{22}Na decay scheme

The typical range of gamma-ray energies existing in nuclear power plants is up to 3 MeV. For this range of energies, common gamma-ray detectors and spectrometers employed are those of high atomic number Z due to the likeliness of registering a full energy peak in the detector.

1.2.2 Neutron Detection

Similarly to photons, neutrons are also indirectly ionizing so they must also undergo a significant interaction to produce secondary charged particles in order to be detected. The complexity arises because neutrons produce different types of charged particles depending on the material the interaction occurs with and the neutron energy. Both absorption and scattering reactions are used for neutron detection. Based on absorption reactions, protons, alpha particles, deuterons, tritons, and fission products are used. Based on scattering reactions, the transfer of kinetic energy from the neutron to the target nucleus is used. The choice of reaction and material used depends highly on the incident neutron energy and its neutron cross section. Therefore, neutron detection requires:

a. Large cross section of reaction
b. Relatively high released energy or high conversion of kinetic energy
c. Ability to discriminate between gamma-ray and neutron induced events

If absorption reactions like (n,p) and (n,α) are used, full energy peaks are observed in the response indicating that a neutron was detected. If scattering reactions like elastic scattering is used, a continuum of energies is observed in the response with its edge being equal to the incident neutron energy. Due to this, a variation in detector response is observed, but which each having the same underlying principle.

Two possibilities can be changed to obtain the desired response. Either the material is changed to one that has a high neutron reaction rate, or the energy distribution is modified (i.e. moderation) to be compatible with the interacting medium. Consequently, a variety of detectors exist for different neutron energy groups. Typically they are divided into two groups, those that detect slow neutrons (thermal, epithermal, resonance) and those that detect fast neutrons.

1.2.3 Specification of Scintillators Detector Properties

1.2.3.1 Detector Modes

The most common mode of detector operation is pulse mode. In this mode, the detector registers each quantum of radiation that passes through it. Using this mode, the energy of the ionizing radiation can be obtained since there is a direct relationship between the total charge generated and the deposited energy in the detector. The advantage of this mode is that each individual quantum of radiation contributes to an individual pulse.

The two other modes of operation are current mode and mean square voltage mode. Current mode is useful when events in the detector overlap, making it hard to distinguish between them. This is due to very little time between the events. In this mode, an average current is produced using the product of the event rate and the average charge per event. Therefore, this mode is used especially when event rates in the detector are quite high.

Mean square voltage mode is used especially in mixed fields of radiation. The signal that is recorded in this mode is proportional to the event rate and the square of the charge generated in each event. Since it is the square of the charge that is recorded, one can distinguish between the different types of radiation in the signal based on their charges.

Each mode has its applications; however pulse mode remains the most popular choice in nuclear instrumentation.

1.2.3.2 Pulse Height Spectra

Since radiation detectors operate more in pulse counting mode, one needs a convenient way to display the pulse distribution. The pulse height spectra can be illustrated by either differential or integral pulse height distribution. The differential pulse height spectrum gives the area under the distribution between two pulse height limits. It is plotted as the differential number of pulses per differential height ($volts^{-1}$) versus the pulse height (volts). The integral pulse height spectrum gives the total area under the distribution. It is plotted as the number of pulses exceeding pulse height versus the pulse height. The differential pulse height spectrum is most commonly used to display the pulse height spectrum.

These pulses from the detector can now be fed to a counting device. Its purpose is to register a pulse as a count if the pulse height exceeds a fixed pulse height discrimination level. This level can be changed and generally operates around the minimum slope of the integral distribution known as the plateau. At this point, drifts from the discrimination level are kept at a minimum which would have minimal effect on the counts registered.

1.2.3.3 Energy Resolution

Energy resolution is an important property of a detector in radiation spectroscopy. It is the ability of the detector to identify a mono-energetic source of radiation. The pulse height spectra of the detector will typically have a Gaussian shaped peak corresponding to a single energy from various events. The amount of fluctuations in the events corresponds to the width of the peak. The smaller the width, the less amount of fluctuations there were, hence a better resolution. Energy resolution, E_R, is determined by measuring the full width at half maximum (FWHM) in units of energy divided by the location of the peak centroid, E_0. As such, energy resolution is dimensionless, usually expressed as a percentage.

$$E_R = \frac{\text{FWHM}}{E_0} \tag{22}$$

Factors that affect energy resolution are statistical fluctuations in the number of charge carriers produced in the detector, random electronic noise in the detector and instrumentation system, incomplete collection of the charge produced in the detector, and the statistical noise from the discrete nature of measuring the output signal. The combination of these fluctuations gives the overall energy resolution of the entire measuring system.

Statistical fluctuations can be thought as some variation that is inherent. In scintillation detectors, the charge carriers are the electrons produced when the light photons interact with the photocathode. In the scintillation detector itself, the amount of energy that is deposited in each event is the same; however the amount of charge carriers can fluctuate per event. This results in the registration of different energies from the distinct energy that contribute to the width of the peak in the pulse height spectra.

Factors that contribute to the line width (resolution) are:

1. Emission of photons by the scintillator
    a. There may be local variations in the scintillation efficiency, due to a non-uniform distribution of activator ions, crystal defects, or flaws.
    b. Successive particles may dissipate different amounts of energy in the scintillator due to scattering and edge effects.
    c. An important source of scintillation variance may arise from the fact that the scintillation efficiency depends on dE/dr, and that the scintillator may be excited not only directly by primary charged particles, but also by delta rays of different dE/dr, the number of which is small and thus subject to significant statistical fluctuations. In the case of excitation by mono-energetic gamma-rays, the scintillations in the full-energy photo-peak are due to the incident energy which is partitioned in various ways between secondary (photo, Compton, pair, Auger) electrons of differing dE/dr.
2. Collection of photons by the photocathode – the optical efficiency varies from point to point within the scintillator, due to the variations in optical geometry. Self-absorption, reflection losses, light trapping, optical flaws and inefficient light piping may all contribute to a reduction in this, and an increase in its fractional variance.
3. Emission of photo-electrons and collection at dynode 1 – the efficiency factor depends in a complex manner on the wavelength and the point of incidence on the photocathode of the scintillation photons.
    a. The spectral matching factor depends both on the cathode response and the scintillator spectrum and depends on the cathode material and its thickness.
    b. The electron collection efficiency depends on the photocathode-dynode 1 structure and potential.
    c. The degree of uniformity of the photomultiplier response over the area of the photocathode.
4. The electron multiplication process – the use of a high cathode-dynode 1 potential.

When a scintillator is coupled to a photomultiplier, both types of resolution need to be incorporated. The sum of the quadrature is thus,

$$\left(\frac{\Delta E}{E}\right)^2 = \delta_s^2 + \delta_p^2 \tag{23}$$

where δ_s^2 is the intrinsic resolution of the scintillator and δ_p^2 is the photoelectron statistics. More specifically, the photoelectron statistics is described as,

$$\delta_p^2 = 2.36^2 \times \frac{1}{N} \times (1 + \nu) \tag{24}$$

Where: N is the amount of photoelectrons produced and ν is the variance of photomultiplier gains. The variance is the number of photoelectrons in the photopeak obtained for each energy.

1.2.3.4 Detector Efficiency

Detector efficiency is the ability of the detector to register the exact number of pulses based on the amount of radiation that it is exposed to. For example, a detector that registered the same number of pulses as there were incident particles on the detector would be 100% efficient.

There are two types of efficiencies that can be determined, absolute and intrinsic. The absolute efficiency is defined as,

$$\epsilon_{abs} = \frac{number\ of\ pulses\ recorded}{number\ of\ radiation\ quanta\ emitted\ by\ source} \tag{25}$$

and the intrinsic efficiency as,

$$\epsilon_{int} = \frac{number\ of\ pulses\ recorded}{number\ of\ radiation\ quanta\ incident\ on\ detector} \tag{26}$$

Charged particles like alpha and beta particles will ionize or excite quickly once entering the detector; whereas neutral particles like gamma-rays and neutrons can travel a longer distance without any interaction. Therefore, detectors for charged particles are generally 100% efficient whereas for neutral particles are less efficient.

1.2.3.5 Scintillation Efficiency

In any scintillator, the amount of energy from the incident particle that is converted to visible light is known as the scintillation efficiency. It is desirable to have this value to be as high as possible. However, when alternate de-excitation modes occur that are radiationless, such as heat, no photons are emitted. These processes are collectively known as quenching. Subsequently, this affects and decreases the light output. Quenching occurs in both inorganic and organic scintillators.

1.2.3.6 Light Output

Light output is probably one of the most important properties of a scintillation material. It is the coefficient of converting the ionizing radiation into light. Only part of the kinetic energy from the charged particle is converted into light. The rest is lost through lattice vibrations or heat. In fact, much of the energy from the radiation goes towards non-radiative means. The combined efficiency of the scintillator and photocathode is what is generally used in high energy physics to define light output. Light output is measured in number of photons per MeV of absorbed radiation.

The main factors that determine the light output of a scintillator:

- Scintillator material
- Type of incident particles
- Energy of particles
- Temperature
- Ionization density

This can be illustrated in Fig. 7 for the NE-102 scintillator, where the light output for electrons is higher than that for protons at equal energy due to their ionization density.

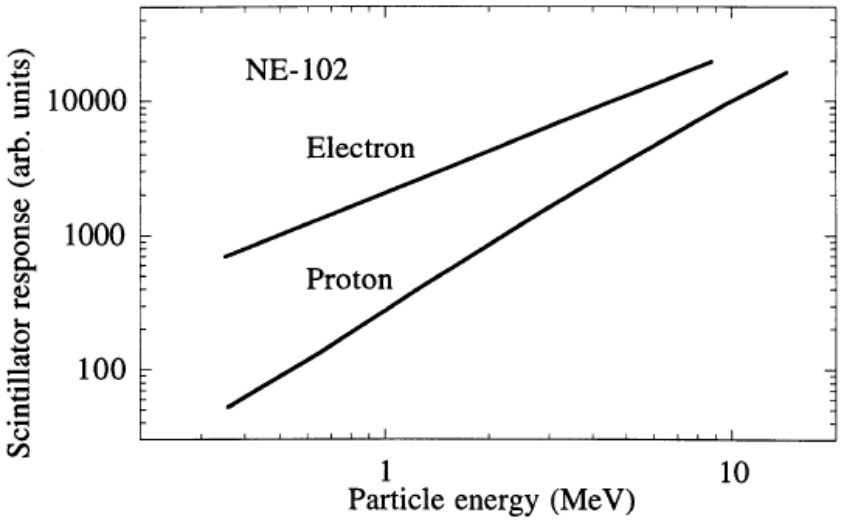

Figure 7: Light output curve for NE-102 [8]

Light output can change considerably if the impurity concentration in the material is changed. A point to remember is that the production of scintillation light is a very inefficient process since most of the energy delivered by the radiation goes to radiationless transitions.

1.2.3.7 Decay Time

Scintillation light output does not happen instantaneously. The prompt fluorescence takes some time to occur after the molecules have been excited. This is known as decay time. It is the rate at which the scintillation light is emitted following the excitation of the material. They are characteristic to the scintillator and can range from a few nanoseconds to several microseconds. Most scintillators are characterized by a single decay time. Some scintillators however have a more intricate scintillation mechanism resulting in a more complicated time behaviour. A short decay time is what is sought for in scintillators used for radiation detection.

The rate at which the excited electron decay back to ground state is represented by,

$$I = I_0 e^{(-\frac{t}{\tau})} \tag{27}$$

where I is the instantaneous emission intensity, I_0 is the initial emission intensity, and τ is the fluorescence decay time.

Figure 8 illustrates the decay time for different incident particles in stilbene. Ionization density also has an effect on decay time. The light emitted from lighter charged particles like electrons is faster than that of heavier charged particles like alpha.

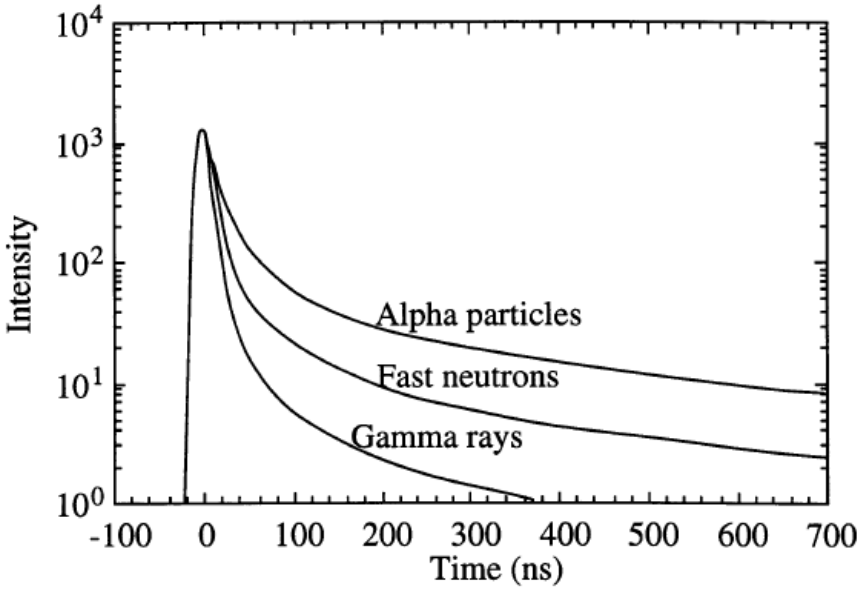

Figure 8: Decay time for stilbene [8]

1.2.3.8 Emission Spectrum

Emission spectrum is the spectrum of wavelengths of the emitted scintillation light. This spectrum depends on the energy structure in the crystal lattice. As a result, each scintillator will emit a characteristic emission spectrum; that is the amount of photons emitted as a function of wavelength. The photons emitted have a distribution of wavelengths in the visible region of the electromagnetic spectrum. Figure 9 shows the emission spectra of commonly used scintillators. It is necessary to know the emission spectra of each scintillator in order to appropriately match it with a PMT. That is, most of the scintillation light that will be detected should fall near the wavelength region of maximum sensitivity. The response of two commonly used photocathodes is also plotted in Fig. 9 for reference to the scintillators' spectra.

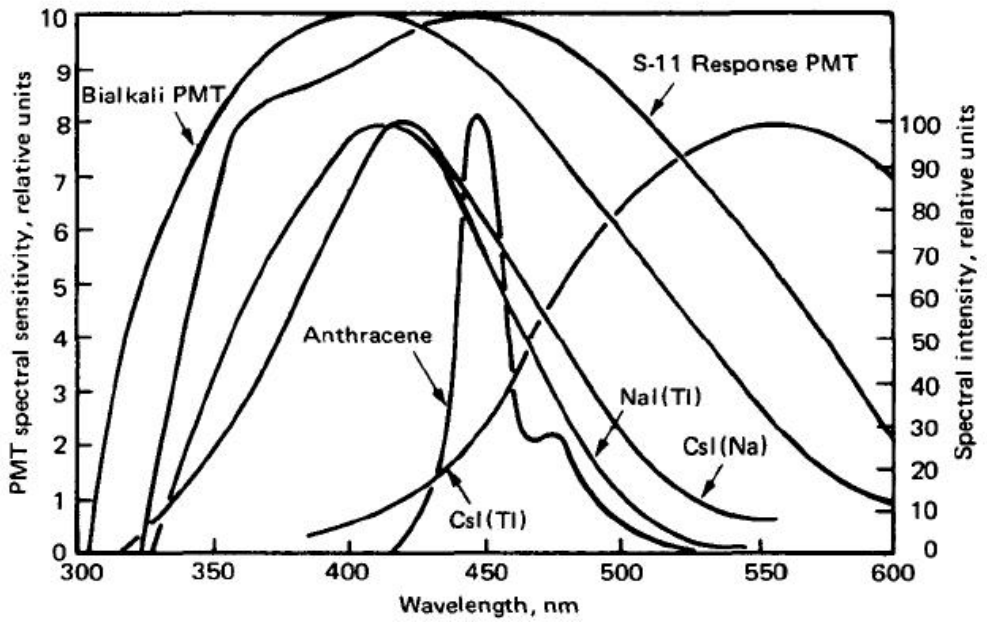

Figure 9: Emission spectra of common scintillators [8]

1.2.3.9 Light Collection

Ideally, the greatest fraction of light should be collected that was produced from the ionizing radiation. There are however factors that prevent this from occurring. These factors include self-absorption within the scintillator and losses at the surface. The scintillator should be transparent to the scintillation light. In pure inorganic crystals, the same energy required to create an electron-hole pair is needed to recombine them, resulting in an identical emission and absorption spectra, leading to self-absorption. In activated crystals, the energy is less for emission than absorption, and therefore the subsequent emission and absorption spectra do not have the same wavelengths, and is therefore transparent to its own light. The scintillation light is also being emitted in all different directions, and therefore only part of it will reach the surface of the PMT. One way to counter this is by adding a reflector to all of the surfaces of the scintillator except which the PMT is mounted at.

1.2.3.10 Wall Effect

The wall effect occurs when the detector is not large enough compared with the range of the charged particle, therefore the charged particle cannot deposit all of its energy in the detector. Instead, it will end up interacting at the wall of the detector, contributing to a smaller pulse. The amount of energy deposited at the wall will depend at which point in the detector the interaction took place, the type of particle and its energy.

1.2.4 Scintillation Mechanism

Scintillators are materials that fluoresce after absorption of ionizing radiation. Essentially, charged particles excite the atoms or molecules in the medium. These excited states then decay by emitting photons that are detected and transformed into electric signals. The basic principle can be illustrated in Fig. 10.

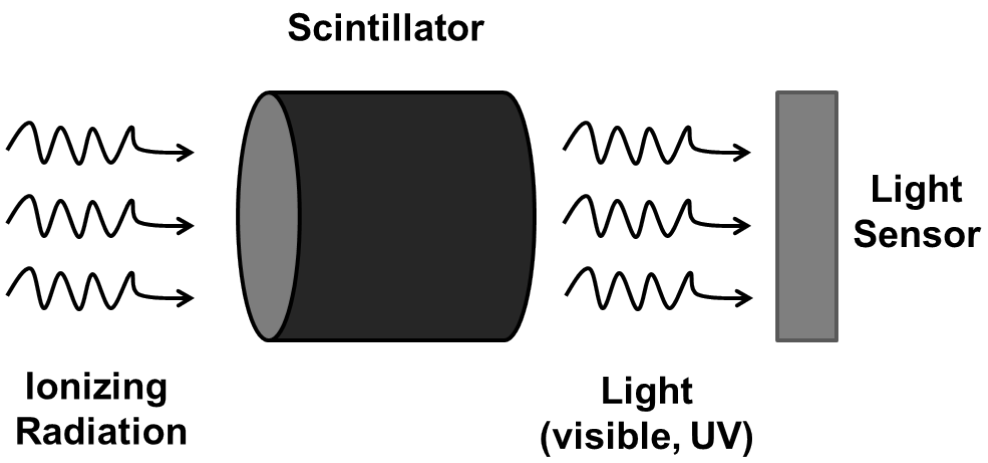

Figure 10: Scintillation detector principle

Scintillating materials can be both organic and inorganic and be in the solid, liquid, or gaseous states. The scintillation mechanism however, differs depending on the type of scintillator.

1.2.4.1 Inorganic Scintillators

In inorganic scintillators, the scintillation depends on the crystal lattice which determines the energy states. Additionally, a pure inorganic crystal and an activated crystal also exhibit different

scintillating behaviour. When radiation passes through the medium, electron-hole pairs are created. Naturally, they will recombine and emit a photon with energy equivalent to the energy band. In pure inorganic crystals, electrons can never be found in the intermediate band of energies known as the forbidden band. When energy is absorbed, electrons jump from the valence band to the conduction band, leaving a hole or gap in the valence band. If the electron returns to the valence band, more of the energy is emitted by non-radiative means, resulting in fewer photons. Further, the band gap width is too high therefore its energy it too great to exist in the visible region of the electromagnetic spectrum, and the emission wavelength will be equivalent to the absorption wavelength and therefore be self-absorbed. As a result, this process in pure crystals becomes inefficient.

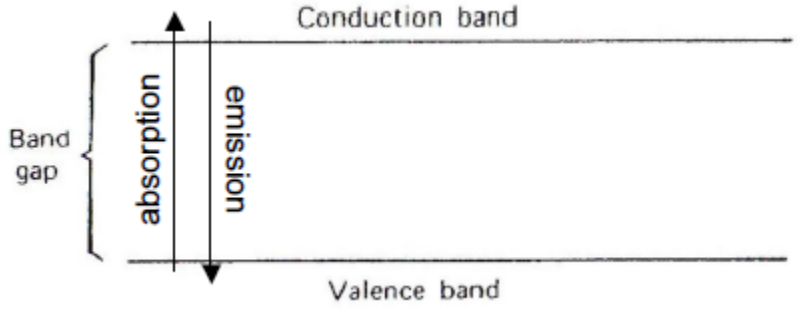

Figure 11: Pure inorganic crystal energy band structure [8]

To improve the efficiency, an activator is added to the crystal. This will increase the number of photons emitted in the visible region. Tiny amounts of impurities that are known as activators or dopants are added. By adding this, it modifies the energy band structure, creating additional sites in the crystal lattice. During the de-excitation process, the electrons will fall into these newly created sites within the forbidden band that are known as luminescence centers. These gaps are smaller than the forbidden band and will therefore be of less energy creating more visible photons. Since the electron transitions will be lower energy than that of a pure crystal, the emitted photons will have a longer wavelength and not be absorbed by the crystal. The formation of these activator sites or luminescence centers produces a more efficient scintillation process.

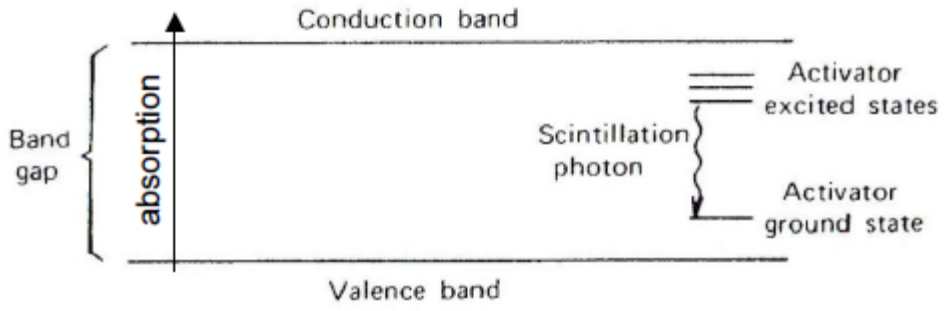

Figure 12: Activated inorganic crystal energy band structure [8]

More specifically, when electron-hole pairs are created as the electron jumps from the valence to the conduction band, the positive hole will shift towards an activator site and ionize it due to the lower ionization energy of the activator as opposed to the pure lattice. The free electron migrates throughout the crystal and drops into an activator site, creating a neutron configuration. As illustrated in Fig. 12, this site has its own energy states. If the activated state is excited, it will de-excite rapidly emitting photons within a range of 30-500 ns. This decay time notably determines the time characteristics of the scintillation light. This prompt type of luminescence is known as fluorescence.

A delayed light component can also be emitted. If the electron once arriving to the activated site is excited but cannot transition to the ground state, additional energy must be applied to raise them to a higher energy state such that is can de-excite. Often times, this extra energy source can be from thermal excitation. This delayed type of luminescence is known as phosphorescence.

Another possibility of emission exists if the transition of the electron, once captured at the activated site, is radiationless; this is known as quenching. No photon will be emitted thus resulting in a loss of the deposited particle energy to scintillation light.

It is also possible that instead of the excited electron and hole migrating freely, the pair could migrate together which is known as an exciton. The associated electron and hole can travel throughout the crystal together, upon reaching activator site in which the excited activator configurations can be created and the aforementioned process of emitting scintillation light can occur.

1.2.4.2 Organic Scintillators

Organic scintillators behave much different than inorganic scintillators. While in inorganic scintillators, the scintillation is due to the physical structure of the crystal lattice. In organic scintillators, the fluorescence process is due to the transitions in the energy levels of a single molecule and therefore does not depend on the physical state of the material. Whether it exists as a solid, liquid or gas, the fluorescence process is the same.

Organic scintillators are comprised of organic molecules with symmetry properties that are associated with a π–electron structure. The energy levels of this structure can be seen in Fig. 13.

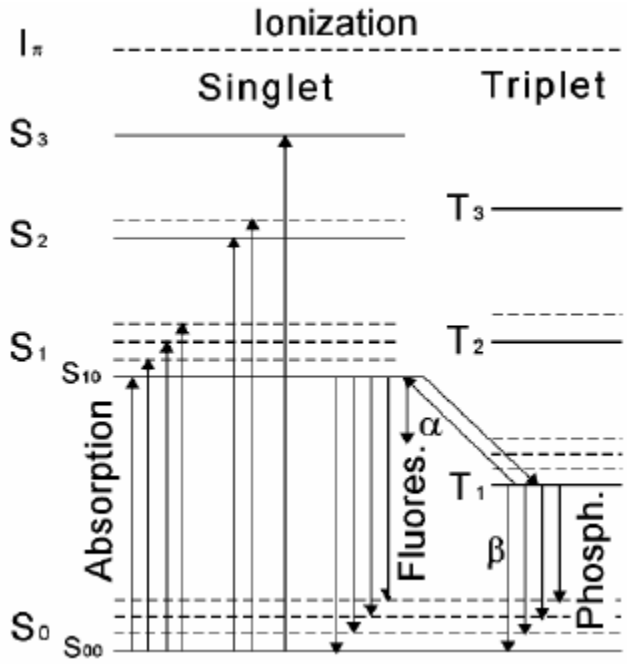

Figure 13: Energy levels of organic molecules [113]

A series of singlet states are S_0, S_1, S_2, and S_3,…and the triplet electronic levels are T_1, T_2, and T_3. The spacing between S_0 and S_1 is 3 or 4 eV, whereas the spacing for the upper states is far less. The S levels are further divided to smaller levels with a spacing of 0.15 eV which correspond to the vibrational states which is denoted as an additional subscript like S_{00}.

When a charged particle passes through the medium, the energy is absorbed by the molecules, and the electrons are excited to upper states. In Fig. 13, the upward arrows represent the

absorbed kinetic energy from the charged particle. The upper states, S_2 and S_3 de-excite rapidly to S_1, in the order of picoseconds, through radiationless conversion. States that have excess vibrational energy, like S_{11} or $S_{12,}$ will rapidly lose its energy. The net result is a populated S_{10} state with excited molecules. The prompt fluorescene in organic scintillators occurs in transitions between the S_{10} state and the ground electronic state. The downward arrows in Fig. 13 represent this emission. This prompt fluorescence is usually in the order of a few nanoseconds, therefore making organic scintillators fast.

Some excited singlet states may be converted to triplet states. The duration of the T_1 state as compared to S_1 state is much longer, in the order of milliseconds. Once the de-excitation occurs from T_1 to S_0, the delayed scintillation light, known as phosphorescence, is emitted.

Organic scintillators are practically transparent to their own light emission because wavelength of emission is greater than that of absorption. This can be related in Fig. 13 by looking at the lengths of the arrows as they correspond to the energy needed. The energy required for emission, represented by shorter arrows, is less than that of absorption, represented by longer arrows. As a result, there is little overlap between spectra which means most of the light goes through the medium. This is known as Stokes shift and can be seen in Fig. 14.

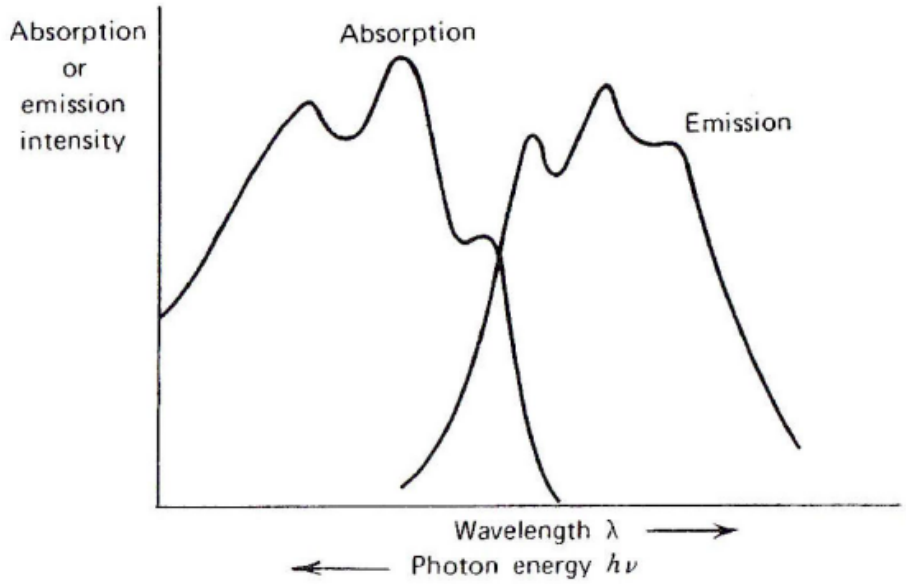

Figure 14: Absorption and emission spectra for organic scintillators [8]

It is important that impurities are eliminated when creating and using organic scintillators, as this will cause quenching, due to alternate mechanisms that can occur for de-excitation.

1.3 Neutron Spectrometry and Dosimetry

Radiation spectrometry is used to describe the intensity of a radiation field, with respect to some quantity such as energy. This distribution of intensity with regards to energy is referred to as a spectrum. Spectrometers have long been used for measuring neutron energy spectra. Over time, the detection mechanisms have improved and have been enhanced by modern techniques. In this process, spectrometers have played a critical role in helping to improve the understanding of the inherent nature and origins of ionizing radiation, contributing much knowledge to the field of nuclear physics.

The type of spectrometer that will be discussed is to be applied in environments where individuals receive radiation doses. The reason for developing these spectrometers is so that individuals that are exposed to radiation fields due to their occupation can receive the proper radiation protection needed. These measurements are then required to increase the knowledge of such fields.

More precisely, this thesis aims to discuss neutron spectrometry; with the goal in neutron spectrometry being to measure the energy distribution from incoming neutron radiation.

1.3.1 Fluence

Fluence is a key quantity in spectrometry. The fluence that is of concern in dosimetry is particle fluence and energy fluence and in time, particle fluence rate, and energy fluence rate. In this case, the focus is neutron and photon fluence. Particle fluence is the number of particles that are incident on a sphere of cross-sectional area. It is the quotient dN by dA_c,

$$\Phi = \frac{\mathrm{d}N}{\mathrm{d}A_c} \tag{28}$$

It is represented in units of m^{-2}.

The energy fluence is the radiant energy incident on a sphere of cross-sectional area. It is the quotient of dE by dA_c,

$$\Psi = \frac{\mathrm{d}E}{\mathrm{d}A_c} \tag{29}$$

It is represented in units of J/m^2. It can also be calculated from the particle fluence by,

$$\Psi = \frac{\mathrm{d}N}{\mathrm{d}A_c}E = \Phi E \tag{30}$$

where E is the particle energy with the number of particles dN with energy E.

In reality, most neutron or photon beams are not monoenergetic, therefore the particle fluence spectrum and energy fluence spectrum differential in energy E is defined as,

$$\Phi_E(E) = \frac{\mathrm{d}\Phi}{\mathrm{d}E}(E) \tag{31}$$

and

$$\Psi_E(E) = \frac{\mathrm{d}\Psi}{\mathrm{d}E}(E) = \frac{\mathrm{d}\Phi}{\mathrm{d}E}(E)E \tag{32}$$

The particle fluence rate is the rate of change of fluence in the time interval and is defined as,

$$\dot{\Phi} = \frac{\mathrm{d}\Phi}{\mathrm{d}t} \tag{33}$$

It is represented in units of m^{-2}·s^{-1}.

Similarly, the energy fluence rate is the rate of change of fluence in the time interval and is defined as,

$$\dot{\Psi} = \frac{\mathrm{d}\Psi}{\mathrm{d}t} \tag{34}$$

It is represented in units of W/m^2 or J·m^{-2}·s^{-1} [10].

1.3.2 Kerma

Kerma stands for kinetic energy released per unit mass. It is a non-stochastic quantity and relates to indirectly ionizing radiation, like photons and neutrons. As we know, indirectly ionizing

radiation only imparts its energy to matter through their secondary charged particles. So, kerma is the average amount of energy transferred from indirectly ionizing radiation to directly ionizing radiation. It is defined as the energy imparted in a medium per unit mass from photons or neutrons to charged particles,

$$K = \frac{\mathrm{d}\bar{E}_{tr}}{\mathrm{d}m} \tag{35}$$

It is represented in units of J/kg or Gray (Gy) [10].

1.3.3 Absorbed Dose

Absorbed dose quantifies the energy imparted to matter from any type of radiation. Like kerma, it is also a non-stochastic quantity. For directly ionizing radiation, the charged particles deposit its energy giving the absorbed dose. For indirectly ionizing radiation, the absorbed dose is produced in two steps. The first step gives the kerma, when the indirectly ionizing radiation transfers its energy to secondary charged particles, and the second step gives the absorbed dose, where these charged particles deposit its energy to the medium. This energy is the sum of all of the energy that enters the volume minus the energy that leaves the volume. The absorbed dose is defined as the mean energy imparted by ionizing radiation to matter of mass in a finite volume,

$$D = \frac{\mathrm{d}\bar{\varepsilon}}{\mathrm{d}m} \tag{36}$$

It is represented in units of J/kg or Gy [10].

The neutron dose can be related to the neutron fluence by,

$$D = \int_0^\infty \phi(E)k(E)dE \tag{37}$$

Where: D is the absorbed dose in Grays, ϕ is the neutron fluence in n/MeV/m^2, and k is the neutron kerma factor [11].

1.3.4 Dose Equivalent

Absorbed dose is not very useful in determining the biological effect of a particular radiation. Therefore, another quantity must be introduced, this is known as the dose equivalent. This is the absorbed dose *D* multiplied by a quality factor *Q* which corresponds to the effectiveness of a given radiation. Dose equivalent *H* is given by,

$$H = D \cdot Q \tag{38}$$

It is represented in units of a Sievert (Sv).

The neutron dose equivalent can be related to the neutron fluence by,

$$H = \int_0^\infty \phi(E) k(E) \bar{Q}(E) dE \tag{39}$$

Where: *H* is the dose equivalent in Sieverts and $\bar{Q}$ is the mean quality factor for the interactions of neutrons at energy *E* [11].

1.3.5 Neutron Fluence-to-Dose Equivalent Conversion Factors

The relationship between fluence and dose is given by a conversion factor. This conversion factor is the dose given by one particle when passing through an area of 1 cm^2. Therefore, if the neutron fluence and neutron energy is known, the correct dose equivalent can be determined. There have been various sets of conversion factors presented by different organizations. They are The National Council on Radiation Protection (NCRP), The International Commission on Radiation Protection (ICRP), Nuclear Regulatory Comission (NRC) in the United States, a publishing in a popular textbook called Auxier, and publishing from literature called Chilton. These values can be seen in Table 2. A graphical representation of values from ICRP-74 is seen in Fig. 15 [118].

Table 2: Sets of neutron fluence-to-dose equivalent conversion factors [12]

Energy (MeV)	Conversion Factor, 10^{-10} Sv·cm^2				
	NCRP	ICRP	NRC	Auxier	Chilton
Thermal	0.102	0.107	0.103	0.115	0.095
10^{-7}	0.102	0.116	–	–	–
10^{-6}	0.124	0.126	–	0.134	0.118
10^{-5}	0.124	0.121	–	0.121	0.116
10^{-4}	0.12	0.116	0.139	0.101	0.110
10^{-3}	0.102	0.103	–	0.086	0.095
5×10^{-3}	_	–	0.122	–	–
10^{-2}	0.099	0.099	–	0.099	0.095
2×10^{-2}	_	–	0.250	–	–
0.1	0.604	0.579	0.833	0.486	0.781
0.5	2.57	1.98	2.33	1.89	2.44
1	3.65	3.27	3.85	3.26	3.79
2	_	3.97	–	–	–
2.5	3.47	–	3.45	3.50	3.41
5	4.34	4.08	3.85	4.41	3.90
7	4.08	–	–	4.03	–
7.5	_	–	4.17	–	4.11
10	4.08	4.08	4.17	4.31	4.14
14	5.79	–	–	6.15	5.26

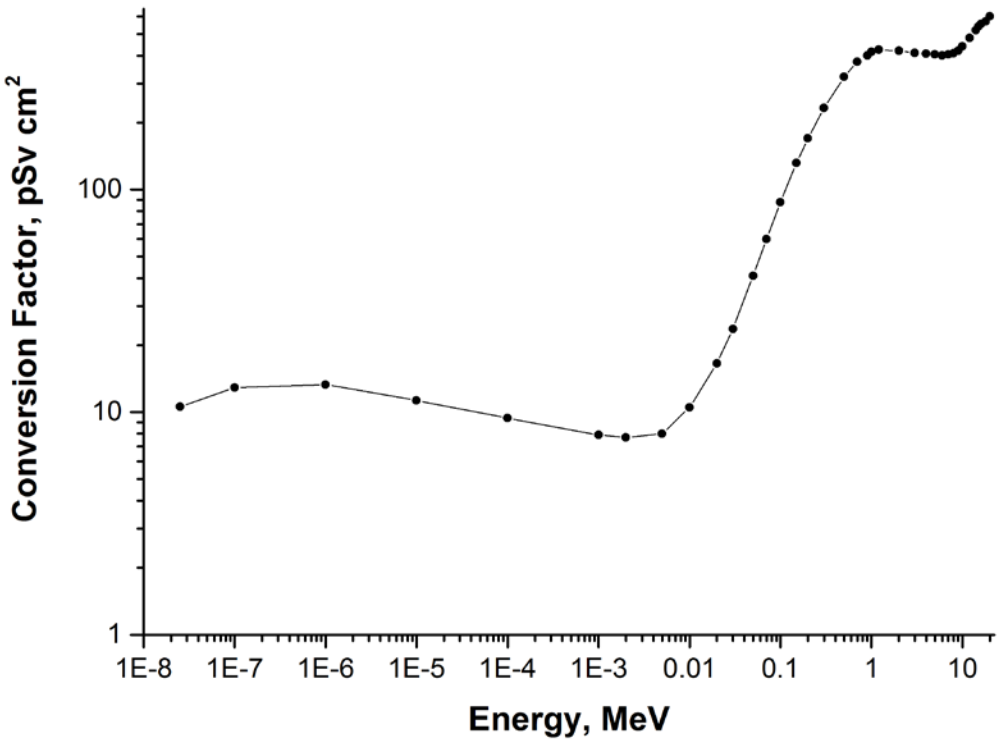

Figure 15: ICRP-74 Neutron fluence-to-dose equivalent conversion factors vs. neutron energy [118]

For thermal and low neutron energies, the conversion factor is fairly constant. In the region of 10 keV to 1 MeV, it increases drastically. For energies greater than 1 MeV, it becomes fairly constant again. However, it is important to note that even though it does not change much in this region, the conversion factor is at its highest values. This means that doses that contribute to this region are quite high.

1.3.6 Detector Response Function

To determine the radiation present, a detector must provide a response that gives the total flux integrated over all energies. The reading, M_i, of a spectrometer is the integral over the energies E of the incident particles. For isotropic detectors, this reading is given as,

$$M_i = \int_{E_{max}}^{E_{min}} dE\ R_{\Phi,i}(E)\Phi_E(E) \tag{40}$$

where M_i are the elements of the multi-channel spectrum with k channels (i =1,…,k), and $R_{\Phi,i}$,(E) is fluence response function for the detector for gamma or neutron irradiation at gamma or neutron energy, E. The energies, E_{min} and E_{max}, represent the integration region. In the case of non-isotropic detectors, the response function requires the direction of the incident radiation.

If the field has a mono-energetic fluence that uses a fewer channel spectrometer such as with Bonner spheres, Equation 40 becomes,

$$M_i = R_i(E_0)\Phi \tag{41}$$

where a mono-energetic fluence, Φ, replaces the fluence $\Phi_E(E)$ at energy $E = E_0$.

For multichannel detectors like scintillators, the M_i values are the elements of the pulse height spectrum. These set of values, M_i(i =1,…,k) is the response function of the detector to particles of energy E_0. Accordingly, there is a response function that corresponds to each energy that the detector gives a response for [13].

1.3.7 Energy Spectrum

To carry out neutron spectrometry, the energy spectrum is essential. The energy spectrum is essentially the energy distribution of the neutron fluence. The fluence spectra is given as integrals over small energy intervals,

$$\Phi_i = \int_{E_i}^{E_{i+1}} \Phi_E dE \tag{42}$$

where ΔE is the energy interval between E_i and E_{i+1}.

Typically, Φ_i is computed and given in tabular form together with the upper or lower energy value. In MCNP, the Φ_i are computed against the upper energy limit of the interval [13].

1.3.8 Efficiency

The efficiency can be described as the ratio of an output quantity to the input quantity. In spectrometry, the efficiency can be defined as,

$$\epsilon = \frac{O}{\Phi A_c} \tag{43}$$

Where: O is the output signal of the device in counts, Φ is the fluence in cm^{-2}, and A_c is the cross-sectional area of the device in cm^2. Therefore, efficiency is dimensionless [13].

1.3.9 Sensitivity

The sensitivity can be described as the change in the output of an instrument to a change in the input signal. In spectrometry, the sensitivity can be defined as,

$$S = \frac{\Delta O}{\Delta \Phi} \tag{44}$$

In order to get a dimensionless quantity, relative values which may be given as a percentage may be given,

$$S_{relative} = \frac{\Delta M/M}{\Delta Y/Y} \tag{45}$$

where M is the reading and Y is that which influences the signal [13].

Chapter 2: Literature Review

2.1 Neutron Spectrometers

2.1.1 Thermal Neutrons

2.1.1.1 ^{6}Li-Based Detectors

The ^{6}Li(n,α) reaction has been applied for thermal neutron detection in many neutron devices. It is primarily used for detecting thermal neutrons due to its high neutron cross section of 940 barns. In the early stages, scintillation crystals have been created with different activators and tested to determine the most effective combination for good response in neutron detection [14]. In one instance, the lithium iodide crystal was tested with three activators and compared with a sodium iodide crystal. It was doped with samarium, europium, and tin. After testing and formulating the data, it was determined that lithium iodide doped with europium was the best candidate as a scintillator for the detection of thermal and resonance neutrons [15]. In another case, lithium based phosphors were tested against "pure" lithium iodide for their luminescent characteristics [16]. That is, the region of the emission spectrum in which each crystal emits the greatest luminescence. The activated crystals were deemed more promising. One of the most efficient scintillators has been lithium iodide doped with europium [17].

The response of this sensor to ionizing radiation such as neutrons and gamma-rays has been reported through various studies. It can serve as a counter and/or spectrometer. It has also been tested and compared with other types of scintillators to determine its effectiveness for different situations [18]. Comparing with thallium activated sodium iodide, its light output is 35% of that.

Portable radiation monitoring devices have used its gamma spectroscopic features for isotope identification [19]. Similarly, mixed radiation fields with thermal neutrons and gamma-rays have been surveyed [20-22]. In many instances, the goal is to determine the presence of neutrons. While some sensors, that are sensitive to both gamma-rays and neutrons, can be challenging in distinguishing the two types of radiation, this sensor has proven to be a good discriminator against gamma-rays up to a few hundred keV. The energy liberated from the reaction ^{6}Li(n,α) is very large, so when the alpha particle and triton deposit their full energy into the detector, its peak can be seen at 4.78 MeV, while the energy deposition from the electrons are found on the

lower end of the response function. In these studies, thermal neutron sources such as PuBe with a paraffin moderator and ^{252}Cf with a polyethylene moderator were used. The common gamma-ray source used was ^{137}Cs. A typical energy resolution of ^{137}Cs was around 8% and around 4% for the thermal peak.

One of the main characteristics of scintillators is its light output. Therefore, means to increase this have also been considered. Scintillators containing lithium have been mixed with other elements to produce a larger light output [23]. Using a borate scintillator foil, and a new scintillator crystal $^{6}Li^{158}Gd(^{11}B_3O)_3$, an increased response in neutron pulse height was observed. Contributions of thermal neutrons were from a paraffin moderated ^{252}Cf source, gamma-rays from a ^{60}Co and ^{252}Cf source, and beta particles from a ^{90}Sr source.

Other lithium based scintillators have been grown and applied to thermal neutron applications. A new rare-earth-ion-doped $LiSrAlF_6$ scintillator with 1% and 2% europium, and 1% cerium was tested for its scintillation properties under gamma-ray and thermal neutron irradiation [24]. These were chosen due to their good scintillation properties under nuclear excitation. Their results indicated high absolute light yields for this scintillator and reasonable decay times. Another rare-earth-ion-doped $LiCaAlF_6$ scintillator with cerium was tested for neutron-gamma discrimination using pulse shape discrimination [25]. This technique was based on the rise time of the scintillation light pulse. Thermal neutron and gamma-ray sources were from ^{252}Cf and ^{60}Co. Results showed that this technique is useful in separating neutron and gamma-ray events. Pulse shape discrimination has also been done using other crystals like $LiBaF_3$ for thermal [26-27] and fast neutron spectra [28]. This technique was based on the difference in luminescence that the neutron and gamma-ray exhibit, which using pulse height discrimination methods, the two types of radiations can be distinguished.

Ongoing attempts have been made to create scintillators with better detection efficiencies. New elpasolite and monoclinic based thermal neutron scintillators have been developed. Some of these include cerium doped Cs_2LiYBr_6, Cs_2LiYCl_6 [29-31], $Rb_2LiScBr_6$, Rb_2LiYBr_6, $Rb_2LiLaBr_6$, Rb_2LiYI_6, and Li_3YBr_6 [32]. The pulse height spectrum was observed for thermal neutrons and a gamma-ray source ^{137}Cs. These scintillators produced very high light yields under thermal neutron irradiation, sufficiently higher than that of the well known LiI:Eu scintillator. In mixed fields, the gamma-ray and neutrons were easily distinguishable due to the difference in

their pulse amplitudes. Excellent thermal peak resolution were also reported [32-33], higher than ^{6}Li glass and LiI:Eu. Using a variety of elpasolite compositions, one can conclude that absorption was better in the bromides and iodides than the chlorides, as well as using rubidium instead of cesium yielded better detection efficiency, Yttrium was the best choice of ions, and using lithium instead of cesium or bromine gave better detection efficiency. From their experimental results, the best overall choice were Cs_2LiYBr_6 and Rb_2LiYBr_6.

While LiI:Eu has been very effective in counting thermal neutrons, it has also been applied to fast neutron spectroscopy. A technique had been employed using a combination of ^{6}Li/^{7}Li glass detectors to detect mono-energetic fast neutrons in the range of 1-14 MeV while eliminating any gamma-ray contributions [34]. It was used as an alternative to recoil-proton methods. The detection efficiency was high, however the energy resolution was quite low.

2.1.1.2 ^{10}B-Based Detectors

Detectors based on ^{10}B have been widely used for neutron detection. Typically, it has been used for thermal neutron detection due to its high neutron capture cross section of 3840 barns. Recent studies have shown new types of scintillators that are also sensitive to fast neutrons. These scintillators are mostly mixed with some material that has a high neutron scattering cross-section, usually hydrogen. In particular, these types of scintillators are advantageous for spectroscopy because both materials responsible for neutron thermalization and capture are essentially mixed together. This leads to a type of spectrometry known as capture-gated, whereby some organic material, liquid or plastic, is loaded with a material of high neutron capture cross section [35]. In this detector, two signals are obtained from the same neutron, each event producing scintillation light. The first pulse is from the scattering event and the second pulse is from the capture event, happening with a difference of a few hundred nanoseconds. After scattering, the neutron can either escape from the detector or be captured; therefore both pulses must occur for it to be considered as ‘true’. The first pulse gives a good estimate for the incident neutron energy [36-37].

The thermal capture reaction also leads to the production of gamma-rays [38]. Therefore, radiations interacting with these types of detectors will lead to three types of charged particles;

electrons from the gamma-rays, protons from the elastic scattering with fast neutrons, and alpha and lithium pairs from the thermal neutron capture. These charged particles will deposit their energy in the medium, and as a result, the incident particle would be detected

Both liquid and plastic loaded detector types have been explored. Boron-loaded liquid scintillators allow for larger volumes which creates high detection efficiency [39]. They are highly sensitive to thermal and fast neutrons as well as gamma-rays [40]. If proper discrimination is adhered to, sensitivity to different types of radiation is advantageous. Experiments and simulations have been carried out by varying the ^{10}B content at 2% and 2.5% [40], and 4.4% [36,40-41] being irradiated by different gamma and neutron sources. Results showed that the greater the boron content, the lower the light output.

Boron-loaded plastic scintillators are also sensitive to gamma-rays and neutrons, and have high detection efficiency. Previous studies have been done to characterize this detector for neutron measurements [42-46].

2.1.1.3 ^{3}He-Based Detectors

Detectors that use ^{3}He have been one of the prevailing choices for thermal neutron detection [47-48]. This reaction, $^{3}He(n,p)$, has a very high neutron cross section of 5530 barns at thermal energy. It also is capable of implementing gamma-ray rejection. From the typical thermal sensor choices, ^{3}He gas exhibits the best resolution.

While ^{3}He is commonly used for thermal neutron detection, it has also been tested and used for higher neutron energies [49-51]. It is also an option for neutron spectrometry, however its main drawback is due to the ^{3}He recoil distribution from the elastic scattering process on higher energy neutrons, since it covers the $^{3}He(n,p)$ peak resulting from low neutron energy interactions [52].

The sensitivity of this detector to thermal neutrons is a function of the amount of ^{3}He gas which increases with pressure in a fixed volume. This brings about another limitation of using this gas, its low sensitivity. It would take a fairly long time to achieve reasonable counting statistics.

There are several applications for these detectors. These include health physics, oil well logging, security, safeguards, x-ray fluorescence, contamination monitoring, waste assay, etc.. With applications in several industries, there is a current worldwide shortage of this gas. This also leads to a higher cost. For this reason, other sensors have to be explored.

2.1.1.4 Elpasolite Detectors

Ongoing attempts have been made to create scintillators with better detection efficiencies. Pure and Ce^{3+} doped elpasolites with the structural composition of A_2BMX_6 (where A = Rb, Cs, B = Li, Na, K; M = Y, La-Lu and X = F, Cl, Br, I) have been studied [53-56]. These groups of compounds derive its name from the mineral elpasolite, K_2NaAlF_6, which was named after the town El Paso, Texas. These crystals have been grown using the Bridgman technique [57]. Some of these include cerium doped Cs_2LiYBr_6, Cs_2LiYCl_6, $Cs_2LiLaCl_6$, Rb2LiScBr6, Rb_2LiYBr_6, $Rb_2LiLaBr_6$, Rb_2LiYI_6, and Li_3YBr_6 [58-60]. Due to containing Li, these scintillators have potential of being thermal neutron detectors using the $^6Li(n,\alpha)$ reaction. In addition, the type of luminescence that these scintillators exhibit after interacting with photons and neutrons are different. The luminescence from the scintillator emits light at different times. A fast luminescence is produced when interacting with gamma-rays and a slow luminescence is produced when interacting with neutrons. Using pulse shape discrimination techniques, the two types of radiation can be distinguished.

The most promising scintillators from the elpasolite family due to their properties for neutron and gamma-ray detection are Cs_2LiYCl_6 (CLYC), $Cs_2LiLaBr_6$ (CLLB), and $Cs_2LiLaCl_6$ (CLLC) doped with Ce^{3+} [61]. All of these crystals have relatively high light yield; under thermal neutron irradiation it is sufficiently higher than that of the well known LiI:Eu scintillator. In particular, dual gamma and thermal neutron detection has been investigated using Cs_2LiYCl_6:Ce [61-66]. Different crystal sizes and compositions were tested under different radiation sources. The scintillator has been reported to be comparable in energy resolution to NaI:Tl or CsI:Tl at 662 keV and has excellent thermal peak resolution higher than ^6Li glass and LiI:Eu. Additionally, neutron and gamma-ray events can be distinguished using pulse height discrimination. This has been achieved for gamma-ray events below 3 MeV. Due to the different

time decay constants, both types of radiation can also be differentiated using pulse shape discrimination [67].

2.1.2 Fast Neutrons

Fast neutron spectrometry deals with measuring the energy distribution from a fast neutron source. Spectrometers are required in nuclear facilities for dosimetry. Their applications include processes in the nuclear fuel cycle, nuclear power reactors, areas where there is production, storage, and use of radionuclide neutron sources, nuclear research facilities, medical therapy facilities, and for cosmic-ray-induced neutrons. They should meet requirements such as covering the energy range of the field with good sensitivity; be either insensitive or can discriminate radiation that is not wanted; and be able to perform well under harsh environmental conditions. The most important quantities in a radiation environment are dose equivalent rate and occupancy time. These will give the radiological effects that this field can have. These quantities are characterized by the radiation type that is present and their energies. Any facility or area that emits radiation will have an area dose rate. The main concern is when people are present, where individual doses are allocated. The dose equivalent cannot be measured directly with conventional dosimeters because these measurements rely on a fluence measurement (except the tissue-equivalent proportional counter). Therefore, spectrometry allows the dose to be determined directly. Without good knowledge of the neutron spectra, health physicists cannot accurately calibrate radiation protection instruments and dosimeters, which may result in incorrect determination of dose received by radiation workers.

Existing spectrometers are quite developed for lower energy neutrons, in that their fluence spectra and dose can be determined. Though, thermal neutron detection is not a very good indication of a neutron source, since its fluence is easily influenced by materials in the vicinity. This puts more emphasis on the ability to detect a wider range of energies. As neutron energy rises into the fast region, most current spectrometers almost fail at this. They may require multiple measurements using different detectors and determining their fluence becomes more challenging.

Fast neutron spectrometers cannot use the same sensors as thermal neutrons, simply due to their cross section. If they did, their detection efficiency would be quite low. Due to this, fast spectrometers must alter or utilize different detection mechanisms to achieve acceptable

detection efficiency. The most useful neutron interaction with matter for fast neutrons is elastic scattering. Incident neutrons can transfer a portion of its kinetic energy to the scattered nucleus, creating a recoil nucleus. The energy of the neutron can thus be deduced by measuring the energy of the recoils subtracted by the Q-value of the reaction. However, since in elastic scattering the Q-value is zero, the neutron energy can be measured directly. Materials with high neutron elastic scattering cross section are sought. The most popular being hydrogen, since it can transfer almost all of its energy in a single collision. This is why many fast spectrometers use recoil protons in their main detection scheme.

There have been different types of spectrometers that have been developed for mixed fields. Of these, there are four main types that exist. They are multisphere spectrometers, proportional counter spectrometers, liquid scintillation spectrometers, and superheated drop bubble detectors.

2.1.2.1 Bonner Sphere Spectrometers

The most common spectrometer used is the multisphere or Bonner sphere spectrometer (BSS). This is due to its large span of energies from thermal to GeV, its isotropic response, and its ease of operation. The configuration of a Bonner sphere spectrometer comprises of a thermal detector in the center and moderating sphere with variations in diameter surrounding it. This increases the neutron sensitivity over a large range of energies, though this is also dependent on the sphere's diameter. The first BSS can be traced back to 1960 [68]. It consisted of a LiI:Eu scintillator and polyethylene moderating spheres for neutron energies of thermal to 15 MeV. Polyethylene $(C_2H_4)_n$ has been frequently used as a moderator for BSS.

The operation of a BSS is dictated by the various interactions that may take place when it is hit by an incident neutron of energy, E_n. There are four possible paths in which a neutron will undergo upon interaction as can be seen in Fig. 16.

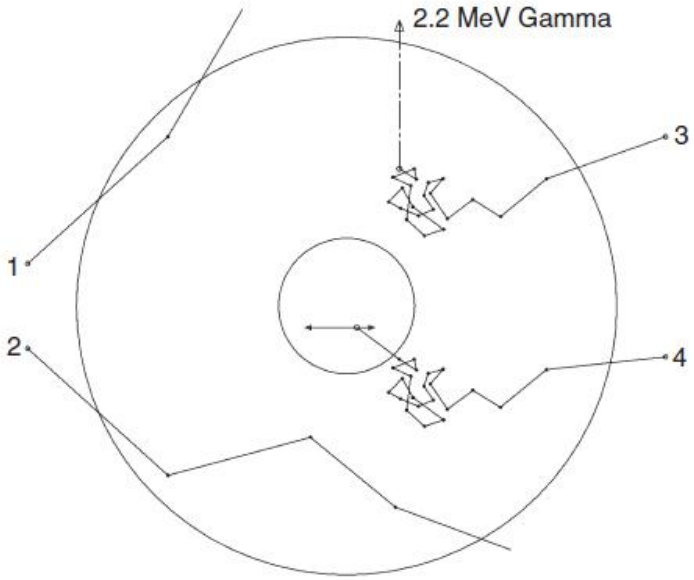

Figure 16: Neutron trajectories in a Bonner sphere [41]

The inner circle is the thermal neutron sensor and the outer circle is the polyethylene moderator. The first neutron interacts with the carbon or hydrogen in the polyethylene and elastically scatters, and thus escapes from the BSS. The second neutron has several collisions in the polyethylene, becoming less energetic, but eventually escapes from the BSS. This type of trajectory is common with neutrons of high energy that undergo (n,p), (n,d) or (n,α) reactions with carbon. The third neutron interacts with the polyethylene enough to become thermalized but does not enter the thermal sensor, but instead interacts with hydrogen releasing a 2.2 MeV gamma-ray, which is likely to escape or could interact with the polyethylene and produce secondary electrons. The fourth neutron has become thermalized and enters the thermal sensor which has a high probability of interacting, therefore easily detectable. The probability of these interactions depends on their neutron cross section; this means it is dependent on neutron energy. For carbon, it can be seen in Fig. 17 and hydrogen in Fig. 18.

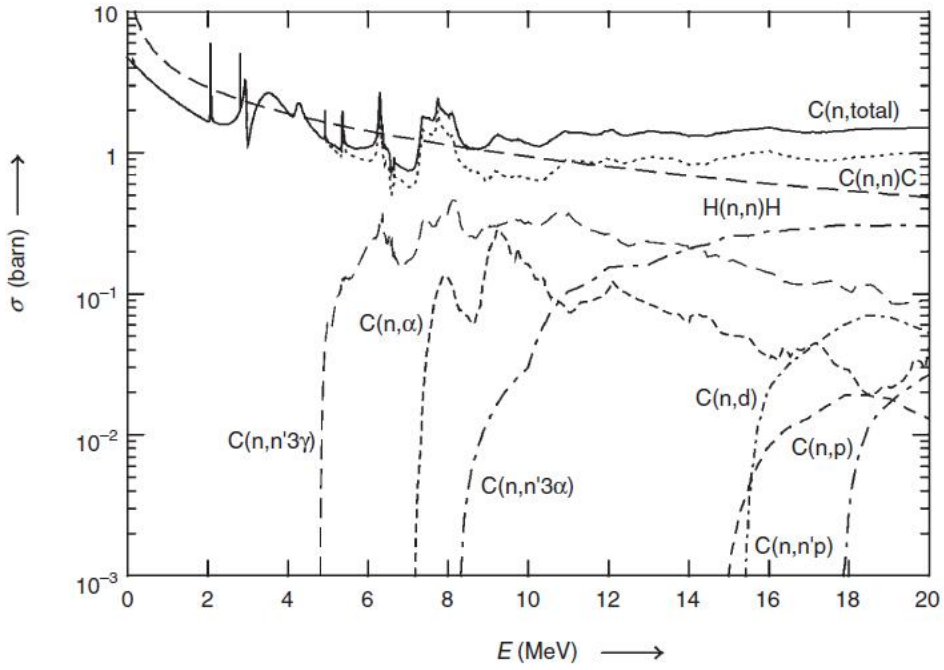

Figure 17: Macroscopic cross section versus energy of carbon for various interactions in a Bonner sphere [41]

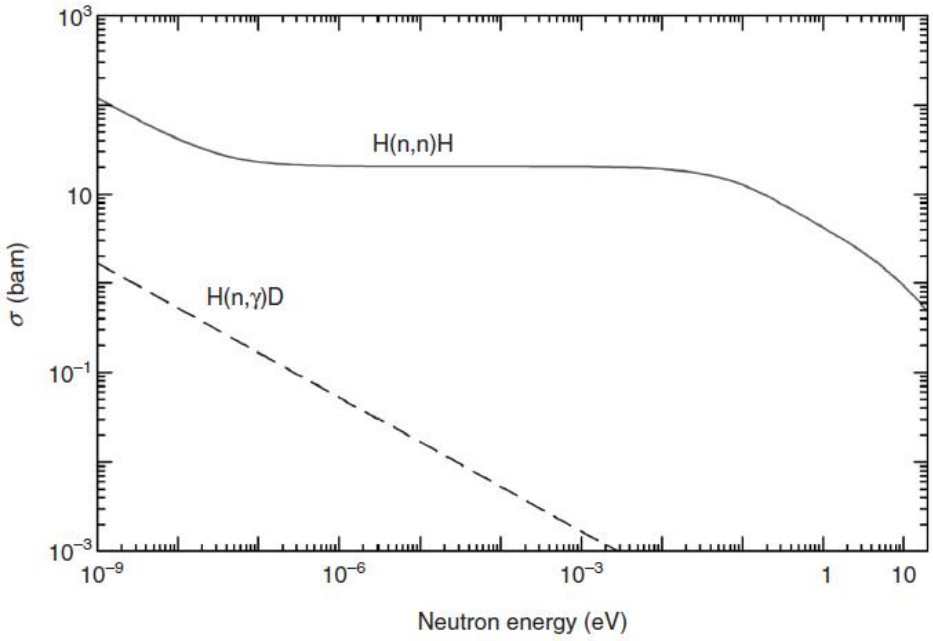

Figure 18: Macroscopic cross section versus energy of hydrogen for interactions in a Bonner sphere [41]

The distance the neutron travels through the BSS also affects which interaction takes place, therefore it is also dependent on the diameter of the sphere. Knowing this, one can expect different responses from spheres of different sizes. The response function for a PTB Bonner sphere spectrometer can be seen in Fig. 19 where the number of each line indicates the sphere's diameter in inches.

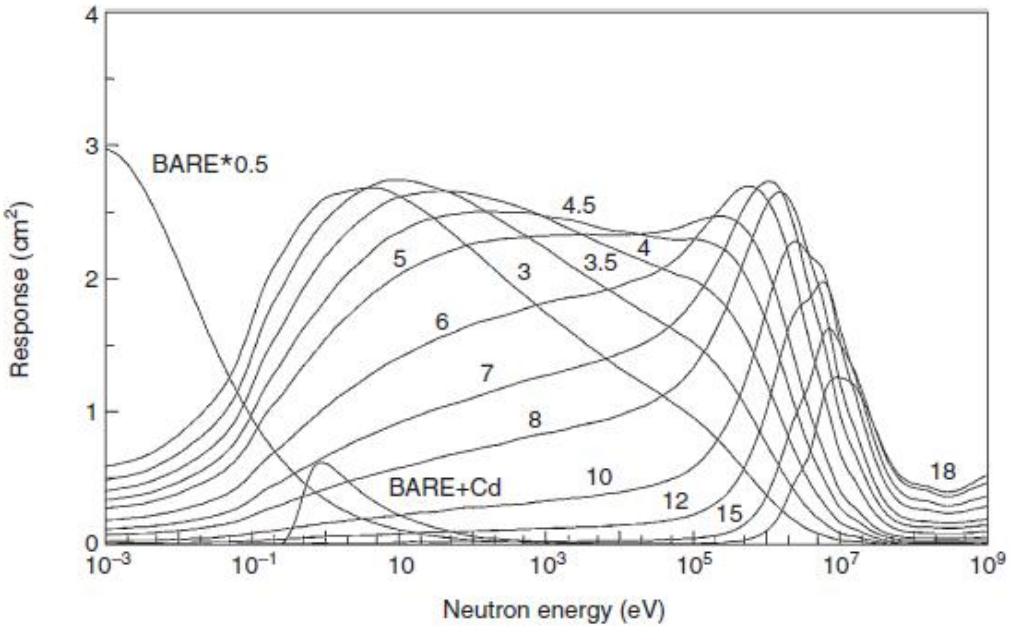

Figure 19: Neutron fluence response functions for different sizes of spheres [69]

For lower energies, smaller spheres have a greater neutron fluence. This is because at low energies the neutron will undergo all four types of reactions and a substantial amount will enter the thermal sensor and be detected. Those neutrons at high energies will pass through the sphere without much interaction. For higher energies, larger spheres have a greater neutron fluence. This is because those fast neutrons will interact more and be more likely to become thermalized and picked up by the thermal sensor. Those neutrons at low energies have a high probability of reacting via the H(n,γ)D reaction, therefore many neutrons will not be picked up by the detector.

Like every system, there exist advantages and shortcomings. Advantages of the Bonner sphere spectrometer are that it covers a large range of neutron energies; has good gamma-ray discrimination; has good efficiency; and is fairly portable. Some shortcomings include its poor

energy resolution due to overlapping of the response functions; measurements take quite a bit of time; and to unfold the spectrum, it requires good knowledge and skill.

Nonetheless, this type of spectrometer has been developing and growing and continues to provide useful neutron spectral information in various areas. There is no set type of BSS that exists. They are usually tailored to a specific application. The detectors can be broken down into two categories, active or passive [70]. Active detectors include scintillators and gas counters. Advantages include real time data acquisition and usually good gamma-ray discrimination. They provide information immediately. Passive detectors include activation foils and thermo-luminescence dosimeters. Advantages include portability and lower unit cost. Choices of active detectors are typically LiI:Eu crystals or ^{3}He gas filled counters [71]. Some even employ the use of both a scintillator and gas counter [72]. Cadmium or boron is sometimes added as an envelope surrounding the moderator to enhance thermal detection and enhance the energy resolution [73]. In areas of high photon components, activation foils are suitable like gold as the thermal neutron sensor [74]. At energies greater than 20 MeV, the sensitivity of the BSS decreases substantially. Attempts have been made to increase the sensitivity by using a Bonner Sphere Extension (BSE) [75].

A new type of spectrometer that operates under the same principles as a BSS has been developed intending to improve the use of this technique. It uses a thermal neutron sensor with a surrounding moderator, except that the moderator is cylindrical and each cylinder of different thicknesses is inserted into one another, like nested Russian dolls [76-77].

2.1.2.2 Proportional Counter Spectrometers

In the context of this work, the spectrometers described are for dosimetric purposes. Therefore, it is crucial to keep going back to those requirements in order to determine a suitable spectrometer. One of the drawbacks of the Bonner sphere spectrometer was its poor energy resolution. For low to intermediate energies, the dose equivalent does not vary much. However, for high energies, there is a significant increase in dose equivalent, by a factor of approximately 30 times. For this reason, this area of the spectrum must be much more resolved. Between the energy range of 10 keV to 1.5 MeV, proportional gas counters are used.

In determining the neutron spectra, there are two types of reactions that can be used. The first type can be based on exothermic reactions using the production of charged particles. By knowing the resulting pulse height of the charged particles will give the neutron energy because it is proportional to the Q-value plus the neutron energy. For example, in the case of a detector based on the reaction $^{3}He(n,p)^{3}H$, the pulse height spectrum should look like Fig. 20.

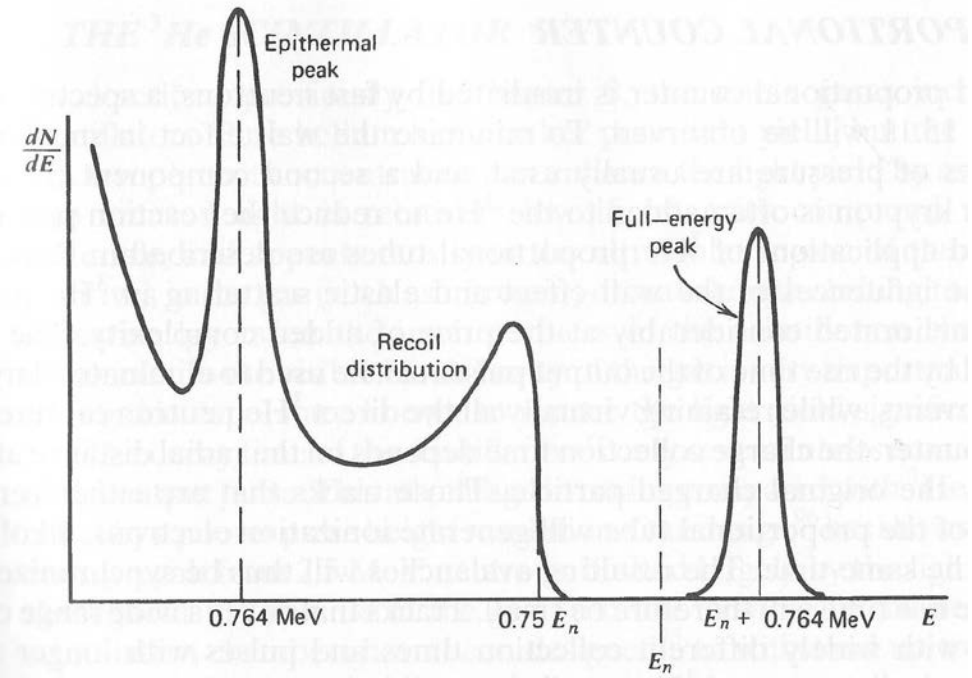

Figure 20: Pulse height spectrum of charged particles expected from fast neutrons incident on a ^{3}He detector [8]

The full energy peak is when full deposition occurs in the (n,p) reaction, such that the peak occurs at an energy equal to the Q-value plus the incident neutron energy. The recoil distribution occurs when the incident neutron elastically scatters with the helium nucleus, and only partial deposition occurs. The energy deposited depends on the angle of scattering, which is why there is a distribution of energies. The maximum energy that can be transferred is 75% of the neutron energy. The epithermal peak occurs when the fast neutrons have become thermalized by external materials, and thus deposits an energy equal to the Q-value of the (n,p) reaction.

The second type can be based on elastic scattering interactions with the gas nuclei. The transfer of energy from the incident neutron to the gas nuclei will give the energy of the neutron based on the difference between the Q-value, which is zero, and measured kinetic energy. Therefore, the

amount of energy transferred depends on the scattering angle. This value can range from zero to the neutron energy. The maximum amount of energy that the recoil nucleus can have is determined by,

$$E_{max} = \frac{4M}{(1+M)^2} E_n \tag{46}$$

where M is the mass of the recoil nucleus and E_n is the energy of the incoming neutron. Recoil proton detectors typically use filling gases like H_2, CH_4 or ^4He. Their maximum fractional energy transfer is given in Table 3.

Table 3: Maximum Fractional Energy Transfer in Neutron Elastic Scattering

Target Nucleus	M	E_{max}
$^{1}_{1}H$	1	1
$^{2}_{1}H$	2	0.889
$^{3}_{2}He$	3	0.750
$^{4}_{2}He$	4	0.640
$^{12}_{6}C$	12	0.284
$^{16}_{8}O$	16	0.221

From Table 1, it can be seen that ^1H can transfer the maximum fraction of energy, which is why it is the most common nucleus to use. In either case, it is expected that the reaction product has sufficient information that the energy of the incident neutron can be derived.

Advantages of using this spectrometer are its energy resolution, which is typically 2-6%, and detector efficiency, which is typically 1-3%. One of the main limitations to this type of spectrometer is its energy range. At the lower end, there is difficulty discriminating between gamma-rays, and at the higher end, the wall effect of the recoil protons becomes effective [78]. Therefore, choice of detector geometry, gas quality, and other factors must be chosen carefully for optimization.

Specific proportional counter spectrometers have been introduced for different purposes. The energy region between 50 keV and 4.5 MeV is the main contribution to dose equivalent from

neutrons [79]. As such, a spectrometer designated for this region would be useful. This is known as the ROSPEC (ROtating SPECtrometer). This type of spectrometer can be traced as far back as the 1980s. It typically uses four spherical proton recoil counters containing hydrogenous gases that rotate among a common axis. Each counter is optimized to detect a certain range of energy. Therefore, the use of four detectors would divide the energy range into four regions.

In more recent studies, ROSPEC has been developed to cover neutrons with larger ranges of energy using a Simple Scintillation Spectrometer (SSS). The use of a scintillator allows the range of energies to span from thermal to 17 MeV [80] or to 18 MeV [81]. The four counters are responsible for the energy range of 50 keV to 4.5 MeV and the SSS for 4 MeV to 18 MeV. The combination of two techniques allows for greater applicability to poly-energetic neutron fields.

2.1.2.2 Liquid Scintillation Spectrometers

Organic scintillators are preferred when neutron energies exceed 1 MeV. Scintillation detectors are advantageous over proportional gas counters because of their high density and larger detection efficiency due to the high (n,p) elastic scattering cross section. These scintillators are generally fast so they are suitable for high count rates. The types of scintillators include plastic, anthracene, stilbene, or liquid. Organic scintillators are equally sensitive to neutrons and photons; and thus one of their limitations includes neutron-gamma discrimination. Neutron spectrometry can only be possible by separating the two. Pulse-shape analysis techniques can be utilized to differentiate the two types of radiation [82-83]. That is scintillation pulses created from protons and electrons can be distinguished based on their pulse shape. Two types of scintillators have been an exception. They are stilbene crystals and NE213/BC501A liquid scintillators.

Stilbene crystals are based on a hydrocarbon composition. Their neutron detection efficiency is based on their thickness and (n,p) scattering cross section. This scintillator can generally tolerate from 1 MeV to around 10 MeV neutrons. As higher energies are approached, the wall effect becomes prominent [84-85]. The stilbene crystals have very good neutron-gamma discrimination; however their response depends highly on the angle of incidence, and therefore can only be used for neutron sources that are localized.

The NE213 and BC501A liquid scintillators derive their names from Nuclear Enterprise Ltd, Edinburgh, UK and Bicron Radiation Measurement Products, Newbury, OH, USA, respectively. Both are hydrocarbons in the liquid state. The NE213 liquid scintillator was introduced as a neutron spectrometer in 1968 [86]. It has an isotropic response and better neutron-gamma discrimination than stilbene. The shape and size of the scintillator should be larger than the maximum range of the secondary charged particles produced. An example of the charged particles ranges and their energies in NE213 to photon and neutron radiation is given in Fig. 21.

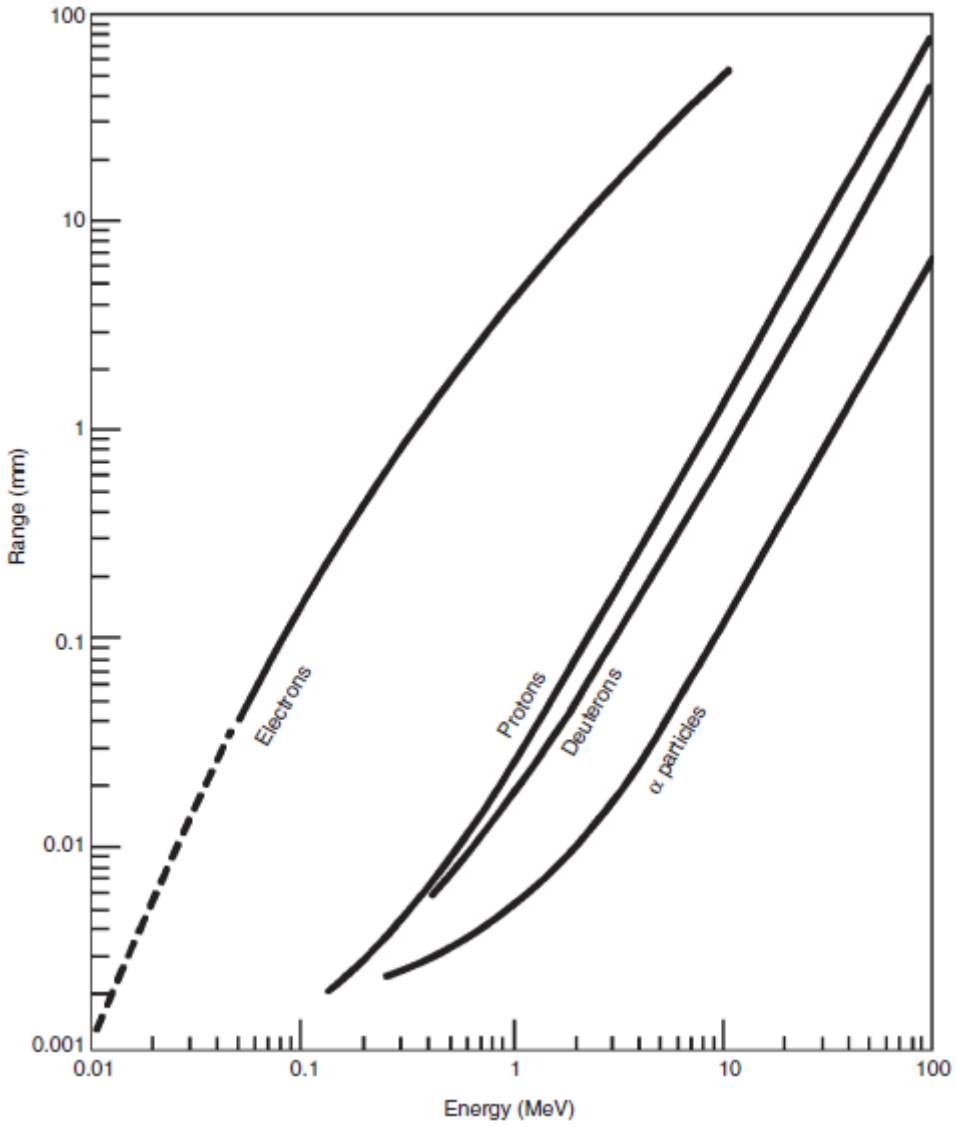

Figure 21: Ranges of charged particles produced NE213 from photons and neutrons [87]

Each charged particle with the same energy has a different range. For example, a 1 MeV electron has the greatest range, followed by a proton, deuteron, and then alpha particle. Studies have showed that it can tolerate photons up to about 10 MeV and neutrons up to around 20 MeV [87]. The higher energy limit for neutrons is still being investigated.

2.2 Neutron Spectrometry Applications

Neutron spectrometers are required for a large array of applications. The presence of neutrons exists in many nuclear facilities with working personnel. Therefore, the deployment of this device is critical to monitor their radiation exposure. These applications include the nuclear power industry, radionuclide sources, nuclear research facilities, medical facilities, and cosmic ray fields.

2.2.1 Nuclear Power Industry

Neutrons are encountered at different stages within the nuclear power industry; from fuel fabrication and power generation to reprocessing of spent fuel, waste management transport and storage. In fresh and spent fuel, much of the neutrons are from (α,n) or spontaneous fission reactions and are around 1 MeV. An example of the neutron spectra measured with three types of spectrometers at a PuO_2 repository can be seen in Fig. 22 [88].

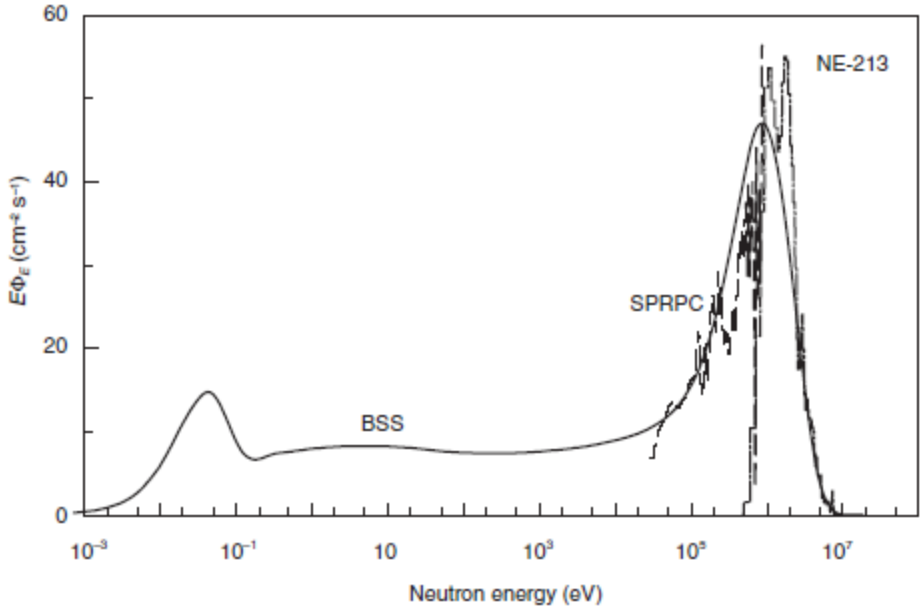

Figure 22: Neutron spectra of PuO_2 repository (BSS – Bonner sphere spectrometer, SPRPC – ^{2}H-filled proportional counter, NE-213 – Scintillation spectrometer) [88]

Since many of these facilities usually have radiation shielding, in particular reprocessing plants, it will increase the thermal component in their spectra.

In nuclear power reactors, a large portion of neutrons are found in the thermal and intermediate energy region. These reactors include light water reactors like Pressurized Water Reactors (PWR) and Boiling Water Reactors (BWR); and Gas Cooled Reactors (GCR). An example is given of the neutron fluence spectra taken at four Swiss plants, two PWR and two BWR, in the primary and secondary containment in Fig. 23 [89]. The inverted triangles are in the primary containment and the upright triangles are in the secondary containment.

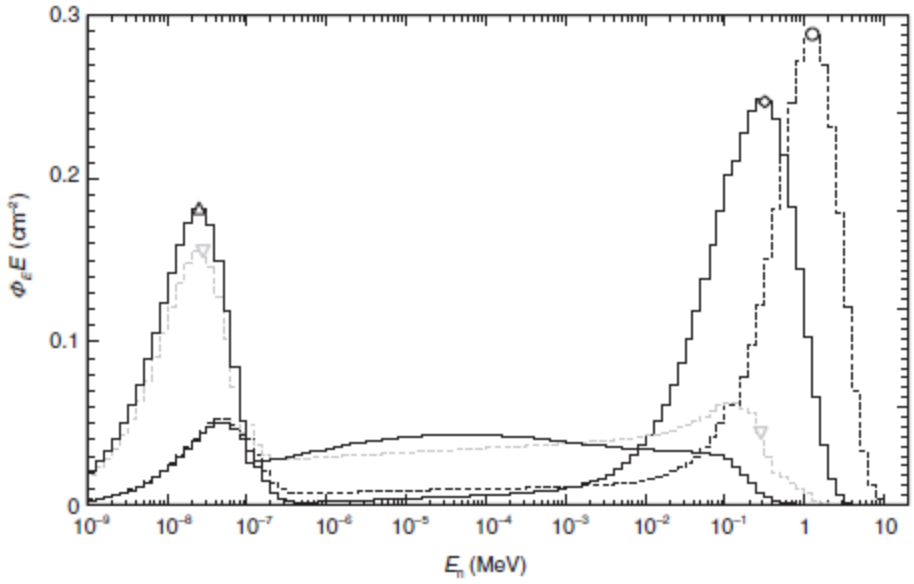

Figure 23: Neutron fluence spectra at four Swiss nuclear power plants [89]

Even though the fluence is high in the thermal and intermediate energy regions, this area is not as hazardous as the fast region, even while the fluence is much less. This can be seen in the dose equivalent spectra in Fig. 24 [89].

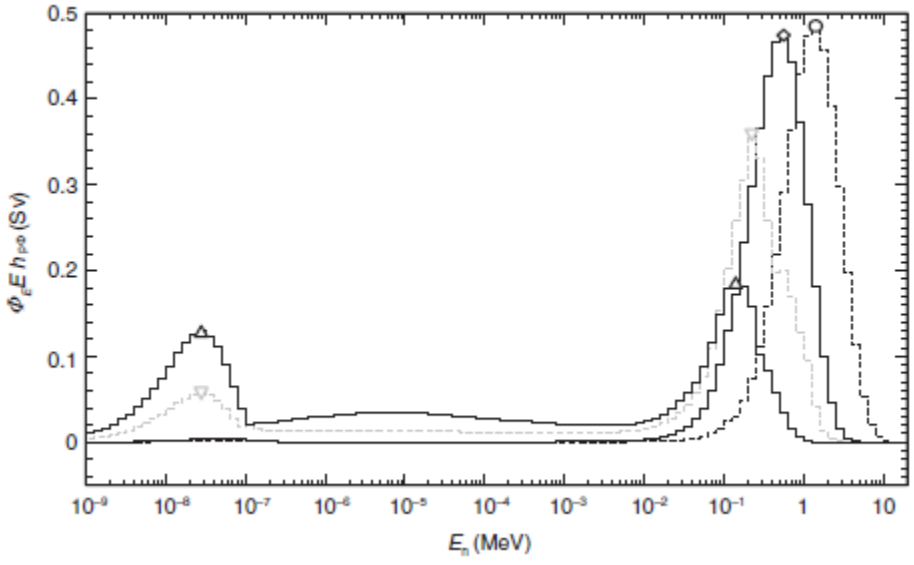

Figure 24: Dose equivalent spectra at four Swiss nuclear power plants [89]

2.2.2 Radionuclide Sources

Radionuclide neutron sources are produced and used for research, technology, medicine, and calibrating radiation protection instruments. These neutrons are produced by (α,n), (γ,n), and spontaneous fission reactions. Alpha emitting nuclides, ^{241}Am and $^{238/239}$Pu together with beryllium, boron, lithium, or fluorine, and ^{252}Cf which undergoes spontaneous fission, are the most common sources. An example of their neutron spectra is given in Fig. 25 [90].

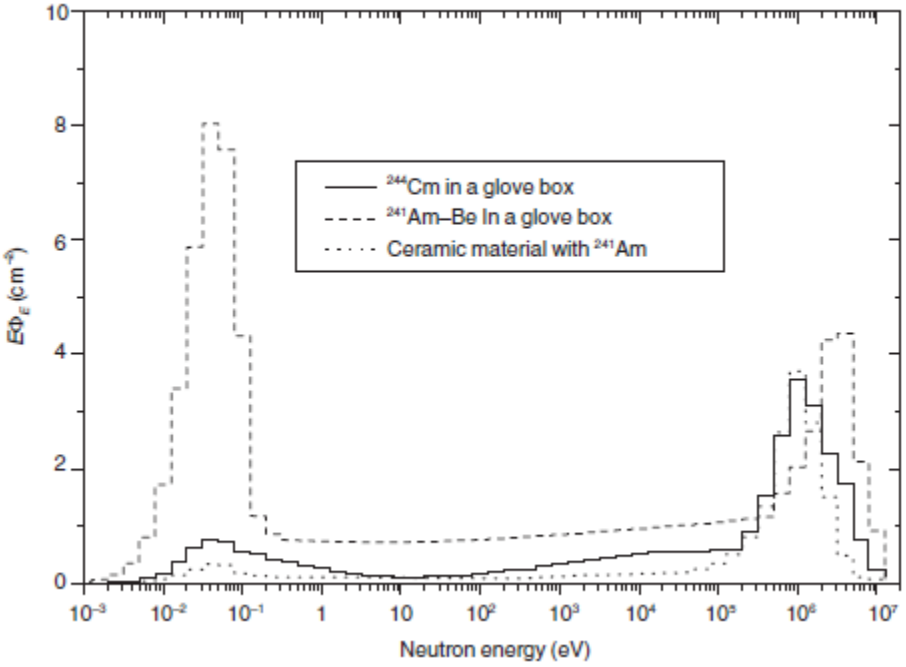

Figure 25: Neutron spectra in a radionuclide source production plant [90]

All of the sources have a distinct fluence in the thermal and fast region, mostly around 1 MeV. The varying of the high energy peak depends on the nuclide and if it is an (α,n) source, the target nuclide. The source strength and shielding would dictate the dose equivalent rates.

2.2.3 Nuclear Research Facilities

Research facilities contain accelerators and/or reactors. Some accelerators produce neutrons with energies from keV to GeV by (p,n) and (d,n) reactions. An example of the neutron fluence at the Paul Scherer Institute (PSI) in Switzerland for a cyclotron that produces high energy neutrons from a 590 MeV proton beam with targets is given in Fig. 26 [91].

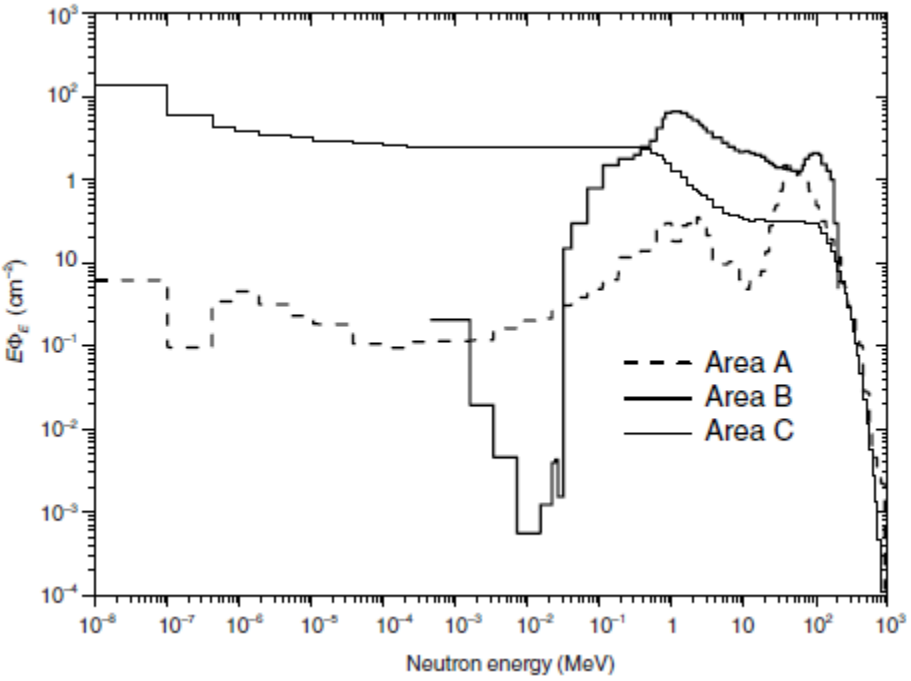

Figure 26: Neutron fluence at 590 MeV cyclotron [91]

Three different points were chosen based on areas of working personnel, areas that can give a reasonable dose rate based on the duration of measurement, and different estimated neutron spectra [91]. Area A peaks in the high energy region, Area B peaks even more at higher energies, and Area C has a large thermal energy component. This distribution of energies shows that a wide range of energies can be found in a research facility containing a single cyclotron.

At research reactors, much characterization of the field is done related to research projects. The VENUS reactor at the Belgian Nuclear Research Centre is a zero-power research reactor whose measured and calculated neutron fluence can be seen in Fig. 27 [92]. Calculations were done using the TRIPOLI-3 code.

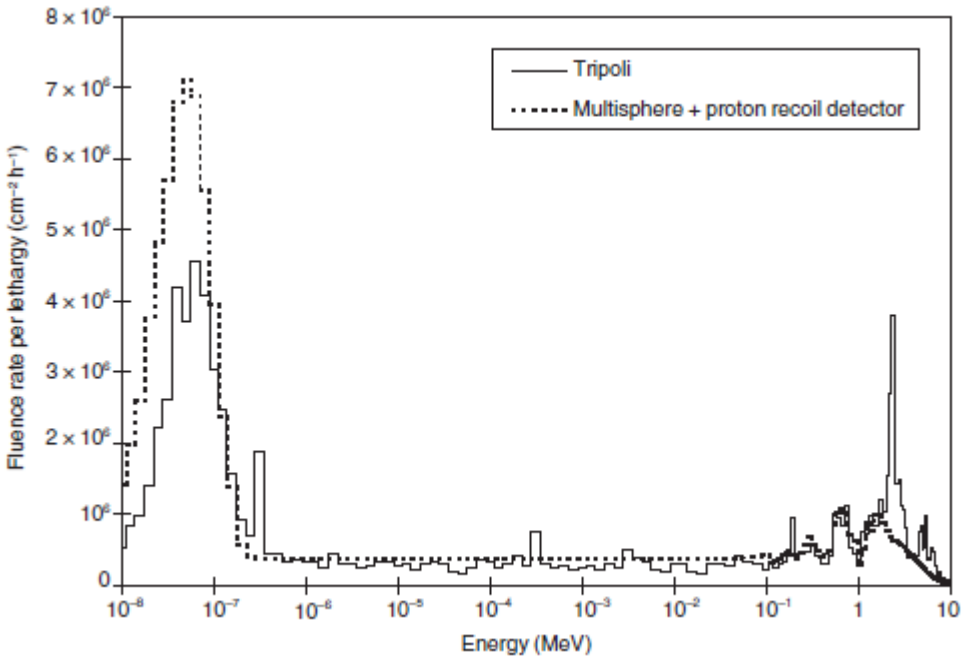

Figure 27: Calculated and measured neutron fluence spectra at the VENUS research reactor [92]

In the measured spectra, a high peak of thermal neutrons can be seen with a smaller peak around 1 MeV.

2.2.4 Medical Facilities

At medical facilities, radiation therapy is given for treatment of patients with cancer. Neutrons are produced by (γ,n) reactions and as by-products from charged particle accelerators. These fields tend to have a large photon component, and therefore obtaining its neutron spectra is sometimes challenging. In one example, fast neutrons are produced to treat superficial tumours at the RENT facility with the FRM research reactor in Garching. In another example, a Siemens Mevatron KD-2 linear accelerator operates at 15 MeV and produces bremsstrahlung and thus generates neutrons by this reaction. Their spectra can be seen in Fig. 28 [93].

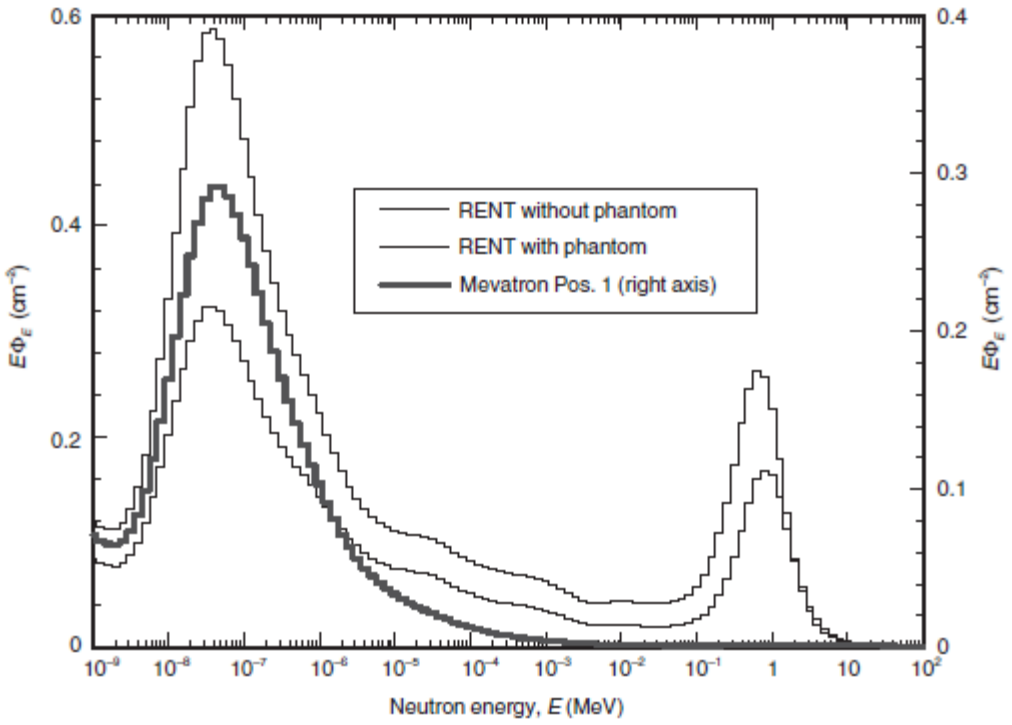

Figure 28: Neutron spectra of the RENT facility and Mevatron linac [93]

Measurements were taken outside the facility with and without a phantom, which represents the same composition as a human being, at the position of a potential patient. Even with shielding of 2 m thick concrete at the RENT facility, the fission spectrum can be seen although an enhanced thermal peak is observed. A softer spectrum is seen at the Mevatron where measurements were taken behind the entrance door. The opposite is observed for the dose equivalent at the RENT facility, where the spectra are dominated by fast neutrons as seen in Fig. 29 [93].

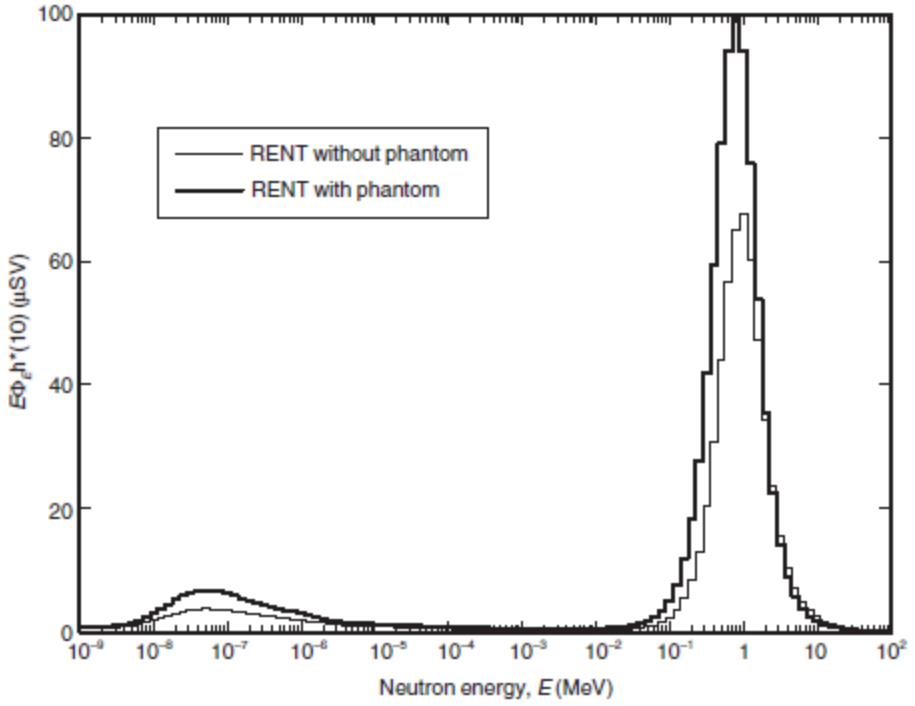

Figure 29: Dose equivalent spectra at the RENT facility with and without a phantom [93]

2.2.5 Cosmic-ray Fields

Protons interact with atoms in the upper atmosphere to produce neutrons. When passing through the earth's atmosphere, however, they are absorbed. However, this neutron dose makes up the largest to the population, contributing to 10% of the effective dose equivalent from natural radiation sources. The intensity of the source increases as a function of altitude. As a result, radiation exposure to aircraft crew is significant. Neutron spectra at different altitudes and on the ground have been measured and are given in Fig. 30 [94].

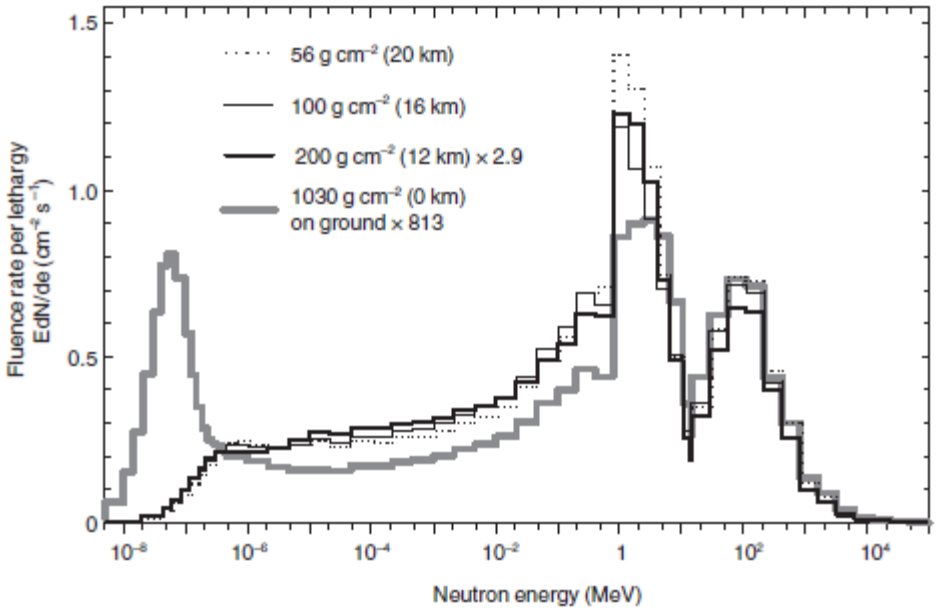

Figure 30: Neutron spectra from cosmic-induced neutrons on the ground and at different altitudes [94]

The peak on the far right is from spallation neutrons and the peak to its left is due to evaporation neutrons. Backscattering on the ground explains the large thermal component. For 12 km to 20 km, only slight variations occur with the majority of the neutrons being fast.

From all of these facilities, one can see that a large range of neutron fluence spectra exists where operational quantities must be determined.

Chapter 3: Methodology Description

This thesis takes an empirical approach involving two phases to investigate the spectrometric properties of different sensors in order to develop a neutron spectrometer for mixed neutron gamma fields. The sensors cover a neutron energy range from thermal to 4 MeV and gamma energies up to 3 MeV. The first phase consists of building simulation models of the chosen detectors. Monte Carlo calculations have been done to optimize the detectors' isotope content. All detectors were simulated and tested before undergoing any experiments. The second phase of the thesis consists of conducting a series experiments in different neutron gamma fields. Measurements were carried out with each detector to study their response and spectrometric characteristics in different energy fields.

The neutron energy region was divided into two parts, and is thus comprised of two sensors to cover the entire above-mentioned range. For thermal and epithermal neutrons, a LiI:Eu scintillator, boron-loaded plastic scintillator, and ^{6}Li enriched Cs_2LiYCl_6:Ce scintillators were investigated. These sensors were chosen due to the ^{6}Li and ^{10}B isotopes having a high neutron absorption cross section in the low energy region. For energies greater than 100 keV, a custom crystal was used with different concentrations to allow different nuclear reactions to occur. Thus, the Cs_2LiYCl_6:Ce scintillator with less ^{6}Li content was used. This sensor was chosen due to a significant contribution from the (n,p) reaction with ^{35}Cl isotope at higher energy neutrons. Therefore, a distinct neutron induced peak indicating the signature of protons on the pulse height spectra provides precise information about the incident neutron energy. This is mainly the key feature of utilizing this detector for fast neutron spectrometry. It is important to note that the difference between the two Cs_2LiYCl_6:Ce scintillators lies in their isotopic abundance.

3.1 Monte Carlo Simulation

The first phase was comprised of creating Monte Carlo simulations of the different detectors to test their response to neutron and gamma radiation. Each detector was modeled and numerous calculations were done to obtain and interpret the response of the detector to a given radiation source.

3.1.1 Description of Monte Carlo N-Particle eXtended Code

MCNPX is a three-dimensional general-purpose Monte Carlo radiation transport code that can model radiation interactions with any material. It was developed by the Los Alamos National Laboratory and the program began in 1994. The first version of MCNPX was released in 1997. The extension is the next generation of MCNP which combines MCNP4B and LAHET 2.8. It can track more particles over a larger range of energies and incorporates the latest nuclear physics models and cross section libraries. It is written in FORTRAN 90 and is able to operate using PC Windows, Linux, and Unix. This program has been improved by the enhancement of physics simulation models, extended neutron, proton, and photonuclear libraries to 150 MeV, and the development of more variance reduction and data analysis techniques.

Beta-test teams function to test the codes prior to being released officially. There are a variety of applications ranging from nuclear criticality safety, nuclear safeguards, nuclear medicine, outer space, accelerator based programs, shielding for nuclear facilities, medical physics, nuclear material detection, dosimetry etc.

Input files are created by using cards to describe the geometry of the model and its properties. Tally cards are assigned to retrieve a desired output [95].

3.1.2 Monte Carlo Visual Editor

In earlier versions of MCNP, a user was unable to visualize the model, however with the introduction of The Visual Editor (Vised), it has enabled users to display the geometries created in the input files. It became a part of MCNP in version 5 and has been adapted to MCNPX. Some of its capabilities include 2D geometry plots, 3D dynamic display, dynamic inputs of surfaces, cells, materials etc., and dynamic displays of cross sections, particle tracks, and tallies [96].

3.1.3 Monte Carlo Simulation Models

The versions used for earlier simulations was MCNPX Version 2.6.0 and Visual Editor Version 22S. Later on when released, MCNPX Version 2.7.0 and Visual Editor Version 24E was used because of the significant enhancement in tracking heavy ions.

3.1.3.1 LiI:Eu Scintillator

Neutrons interact with the ^{6}Li isotope through (n,α) which has a significant absorption reaction cross section. At thermal energies, its high neutron absorption cross section is 940 barns, therefore making it useful for thermal neutron detection. This reaction is exothermic with a Q-value of 4.78 MeV. In this reaction:

$$ {}_{0}^{1}n + {}_{3}^{6}Li \rightarrow {}_{1}^{3}H + {}_{2}^{4}He \tag{47} $$

The alpha particle takes 2.05 MeV and the triton takes 2.73 MeV. The presence of iodine is useful for gamma-ray spectroscopy due to its high atomic number.

A cylindrical lithium iodide scintillator enriched with 99% ^{6}Li and 1% ^{127}I was modeled. It has a density of 4.06 g/cm^{3} and dimensions of 1x2.5 cm. The MCNPX model for gamma simulations is presented in Fig. 31. An identical model was used for neutron simulations by surrounding the detector with a paraffin moderator of 3.5 cm thick.

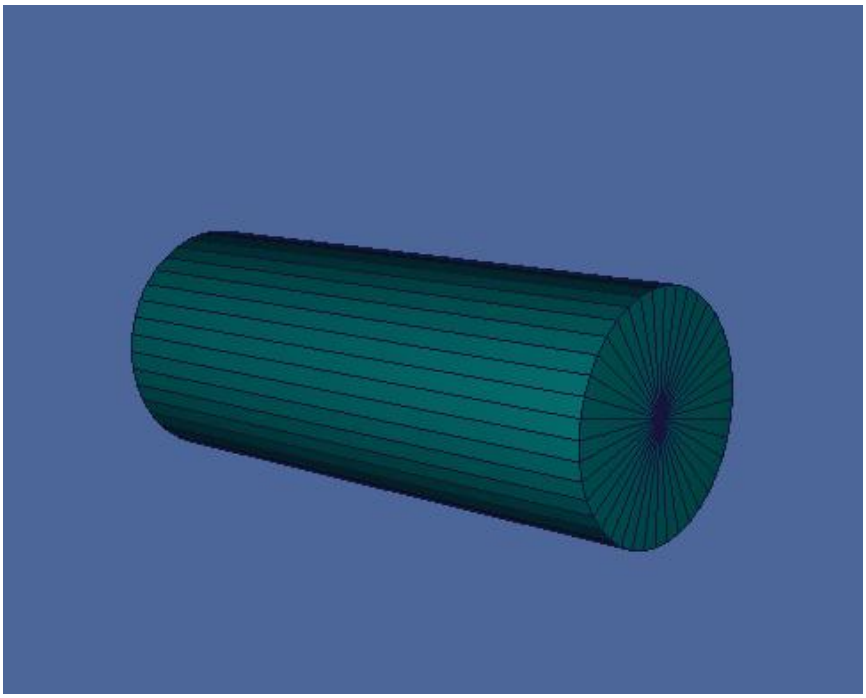

Figure 31: Model of the LiI:Eu scintillator in VisEd

3.1.3.2 Boron-loaded Plastic Scintillator

Neutrons may interact with this scintillator through either absorption or scattering reactions. Boron has been typically used for thermal neutron detection due to its large neutron absorption cross section of 3840 barns. Neutrons interact with ^{10}B with two possible outcomes, an alpha particle with a ^{7}Li recoil nucleus in its excited or ground state. The two reactions are:

$$ {}^{1}_{0}n + {}^{10}_{5}B \rightarrow {}^{7}_{3}Li^{*} + {}^{4}_{2}He \quad (48) $$

$$ {}^{1}_{0}n + {}^{10}_{5}B \rightarrow {}^{7}_{3}Li + {}^{4}_{2}He \quad (49) $$

94% of the time the outcome is the excited state, and 6% of the time the outcome is the ground state. These reactions are exothermic and their Q-values are 2.792 MeV and 2.310 MeV, respectively. The energy is distributed between the alpha particle and the ^{7}Li. In the excited state, the alpha particle has an energy of 1.47 MeV and the ^{7}Li has an energy of 0.84 MeV. In the ground state, the alpha particle has an energy of 1.78 MeV and the ^{7}Li has an energy of 1.02 MeV. When in its excited state, ^{7}Li will de-excite into stable ^{7}Li releasing a gamma-ray of 0.478 MeV.

The presence of hydrogen and carbon leads to elastic scattering reactions with neutrons due to their large scattering cross section. In these reactions, recoil protons and recoil carbon are produced. The energy transferred from the incoming neutron to the hydrogen or carbon nuclei is determined by the scattered angle.

A boron-loaded plastic scintillator with 5% boron loading containing about 1% of ^{10}B isotope was modeled. The rest of the composition was carbon and hydrogen. The density of the scintillator is 1.026 g/cm^{3}. It has a cylindrical geometry and dimensions of 2.5x2.5 cm.

Simulations were initially done using MCNPX Version 2.6.0, however since this version is unable to track most heavy ions, particularly ^{7}Li; a series of simulation runs were done using a more recent version, MCNPX Version 2.7.0, which has more extended features that include the capability to track heavy ions.

The model for the neutron simulations is presented in Fig. 32. An identical model was used for gamma simulations without the moderator.

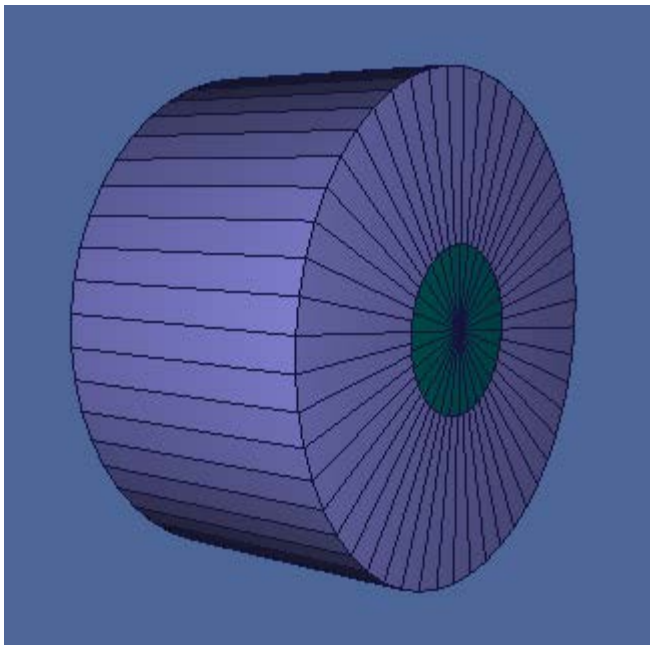

Figure 32: Model of the boron-loaded plastic scintillator with surrounding moderator in VisEd

3.1.3.3 Cs_2LiYCl_6:Ce Scintillators with Different Isotope Content

Two Cs_2LiYCl_6:Ce scintillators have been modeled in MCNPX with various isotope compositions. A series of simulations has been performed to optimize the isotope content due to the large difference in the cross section between the (n,p) and (n,α) reactions occurring when neutrons interact with the crystal. The (n,α) reaction with ^{6}Li is dominant due to its high cross section at low neutron energies. Thus to allow the (n,p) reaction which has smaller cross section, the isotope composition of ^{6}Li has been reduced to a minimum value. Initially, since the reaction ^{6}Li(n,α) has such a high neutron cross section for thermal and epithermal neutrons, a ^{6}Li-enriched Cs_2LiYCl_6:Ce crystal was investigated using multiple simulation runs to optimize the isotope content from one side, and guide the experimental investigation from another side. This aforementioned reaction has a Q-value of 4.78 MeV and is shown in Equation 47.

For detecting higher energy neutrons, the reaction of interest is shifted to a ^{35}Cl(n,p) reaction. This reaction is exothermic and has a Q-value of 0.615 MeV,

$$ {}^{1}_{0}n + {}^{35}_{17}Cl \rightarrow {}^{35}_{16}S + {}^{1}_{1}p \tag{50} $$

Thus, in the second Cs_2LiYCl_6:Ce, the ^{6}Li content has been reduced, in order to give the reaction with ^{35}Cl more frequency. A natural Cl content, which was 75% ^{35}Cl and 25% ^{37}Cl, was left since this abundance was already high in the ^{35}Cl isotope. Subsequently, a natural Li content crystal was tested, with 7% ^{6}Li and 93% ^{7}Li. To further enhance the probability of a neutron being absorbed by ^{35}Cl and not ^{6}Li, a 99% enriched ^{7}Li crystal was investigated. Numerous calculations have been done to determine the optimal content for the Li isotopes. Therefore two cylindrical Cs_2LiYCl_6:Ce scintillators enriched with 95% ^{6}Li and 5% ^{7}Li, and enriched with 99% ^{7}Li and 1% ^{6}Li were chosen. The remaining elements that constitute the crystal's composition were in their natural abundances. For instance, chlorine which is 75% ^{35}Cl and 25% ^{37}Cl was kept in its natural abundance. These crystals have a high average atomic number and therefore are useful not only for neutrons, but also for gamma-ray spectroscopy as well. Consequently, one can benefit from their high density and their multi-element content for a mixed neutron gamma radiation field. The density of the first and second crystal is 3.31 g/cm^3 and both have dimensions of 2.54x2.54 cm. One of the investigated models is presented in Fig. 33. This model was used for gamma and fast neutron simulations. However for thermal neutrons simulations, a 3.5 cm thick paraffin moderator surrounding the detector has been added to the current model.

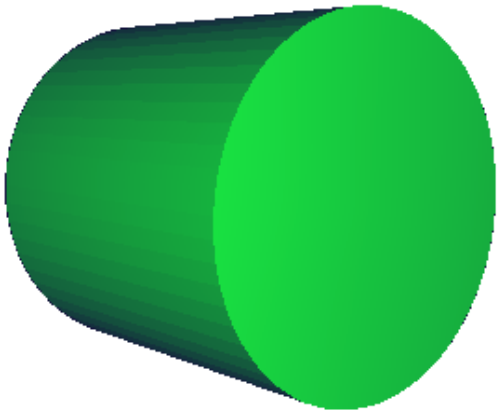

Figure 33: Model of the Cs_2LiYCl_6:Ce scintillator in VisEd

3.2 Experimental Investigation

Guided by extensive Monte Carlo simulations and calculations, a series of experiments were conducted at three different facilities. These facilities/laboratories were used with different sources to generate the desired neutron energies. Two of these laboratories, namely an AmBe source and neutron generator, were used at UOIT, and a KN Van De Graff accelerator at McMaster University. Below is a brief description of the facilities.

3.2.1 UOIT Facilities Descriptions

3.2.1.1 AmBe Source

The University of Ontario Institute of Technology (UOIT) Neutron Facility opened in the year 2010. It is the first research lab at UOIT in the nuclear and radiation sciences. This facility houses an AmBe neutron source of 120 mCi and it is presented in Fig. 34.

Figure 34: AmBe Facility at UOIT

This source is comprised of a homogenous, compressed mixture of americium oxide and beryllium. Neutrons are created by alpha particles from the decay of ^{241}Am bombard ^{9}Be nuclei.

$$^{241}_{95}Am \rightarrow ^{237}_{93}Np + ^{4}_{2}He \tag{51}$$

There are three types of reactions that could occur with ^{9}Be to produce neutrons:

$$^{9}_{4}Be + ^{4}_{2}He \rightarrow ^{12}_{6}C + ^{1}_{0}n \tag{52}$$

$$^{9}_{4}Be + ^{4}_{2}He \rightarrow ^{8}_{3}Be + ^{4}_{2}He + ^{1}_{0}n \tag{53}$$

$$^{9}_{4}Be + ^{4}_{2}He \rightarrow 3^{4}_{2}He + ^{1}_{0}n \tag{54}$$

Where, the first reaction is the most probable. For every 10^6 alpha particles, only 70 neutrons can be created using this source. The source inherently has gamma-rays emitted, but at low energies. The neutron flux of this source as a function of distance can be seen in Fig. 35.

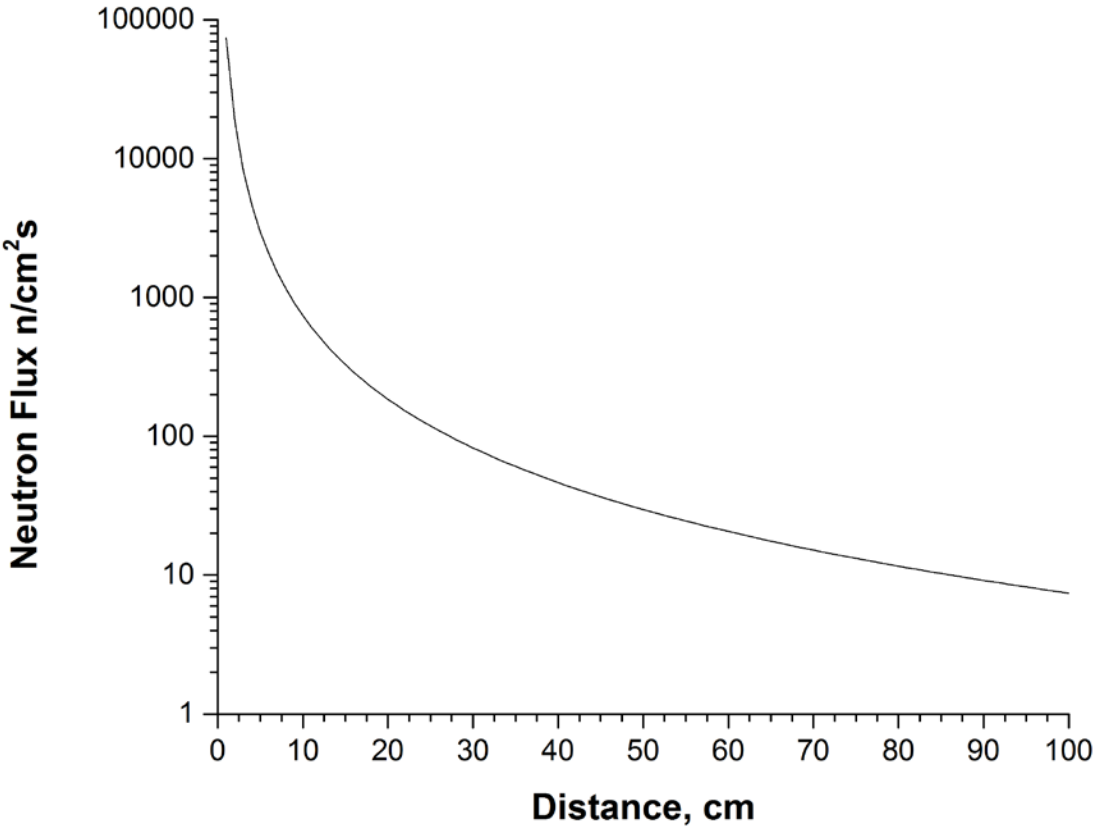

Figure 35: Calculated neutron flux of an AmBe source as a function of distance

Inside this facility, a rectangular grid case encloses the source. This gives the operator, outside the cage, enough distance to reduce the neutron flux to an acceptable level; as per the inverse square law, the intensity of the source is inversely proportional to the square of the distance from the source.

$$\text{Intensity} \propto \frac{1}{r^2} \tag{55}$$

A tank of water for shielding purposes is located in the center of the cage. In this tank, there are nine vertical cylindrical Aluminium tubes. Three sources of 40 mCi each are currently placed inside three Aluminum tubes. When the sources are in use, they are vertically raised out of the tank of water by a pulley system outside of the cage, and released back into the water tank at the end of each experiment. In each experiment, using this facility, the detector has been placed on

top of a conveyor and brought closer or further from the source by, manually, adjusting its position from outside of the cage.

The source emits a range of neutron energies, averaging around 4.16 MeV [97]. The radioactive isotope ^{241}Am has a half-life of 432 years and is therefore a relatively long-lived source that does not require frequent replacement. The neutron emission spectrum can be seen in Fig. 36.

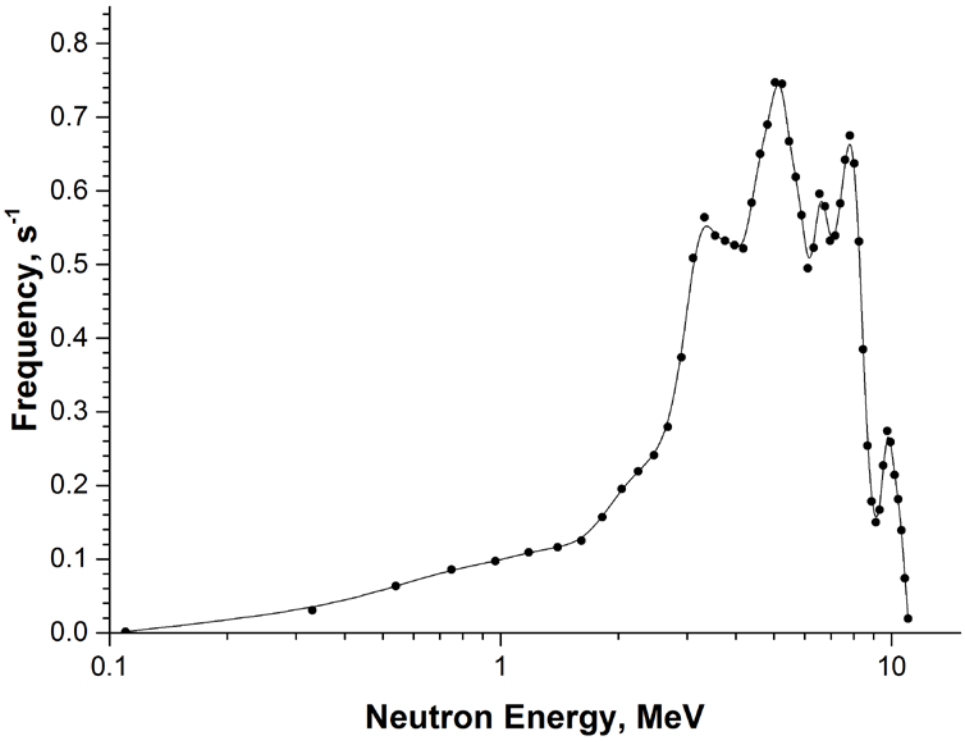

Figure 36: ISO 8529 AmBe neutron emission spectrum [97]

In addition to neutrons emitted from the AmBe source, standard gamma-ray sources with an activity of 1 μCi were used. The gamma sources are sealed in plastic with epoxy to prevent contamination. The standard size is 1” in diameter. These sources can be seen in Fig. 37.

Figure 37: Sealed gamma-ray sources

To thermalize neutrons emitted from the AmBe source, a paraffin cylindrical moderator was used. In a front collision with hydrogen atoms, a neutron loses approximately half of its energy, so after ~33 collisions, the neutron will reach thermal energy. Figure 38 shows two commonly used materials for moderation and the amount of energy loss as a function of the number of collisions.

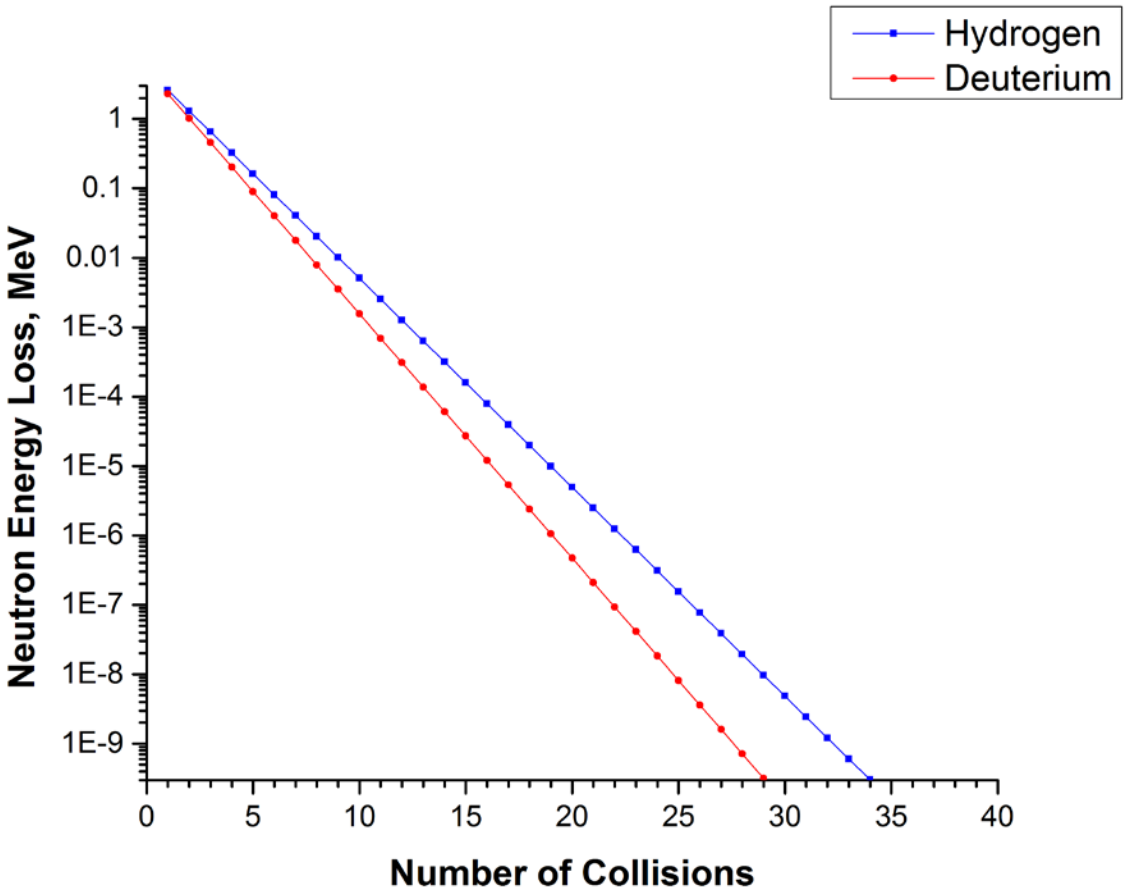

Figure 38: Calculated energy loss of a neutron per collision for hydrogen and deuterium

Based on this, paraffin wax, $C_{30}H_{62}$, was determined suitable as a moderator because it is highly concentrated with hydrogen and can be shaped in any form. The appropriate thickness of the moderator depends on the distance it takes for a neutron to go from its initial neutron energy to thermal energy. With a density of 0.91 g/cm^3, the required thickness to thermalize neutrons was determined to be ~3.5 cm. To accommodate the detector, many blocks of the paraffin moderator has been melted and shaped in a cylindrical form, with a hole made in the center. An illustrated photo of the moderator is shown in Fig. 39.

Figure 39: Paraffin moderator

The experimental setup using the LiI:Eu detector at the facility with moderator is presented in Fig. 40 from the front and in Fig. 41 from the side. Lead was used for various measurements to reduce the gamma-rays being picked up by the detector.

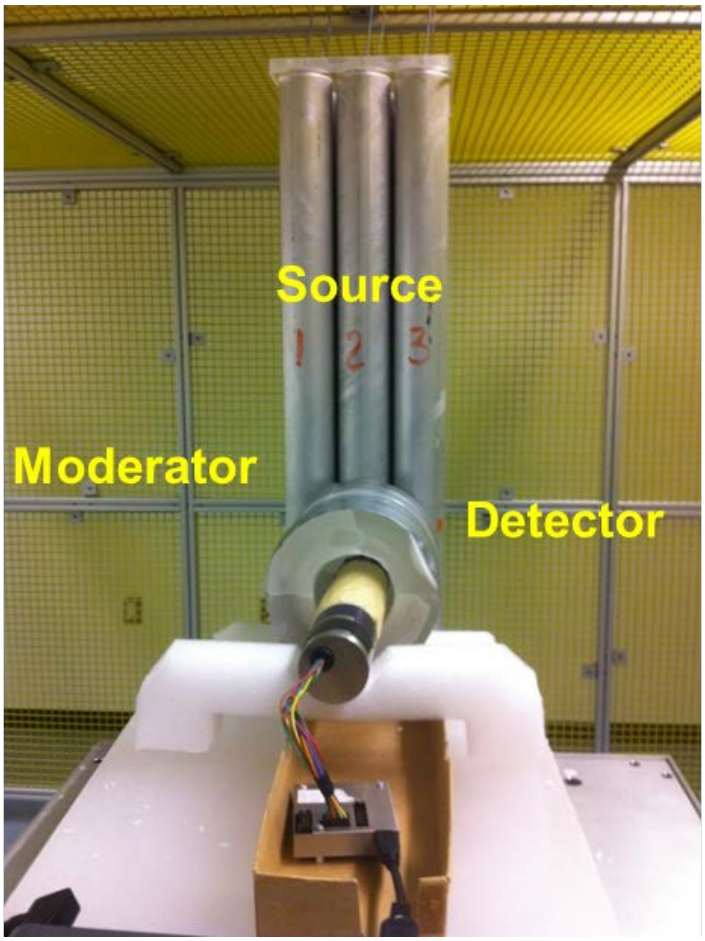

Figure 40: Front view of the experimental setup of a LiI:Eu detector with moderator using an AmBe source

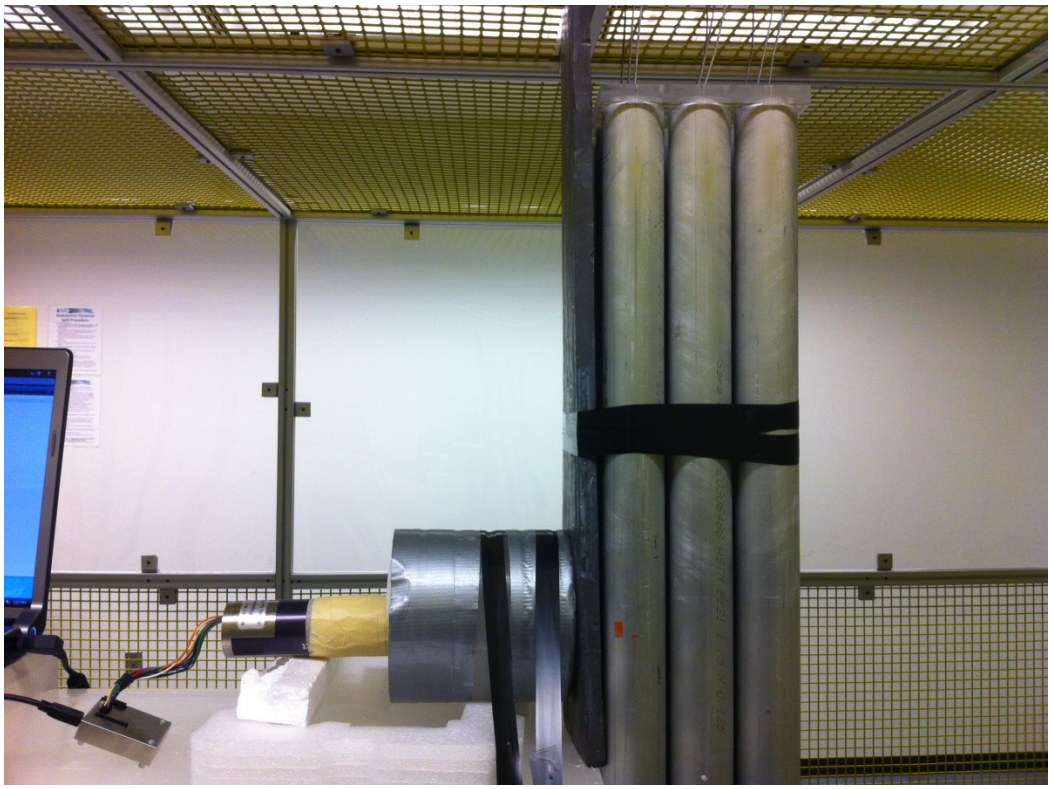

Figure 41: Side view of the experimental setup of a LiI:Eu detector with moderator using an AmBe source

3.2.1.2 Neutron Generator

A neutron generator at UOIT began operation in 2013. This generator is a part of the applied radiation laboratory in the Energy Research Centre at UOIT. The generator along with the detection system is shown in Fig. 42.

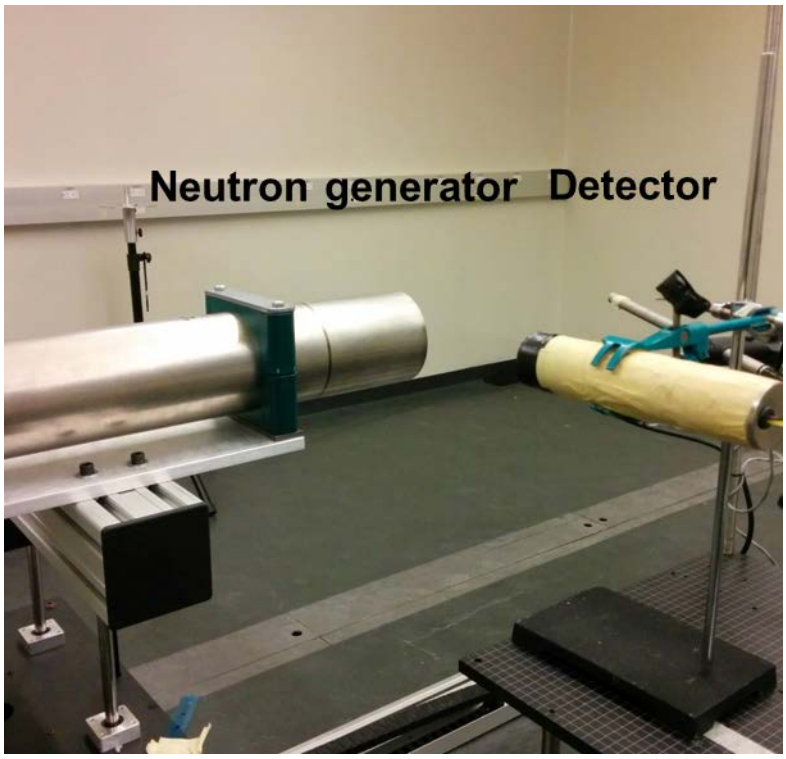

Figure 42: Experimental setup of the detection system and neutron generator

This generator uses a deuteron beam and deuteron target to generate 2.45 MeV neutrons at 90° based on the following reaction:

$$ {}^{2}_{1}H + {}^{2}_{1}H \longrightarrow {}^{1}_{0}n + {}^{3}_{2}He \tag{56} $$

Where ^{3}He takes 0.82 MeV and the neutron takes 2.45 MeV. The Q-value for this reaction is 3.269 MeV. This reaction occurs 50% of the time, and the other 50% of the time. Another reaction that generates a proton and tritium takes place:

$$ {}^{2}_{1}H + {}^{2}_{1}H \longrightarrow {}^{1}_{1}p + {}^{3}_{1}H \tag{57} $$

Where ^{3}H takes 1.01 MeV and the proton takes 3.02 MeV.

The neutron yield depends on the current and high voltage given under which the generator is operated. This yield changes linearly with current. The system can tolerate a current in the range between 20 to 70 μA. The relationship between neutron output and high voltage is $X^{3/2}$. It is

important to note that a high voltage of at least 40 kV must be applied to the system in order to generate neutrons. The system runs up to 130 kV, but at such values, it is more susceptible to a faulty condition and should be avoided. For an extended lifetime the device should operate at lower currents and higher voltages.

For instance, a high voltage of approximately 90 kV and 50 μA, would generate a neutron intensity of around 10^8 n/s is produced. The optimal parameters for generating 2.45 MeV neutrons while maintaining the system, was determined to be a current of 60 μA and high voltage of 90 kV which was used for the three measurements.

3.2.2 McMaster Facility Description

A KN Van De Graaff Accelerator at McMaster University is a linear, horizontal, single ended accelerator with 3 MV. It was built in 1956 by High Voltage Engineering Corporation of Burlington, Massachusetts. Later in 1970, it was used for cancer research by the Princess Margaret Hospital in Toronto. It is now used to perform measurements in a variety of science and engineering areas. The accelerator hall is shown in Fig. 43.

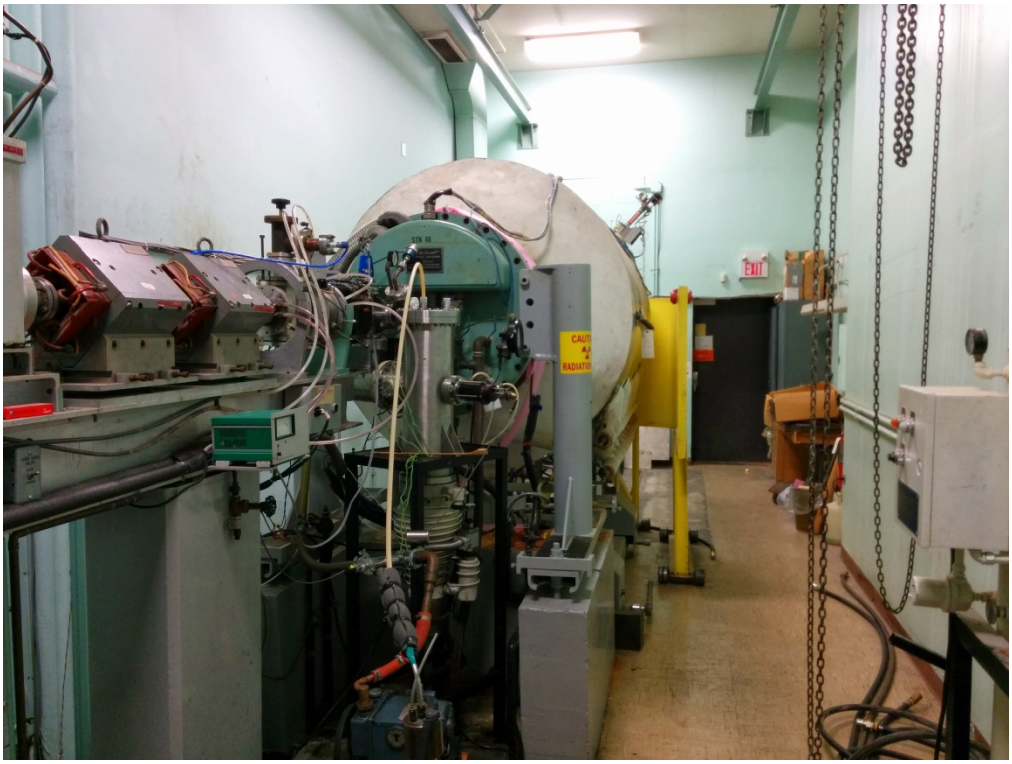

Figure 43: KN Van De Graaff Accelerator at McMaster University (Hamilton)

This facility was used to conduct several experiments using fast neutrons. Neutron energies generated ranged from 300 keV to 4 MeV. For the first range of energies in the keV region, a LiF target was used with different proton beams following the reaction:

$$ {}_{1}^{1}p + {}_{3}^{7}Li \longrightarrow {}_{0}^{1}n + {}_{4}^{7}Be \tag{58} $$

This reaction has a Q-value of -1.644 MeV i.e. is an endothermic reaction, meaning that the beam energy must be greater than the threshold value for it to occur. This value is defined in [98],

$$ E_{th} = \frac{-Q(M_3 + M_4)}{M_3 + M_4 - M_1} \tag{59} $$

and yields a value of 1.88 MeV. It is important to note that if the beam energy exceeds the threshold value but is less than a second critical energy value, two neutron energies are possible for each angle. This value is defined in [98]:

$$E'_1 = \frac{-QM_4}{M_4 - M_1} \tag{60}$$

and yields a value of 1.94 MeV. Above this energy, each angle produces single neutron energy.

The minimum theoretical neutron energy that can be produced is at a beam energy of 1.88 MeV, which is determined by [99],

$$E_n = \frac{M_1 M_3 E_{th}}{(M_4 + M_3)^2} \tag{61}$$

and yields a value of 0.03 MeV. Since the neutron energy is a function of the outgoing angle, it can be determined by [98],

$$E_n^{1/2} = \frac{(M_1 M_3 E_1)^{1/2} \cos\theta \pm \{M_1 M_3 E_1 \cos^2\theta + (M_3 + M_4)[M_4 Q + (M_4 - M_1)E_1]\}^{1/2}}{M_3 + M_4} \tag{62}$$

Neutron energies that can be generated range from 100 to 800 keV. In the experiments, the energies used with this beam and target were 300 keV, 400 keV, and 600 keV. These neutron energies were obtained by keeping the angle with respect to the detector constant at 0° using a lining laser beam, but changing the proton energy. The beam current was 200 nA throughout these measurements.

For the second range of energies i.e. 0.8 MeV to 4 MeV, the beam and target was changed. A deuteron target and deuteron beam was used to generate neutrons from energies 2.67 MeV to 4 MeV using the reaction:

$$^2_1H + ^2_1H \longrightarrow ^1_0n + ^3_2He \tag{63}$$

The energies used with this beam and target were 2.67 MeV, 3.57 MeV, and 4 MeV. Each neutron energy was obtained by keeping the deuteron energy constant at 900 keV, but changing

the angle with respect to the detector, from 0°, 45°, to 90°. The beam current was 800 nA throughout these measurements.

The experimental setup using the facility is shown in Fig. 44. Only a portion of the accelerator is shown in this figure, but the charged particles are accelerated along the route, referred to as beam, to hit the target in the front. For these experiments, since the reactions of interest with this detector were fast neutrons, any presence of low energy neutron energies should be reduced as much as possible. Thus, the detector has been placed at approximately 100 cm, and thin cadmium sheets of few millimetres thickness were used to cover the detector. In this configuration, a large part of thermal and epithermal neutrons generated by scattering processes in the room has been reduced and the fast portion of the beam was dominant.

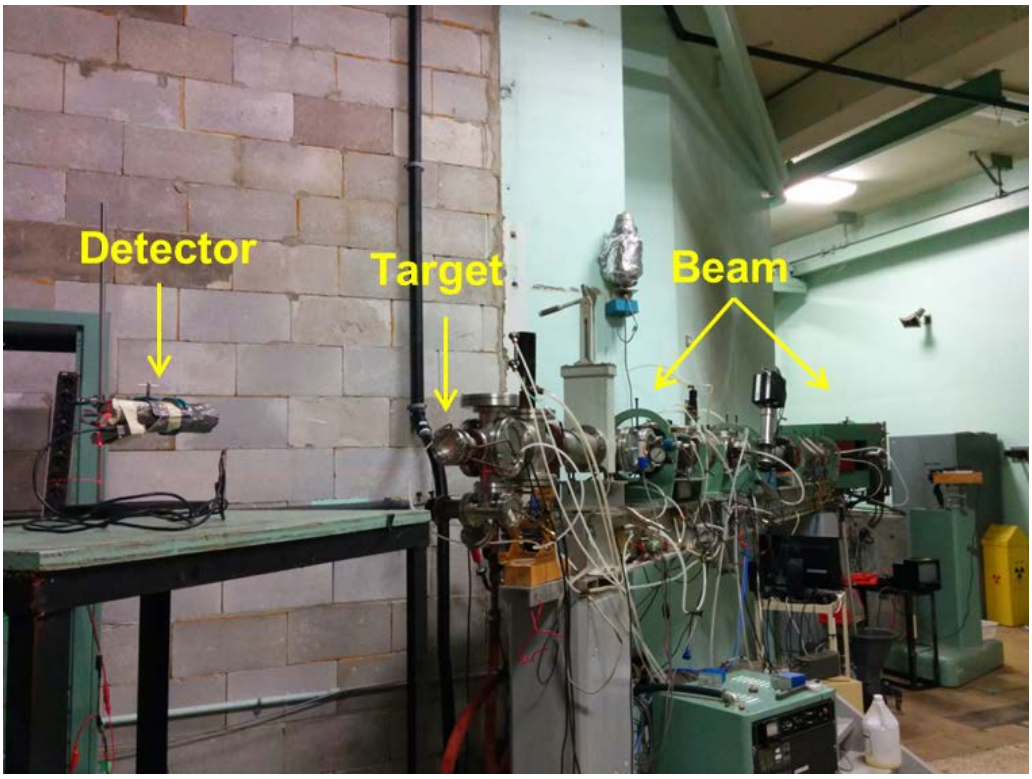

Figure 44: Experimental setup at McMaster Accelerator Laboratory

3.2.3 Detector Characteristics

Four detectors were explored and studied. Of the scintillators, three are inorganic and one is organic. The neutron detection in this study was divided into two main regions, thermal and epithermal, and fast neutrons. Three detectors were investigated for the former, and one for the latter.

3.2.3.1 LiI:Eu Scintillator

A LiI:Eu scintillator from Eljen Technology, presented in Fig. 45, is a hygroscopic material, encased in an aluminum isolated case for protection from any moisture in the air. The scintillator was identical to the model simulated i.e. a cylindrical scintillator enriched with 99% ^{6}Li and 1% ^{7}Li; a density of 4.06 g/cm^{3}, and dimensions of 1x2.5 cm. This sensor has a decay time of 1.4 μs, light yield of 11,000 photons/MeV, and a maximum wavelength of emission of 470 nm.

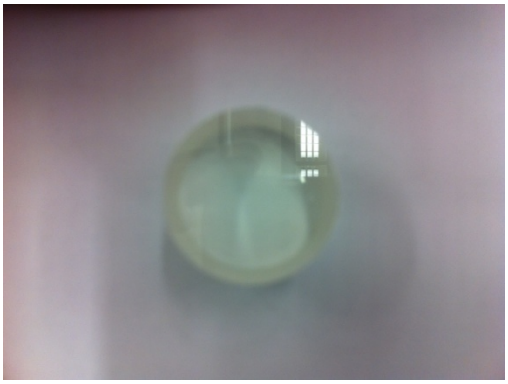

Figure 45: Top view of the LiI:Eu scintillator

3.2.3.2 Boron-Loaded Plastic Scintillator

An EJ254 boron-loaded plastic scintillator from Eljen Technology is presented in Fig. 46. This scintillator is identical to the model built in the previous simulation. It contained 5% boron loading of about 1% of the ^{10}B isotope; and the rest of the composition is carbon and hydrogen. The density of the scintillator is 1.026 g/cm^{3}, and it has a cylindrical geometry with dimensions of 2.5x2.5 cm. It has a decay time of 2.2 ns, light yield of 7500 photons/MeV, and a maximum wavelength of emission of 425 nm.

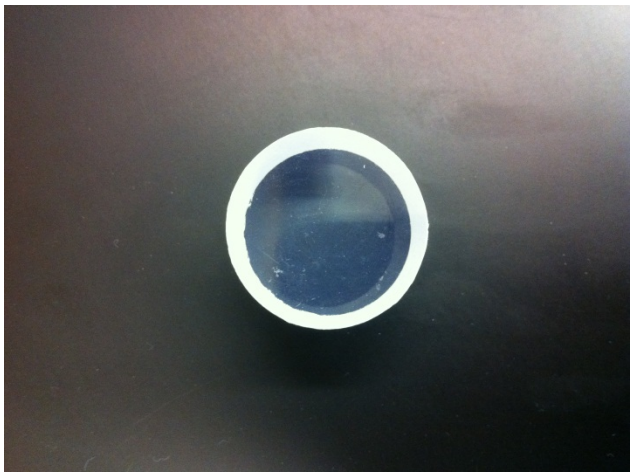

Figure 46: Top view of EJ254 boron-loaded plastic scintillator

3.2.3.3 ^{6}Li-Enriched Cs_2LiYCl_6:Ce Scintillator

A ^{6}Li-enriched Cs_2LiYCl_6:Ce scintillator is presented in Fig. 47. This crystal was enriched with 95% ^{6}Li. The density of the scintillator was 3.31 g/cm^3 and has a cylindrical geometry with dimensions of 2.54x2.54 cm.

Figure 47: Side view of Cs_2LiYCl_6:Ce scintillator

The light yield of photons per neutron is 73,000 and per 1 MeV gamma-ray is 22,000. This crystal has three light decay constants due to different light emissions after radiation has passed through its medium. It undergoes two types of emissions when traversed by gamma radiation. When electrons excite the crystal, it undergoes CVL or core-to-valence luminescence. This decay time is very short of about 1 nanosecond, and the emitted light has a wavelength between

250 and 350 nanometers. However, if the crystal is large enough, this light will be absorbed by the Ce^{3+} ions added as a dopant, and re-emitted at a slower rate than CVL, known as Ce^{3+} prompt. This is one of the types of emissions observed with this crystal. It is important to note that this type of emission occurs only when stimulated by electrons, and is therefore only the case with photons. An even slower light is emitted that has a wavelength between 350 to 450 nanometers. This is known as Ce^{3+}/STE, self-trapped exciton. This is the other type of emission observed. Therefore, CLYC has three different decay constants, 1 nanosecond, 50 nanoseconds, and 1000 nanoseconds; and an emission spectral range of 275 nanometers to 450 nanometers, with a peak wavelength at 370 nanometers [100]. Their respective emission and decay spectra can be seen in Fig. 48.

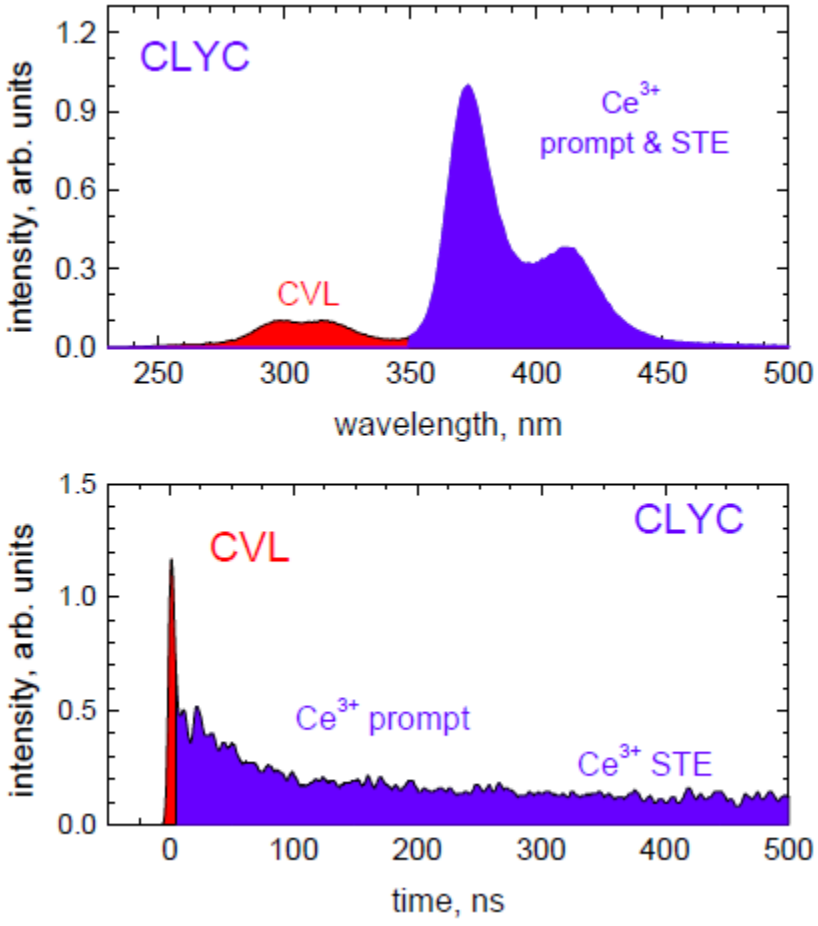

Figure 48: Cs_2LiYCl_6:Ce scintillator Emission and Decay Spectra for Gamma-ray Excitation [100]

When neutron radiation goes through the Cs_2LiYCl_6:Ce scintillator, different emissions are observed than that of gamma radiation. The charged particles produced via neutron induced reactions do not excite the CVL or prompt Ce^{3+} emissions. Only light emitted far later is observed with neutron excitation which means a slower decay time. This is the basis for using pulse shape discrimination for mixed neutron and gamma fields. An oscilloscope trace with a faster rise and decay time is from a gamma-ray, and a slower trace is from a neutron. This is presented in Fig. 49.

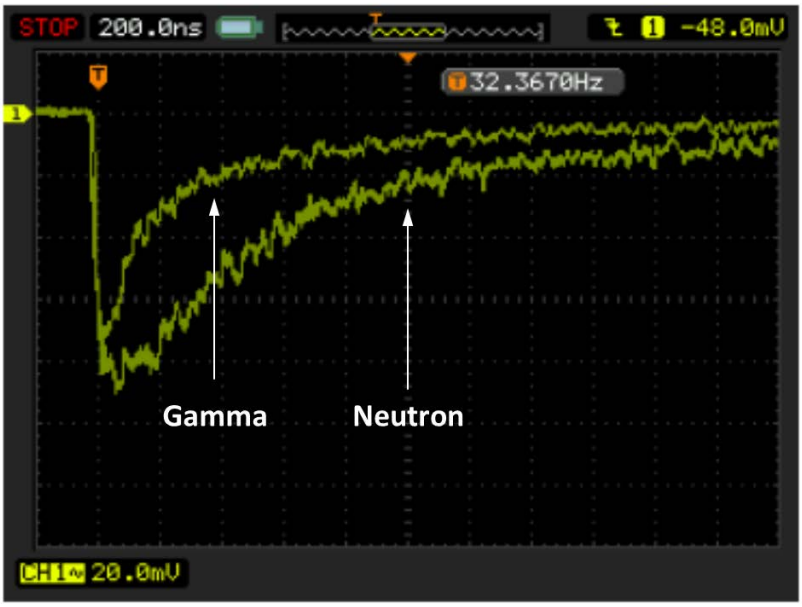

Figure 49: Oscilloscope Traces Due to a Gamma-ray and Neutron in CLYC [100]

3.2.3.4 ^{7}Li-Enriched Cs_2LiYCl_6:Ce Scintillator

The second version of Cs_2LiYCl_6:Ce scintillator was enriched with 99% ^{7}Li to reduce the dominance of the (n,α) reaction with ^{6}Li and is presented in Fig. 50. The chlorine content was in its natural abundance, 75% ^{35}Cl and 25% ^{37}Cl. The density of the scintillator is 3.31 g/cm^3 and has a cylindrical geometry with dimensions of 2.54x2.54 cm.

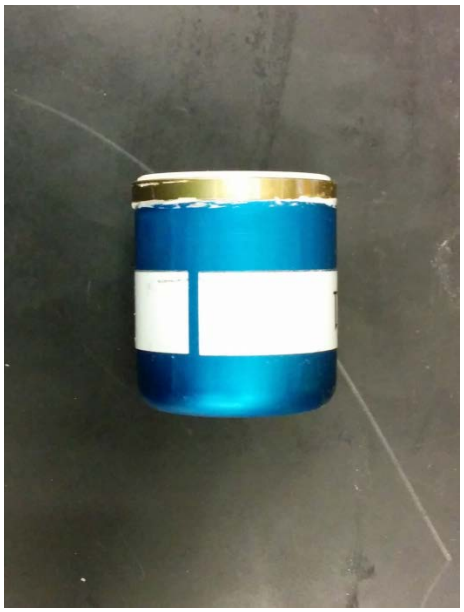

Figure 50: Side view of Cs_2LiYCl_6:Ce scintillator

3.2.4 Detection System Components

The first part of the detection system consists of the scintillators described in previous sections. When radiation interacts with the scintillator material, its produce charged particles such as electrons, protons and alphas in this case, that in turn excites the scintillator and consequently emits light in different frequencies. In order to convert the light into an electrical signal, a photomultiplier tube (PMT) is connected to the scintillator. The functionality of a PMT is based on two fundamental processes, the photoelectric effect and secondary emission. The PMT is composed of a photocathode, many dynodes, and an anode, in a vacuum enclosed glass. When a photon from the scintillator interacts with the photocathode, it ejects a photoelectron due to the photoelectric effect. These photoelectrons are then accelerated towards a series of electrodes called dynodes where they are multiplied by secondary emission. Each dynode is held at a higher voltage than the previous one. This amplification creates a gain of 10^5 to 10^7 electrons for each photoelectron ejected by the photocathode, which depends on the number of dynodes and voltage. This electrical signal is then amplified enough to be collected at the anode. The design of a PMT can be seen in Fig. 51.

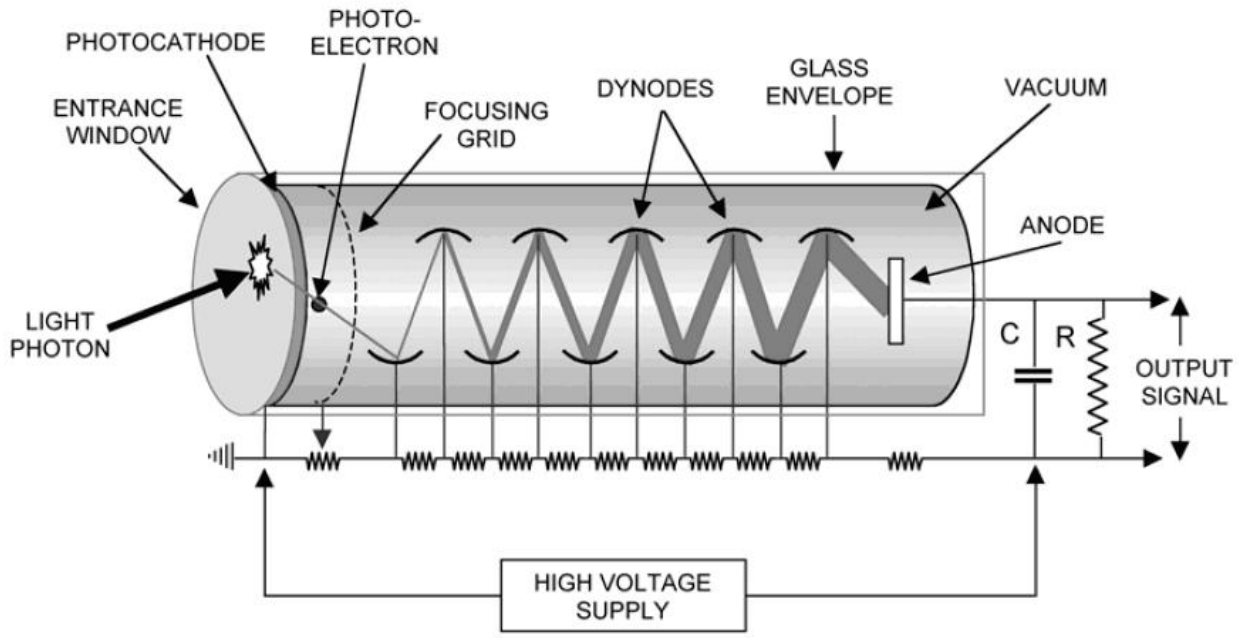

Figure 51: Design of a photomultiplier tube

For all experiments in this work, the scintillator was mounted on a R3998-02 Photomultiplier Tube from Hamamatsu as shown in Fig. 52. Its photocathode is bialkali (Sb-Rs-Cs, Sb-K, Cs) made up of two alkali metals. The PMT is a head-on-type and 2.5 cm in diameter and 6 cm in length. The PMT was chosen to match the emission spectra of the scintillators for the light to be transmitted. Its spectral response ranges from 300 to 650 nm which meets the requirements for all of four investigated scintillators.

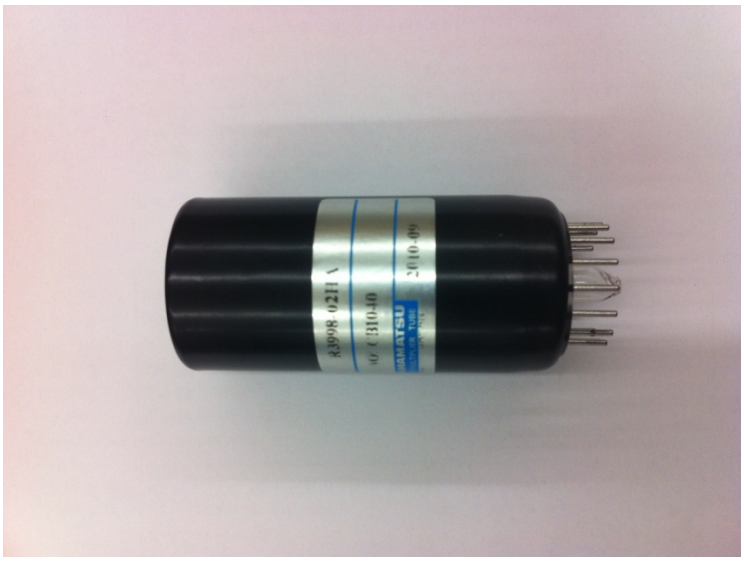

Figure 52: R3998-02 Photomultiplier Tube

The PMT spectral response is given in Fig. 53. The quantum efficiency, which is the percentage of incident photons that get converted to electrons, of the PMT is shown in Fig. 53.

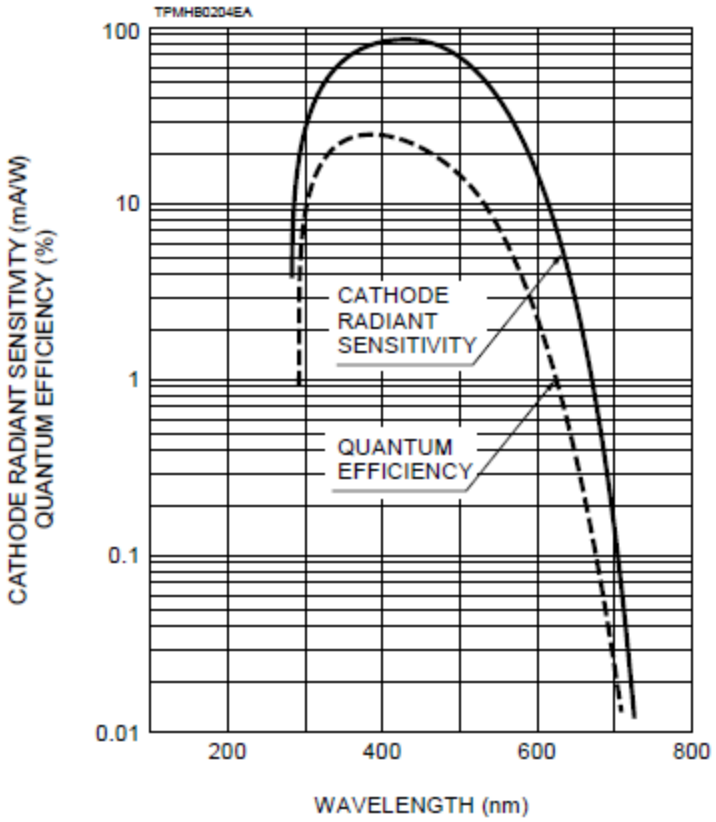

Figure 53: Spectral response of the R3998-02 Photomultiplier Tube [101]

The dimensional outline and basing diagram of the PMT is given in Fig. 54. It can be seen that this PMT has 9 dynodes and is connected via a socket to the rest of the data acquisition system.

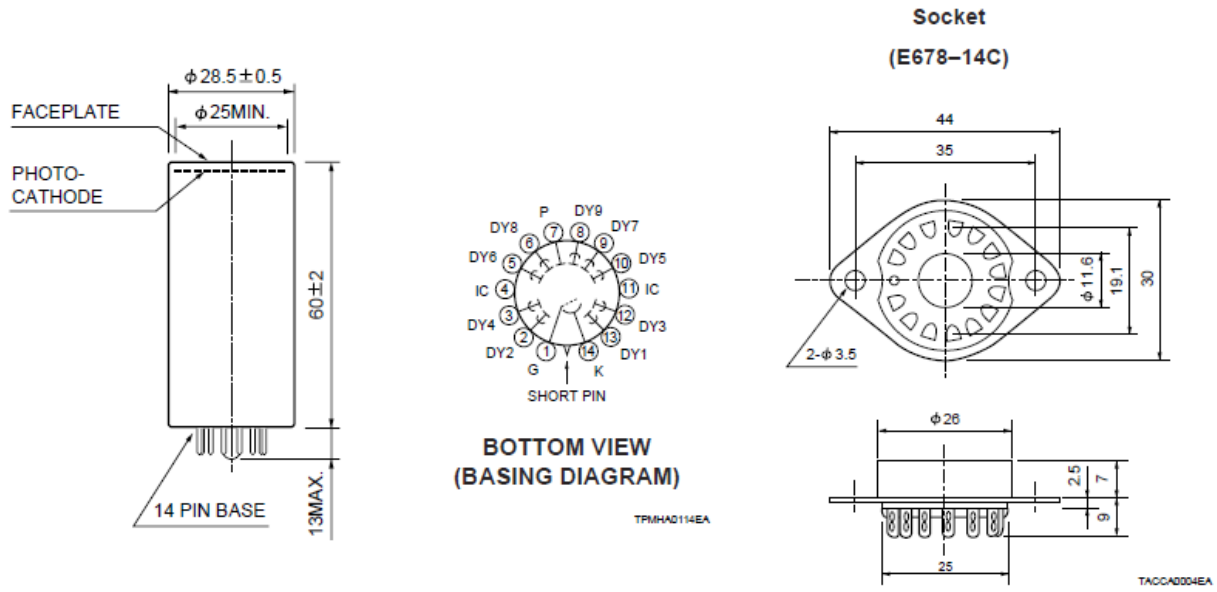

Figure 54: Dimensional outline and basing diagram of the R3998-02 Photomultiplier Tube [101]

To ensure proper coupling of the scintillator to the PMT, Eljen Technology-550 Optical Grade Silicone Grease was used at the beginning of each experiment after a careful cleaning of the photodiode with acetone liquid and soft material. This grease functions to transmit as much of the UV light as possible from the scintillator to the PMT, by preventing the light from being reflected. It is clear and colourless with moderate viscosity and has an index of refraction of 1.46. The percentage of transmission as a function of wavelength is given in Fig. 55.

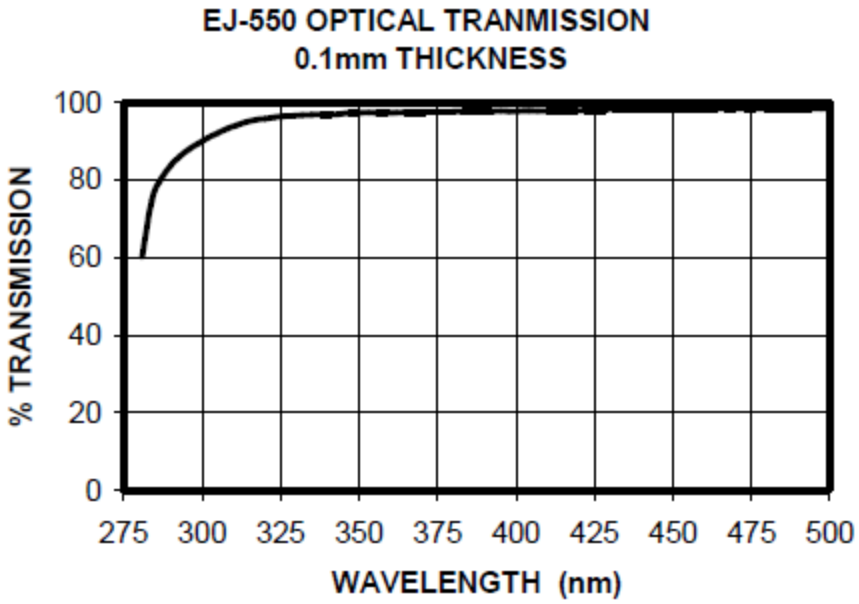

Figure 55: EJ-550 Optical transmission of 0.1 mm grease thickness [102]

For illustration, the detector casing with the LiI:Eu scintillator coupled to the PMT using optical grease is shown in Fig. 56.

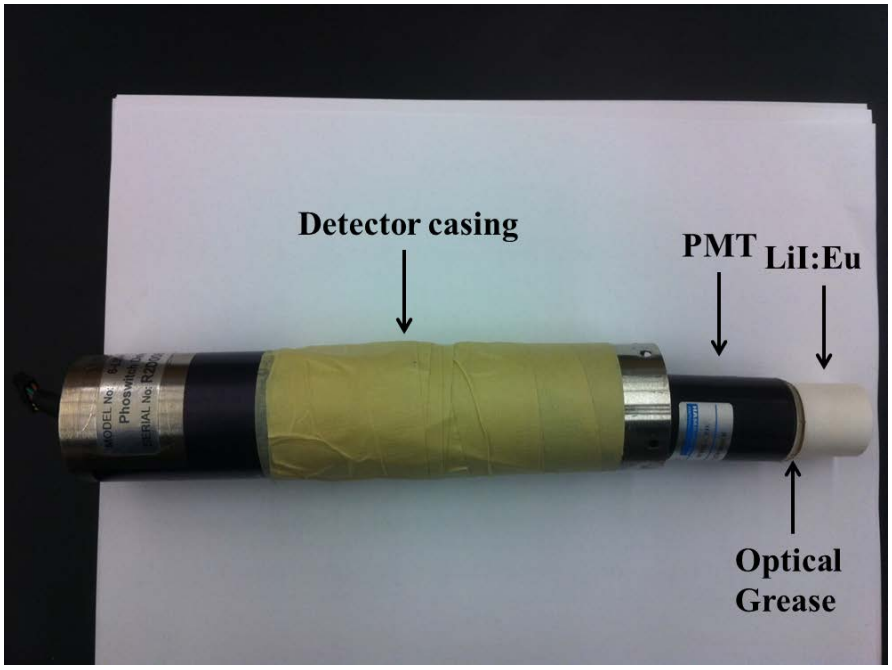

Figure 56: Detection chain with all components

3.2.5 Data Acquisition System and Signal Processing

From the detector, the signal is fed from the anode of the PMT and is transmitted to a customized eMorpho Multichannel Analyser (MCA) from Bridgeport Instruments LLC. The eMorpho is the front-end of the data acquisition system used for scintillator detectors with photomultiplier type readout. This is a high performance MCA embedded with a USB interface that uses digital signal processing. Figure 57 shows the PC-board of the eMorpho MCA. In actuality, a grounded metal housing surrounds it.

Figure 57: eMorpho MCA PC-board [103]

Within the MCA, the pulse processing begins. The basic components in pulse processing are given in Fig. 58.

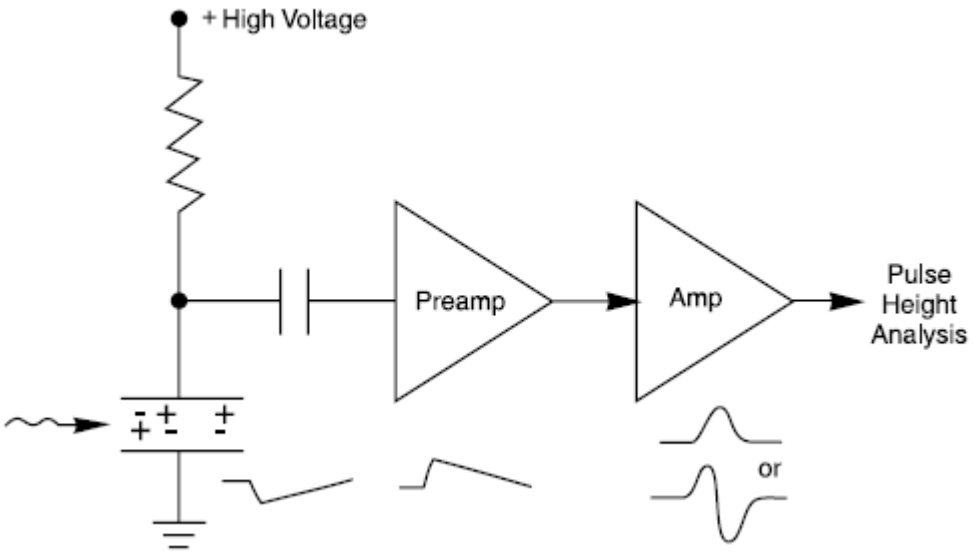

Figure 58: Basic detector and amplification [104]

The first step in digital processing is the pre-amplifier. Just as its name suggests, it is the component that comes before the amplifier, but does not perform any amplification functions. Its role is to collect the charge that was generated in the detector, by extracting the signal from the detector. It does so by applying a detector bias, an external high voltage, such that an electric field is created thereby causing the charge carriers to migrate and be collected. At this point, a small current flows whereby the drop in voltage across the bias resistor is the pulse voltage. The preamplifier is separated from the high voltage by a capacitor. The rise time of the preamplifier's output pulse correlates with the collection time of the charge. This time can range from a few nanoseconds to a few microseconds. The decay time of the preamplifier's output pulse is the RC time constant characteristic of the preamplifier itself. This time is usually around a few microseconds. It is important not to degrade the signal-to-noise ratio. For this reason, it is placed in close proximity to the detector. Therefore, it filters out any contributions from sources other than the detector in order to purify the signal for further processing. For this reason, the capacitance is kept to a minimum by maintaining a short enough cable from the detector to the pre-amplifier so that there is minimal interference with the signal.

The amplifier functions to shape the pulse and as the name suggests, amplify it. It magnifies the amplitude of the preamplifier output pulse between the range of mV into the 0.1 to 10 V range. In this way, pulse height measurements can be done with a peak sensing analog-to-digital convertor (ADC) or a single channel analyzer (SCA). In the case of digital pulse processing, the detector signal is digitized with the ADC directly after the preamplifier. The digitized pulse is shaped and the pulse height is extracted for pulse height analysis. A digital processor is the responsible for this task by either a field programmable gate array (FPGA) or a digital signal processor (DSP). After obtaining the pulse height, one count is added to the memory address to correspond to that pulse height.

The MCA uses a series of SCA with increasing restricted windows that consists of an ADC, control logic, memory, and display. It collects pulses in all voltage ranges and immediately sorts them into a histogram or spectrum of number of events versus pulse height. The output pulse height is proportional to the amount of ionizing radiation incident on the detector and provides information about its energy. The MCA components with digital signal processing can be seen in Fig. 59.

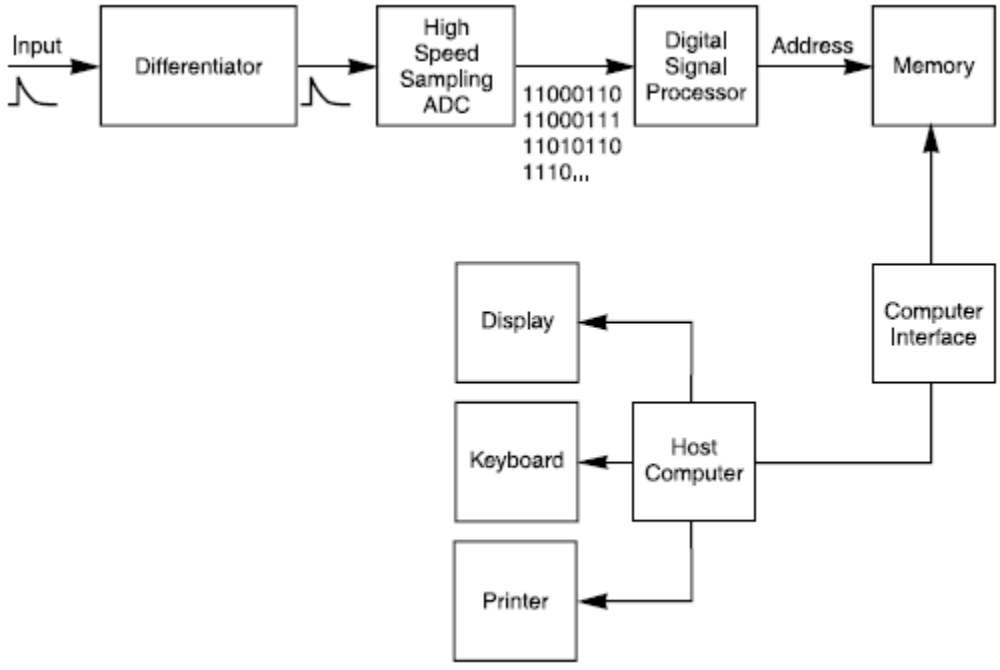

Figure 59: Multichannel analyzer components with digital signal processing [104]

The MCA uses 4096 channels on a 32-bit system. A FPGA (XC3S200) receives the digitized data and carries out the task of histogram and event storage and communicates this information to the computer via the USB cable.

A schematic diagram of eMorpho's functions can be seen in Fig. 60. The Data Acquisition System (DAQ) therefore consists of the MCA and high voltage unit that transfers data to the computer.

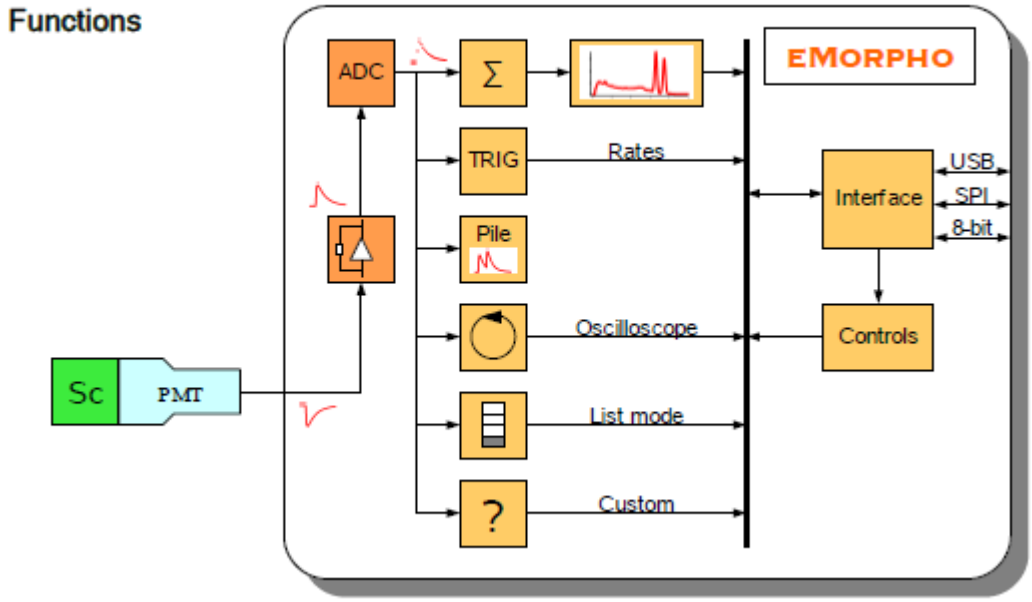

Figure 60: eMorpho functions [105]

The software used for data processing was Igor Pro®. Igor Pro is a technical graphing and data analysis software from Wave-Metrics. It is used for scientific and engineering data from experimentation. Version 6.1.2.1 has been used with eMorpho hardware.

The eMorpho MCA has various features and controls. The control panel in Igor Pro is seen in Fig. 61. The listed controls will be discussed later in this section.

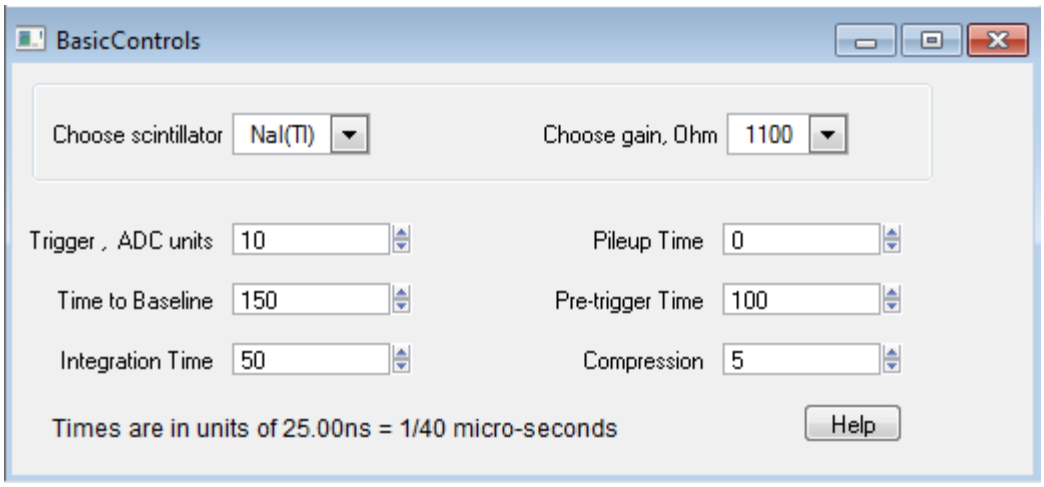

Figure 61: Igor Pro panels with controls

In the analog section, the current to voltage convertor has five gains to select from, 100, 430, 1100, 3400, and 10100 ohms. The trigger (ADC units) will define a level to detect incoming pulses at. This numerical value relates to the number of ADC bins. This level is used to eliminate very small signals. It is typically set to a value that is 2% of the ADC full scale range. The lowest reasonable value that can be entered is 3. Generally, this value should be adjusted to 10 or more in order to a get a reasonable count rate.

Integration time is set to equal the time which the scintillator emits most, 90%, of its light. It can range from 5 clock cycles to 65535 clock cycles. A clock cycle refers to ADC sampling clock cycles and they are counted on the trace panel seen in Fig. 62. The Morpho-DAQ board uses numerical integration to compute the pulse energy.

Time to baseline is the time eMorpho waits after receiving a pulse before it allows a trigger on a later pulse. This value is set to be at least equal to the integration time. This is used for avoiding re-triggering on the end tail of a pulse. If the pulse is longer than the integration time, this parameter allows a waiting time where no measurements are taken.

Pileup time is used for pulse pile up rejection. It is set to a value that is somewhat larger than the full width at half maximum of the pulse as seen in the trace display. This value can be tuned by reducing the pileup until the number of events declines. The pulse shape is compared to what the expected pattern should be. A value set to zero rejects all pulses and the spectrum will remain at zero.

Pre-trigger time is a parameter used for the trace display. It governs the amount of ADC samples that will be visible before the rising edge of the pulse.

Compression is a factor used to squeeze the energy values into the 4096 bin range of the histogram. The scaling factor chosen ensures that a maximum amplitude pulse is able to fit within the allowable ADC input voltage range of the histogram. This generally depends on the decay time of the scintillator.

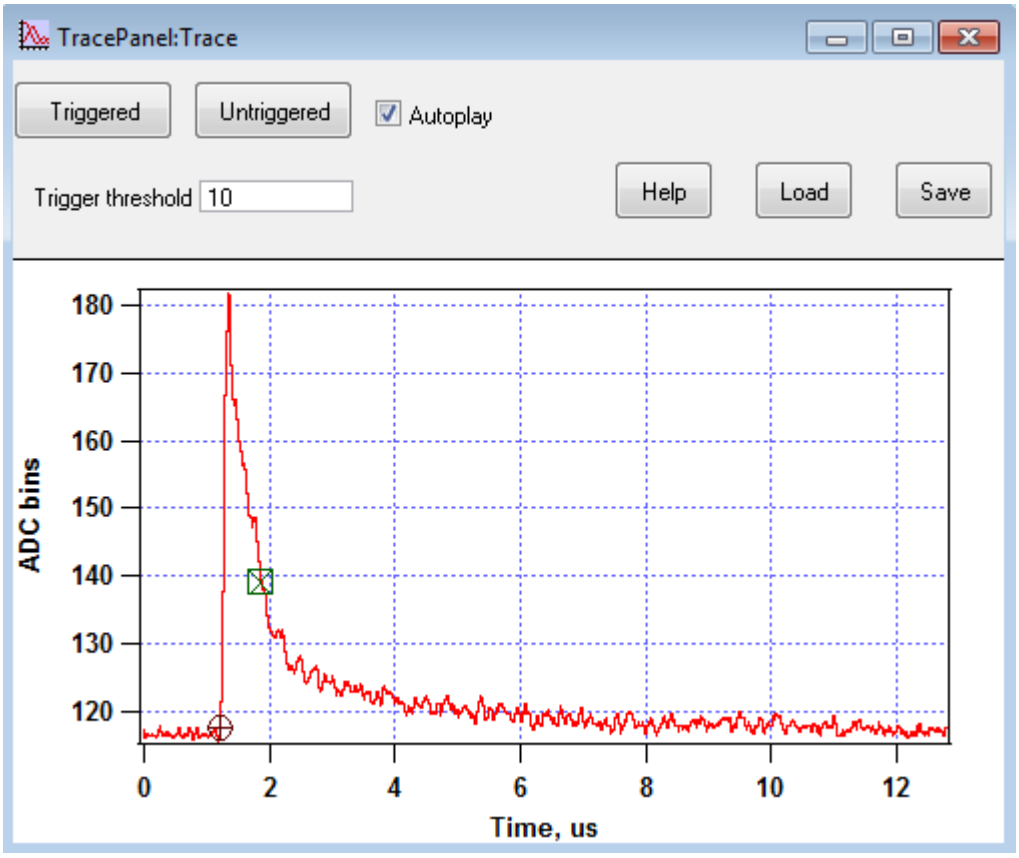

Figure 62: Digital scope trace panel

The scintillators parameters have to be chosen according to their decay and rising time parameters. By selecting the appropriate scintillator, the parameters are adjusted accordingly. In each experiment, the parameters were defined for each crystal, and the experiment therefore runs with optimal parameters of each crystal. For the boron-loaded plastic scintillator and Cs_2LiYCl_6:Ce scintillators, the parameters were defined based on the manufacturer's recommendation and multiple tests with the scope. In the case of the boron-loaded plastic

scintillator, the closest scintillator was plastic scintillator. This scintillator was 75% as fast as plastic, which was the starting point. These values were adjusted and optimized by multiple testing with the detector in a radiation field. Regarding the Cs_2LiYCl_6:Ce scintillators, as a starting point, the decay time of the scintillator was used to determine the integration time. After several testing in a radiation field, by carefully observing the trace panel, the rise and decay times were recorded and all values were fine-tuned suitably. These values were used for measurements with neutron and gamma radiation.

The accumulated data was exported to OriginLab software which is a data analysis and graphing software used for data analysis. Both simulations and experimental data have been processed in OriginLab framework. Various versions were used, since every year it is officially updated with a new release and features. The latest version used was OriginPro 9.1. The features of Origin plus offers extended analysis tools such as peak fitting, surface fitting, statistics, signal processing, and image processing. The user interface is given in Fig. 63.

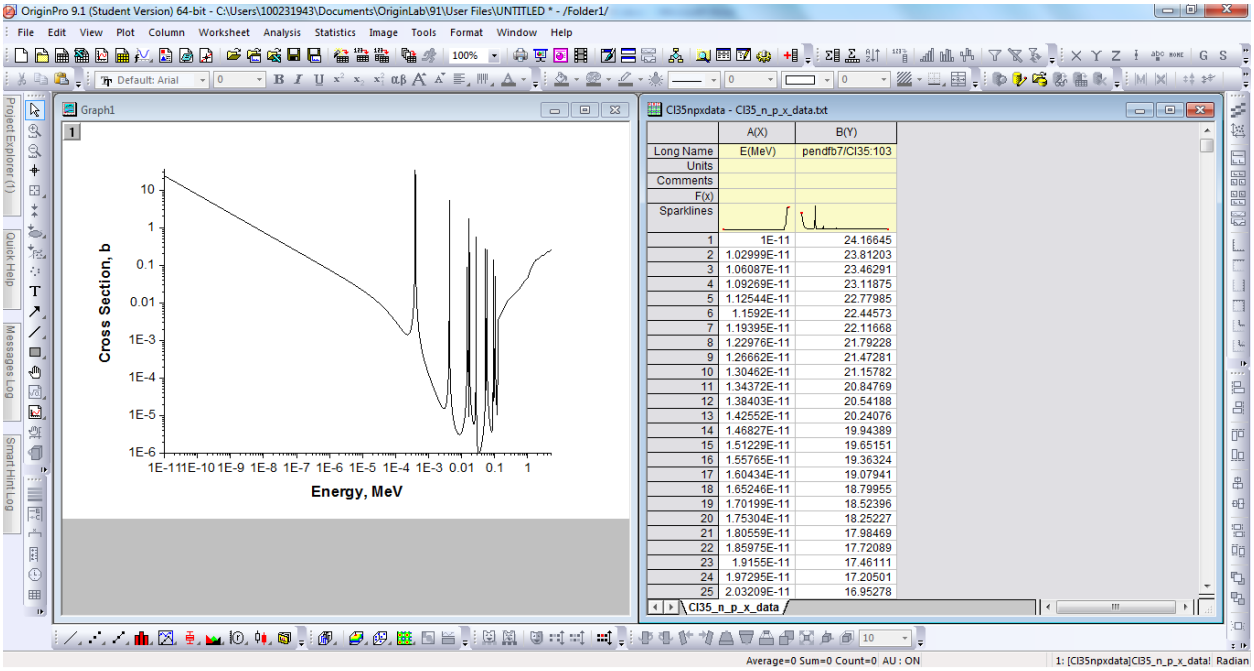

Figure 63: OriginPro 9.1 user interface

Chapter 4: Results and Analysis

The results and analysis presented in this chapter follows the sequence of the methodology described previously in Chapter 3. It is divided into two main sub-sections, simulations and experiments. Simulations are presented first, followed by experimental results. It is further divided by sub-sections regarding the radiation type for detection. Gamma and thermal neutron detection are presented together, while fast neutron detection is, separately, presented after. Mixed fields contain both neutron and gamma components and consequently each scintillator has to be tested to determine its response in different fields. This is crucial since all events are registered in the response function, whether gamma induced or neutron induced.

4.1 Simulation Results

As mention in the methodology chapter, simulations were carried out using MCNPX, where for each detector, an input file was created and output file was generated. In the input file, surface, cell, and data cards were defined. The source definition was a point source in all cases. The number of source particles used for thermal neutron calculations was 10^6, while for fast neutron and gamma-ray calculations, it was 10^7. This was sufficient to provide good statistics while minimizing the computer time for all calculations. To obtain the detector response function when irradiating with gamma radiation, the F8 tally, known as a pulse-height tally was used. This tally provides the output of energy distribution of pulses that were created in the detector. Energy bins were used which sum the energy deposited in a cell from all the tracks in the history. The F8 tally only supports the options of photons or electrons. Consequently, a combination of multiple output designators including the physics card has been used to obtain the detector response function for neutron radiation. The physics card allows the user to specify different options when transporting the selected particle. By default, simulations are created in an ideal circumstance unless otherwise specified. To apply an energy broadening for the detector at a given energy, a Gaussian energy broadening card or GEB, has been used. The parameters implemented define the full width at half maximum. The data collected for each simulation was imported into

OriginPro and further analyzed. For all sub-sections, gamma simulations are presented first, followed by neutron simulations.

4.1.1 Thermal Detection

4.1.1.1 Li Containing Scintillators – LiI:Eu and Cs_2LiYCl_6:Ce

4.1.1.1.1 LiI:Eu Scintillator

The simulated response function of the LiI:Eu scintillator to gamma radiation is presented in Fig. 64. This detector was irradiated with a ^{137}Cs source. An energy resolution of 11%, obtained in a separate experiment, was applied to the response function in the simulation.

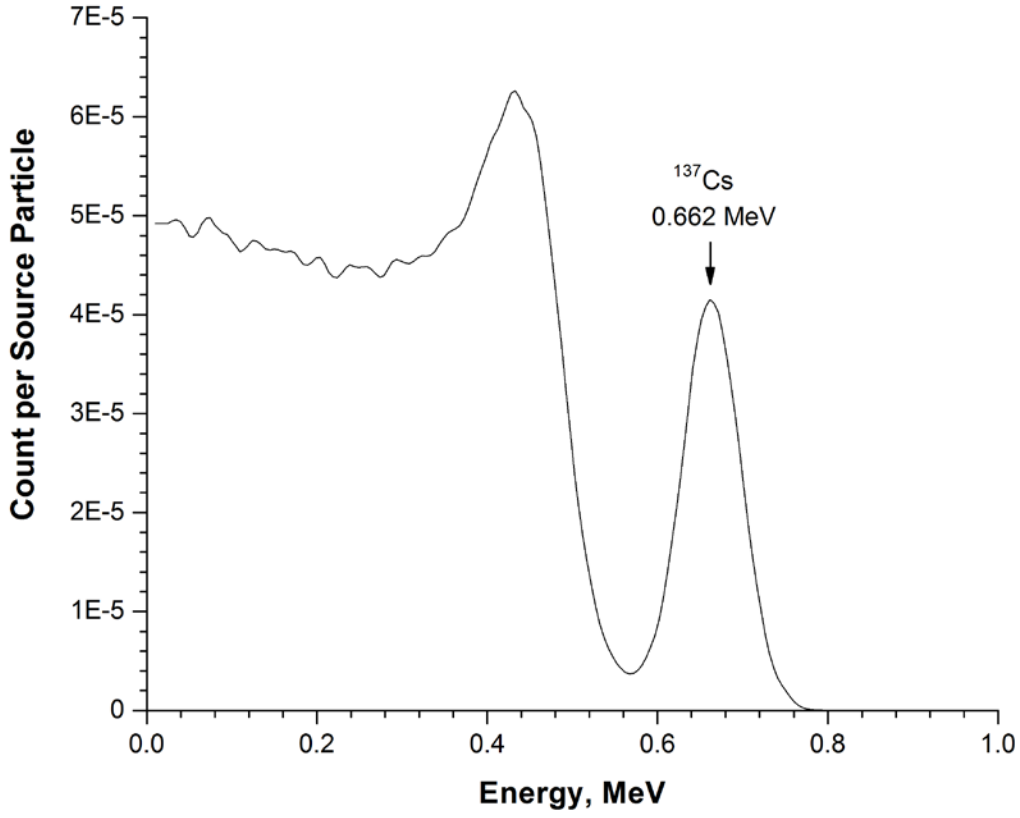

Figure 64: Simulated response function of LiI:Eu scintillator to ^{137}Cs

In Fig. 64, the x-axis represents the energy deposited by secondary electrons in the detector that produced scintillation light. The response function shows the full energy deposition of secondary electrons with the photoelectric peak at 0.662 MeV and Compton edge at 0.48 MeV. The Compton scattering is shown as a continuum from 0 MeV to 0.48 MeV. This distribution stems from the angle at which the incident gamma-ray is scattered from its original direction.

In order for this crystal to sufficiently accommodate gamma-rays of higher energies, it must be large enough in size for the secondary electrons to deposit their full energy. A practical gamma spectrometer is required to operate in the energy range from 0 MeV to 3 MeV, whereby the highest gamma-ray from natural background is ~2.6 MeV from ^{232}Th. It was determined that the range of a 2.6 MeV secondary electron in this crystal is 3.7 mm and the range of a 3 MeV secondary electron is 4.3 mm. Since the dimensions of this crystal are 1x2.5 cm, all of the gamma-rays encountered will undergo a full energy deposition event, and therefore, this crystal has potential to serve as a gamma spectrometer for this energy range, either in a gamma radiation field or in a mixed neutron gamma field.

Since the crystal was chosen to cover low energy neutrons, the detector was irradiated with a moderated AmBe neutron source. The source spectrum only incorporated neutrons and excluded the gamma spectrum produced with this source to solely assess its response to neutrons. This source has a hard spectrum and with the use of a moderator, neutrons lose sufficient energy to become thermalized. Based on a value obtained in a separate experiment, an energy resolution of 8% has been applied to an MCNPX input file and the response function has been generated. The simulated response function of the LiI:Eu scintillator to neutron radiation is presented in Fig. 65.

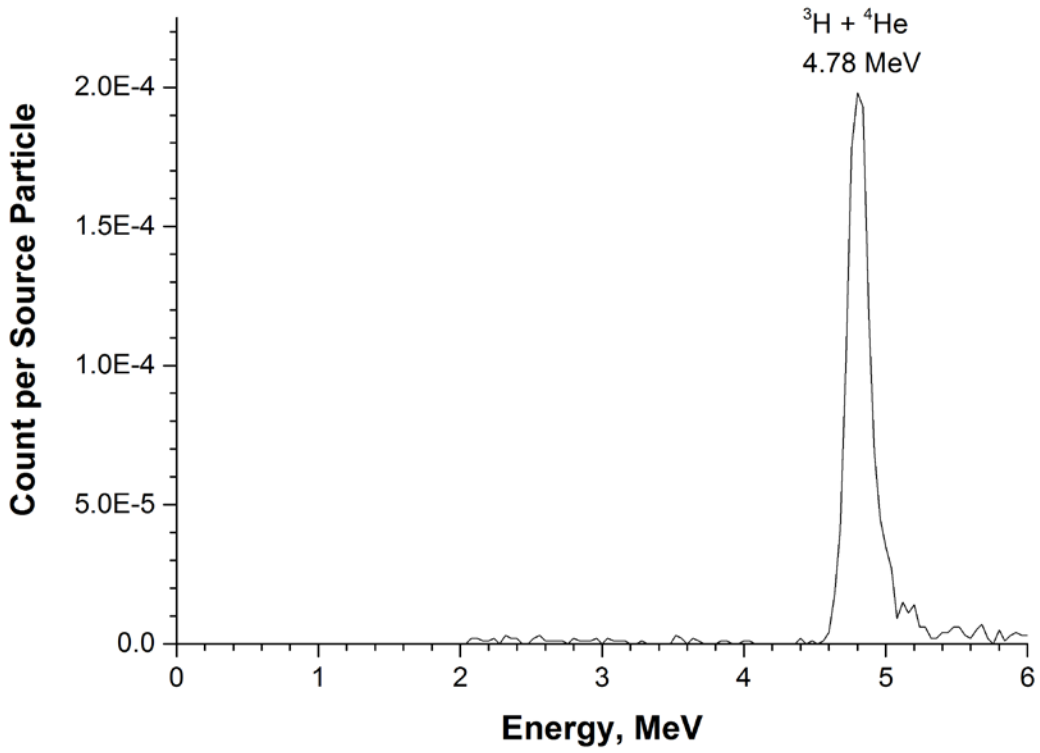

Figure 65: Simulated response function of LiI:Eu scintillator to moderated AmBe neutron source

In Fig. 65, the x-axis represents the energy deposited by alpha particles and tritons in the detector that produced scintillation light. The full energy deposition peak is shown at 4.78 MeV due to thermal neutron capture. Figure 66 shows the neutron absorption cross section of 940 barns at thermal energy.

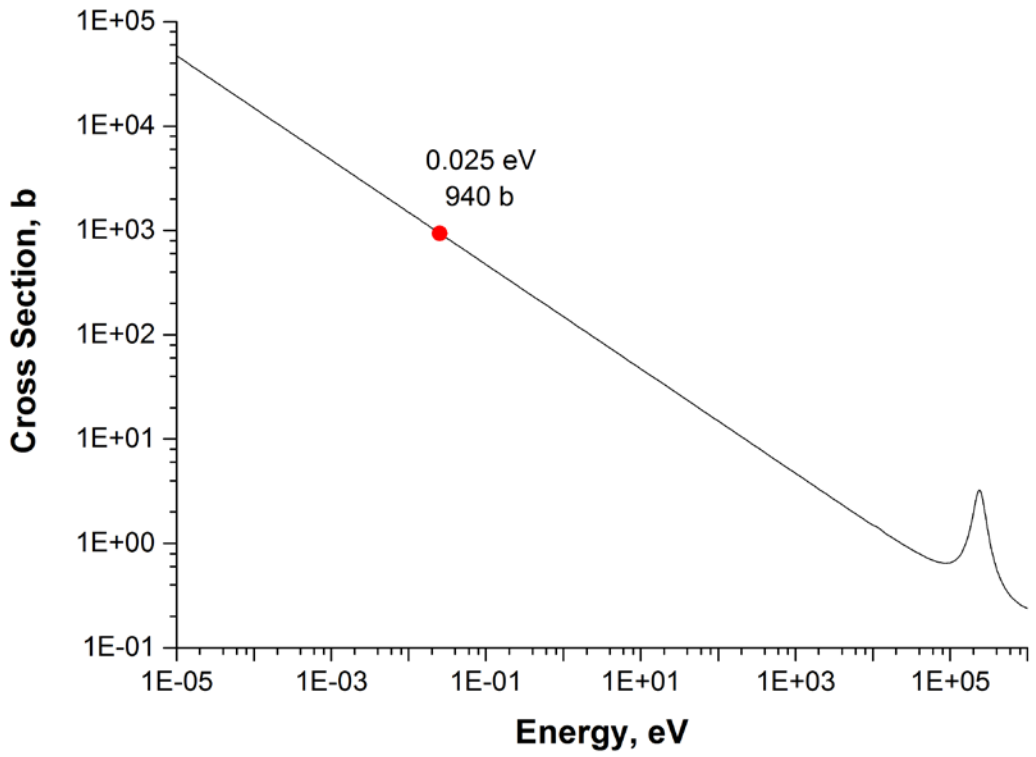

Figure 66: ENDF/B-VII.1 neutron absorption cross section for ^{6}Li(n,α) [106]

In Fig. 65, on the left side of the peak, small deposits are shown from around 2 MeV onwards. This indicates partial deposition of either ^{4}He or ^{3}H in the crystal, where either charged particle escapes from the detector. The neutron capture reaction likely occurred at the edge of the detector creating the wall effect. On the right side of the peak, neutrons with greater energy than thermal have undergone the same reaction, however in these events, the excess energy from the incident neutron is carried by either alpha particle or triton and deposited in the detector volume. As a result and due the low resolution of the detector, these events represent a contribution of fast neutrons as a continuum on the right side of the thermal peak. The population of this event is very small due to the low cross section of the reaction with higher neutron energies. Due to the nature of a point source emitting in all directions, some neutrons will interact with the detector without penetrating the moderating volume; or depending on the incident neutron energy, if it is sufficiently high where it would not undergo enough collisions in the detector to be thermalized,

it will remain at an energy higher than thermal. At these energies, there is still a neutron absorption cross section in the range of millibarns.

4.1.1.1.2 ^{6}Li-Enriched Cs_2LiYCl_6:Ce Scintillator

Due to its better resolution, this crystal has been chosen as an alternative for LiI:Eu. The simulated response functions of the ^{6}Li-enriched Cs_2LiYCl_6:Ce scintillator to gamma radiation is presented in Figs. 67-70. This detector was irradiated with various gamma-ray sources, ^{137}Cs, ^{60}Co, ^{22}Na, and ^{57}Co, covering an energy range of 0.122 MeV to 1.332 MeV. Based on a control experiment, an energy resolution of 6.9%, for ^{137}Cs, was applied to the MCNPX input file and the detector response function has been generated as shown in Fig 67.

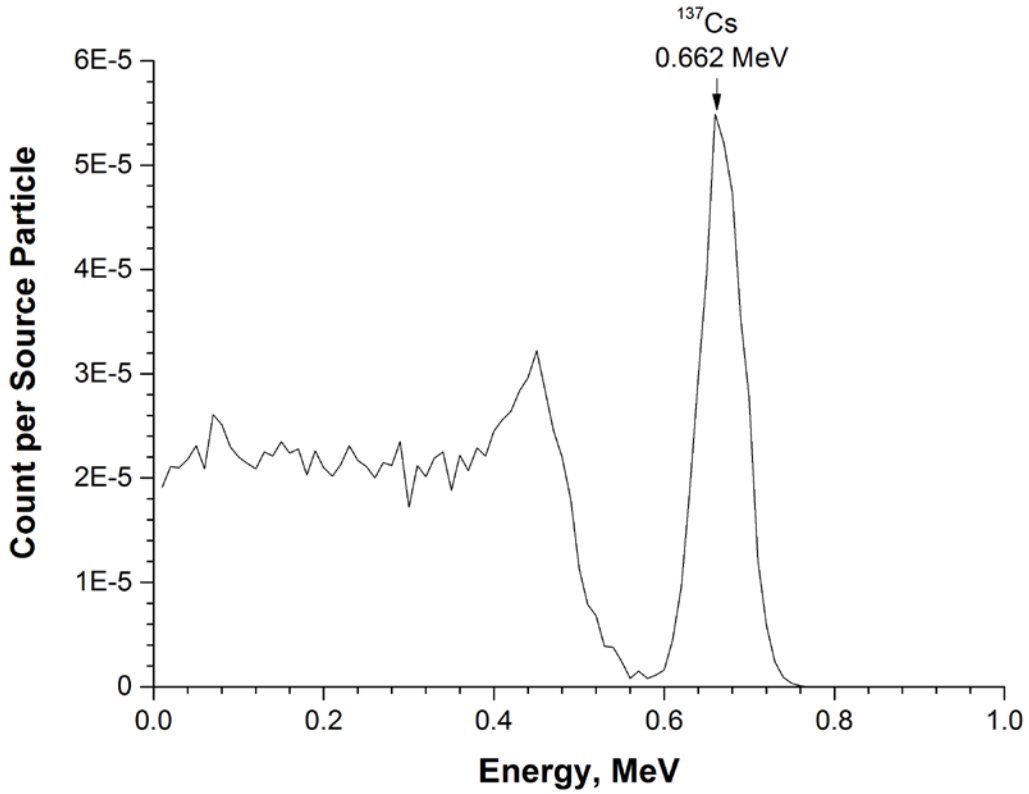

Figure 67: Simulated response function of Cs_2LiYCl_6:Ce scintillator to ^{137}Cs

In Fig. 67, the response function shows the full energy deposition of secondary electrons with the photoelectric peak at 0.662 MeV and Compton edge at 0.478 MeV with the Compton continuum from 0 MeV to 0.478 MeV.

This crystal can also cover the energy range required for gamma spectrometry. It was determined that the 2.6 MeV gamma-ray emitted from ^{232}Th, and essentially 2.6 MeV secondary electron, will need 3.1 mm to deposit its full energy. To cover the entire range up to 3 MeV, 3.7 mm is required. Since this crystal's dimensions are 2.54x2.54cm, it is sufficiently large enough to detect gamma-rays of this range. This is clearly shown in the response function below.

An energy resolution of 4.2% for the corresponding gamma source was applied to the detector response function input file and the result with a ^{60}Co source is shown in Fig 68.

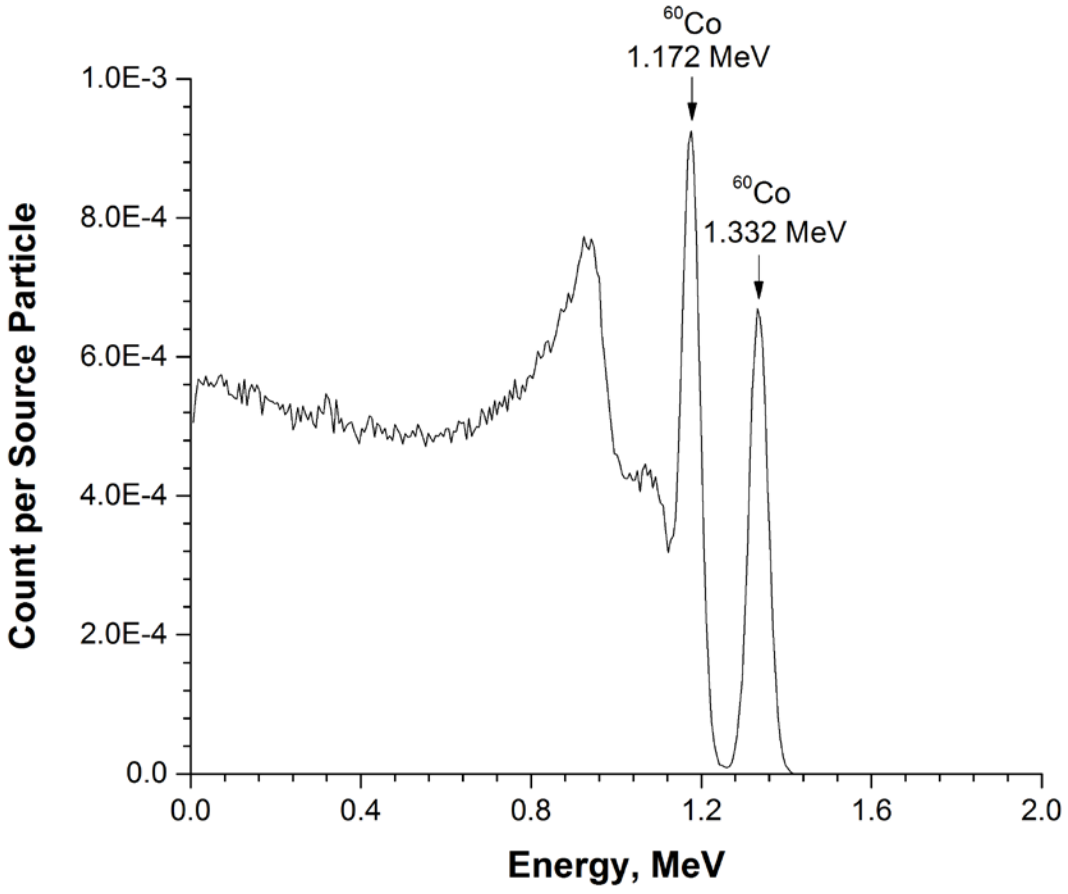

Figure 68: Simulated response function of Cs_2LiYCl_6:Ce scintillator to ^{60}Co

In Fig. 68, the response function shows the full energy deposition of secondary electrons with the two photoelectric peaks at 1.172 MeV and 1.332 MeV. The respective Compton edges are at 0.96 MeV and 1.12 MeV. The same procedure has been followed for the rest of the experiments and an energy resolution of 4.1% was applied to the detector response function to generate the result shown in Fig 69.

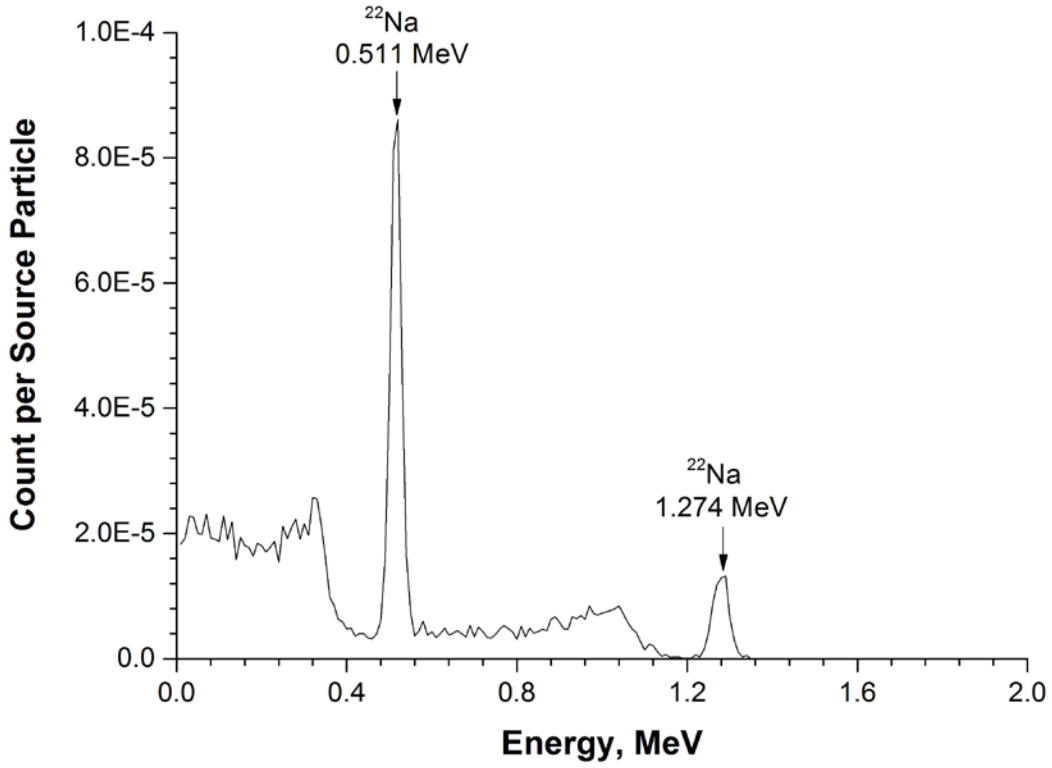

Figure 69: Simulated response function of Cs_2LiYCl_6:Ce scintillator to ^{22}Na

In Fig. 69, the response function shows the full energy deposition of secondary electrons from the annihilation peak at 0.511 MeV and photoelectric peak at 1.274 MeV. The respective Compton edges are at 0.34 MeV and 1.06 MeV. Further, to investigate a full range of gamma radiation, the crystal has been irradiated with a low energy gamma ray of ^{57}Co, which has an energy of 0.122 MeV, and an energy resolution of 15.1% was applied to the detector response function. The response of the detector is presented in Fig. 70.

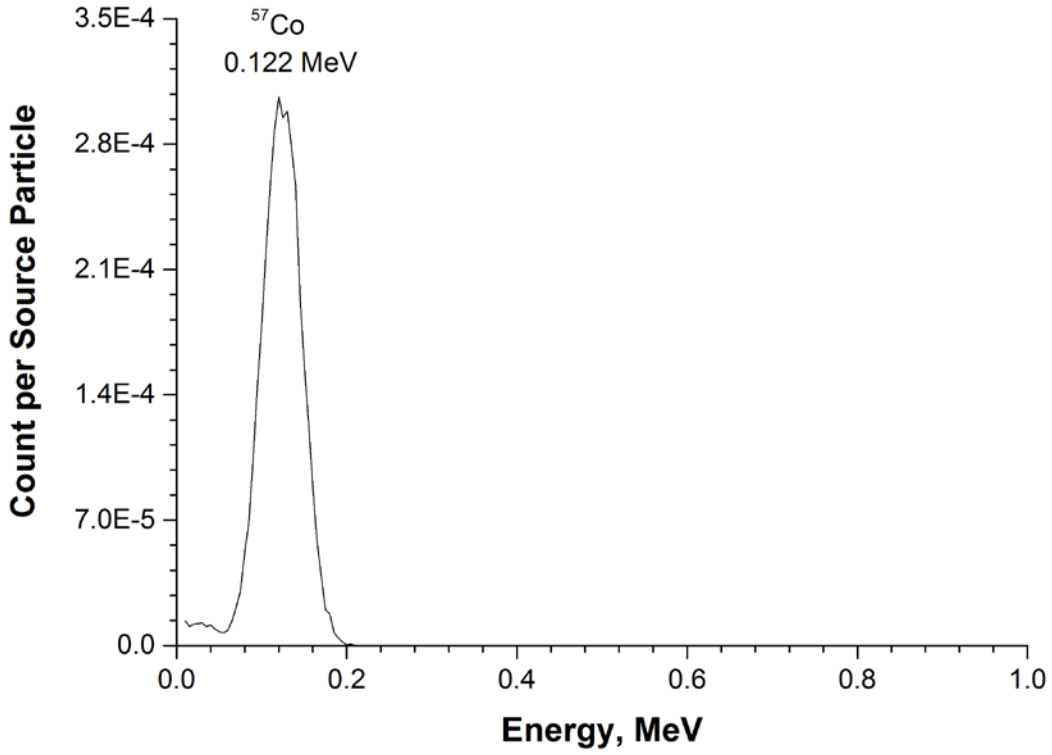

Figure 70: Simulated response function of Cs_2LiYCl_6:Ce scintillator to ^{57}Co

In Fig. 70, the response function shows the full energy deposition of secondary electrons with a photoelectric peak at 0.122 MeV. The Compton continuum exists from 0 MeV to 0.04 MeV which is observed in the very low end of the spectrum. However, there were more full energy deposition events than scattered events for this energy in this crystal.

Furthermore, this new crystal has been investigated in a neutron field. The detector was irradiated with the same moderated AmBe neutron source as previously mentioned. In the simulation model, an energy resolution of 3.3% has been applied to the response function and the results of the performed simulation of the Cs_2LiYCl_6:Ce scintillator to neutron radiation is presented in Fig. 71.

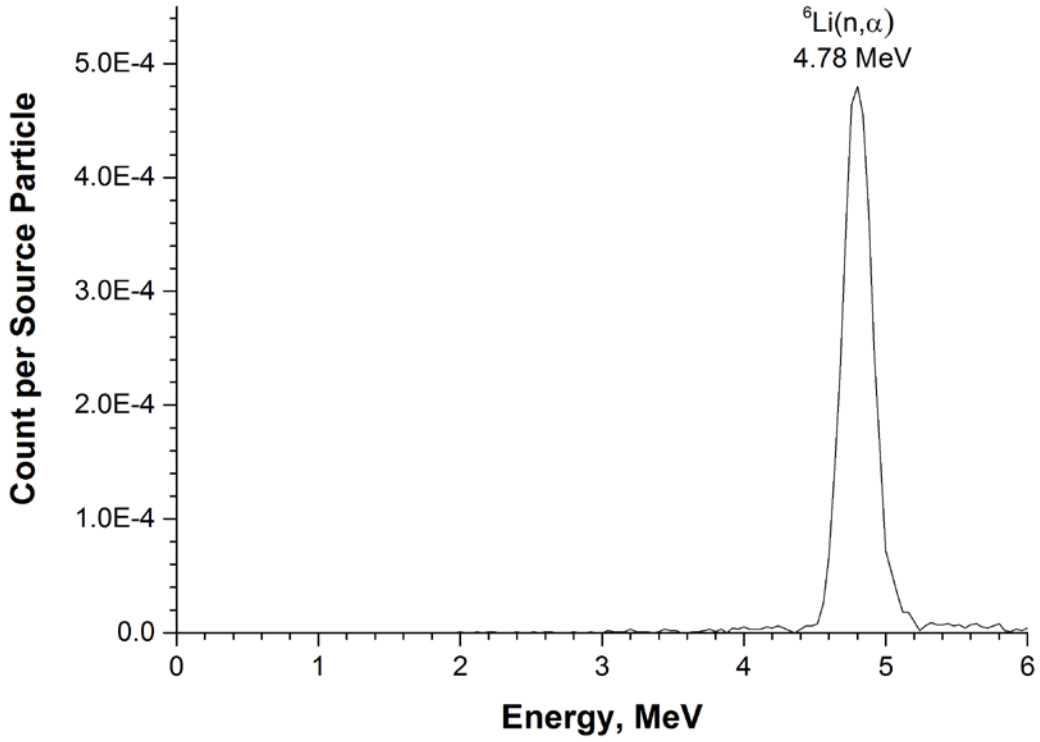

Figure 71: Simulated response function of Cs_2LiYCl_6:Ce to AmBe neutron source

In Fig. 71, similar observations can be made to this response function to the LiI:Eu scintillator. This is mainly due to the fact that the same reaction for neutron capture at thermal energies and the same point source to irradiate the detector are used. Both scintillators show good potential as thermal neutron detectors. However, as it will be shown later in the experimental section, this new crystal has the ability to detect fast neutrons.

4.1.1.2 Boron-loaded Plastic Scintillator

To complete the series of potential candidates to measure thermal neutrons, another scintillator has been investigated. The sensor contains one of the boron isotopes, ^{10}B that efficiently undergoes (n,α) reaction with thermal neutrons. A slight modification to incorporate the dimension and isotope contains of the sensor has been made in the simulation model. The simulated response function of the boron-loaded plastic scintillator to gamma radiation is presented in Figs. 72 and 73. This detector was irradiated with two gamma-ray sources, ^{137}Cs

and ^{60}Co, covering an energy range of 0.662 MeV to 1.332 MeV. The detector response functions are presented with ideal resolution.

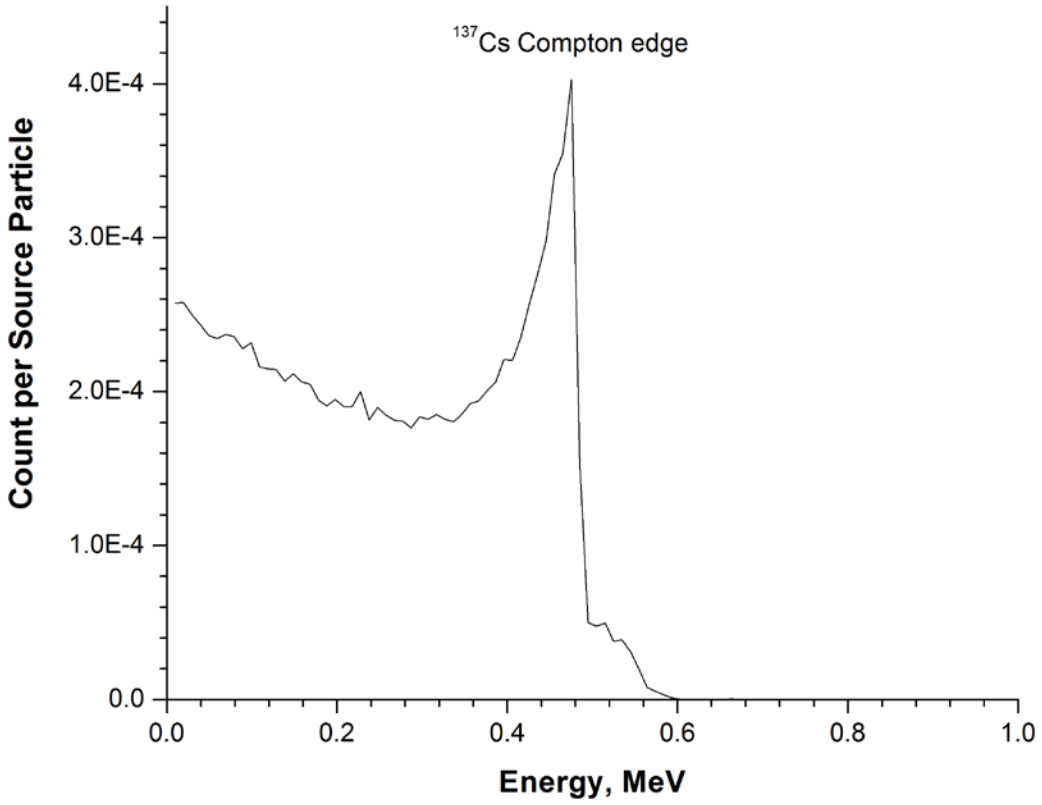

Figure 72: Simulated response function of boron-loaded plastic scintillator to ^{137}Cs

In Fig. 72, it can be seen there is no photoelectric peak, but a Compton continuum from 0 MeV to 0.48 MeV. This sensor is comprised of mainly low Z elements (plastic), and accordingly would result in more scattering events than full energy deposition events. Therefore, the sensor cannot be used for gamma spectrometry due to reasons discussed in the following section.

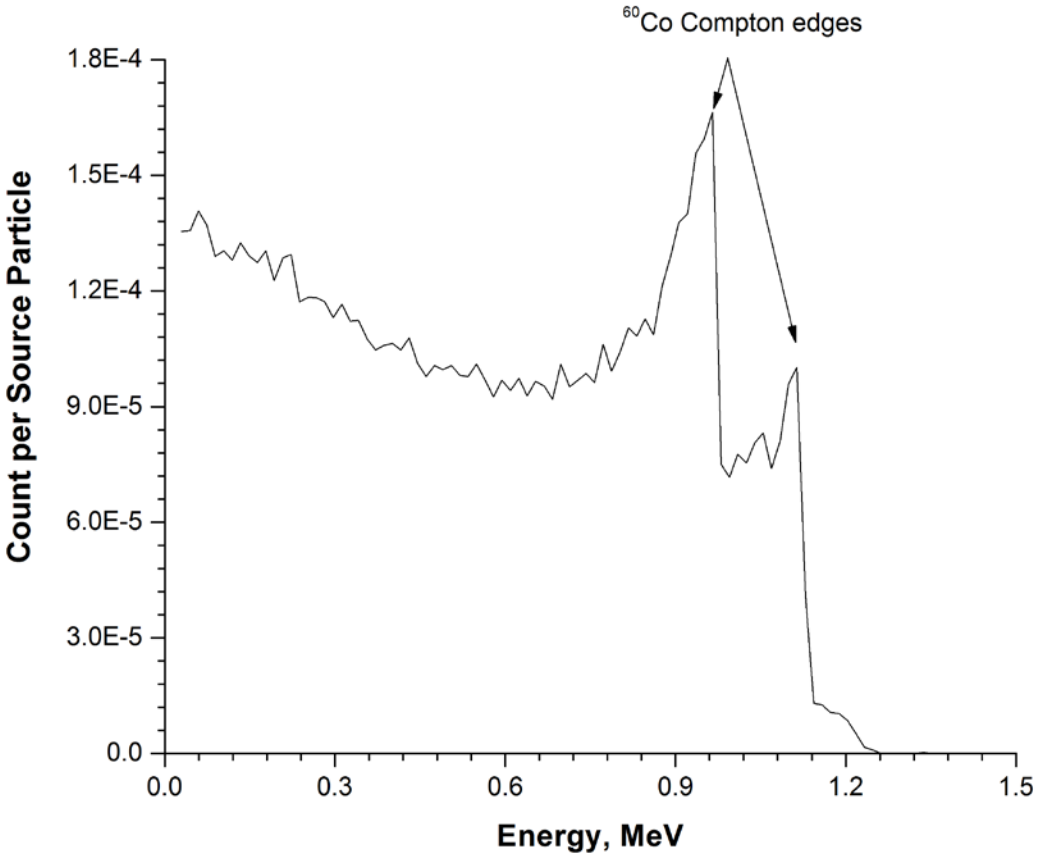

Figure 73: Simulated response function of boron-loaded plastic scintillator to ^{60}Co

In Fig. 73, similar to the previous response, it can be seen there is no photoelectric peak, but two Compton edges at 0.96 MeV and 1.12 MeV, and therefore the Compton continuum starts at 0 MeV and ends at 1.12 MeV.

Due to its sensitivity to neutrons, the boron-loaded plastic scintillator has been irradiated with the same moderated AmBe neutron source, as previously mentioned, and the simulated response function to neutron radiation is presented in Fig. 74. The detector response function has been generated after applying an energy resolution of 3.4% and the result is presented in in Fig.74.

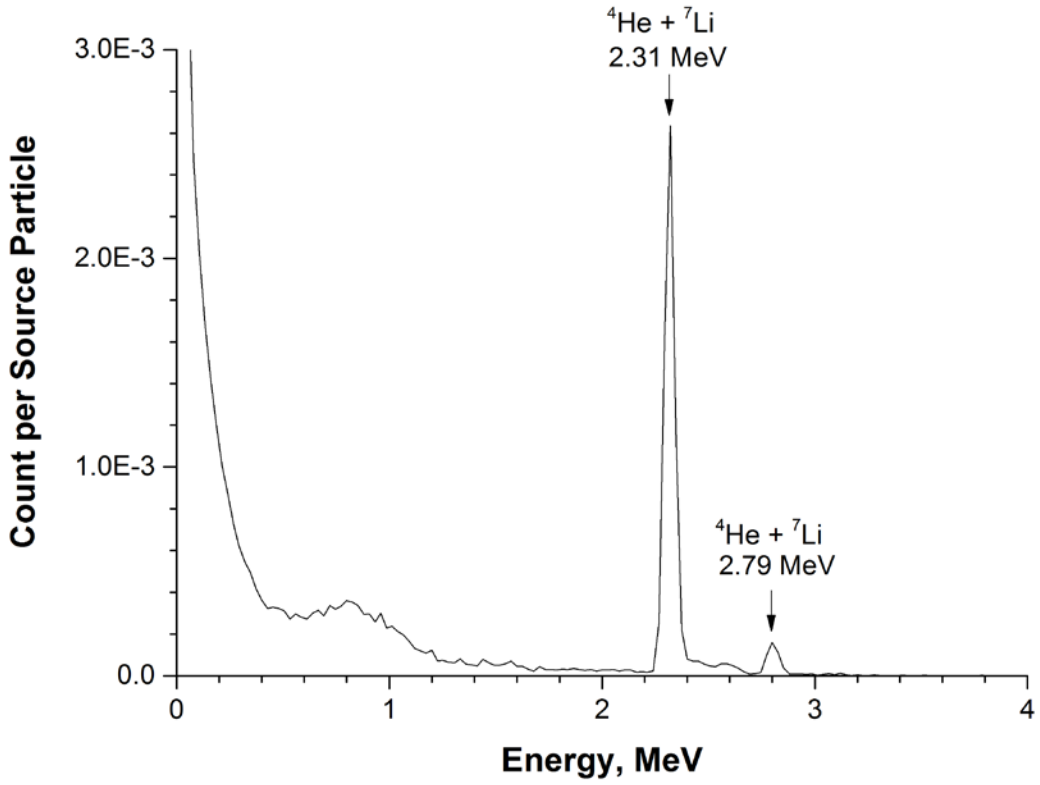

Figure 74: Simulated response function of boron-loaded plastic scintillator to moderated AmBe neutron source

In Fig. 74, the x-axis represents the energy deposited by alpha particles, ^{7}Li ions, electrons, recoil hydrogen, and recoil carbon in the detector that produced scintillation light. There are several observations that can be made in this response function. Firstly, there are two prominent peaks at 2.31 MeV and 2.79 MeV. These features are due to the neutron capture reaction ^{10}B(n,α) at thermal energy. This reaction has a neutron absorption cross section of 3840 barns as seen in Fig. 75.

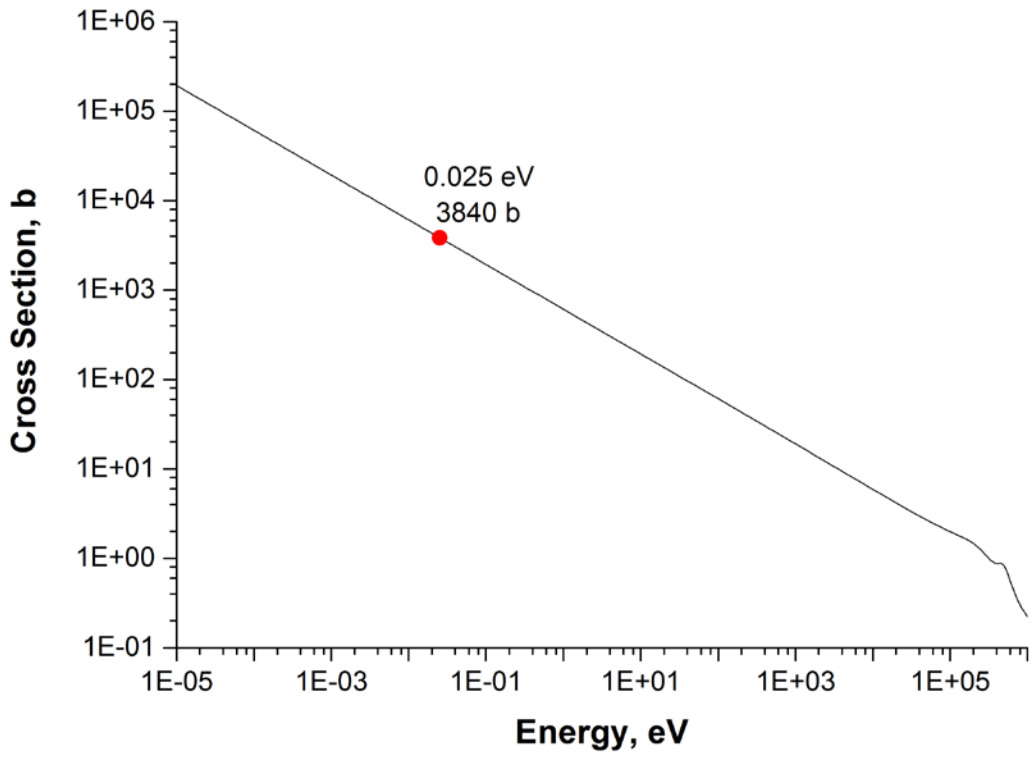

Figure 75: ENDF/B-VII.1 neutron absorption cross section for $^{10}B(n,\alpha)$ [106]

The height of the two thermal peaks is due to the difference in occurrence probability of the corresponding reactions. The reaction with 2.31 MeV occurs 94% of the time, and the reaction with 2.79 MeV occurs only 6% of the time. The difference between the two reactions lies in the ^{7}Li recoil being in an excited or stable state. When in excited state, it will de-excite and emit a 0.48 MeV gamma-ray which is registered in the spectrum in the lower energy region from 0 MeV to the Compton edge, corresponding to a value of 0.31 MeV. However, another continuum of energies is observed on the spectra at energies greater than 0.48 MeV. This feature is due to other recoil nuclei from the scattering processes, mainly hydrogen and carbon that present in the scintillator. Since all heavy ions were tracked in this simulation, all events were tallied in the response function and consequently, recoiled hydrogen has an extended continuum that goes from 0 MeV to 1 MeV, and recoiled carbon goes from 0 MeV to 0.28 MeV, depending on the scattered angle. This scintillator, therefore, has good potential to be used as a thermal detector, due to the high frequency of capture events at thermal energies as denoted by the main peak at

2.31 MeV. However, this scintillator cannot serve in mixed neutron gamma fields, unless careful signal processing is incorporated to analyze the pulses using time shape discrimination instead of pulse shape analysis.

This scintillator is rich in hydrogen; attempts were made to test it with fast neutrons taking benefit from the scattering process on hydrogen nuclei i.e. at higher energies, there is a high probability of neutrons scattering with hydrogen and therefore this reaction was explored by simulating the response functions at various fast energies. The scattering cross section with ^{1}H is given in Appendix A. Two energies were tested with this detector, 1 MeV and 5 MeV. Their response functions are given in the Appendix B. The response showed that for both energies, the continuum due to the elastic scattering is observed and goes from 0 MeV to either 1 MeV or 5 MeV. This is useful for fast neutron spectrometry if the spectrum has adequate resolution. However, using this type of reaction from the response function requires the utilization of complex unfolding techniques to derive the energy spectrum and therefore this crystal was not investigated further.

4.1.2 Fast Neutron Detection

Fast neutron detection has been a challenge for many decades, in particular, the development of neutron spectrometry/dosimetry devices. It is recognized to be a difficult area and it is also fair to say that currently, there is no single device that is capable of offering a solution for neutron spectrometry due to physical limitations of the current neutron sensor technology. Despite over decades of concentrated and well-funded research by civilian and military groups, recent evaluations of existing devices and prototype devices by reputable laboratories have pointed to many deficiencies in the properties of a neutron dosimeter/spectrometer.

However, some recently developed scintillators are giving some hope to overcome some of the challenges facing fast neutron detection, mainly the sensitivity of neutron sensors, their energy resolution, and their ability to discriminate gamma radiation. Among those sensors, a Cs_2LiYCl_6:Ce scintillator has been investigated in different radiation fields. The simulated response functions of the ^{7}Li-enriched Cs_2LiYCl_6:Ce scintillator to gamma radiation is presented in Figs. 76-78. This detector was irradiated with various gamma-ray sources, ^{137}Cs, ^{60}Co,

and ^{22}Na covering an energy range of 0.511 MeV to 1.332 MeV. An energy resolution of 11.1%, 5.7%, and 8.2% was applied to the detector response functions, respectively.

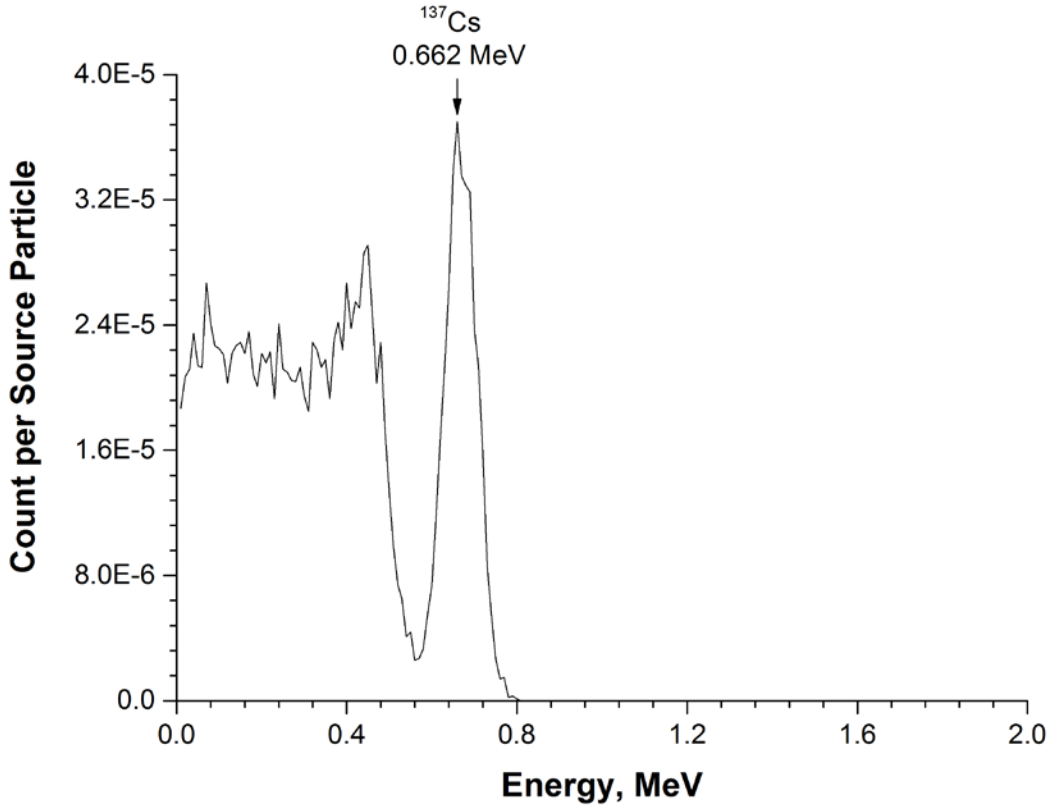

Figure 76: Simulated response function of Cs_2LiYCl_6:Ce scintillator to ^{137}Cs

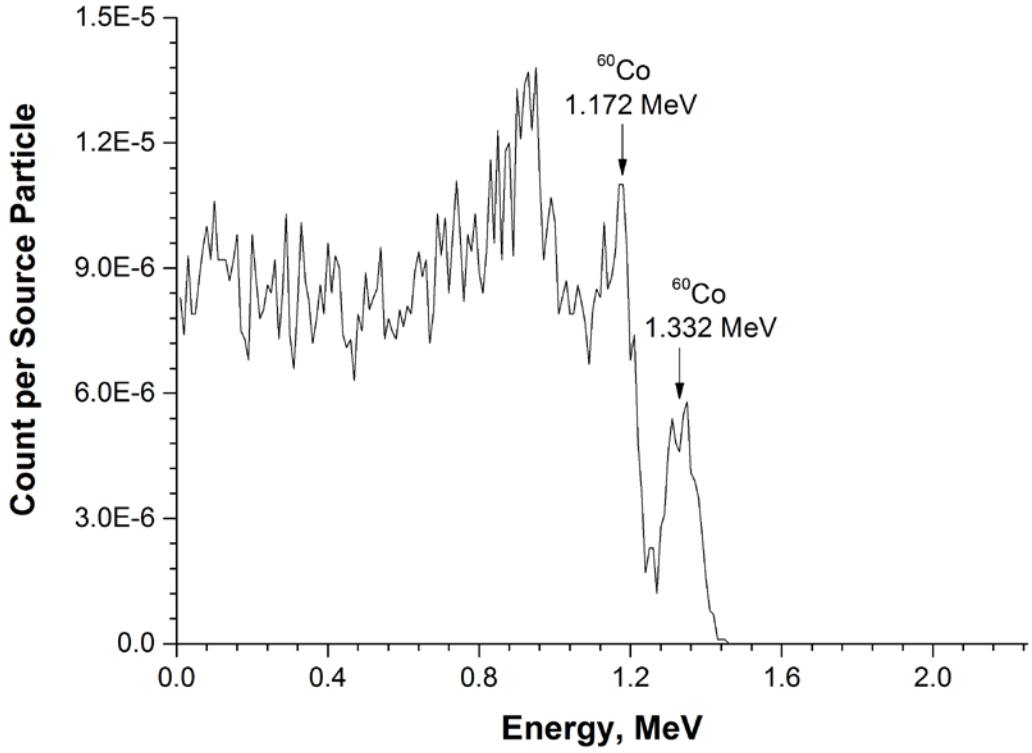

Figure 77: Simulated response function of Cs_2LiYCl_6:Ce scintillator to ^{60}Co

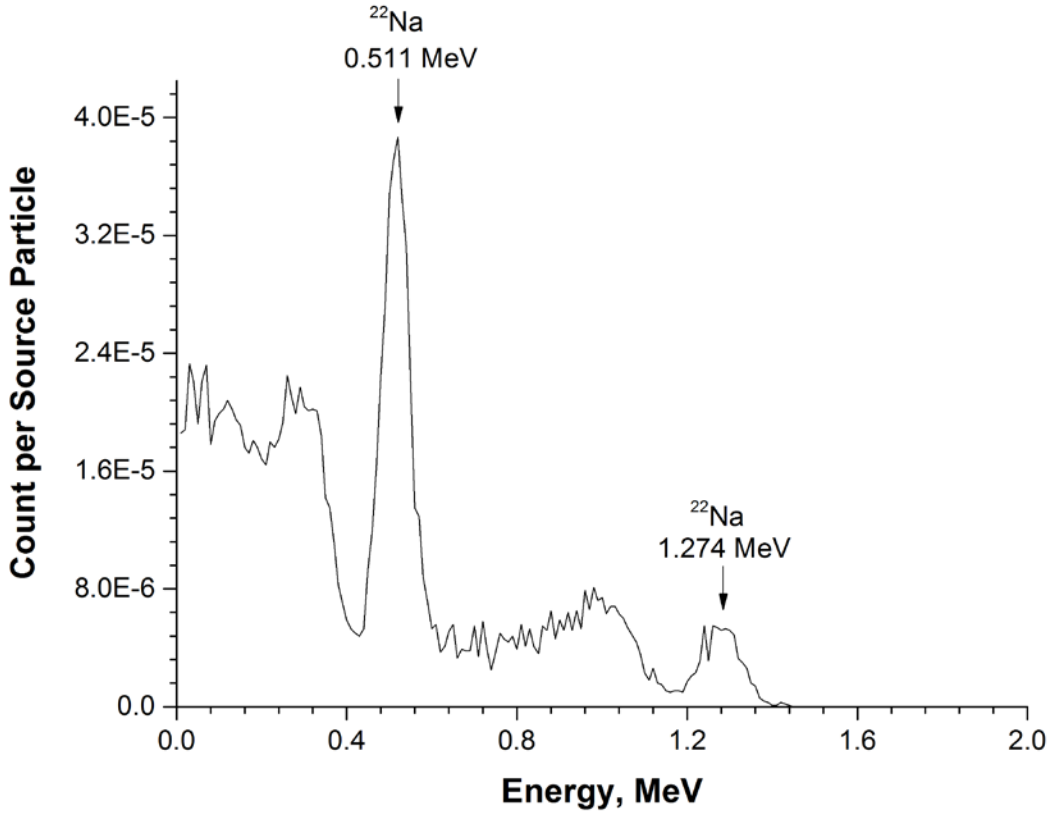

Figure 78: Simulated response function of Cs_2LiYCl_6:Ce scintillator to ^{22}Na

The detector response functions are identical to the first version of the Cs_2LiYCl_6:Ce scintillator since gamma detection does not depend on the isotope, but rather the elements of the crystal. Additionally, the density and dimensions of the crystal were the same. The only difference is the resolution applied to the detector.

For fast neutron detection, this crystal has a useful reaction where the incident energy information of the neutron can be determined by obtaining the detector response function. This aforementioned reaction:

$$^{1}_{0}n + ^{35}_{17}Cl \rightarrow ^{35}_{16}S + ^{1}_{1}p + 0.615\ MeV \quad (64)$$

Where a neutron is absorbed by the ^{35}Cl isotope and a sulphur ion and proton are emitted. Since this is an absorption reaction, a distinct peak on the pulse height spectra resulted from the energy deposition of the proton in the scintillation media is observed. This reaction becomes intriguing after around a few hundred keV, where the cross section increases substantially. The cross

section for this reaction is given in Fig. 79. The energies used in the simulations are 0.6 MeV, 2.67 MeV, 3.57 MeV, and 4 MeV. Particular interest is given to energies greater than a few hundred keV.

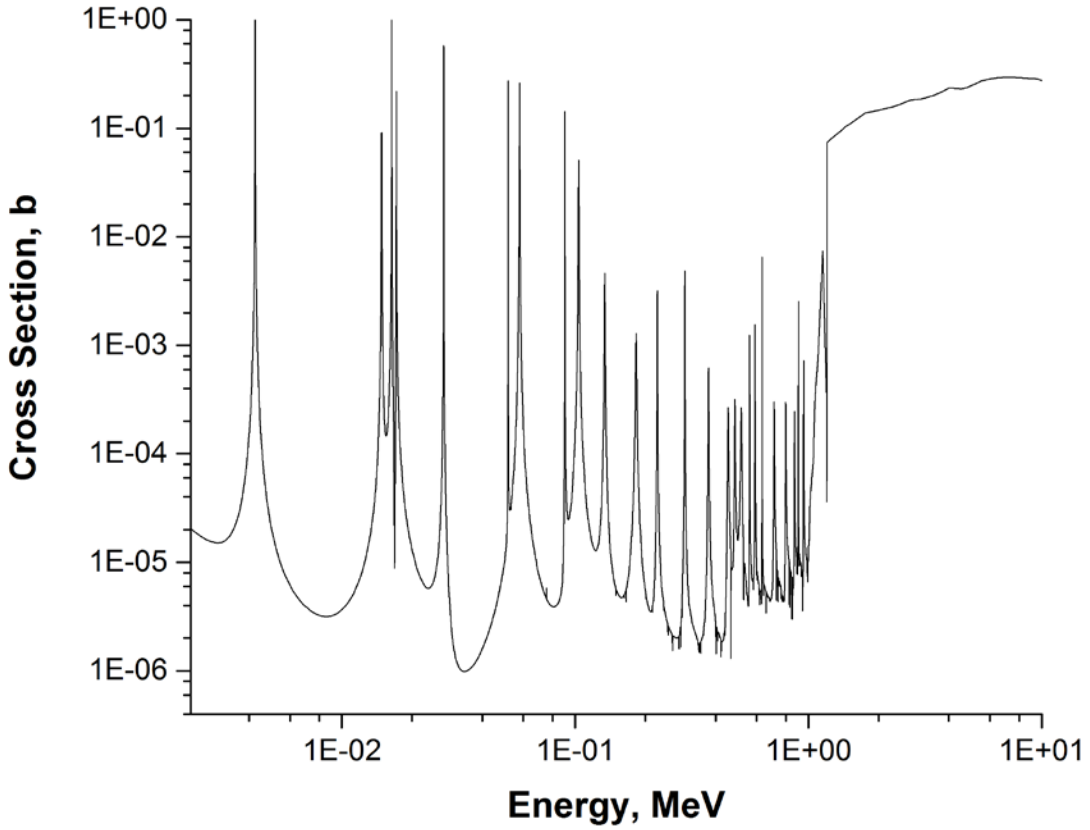

Figure 79: ENDF/B-VII.0 neutron absorption cross section of ^{35}Cl(n,p) [107]

The detector response function to 0.6 MeV neutrons is presented with ideal resolution; however an energy resolution of 10% was applied to the remaining response functions. The response of the detector is presented reflecting the deposited energy in the scintillator media when traversed by charged particles.

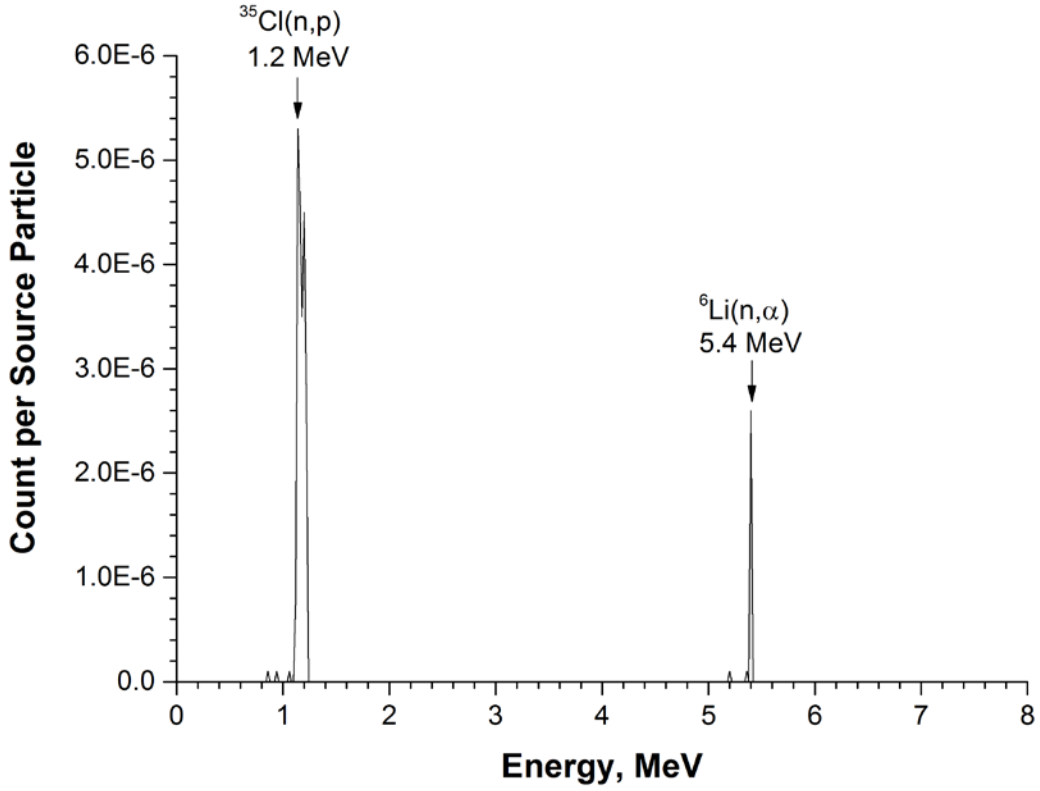

Figure 80: Simulated response function of Cs_2LiYCl_6:Ce scintillator to 0.6 MeV neutrons

In Fig. 80, there are two significant full energy peaks observed. The first is at 1.2 MeV and the second is at 5.4 MeV. There are a few absorption reactions in this crystal that produce charged particles. Two reactions have been previously mentioned, ^{6}Li(n,α) and ^{35}Cl(n,p). Other reactions include:

$$^{1}_{0}n + ^{6}_{3}Li \rightarrow ^{3}_{1}H + ^{4}_{2}He + 4.78\ MeV \quad (65)$$

$$^{1}_{0}n + ^{6}_{3}Li \rightarrow ^{6}_{2}He + ^{1}_{1}p - 2.73\ MeV \quad (66)$$

$$^{1}_{0}n + ^{35}_{17}Cl \rightarrow ^{34}_{16}S + ^{2}_{1}H - 4.14\ MeV \quad (67)$$

$$^{1}_{0}n + ^{35}_{17}Cl \rightarrow ^{33}_{16}S + ^{3}_{1}H - 9.30\ MeV \quad (68)$$

$$^{1}_{0}n + ^{35}_{17}Cl \rightarrow ^{32}_{15}P + ^{4}_{2}He + 0.938\ MeV \quad (69)$$

$$^{1}_{0}n + ^{37}_{17}Cl \rightarrow ^{37}_{16}S + ^{1}_{1}p - 4.08\ MeV \quad (70)$$

$$^{1}_{0}n + ^{37}_{17}Cl \rightarrow ^{36}_{16}S + ^{2}_{1}H - 6.16\ MeV \quad (71)$$

$$^{1}_{0}n + ^{37}_{17}Cl \rightarrow ^{35}_{16}S + ^{3}_{1}H - 9.79\ MeV \quad (72)$$

$$^{1}_{0}n + ^{37}_{17}Cl \rightarrow ^{34}_{15}P + ^{4}_{2}He - 1.55\ MeV \quad (73)$$

$$^{1}_{0}n + ^{89}_{39}Y \rightarrow ^{89}_{38}Sr + ^{1}_{1}p - 0.713\ MeV \quad (74)$$

$$^{1}_{0}n + ^{89}_{39}Y \rightarrow ^{86}_{37}Rb + ^{4}_{2}He + 0.691\ MeV \quad (75)$$

$$^{1}_{0}n + ^{133}_{55}Cs \rightarrow ^{133}_{54}Xe + ^{1}_{1}p \quad (76)$$

$$^{1}_{0}n + ^{133}_{55}Cs \rightarrow ^{130}_{53}I + ^{4}_{2}He \quad (77)$$

$$^{1}_{0}n + ^{136}_{58}Ce \rightarrow ^{136}_{57}La + ^{1}_{1}p \quad (78)$$

$$^{1}_{0}n + ^{136}_{58}Ce \rightarrow ^{133}_{56}Ba + ^{4}_{2}He \quad (79)$$

$$^{1}_{0}n + ^{138}_{58}Ce \rightarrow ^{138}_{57}La + ^{1}_{1}p \quad (80)$$

$$^{1}_{0}n + ^{138}_{58}Ce \rightarrow ^{135}_{56}Ba + ^{4}_{2}He \quad (81)$$

Therefore, the x-axis represents the energy deposition of any of the charged particles produced in any of the above mentioned reactions. These charged particles can be either protons, deuterons, tritons, or alpha particles with their recoils tracked either separately or together. From the Q-values of the reactions, most of the reactions can be eliminated since there is not enough incident energy for the reaction to occur. At 0.6 MeV, there is only one possible reaction that could be at 1.2 MeV and another at 5.4 MeV. The Q-value of the ^{35}Cl(n,p) reaction is 0.615 MeV; the sum of the incident neutron energy and Q-value is 1.2 MeV. The Q-value of the ^{6}Li(n,α) reaction is 4.8 MeV; the sum of the incident neutron energy and Q-value is 5.4 MeV.

The height of the peaks is related to the overall probability at which each reaction occurs in the crystal. More specifically and to quantitatively compare the efficiency of each reaction for fast neutron detection, the effective cross sections have been calculated. This incorporates the neutron cross section, isotopic abundance, and atom fraction for each reaction. The ^{35}Cl isotope is more abundant than the other chlorine isotope, ^{37}Cl, constituting 75%. Chlorine also has the highest atom fraction in the crystal of 6/10. At 0.6 MeV, the respective effective cross sections are 11.9 mb for ^{35}Cl(n,p) and 0.32 mb for ^{6}Li(n,α). By comparing the two values, it is clear to see that the ^{35}Cl(n,p) reaction has more validity to be used for neutron energies in this range.

For the remaining neutron energies, due to the possibility of several reactions occurring at different thresholds, the detector response function was simulated differently. Thus, each charged particle was tracked separately to distinguish between the peaks and their corresponding charged

particles, and then plotted together on one graph. Firstly, any reaction that produced deuteron or triton was automatically eliminated due to the lack of sufficient incident energy for the reaction to take place. For instance, ^{35}Cl(n,d), ^{35}Cl(n,t), ^{37}Cl(n,d), and ^{37}Cl(n,t) have Q-values of -4.14 MeV, -9.30 MeV, -6.16 MeV, and -9.79 MeV, and were eliminated. This leaves only protons and alpha particles to be tracked. However, the triton that was produced in the reaction ^{6}Li(n,α), was also tracked in order to get the full energy peak from both particles (alpha and triton). By tracking them together, it would not create any difficulty in identifying which peaks were due to alpha and which were due to triton, simply because as previously mentioned, triton is not produced elsewhere. The results of such analysis are presented in Fig. 81, where the blue curve corresponds to the response when tracking protons and the red curve corresponds to the response when tracking alpha particles and triton.

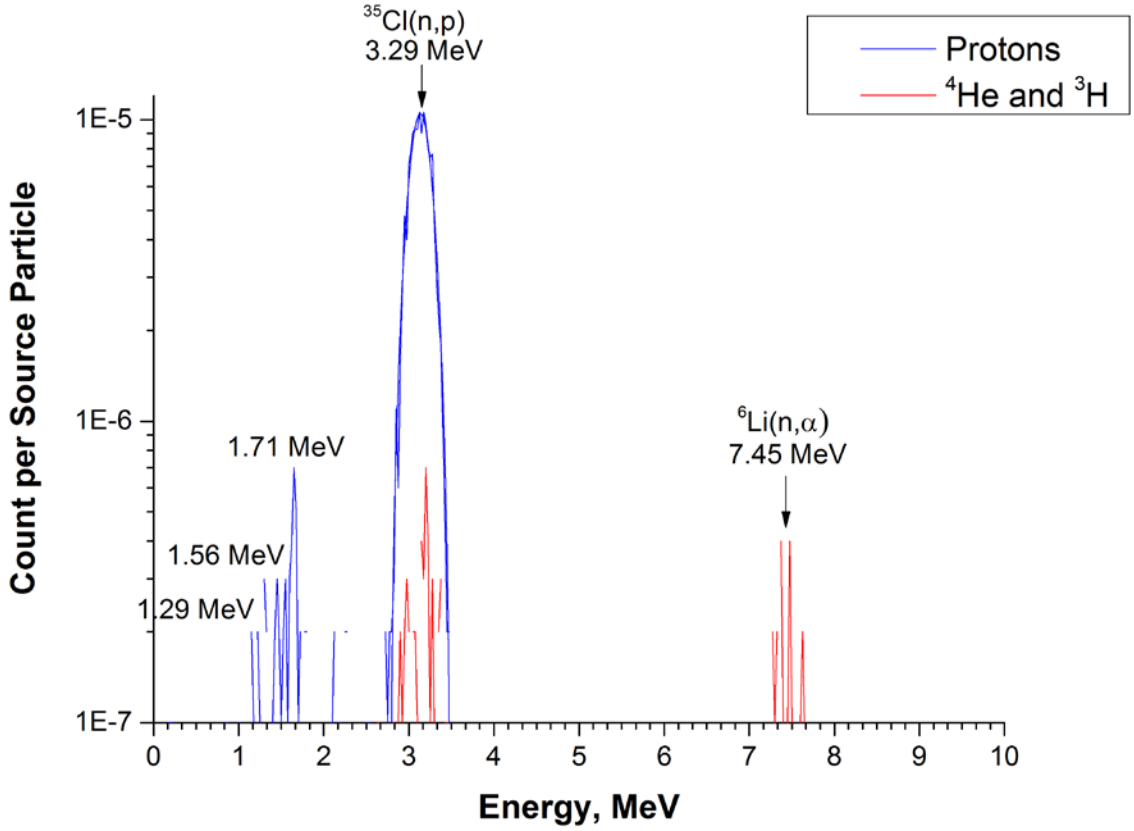

Figure 81: Simulated response function of Cs_2LiYCl_6:Ce scintillator to 2.67 MeV neutrons

At 2.67 MeV neutron energy, the peak at 3.29 MeV can only be due to the ^{35}Cl(n,p) reaction, and the peak at 7.45 MeV can only be due to the ^{6}Li(n,α) reaction. The effective cross sections are

80.2 mb for ^{35}Cl(n,p) and 0.18 mb for ^{6}Li(n,α). This illustrates the significant contribution of the reaction with ^{35}Cl where the number of events being registered in the detector is much greater than the number of events resulted from the reaction with ^{6}Li.

There are some noticeable proton peaks between 1.1 to 1.8 MeV and 2.1, and alpha peaks between 2.9 to 3.4 MeV. By looking at the corresponding neutron cross section values for the different reactions that can occur, one can determine the corresponding reaction that leads to such peaks. A list of these values is given in Table 4. The full cross section plots for all of the reactions in CLYC are given in Appendix A.

Table 4: ENDF/B-VII.0 Neutron cross section of reactions in Cs_2LiYCl_6:Ce scintillator [107]

Cross section (b)	E_n = 0.6 MeV	E_n = 2.67 MeV	E_n = 3.57 MeV	E_n = 4 MeV
^{6}Li(n,p)	-	-	0.017	0.034
^{6}Li(n,α)	0.316	0.181	0.127	0.109
^{35}Cl(n,p)	0.026	0.178	0.207	0.234
^{35}Cl(n,α)	7.538E-8	0.006	0.038	0.063
^{37}Cl(n,α)	-	3.885E-6	7.857E-6	4.812E-5
^{89}Y(n,p)	-	2.107E-5	3.611E-4	8.007E-4
^{89}Y(n,α)	0	0	4.893E-10	2.314E-9
^{133}Cs(n,p)	0	5.597E-7	7.919E-6	1.659E-5
^{133}Cs(n,α)	-	4.056E-8	6.158E-7	1.441E-6

At 2.67 MeV neutron energy, the remaining reactions that produce protons are ^{89}Y(n,p) and ^{133}Cs(n,p). For ^{89}Y(n,p), the theoretical proton peak should be at 1.96 MeV which is not observed on the pulse height spectra. In the case of ^{133}Cs(n,p), the cross section is too small and therefore, it is neither of these reactions. Additional proton peaks are then observed which do not correspond with any of the reactions.

In the same context, at 2.67 MeV neutron energy, the remaining reactions that produce alphas are ^{35}Cl(n,α), ^{89}Y(n,α), and ^{133}Cs(n,α). In the case of the ^{89}Y(n,α) reaction, the cross section is extremely small, and therefore was not included in the analysis. For ^{35}Cl(n,α), the theoretical

alpha peak should be at 3.6 MeV which is not observed on the spectra. For $^{133}Cs(n,\alpha)$, the cross section is also extremely small and no significant contribution is expected. In conclusion, these alpha peaks do not correspond to any of these reactions.

Thorough analysis of the nuclear structure of the sulphur nucleus, ^{35}S indicates that after the emission of the proton, this isotope can be in different quantum states from the ground state at 0 keV to the first, second, and third at energies of 1572 keV, 1991 keV, and 2347 keV, respectively. If one considers this fact, then the 3 peaks observed at 1.29 MeV, 1.56 MeV and 1.71 MeV are mainly resulted from 3 protons energies corresponding to the first, second and third states of the recoiled ^{35}S. The difference in energy is emitted in a form of different gamma rays not tracked in the simulations.

At 3.57 MeV neutron energy, the peak at 4.19 MeV can only be due to the $^{35}Cl(n,p)$ reaction, and the peak at 8.35 MeV can only be due to the $^{6}Li(n,\alpha)$ reaction. The effective cross sections for both reactions are 93.2 mb for $^{35}Cl(n,p)$ and 0.13 mb for $^{6}Li(n,\alpha)$.

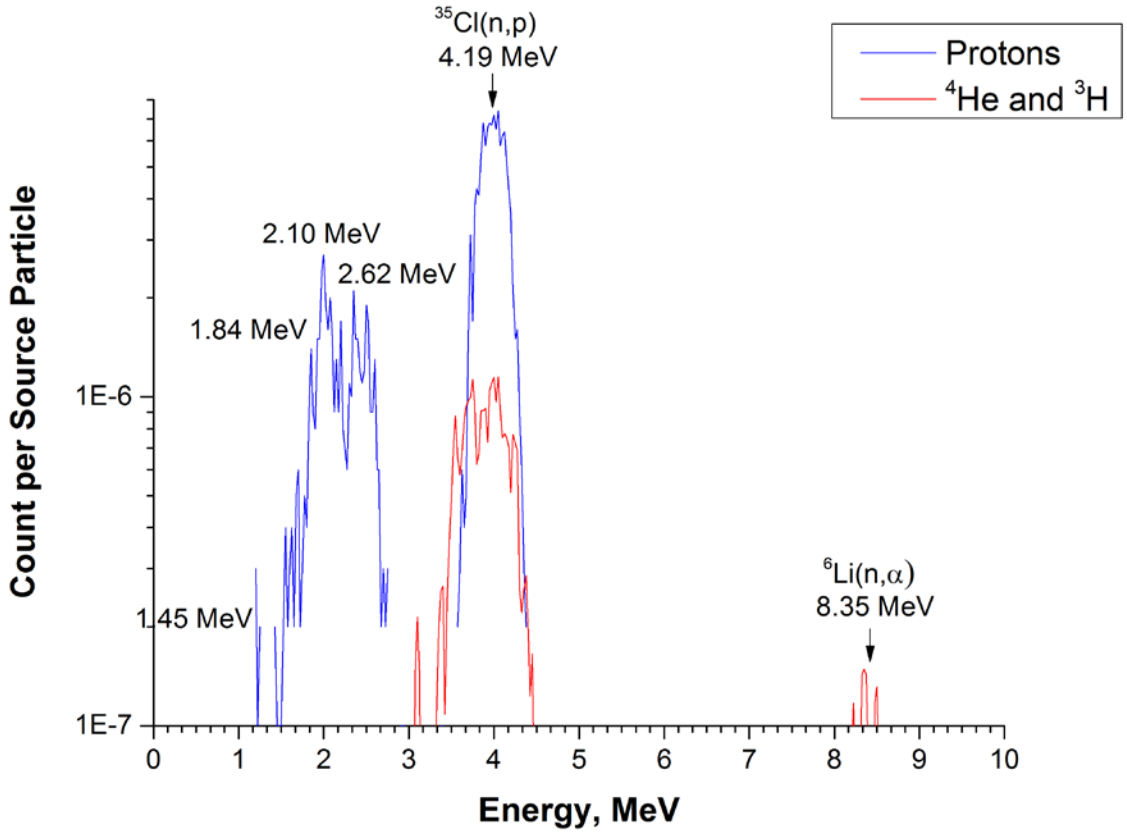

Figure 82: Simulated response function of Cs_2LiYCl_6:Ce scintillator to 3.57 MeV neutrons

There are proton peaks between 1.2 to 2.8 MeV and alpha peaks between 3.1 to 4.4 MeV. At 3.57 MeV, the remaining reactions that produce protons are ^{6}Li(n,p), ^{89}Y(n,p), and ^{133}Cs(n,p). In the case of ^{133}Cs(n,p), the cross section is too small. For ^{6}Li(n,p) and ^{89}Y(n,p), neither proton peak is observed at 0.84 MeV and 2.9 MeV on the spectrum.

The remaining reactions that produce alphas are ^{35}Cl(n,α), ^{37}Cl(n,α), ^{89}Y(n,α), and ^{133}Cs(n,α). For the reactions ^{37}Cl(n,α), ^{89}Y(n,α), and ^{133}Cs(n,α), the cross sections are too small. In the case of ^{35}Cl(n,α), the theoretical alpha peak should be at 4.5 MeV which is not observed on the spectrum.

The fourth energy used to test the scintillator was 4 MeV. The results obtained in a series of simulations are presented in Fig. 83. At this energy, the peak at 4.62 MeV can only be due to the ^{35}Cl(n,p) reaction, and the peak at 8.78 MeV can only be due to the ^{6}Li(n,α) reaction. The effective cross sections are 105.4 mb for ^{35}Cl(n,p) and 0.109 mb for ^{6}Li(n,α).

One should mention that, there some are proton peaks at 0.9 MeV and between 1.3 to 3.2 MeV and alpha peaks between 3.4 to 4.8 MeV. At 4 MeV, the remaining reactions that are a possible candidate to produce protons are ^{6}Li(n,p), ^{89}Y(n,p), and ^{133}Cs(n,p). The ^{89}Y(n,p) and ^{133}Cs(n,p) reactions are eliminated because of their small cross section. In the case of ^{6}Li(n,p), the proton peak is not observed at 1.27 MeV on the spectra. For alpha particles, the remaining reactions, namely, ^{35}Cl(n,α), ^{37}Cl(n,α), ^{89}Y(n,α), and ^{133}Cs(n,α) have insignificant cross sections to be discussed. However in the case of ^{35}Cl(n,α), the theoretical alpha peak is not observed at 4.94 MeV.

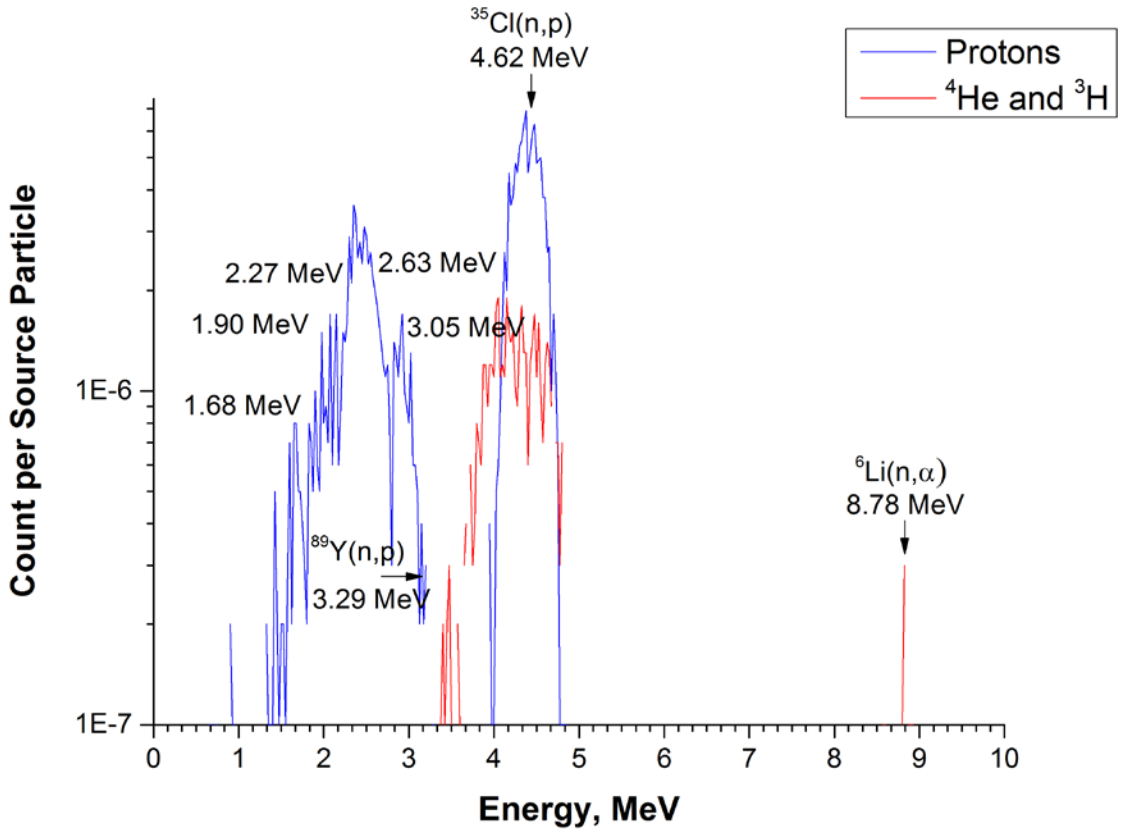

Figure 83: Simulated response function of Cs_2LiYCl_6:Ce scintillator to 4 MeV neutrons

There are some trends that occur across the response functions simulated for all four different energies: as neutron energy increases, the height of the ^{35}Cl(n,p) reaction peak increases i.e. an increase in the population of tracked protons proportional to the cross section of this reaction. This makes this reaction in this crystal highly suitable for fast neutron spectrometry since there is no other known sensor that has such a significance signature of protons in this energy region.

The unidentifiable proton and alpha peaks seem to cover a larger range over the spectrum as neutron energy increases. Their initial values do not seem to shift as energy increases as well.

4.2 Experimental Results

Experiments were carried out at three facilities at the University of Ontario Insititute of Technology and McMaster University. These facilities include an AmBe source, neutron generator, and KN Van De Graaff accelerator. After analysing the simulation data, especially the presence of some unexpected proton and alpha peaks on the pulse height spectra, all experiments were planned before carrying out any measurements at each facility to identify the nature and the significance of the different reactions. Thus, each detector was characterized and its time parameters such as the rising time and decay time of the pulse were determined beforehand. All sensors were tested until their parameters were optimized to function under the appropriate conditions. The data acquisition system was identical for all experiments. Additionally, the same software, Igor Pro, was used throughout. The respective response functions were obtained for gamma and neutron radiation. Gamma sources were used to calibrate the energy scale, and therefore the energy spectra are presented in gamma equivalent energy (MeeV). The data collected for all measurements were imported into OriginPro and further analyzed. For all sub-sections, detector measurements with gamma radiation are presented first, followed by neutron radiation.

4.2.1 Thermal Neutron Detection

Since all detectors were tested for potential use in mixed neutron gamma fields, different experiments have been carried out in different fields (gamma, neutron, or neutron and gamma fields).

4.2.1.1 Li Containing Scintillators – LiI:Eu and Cs_2LiYCl_6:Ce

4.2.1.1.1 LiI:Eu Scintillator

The detector was irradiated with ^{137}Cs and ^{60}Co gamma sources and its measured response functions are given in Fig. 84. The position of the photo-peaks was used to scale the horizontal axis, essentially calibrate the spectra into units of gamma equivalent energy, MeeV. It is well known that the light output of the scintillator is different from one particle to another however, the resulted electrons from gamma interactions were used for calibration.

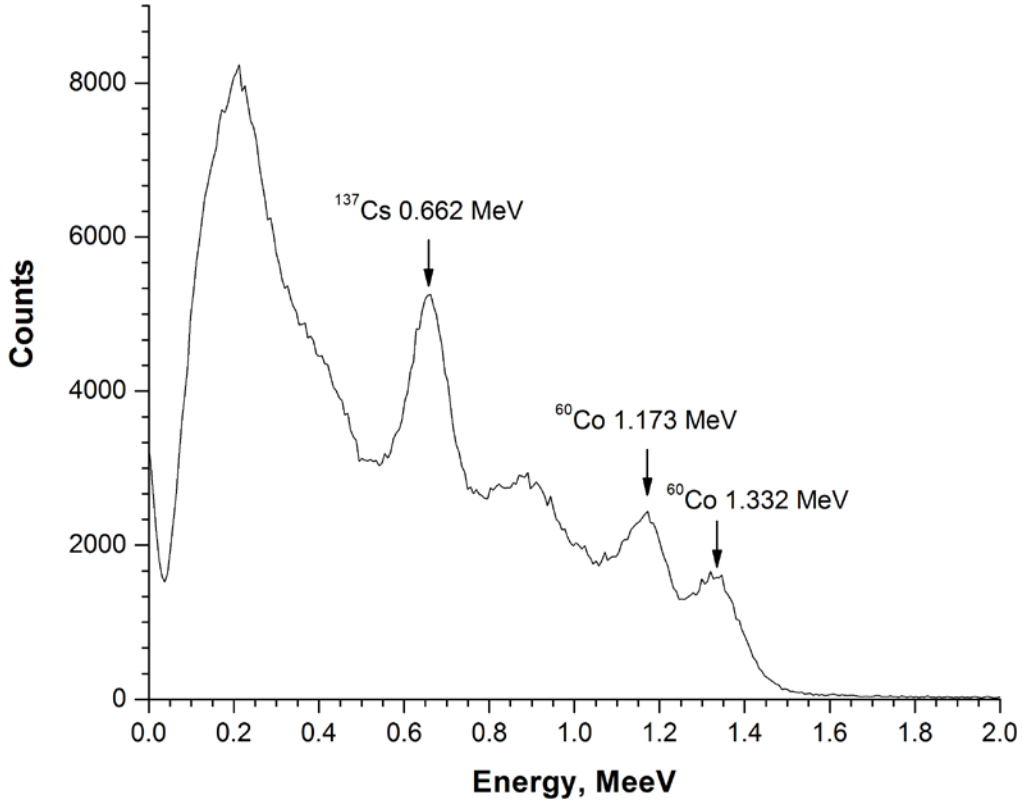

Figure 84: Measured response function of LiI:Eu scintillator to ^{137}Cs and ^{60}Co

In Fig. 84, three full energy deposition peaks corresponding to the three gamma-rays are seen. They are at 0.662 MeV, 1.173 MeV, and 1.332 MeV.

The pulse height spectra were analyzed and the Gaussian function was used to fit the photo-peaks. The calculated full width at half maximum (FWHM) and centroid values of the peaks was obtained from these fits. The energy resolution of these peaks was determined to be between 11% and 6% in the energy range between 0.662 MeV and 1.332 MeV. This means that any nearby peak that falls within the half value of the FWHM will be poorly resolved. The detection system should be linear; this includes the sensor, photomultiplier tube, and associated electronics. To confirm the linearity of the system, these sources were used to acquire the calibration curve for this detector. The channels of the peaks and their corresponding energies were taken. This curve is given in Fig. 84, and it can be seen that the detection system is linear.

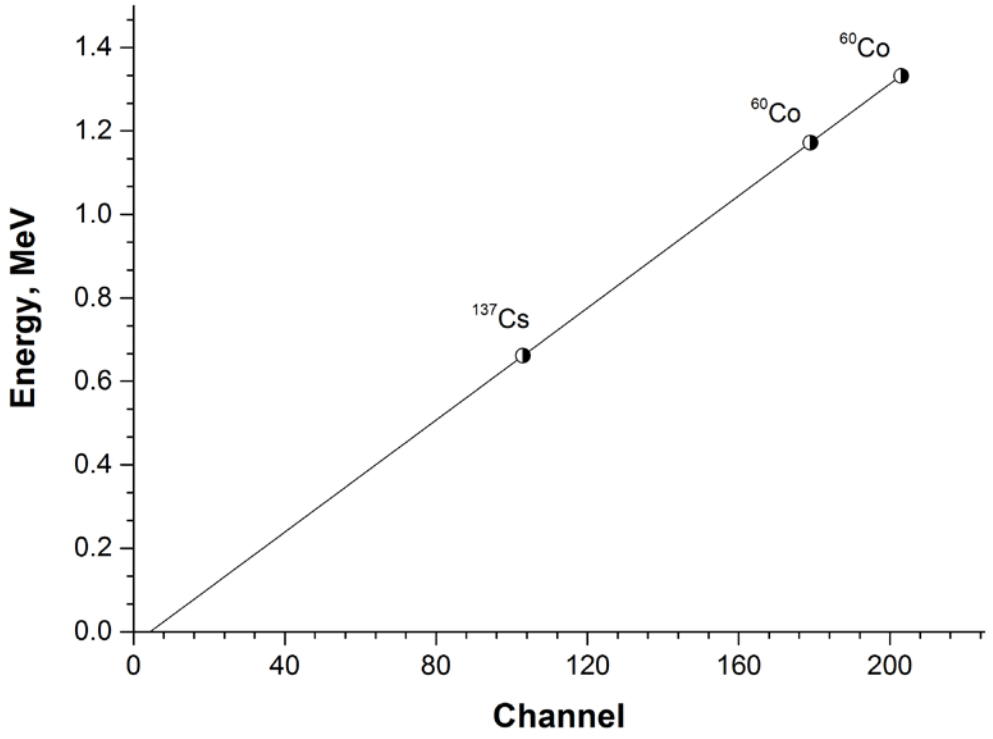

Figure 85: Calibration curve of LiI:Eu scintillator with ^{137}Cs and ^{60}Co sources

For neutrons, the detector was irradiated with a moderated AmBe source and the measured response function is given in Fig. 86. The horizontal axis was calibrated into units of MeeV using the previously mentioned gamma sources.

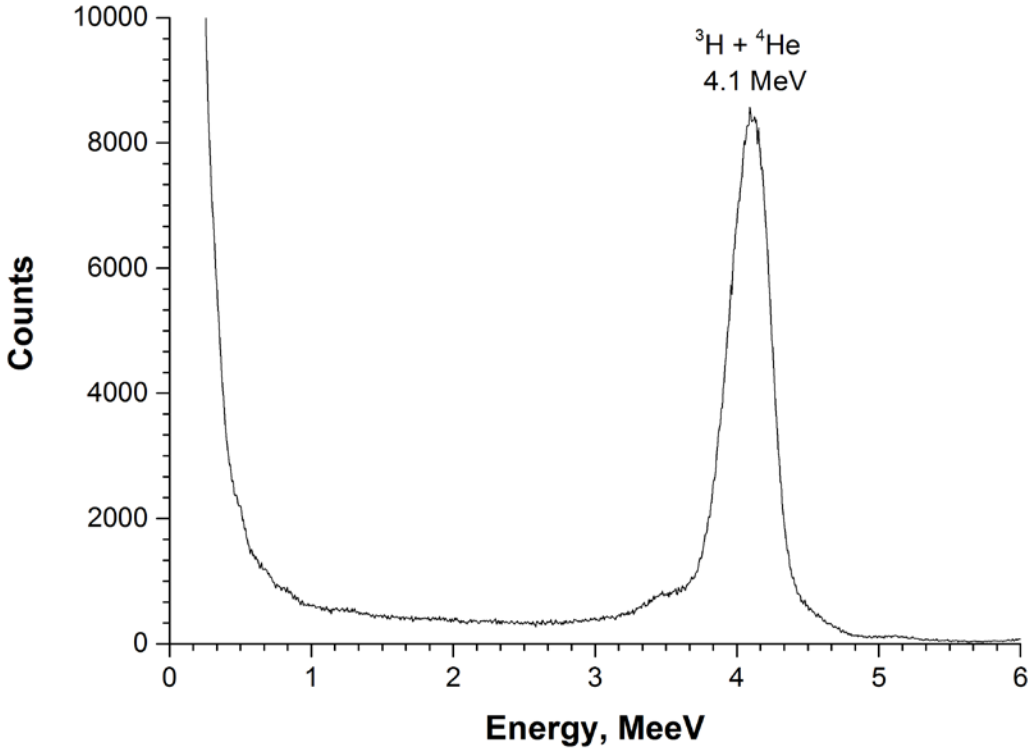

Figure 86: Measured response function of LiI:Eu scintillator to moderated AmBe neutron source

In Fig. 86, a clear peak from the energy deposition of the alpha particle and triton due to neutron capture is seen on the spectrum. This peak has a gamma-equivalent energy of 4.1 MeeV, meaning that it is equal to a gamma-ray of 4.1 MeV. Comparing this value to the theoretical value, 4.78 MeV, there is a difference of 0.68 MeV. This discrepancy is due to the difference in light output of electrons and heavy charged particles, namely alpha particles and triton in this case, compared to electrons resulted from gamma-rays interactions with the crystal. There is a difference in quenching for these charged particles in this crystal. The quenching effect is related to the energy deposited or lost per unit distance, as denoted by *dE/dX*. Alpha particles and triton have a higher *dE/dX* in comparison with electrons. The conversion efficiency was then calculated to be 86%. This means that when 4.78 MeV energy is deposited in the crystal, only 86% of it is converted to gamma-equivalent energy. The energy resolution of the thermal peak was determined to be 8%.

Using pulse height discrimination, neutrons and gamma-rays can be differentiated. Gamma induced events are registered in the lower end of the energy spectra up to 3 MeV. Neutron induced events occur within 4.1 MeeV. There is a large gap between both types of pulses, and therefore, neutron-gamma discrimination can be easily achieved with this crystal.

In addition to thermal neutrons, it was also tested for its response under the irradiation of an un-moderated neutron source. This source produces a poly-energetic spectra of fast neutrons. The measured response function is given in Appendix C. Many neutrons will scatter in the room and as a result be picked up by the detector at or around thermal energies due to the high $^{6}Li(n,\alpha)$ cross section. Any contribution from fast neutrons will be a continuum of energies on the right side of the 4.78 MeV peak. Two peaks were essentially observed, around 4.1 MeeV and 4.8 MeeV. The latter peak would be due to neutrons of energies greater than thermal.

The contribution of epithermal neutrons can be extracted using the procedure illustrated in Fig. 87.

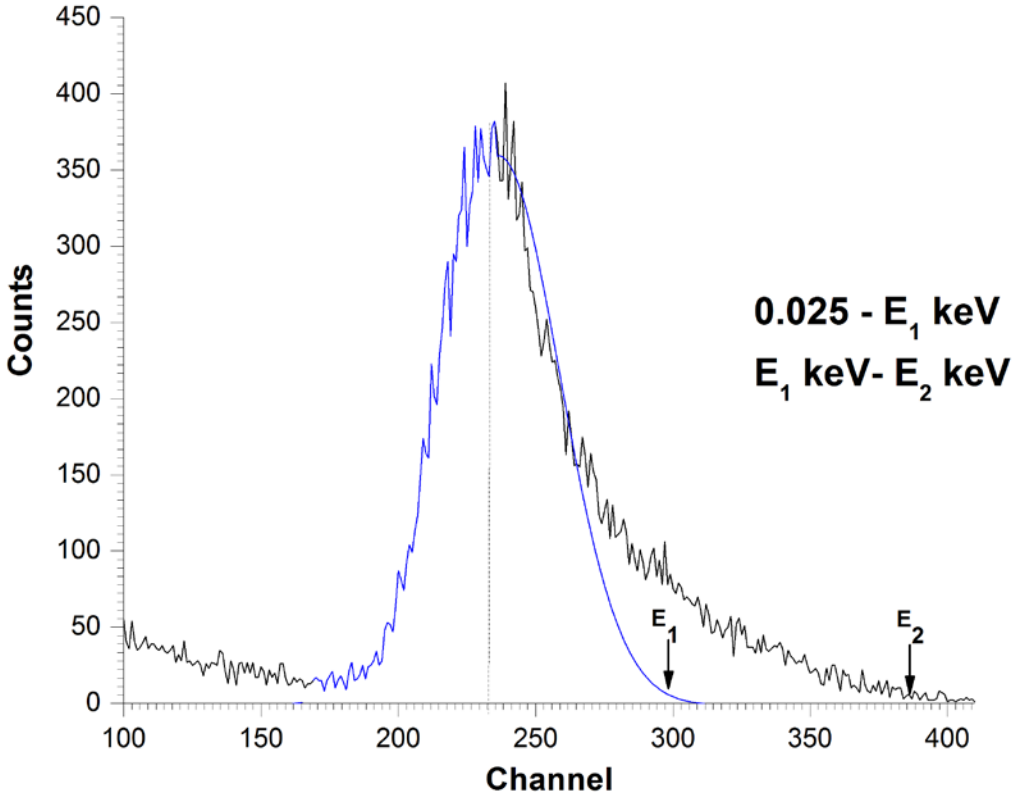

Figure 87: Procedure of extracting the epithermal neutron contribution using LiI:Eu

The procedure consists of taking the right side of the thermal peak symmetrically to its left side using a Gaussian distribution, with one standard deviation, and extracting the number of events between the energy E_1 and E_2, where E_1 represents the end side of thermal peak, and E_2 represents the end side of the overlap resulting from epithermal and thermal neutrons.

4.2.1.1.2 ^{6}Li-enriched Cs_2LiYCl_6:Ce Scintillator

The detector was irradiated with ^{137}Cs, ^{60}Co, ^{22}Na, and ^{57}Co gamma sources and their measured response functions are given in Figs. 88-91.

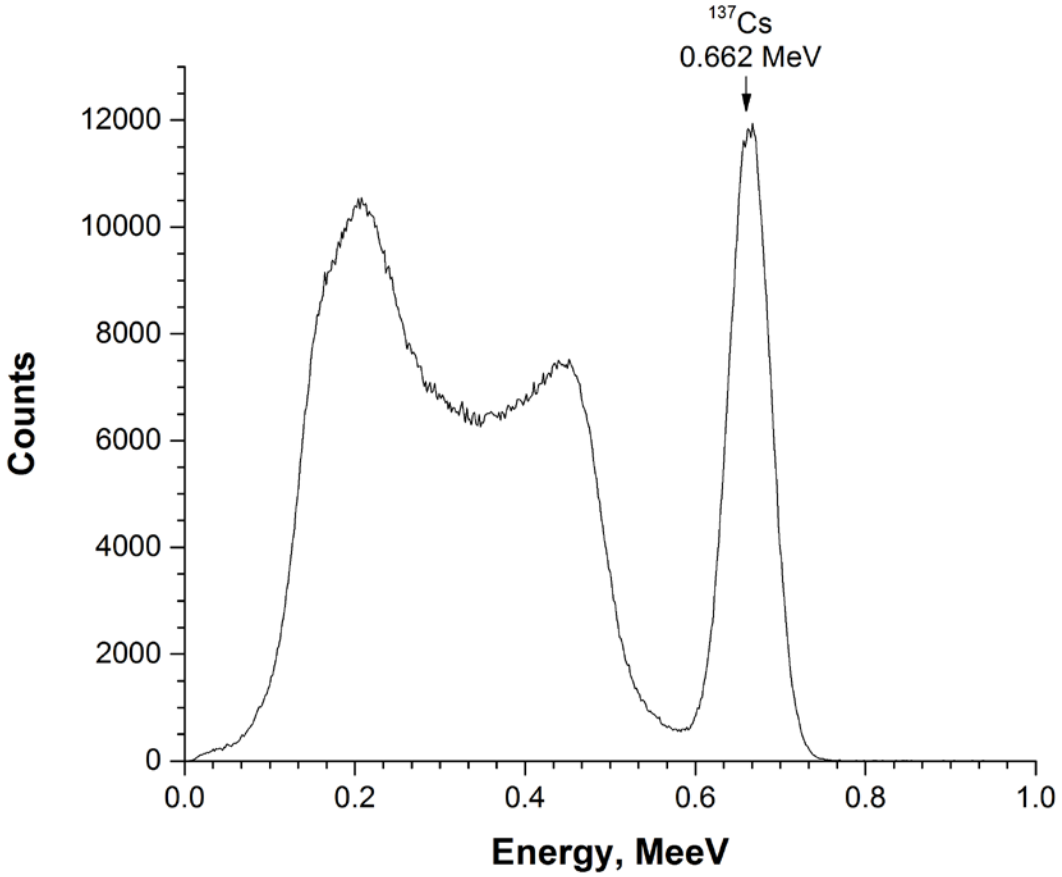

Figure 88: Measured response function of Cs_2LiYCl_6:Ce scintillator to ^{137}Cs

In Fig. 88, the photo-peak has been observed at 0.662 MeV. The Gaussian function was used to fit the photo-peak and the energy resolution of this peak was determined to be 6.9%.

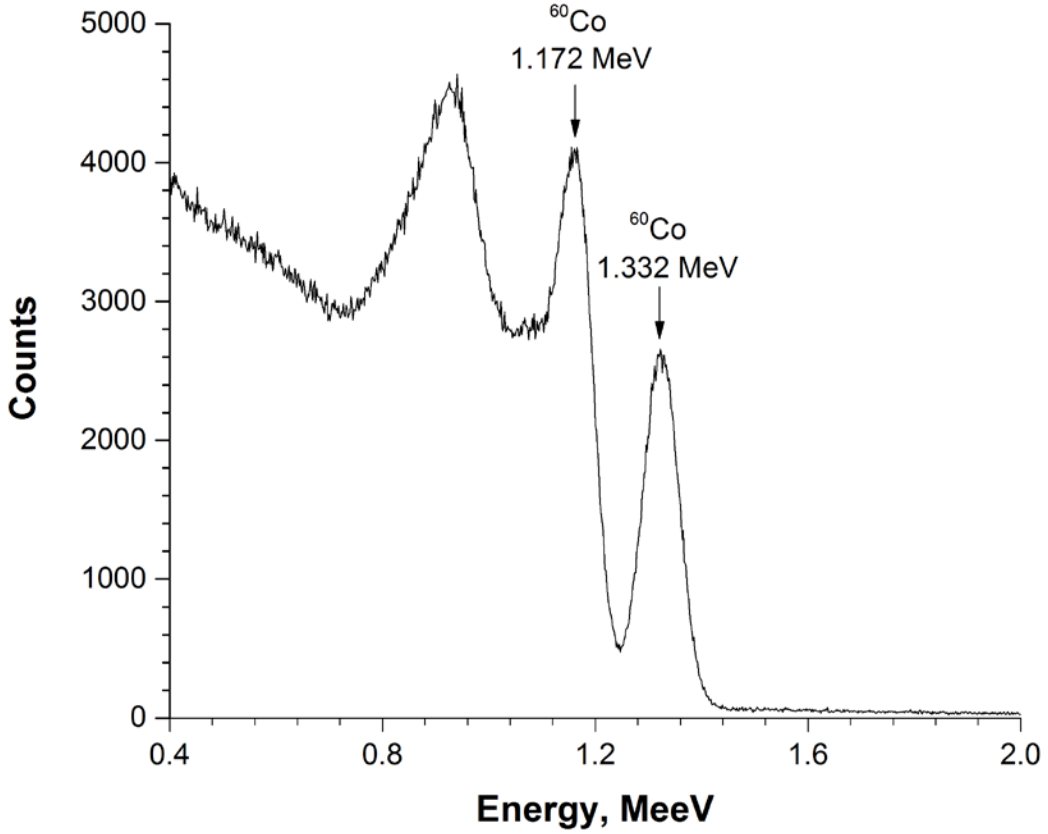

Figure 89: Measured response function of Cs_2LiYCl_6:Ce scintillator to ^{60}Co

For ^{60}Co, in Figure 89, the photo-peaks are seen at 1.172 MeV and 1.332 MeV and the energy resolution of these peaks was determined to be 4.2% and 4.1%, respectively.

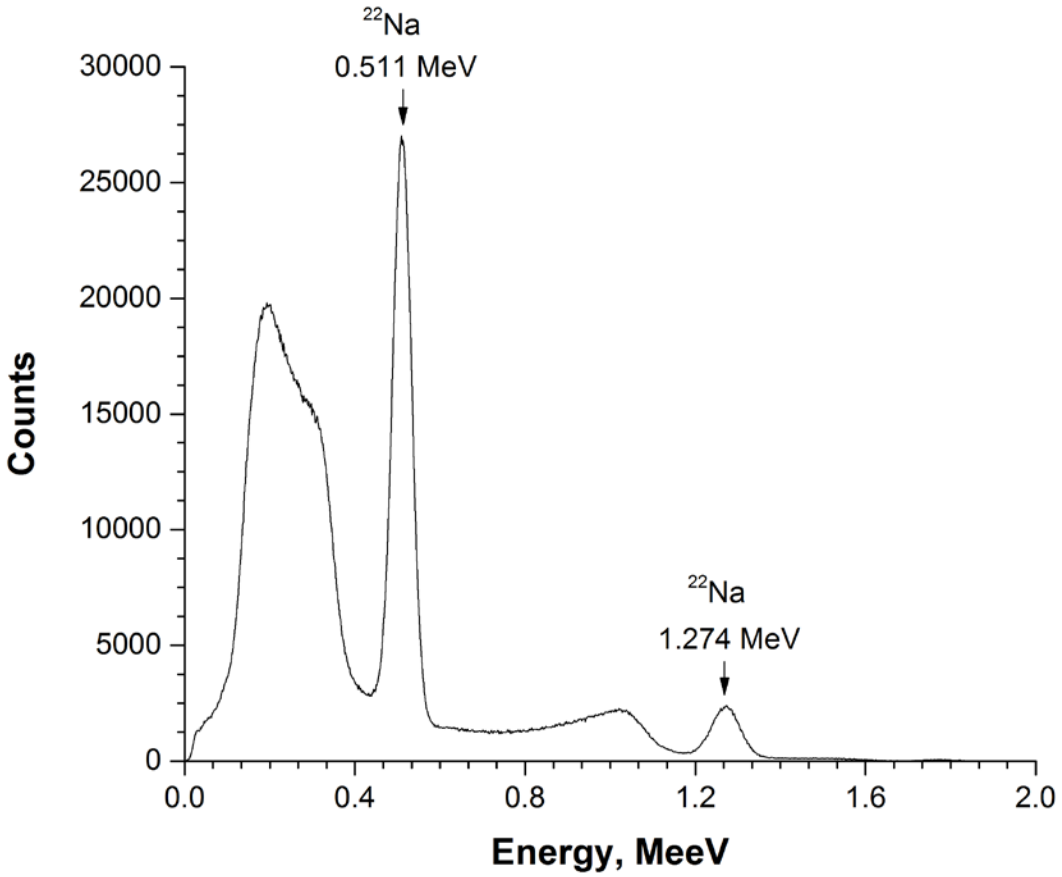

Figure 90: Measured response function of Cs_2LiYCl_6:Ce scintillator to ^{22}Na

To cover a large energy range of gamma radiation, another measurement has been taken out with ^{22}Na and the results are shown in Fig. 90. The photo-peaks are seen at 0.511 MeV and 1.274 MeV. The energy resolution of these peaks was determined to be 7.4% and 4.1%, respectively. Finally, the crystal has been tested for a low energy gamma-ray, namely with ^{57}Co as shown in Figure 90. The photo-peak of 0.122 MeV gamma-ray is observed on the pulse height spectra and the energy resolution at this energy was determined to be 15.1%.

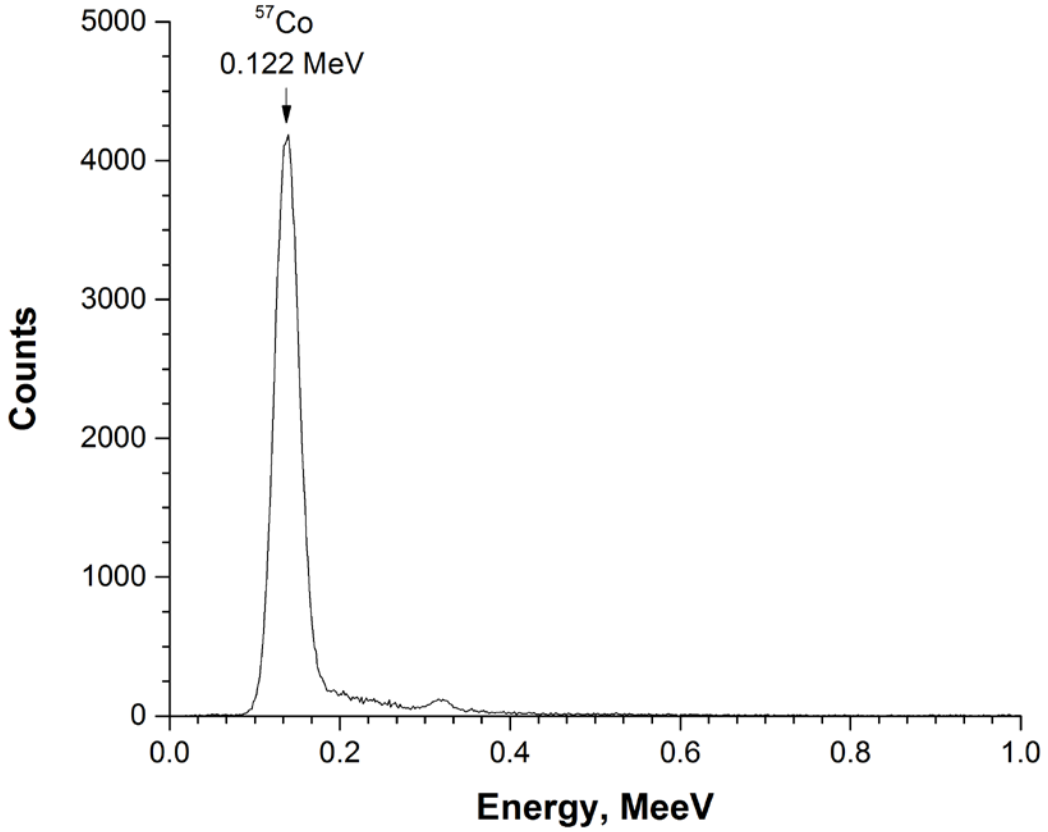

Figure 91: Measured response function of Cs_2LiYCl_6: Ce scintillator to ^{57}Co

The energy resolution of this scintillator has been given in Table 5 and plotted as a function of energy in Fig. 92. The data from all experiments to define the spectrometric characteristics of the scintillator, namely its ability to resolve between close peaks and its linearity has been summarized in Figs. 92 and 93.

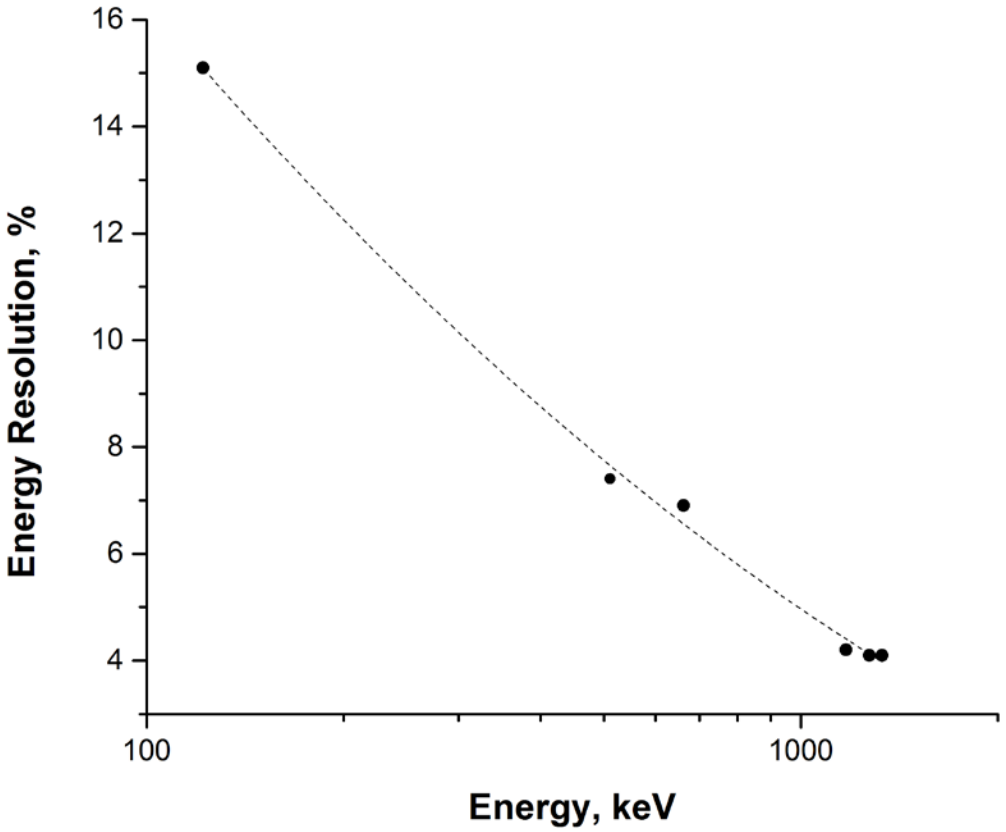

Figure 92: Energy resolution vs. energy for Cs_2LiYCl_6:Ce scintillator

In Fig. 92, the trend shows that as energy increases, the resolution gets better. At 662 keV, a reference for gamma radiation devices heavily used to identify isotopes in many handheld devices, the energy resolution is 6.9% which is better than the well know crystal, NaI.

The four gamma sources were used to obtain not only the calibration curve of this sensor for further neutron measurements but also to check its linearity in the range from 0.122 MeV to 1.332 MeV. The linearity of the detection system is shown in Fig. 93.

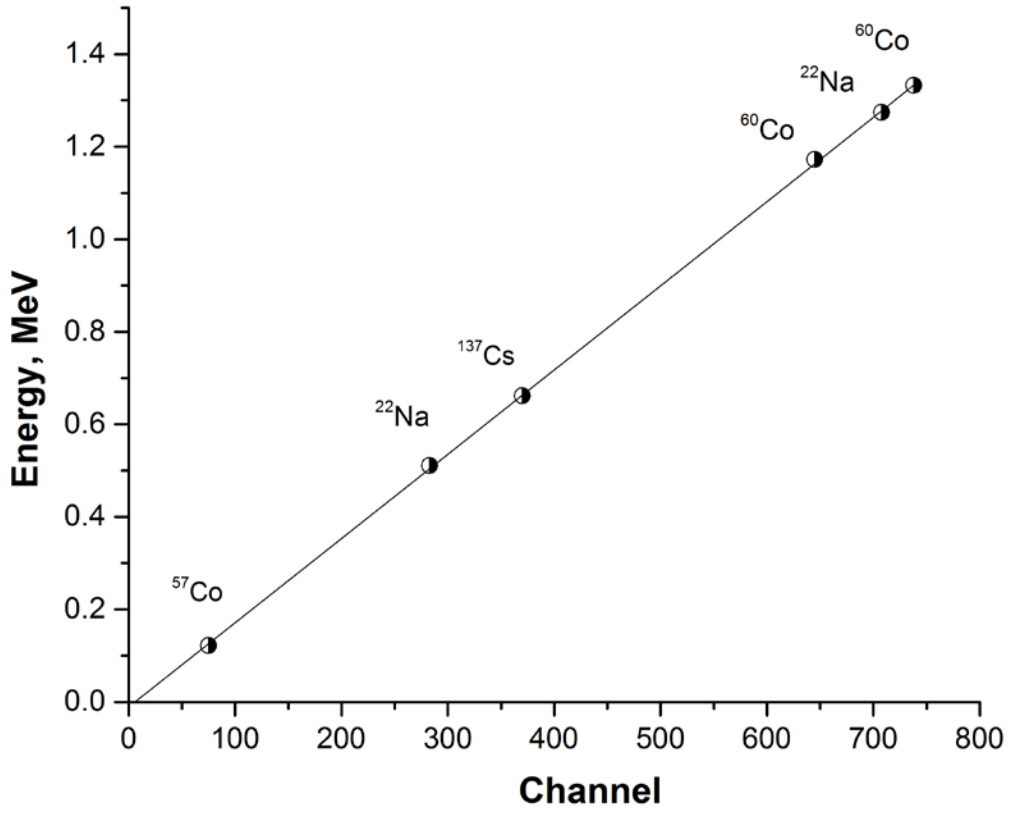

Figure 93: Calibration curve for Cs_2LiYCl_6:Ce scintillator

For thermal neutrons, the detector was irradiated with a moderated AmBe source and ^{137}Cs source for calibration purposes. The measured response function is given in Fig. 94.

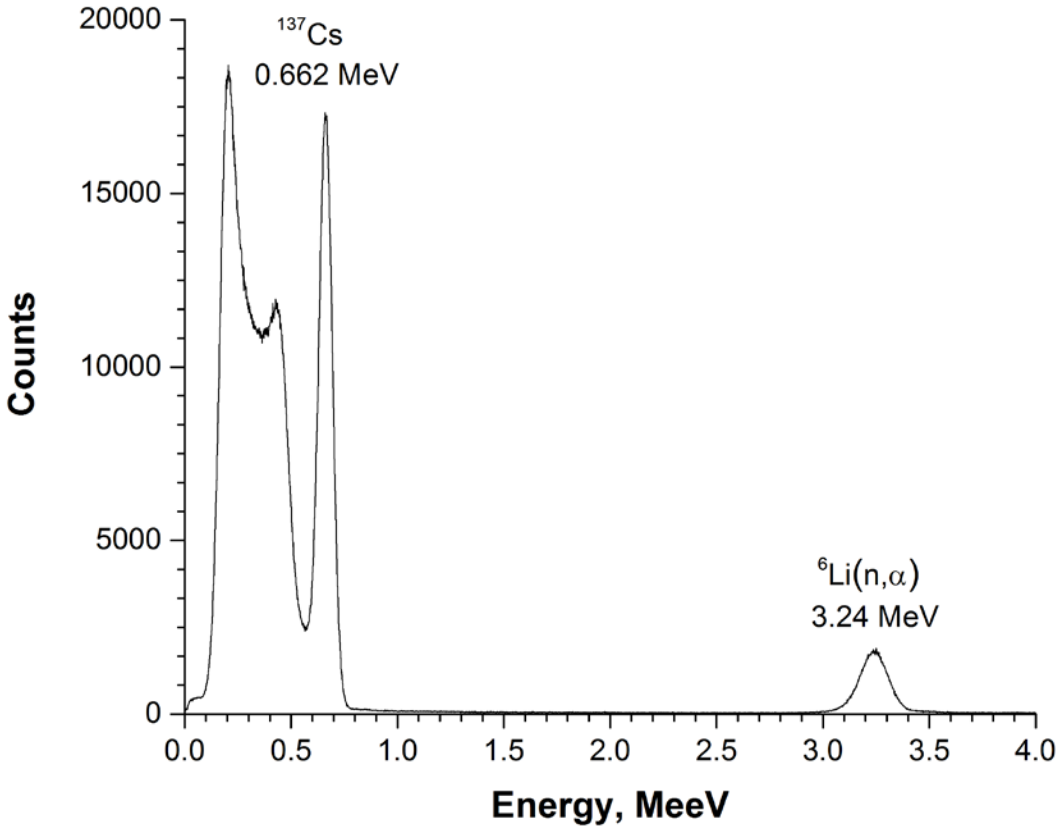

Figure 94: Measured response function of Cs_2LiYCl_6:Ce scintillator to ^{137}Cs and moderated AmBe neutron source

In Fig. 94, a distinct thermal peak from the $^{6}Li(n,\alpha)$ reaction and photo-peak from the 0.662 MeV gamma-ray have been registered on the pulse height spectra. The thermal peak has a gamma equivalent energy of 3.24 MeeV. For this scintillator, there is a difference of 1.54 MeV between the theoretical and measured value of the sum of the incident neutron energy and Q-value of the reaction. The quenching effect of the alpha particle and triton compared to the electrons reduces this value since the energy scale represents the light output from electrons, which can be confirmed by the position of the 0.662 MeV photo-peak. The conversion efficiency was then calculated to be 68%. Therefore, when the energy sum of ^{4}He and ^{3}H are deposited in the crystal, a gamma-equivalent energy event of 3.24 MeV is registered.

The energy resolution of the thermal peak was determined to be 3.3%. Therefore, this detector can resolve nearby energies of ±107 keV of this peak.

Pulse height discrimination can also be used to discriminate neutrons and gamma-rays using this scintillator. Gamma-rays as high as 3 MeV will not interfere or surpass the thermal peak of the GEE value of 3.24 MeV. Therefore, neutron-gamma discrimination can be achieved with this crystal. From these results, this detector demonstrates its ability to be a good thermal neutron detector.

This scintillator was also explored for its response to fast neutrons using an AmBe source. The measured response function is given in Appendix C. Due to the crystal containing ^{35}Cl, its (n,p) reaction would yield a distinct peak providing energy information of the incident neutron. However, the obtained response function did not show any signature of any peak resulting from fast or thermal neutron interaction with ^{35}Cl. Events at thermal energies with ^{35}Cl would be challenging to unravel because of falling in the lower end of the energy spectra where a large background component is seen, and due to the poorly resolved nature of this crystal at lower energies. A similar observation with this scintillator can be made to that of the LiI:Eu scintillator. Two peaks are observed at 3.2 MeV and 3.5 MeV. The former is the thermal neutron peak and the latter is due to fast neutrons from the (n,α) reaction with ^{6}Li.

4.2.1.2 Boron-loaded Plastic Scintillator

For gamma radiation testing, the detector was irradiated with ^{137}Cs and ^{60}Co gamma sources and their measured response functions are given in Figs. 95 and 96.

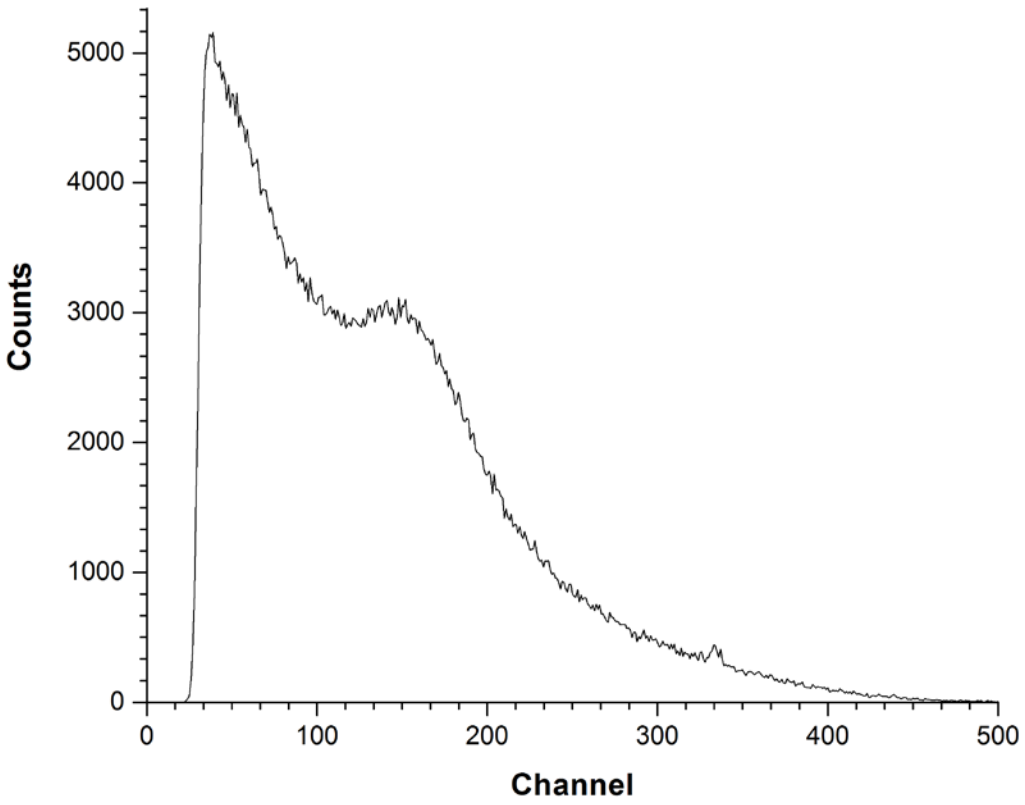

Figure 95: Measured response function of boron-loaded plastic scintillator to ^{137}Cs

Energy calibration of this scintillator could not be carried out due to the inability to identify a distinct energy to a corresponding channel. Due to the dominant scattering behaviour exhibited with gamma radiation, a distribution of energies is observed as opposed to any photo-peaks. Depending on the resolution of the detector, sometimes the Compton edges of different mono-energetic gamma sources can be used to calibrate the energy scale. In Fig. 95, a Compton edge for ^{137}Cs is seen, however it is not resolved enough to be able to identify the channel that the pulses are registered in. Also, part of the Compton continuum also falls into the range of background radiation which makes it more challenging.

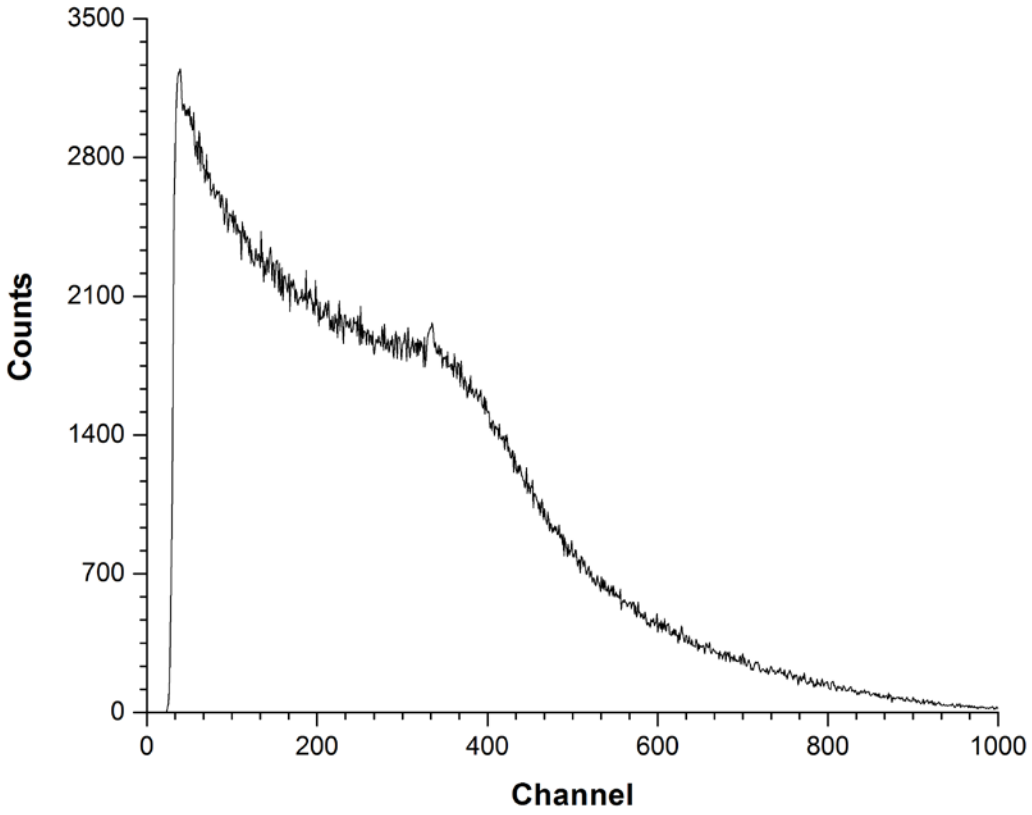

Figure 96: Measured response function of boron-loaded plastic scintillator to ^{60}Co

In Fig. 96, the two gamma-rays emitted from ^{60}Co are unable to be resolved individually. Since both energies are close and plastic scintillators have poor resolution, the two Compton edges overlap. As a result, no calibration can be done using this source.

This scintillator has been tested as one of the candidates to detect neutrons using two different processes. The scattering process on hydrogen using (n,n) and the absorption process on ^{10}B using (n,α). For thermal neutrons, the detector was irradiated with a moderated AmBe source and the measured response function is shown in Fig. 97.

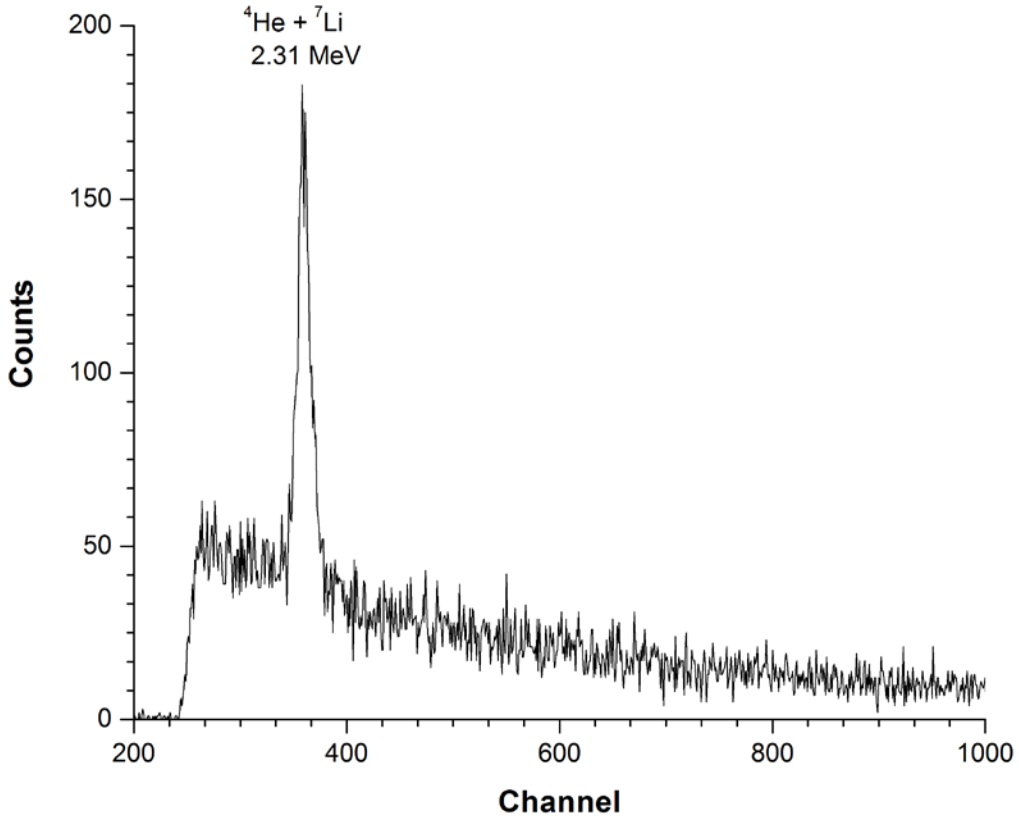

Figure 97: Measured response function of boron-loaded plastic scintillator to moderated AmBe neutron source

In Fig. 97, while the horizontal axis does not represent energies, there are still some observations that can be made about the response function. There is a prominent peak around channel 358 and it is the only distinct peak that can be seen. Due to the very large neutron cross section of ^{10}B(n,α) at thermal energies, and since no other possible absorption reactions can occur in this scintillator with this probability, this peak being the thermal peak is highly plausible. The energy resolution of this peak was determined to be 3.4%.

There are many scattering events taking place in this detector, as seen by the distribution of pulses along the channels. These events are due to the highly probable scattering processes with gamma radiation and at higher neutron energies, with hydrogen and carbon. Consequently, it is difficult to distinguish the types of reactions causing these events. Before the measurements were carried out, the neutron scattering process on ^{1}H was going to be explored using this scintillator

for potential use in fast neutron spectrometry. However, due to the obtained response, fast neutron spectrometry with this scintillator no longer seemed feasible. Nonetheless, this detector would function better as a thermal neutron detector.

4.2.2 Fast Neutron Detection

The results obtained with the previous version of this scintillator which is ^{6}Li-enriched CLYC scintillator did not show any indication of proton peaks with fast neutrons. The absence of such signature is mainly because (n,α) is dominating on the spectra. As discussed in the methodology chapter, the structure of the crystal does not change with the change of isotopes of the same elements; a new version of this scintillator was acquired with a significant reduction of 1% ^{6}Li (i.e.^{7}Li enriched crystal). As in previous experiments, the detector was irradiated in different neutron and gamma fields.

4.2.2.1 ^{7}Li-enriched Cs_2LiYCl_6:Ce Irradiated with Gamma Radiation

The first series of experiments have been carried out with ^{137}Cs, ^{60}Co, and ^{22}Na gamma sources and the measured response functions are given in Fig. 98. The pulse high spectra are similar to that of the previous version of CLYC scintillator since the gamma radiation interactions take place mainly with electrons.

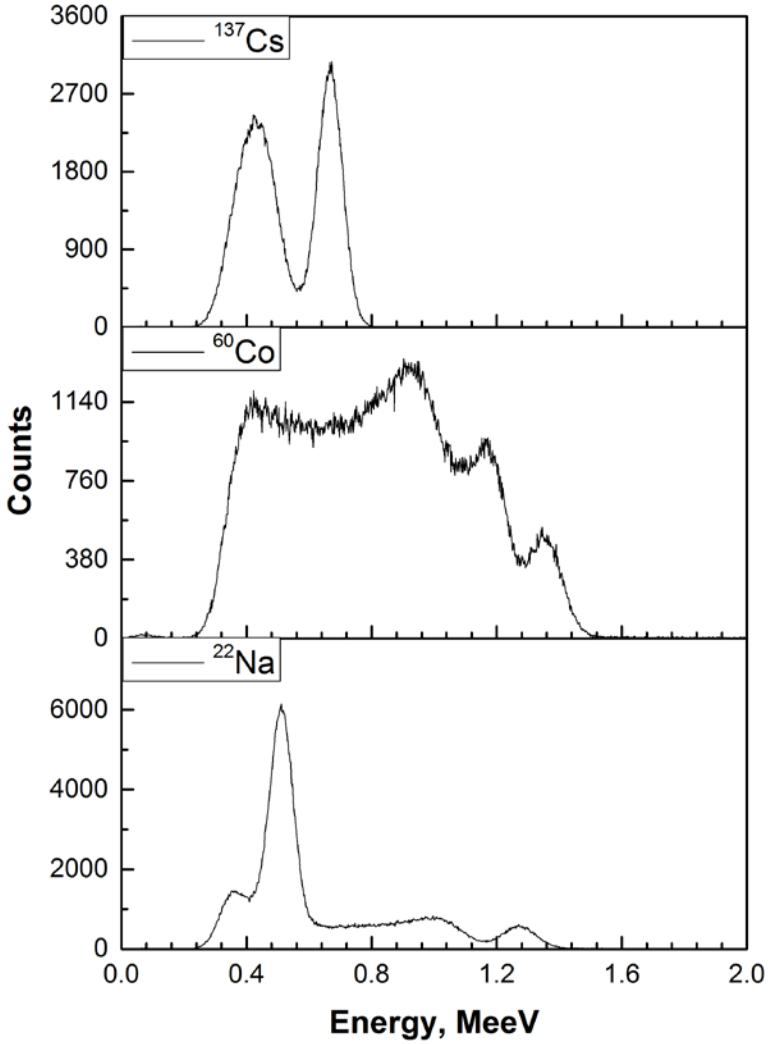

Figure 98: Measured response functions of Cs_2LiYCl_6:Ce scintillator to ^{137}Cs, ^{60}Co, and ^{22}Na

In the top graph of Fig. 98, the photo-peak is clearly seen at 0.662 MeV. The energy resolution of this peak was determined to be 11.1%.

In the middle graph of Fig. 98, the photo-peaks are seen at 1.172 MeV and 1.332 MeV. The energy resolution of these peaks was determined to be 4.2% and 5.7%, respectively.

In bottom graph of Fig. 98, the photo-peaks are seen at 0.511 MeV and 1.274 MeV. The energy resolution of these peaks was determined to be 12.8% and 8.2%, respectively.

The energy resolution of this scintillator has been given in Table 5.

Table 5: Energy resolution of various energies of Cs_2LiYCl_6:Ce scintillator

Energy (MeV)	Energy Resolution, %
0.511	12.8
0.662	11.1
1.172	4.2
1.274	8.2
1.332	5.7

These gamma sources were used to generate the calibration curve for this detector. The linearity of the detection system can be seen in Fig. 99.

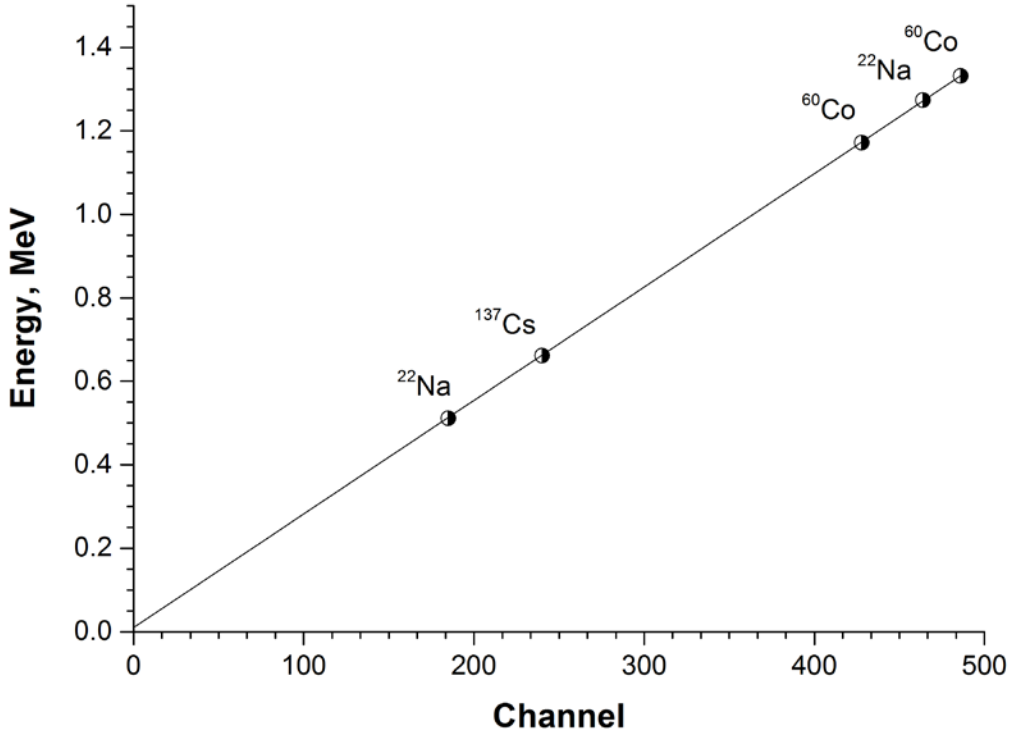

Figure 99: Calibration Curve for Cs_2LiYCl_6:Ce scintillator

4.2.2.2. ^{7}Li-enriched Cs_2LiYCl_6:Ce Irradiated with Mono-Energetic Neutrons

To test the detector with mono-energetic neutrons, McMaster accelerator facilities and the neutron generator at the University of Ontario Institute of Technology were used. The energy range was varied from 300 keV to 4 MeV. In this wide energy range, two different reactions to produce neutrons have been used, namely D(d,n) and ^{7}Li(p,n).

The detector was placed at around 100 cm at different angles from the target axis and was irradiated with the above mentioned mono-energetic neutrons. The abscissa was calibrated using ^{22}Na to get the energy scale for all spectra. The first series of experiments has been carried out with 400 keV mono-energetic neutrons. The pulse height spectra of the obtained results are shown in Fig. 100.

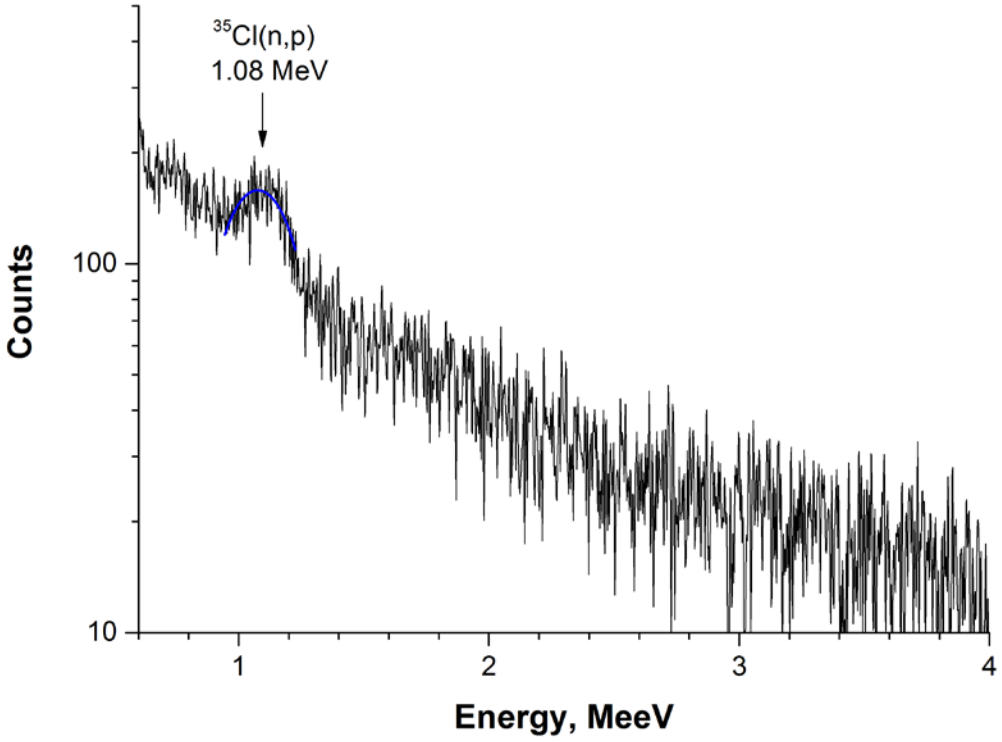

Figure 100: Measured response function of Cs_2LiYCl_6:Ce scintillator to 0.4 MeV neutrons

In Figure 100, a clear peak at 1.08 MeeV is observed. If all of the reactions that could occur in this crystal at this energy are considered, the only possible reaction this peak could be due to is ^{35}Cl(n,p). This peak has a gamma equivalent energy of 1.08 MeeV. Theoretically and from

reaction kinematics, at 400 keV, this peak should be at 1015 keV. However, there is a difference of 65 keV between the experimental and theoretical values. This results from the fact that the light output of the crystal is different when it comes to electrons and protons.

The second series of experiments has been carried out when the detector has been placed at a different angle relative from the target axis with neutron energy of 2.67 MeV. The results of one experimental run are illustrated in Fig. 101.

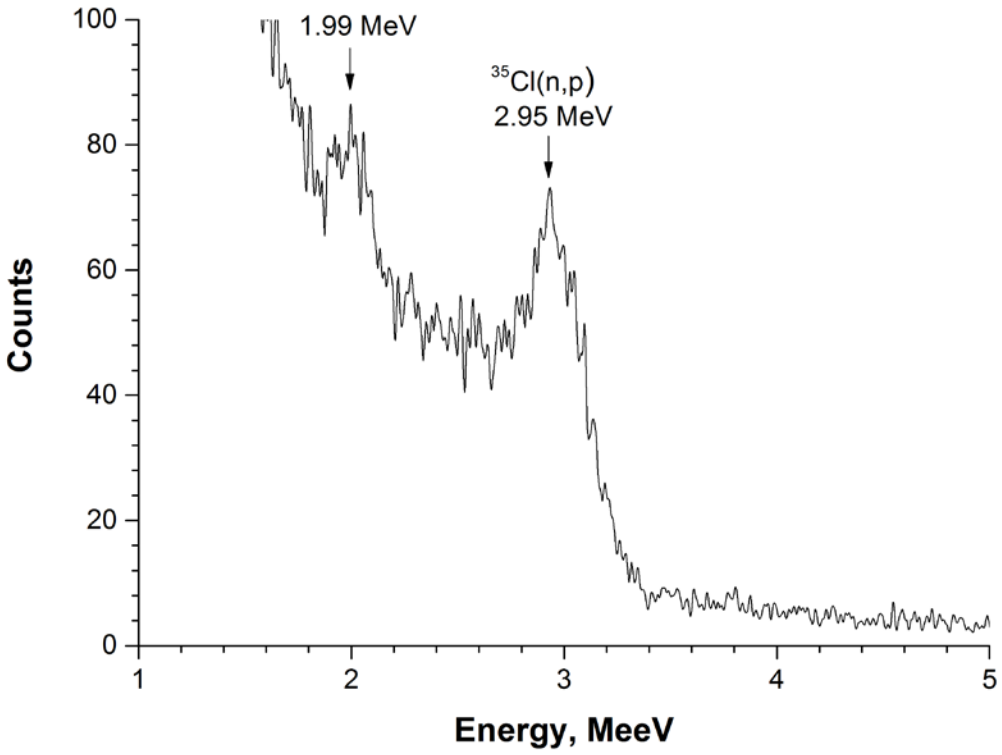

Figure 101: Measured response function of Cs_2LiYCl_6:Ce scintillator to 2.67 MeV neutrons

The pulse height spectra shows two main features, namely, two prominent peaks at 1.99 MeeV and 2.95 MeeV. Similarly to the discussion in the simulation section and considering all of the reactions in CLYC, the only reaction with a substantial cross section at this energy is ^{35}Cl(n,p), and therefore the peak observed at 2.95 MeeV corresponds to the protons emitted from the ^{35}Cl(n,p) reaction. The other peak seems to be evolving further left to this peak around 1.99 MeeV. This peak corresponds either to the contribution from other reactions that take place when

neutrons interact with the isotope content of the crystal or to a quantum state of the recoil nucleus. Further analysis of the cross section of other reactions leads to a conclusion that their contribution is negligible due to their extremely small cross section. The nature of this second peak then may correspond to one of the excited states of the recoil nuclei. So, at 2.67 MeV the prominent proton peak from (n,p) reaction with ^{35}Cl that should theoretically be at 3.285 MeV appears at 335 keeV less on the energy scale of the experimental data due to difference in light output between electrons and protons.

Further in the investigation with mono-energetic neutrons, the detector has been placed at 30 degrees relative to the deuteron beam. At this position, neutrons are produced with 3.57 MeV. In Fig. 102, a distinct peak was observed at 3.74 MeeV which, theoretically, should be at 4.185 MeV. Consequently, there is a difference of 445 keeV due to the light output between electrons and protons. On the same pulse height spectra and similarly to the previous experiments, a second peak seems to becoming more prominent and appears at 2.03 MeeV. Both peaks have shifted to the right on the spectra. One should notice that the proton peak at 3.74 MeeV shifted linearly with the neutron energy and can therefore allow neutron spectrometry.

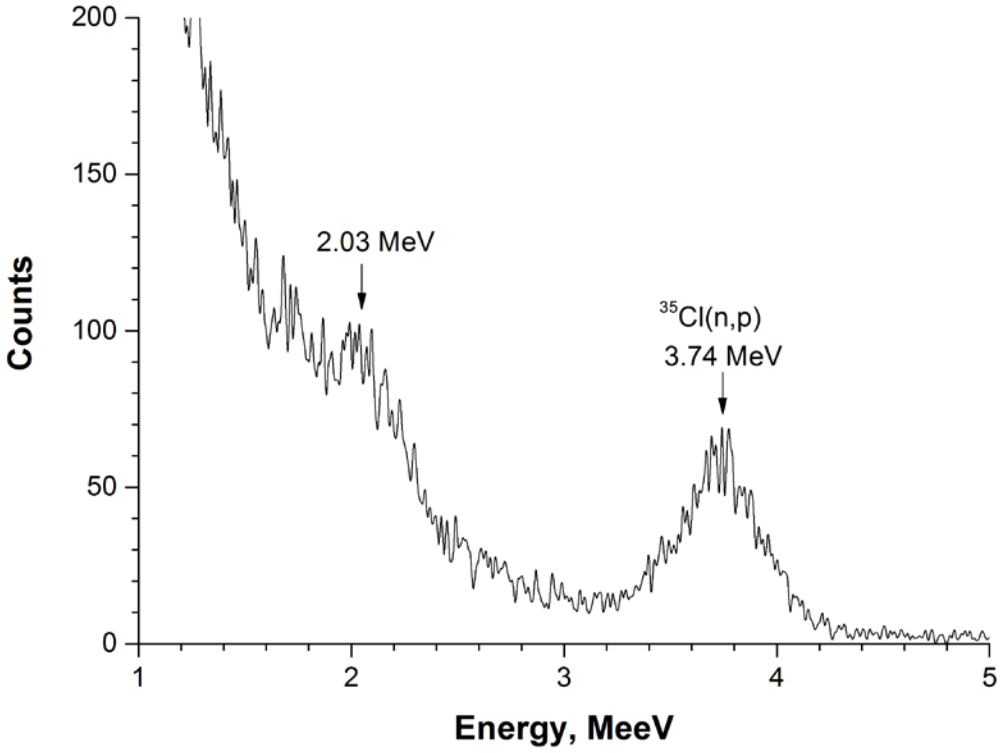

Figure 102: Measured response function of Cs_2LiYCl_6:Ce scintillator to 3.57 MeV neutrons

The last series of experiments has been carried out with 4 MeV mono-energetic neutrons when the detector has been placed at 0 degrees from the deuteron beam. Analogically, in Fig. 103, a distinct peak is observed at 4.14 MeeV. This peak, according to reaction kinematics, should be at 4.185 MeeV. However, there is a difference of 475 keV observed in the experimental value. The second peak at the left side has become much clearer and moves to 2.25 MeeV.

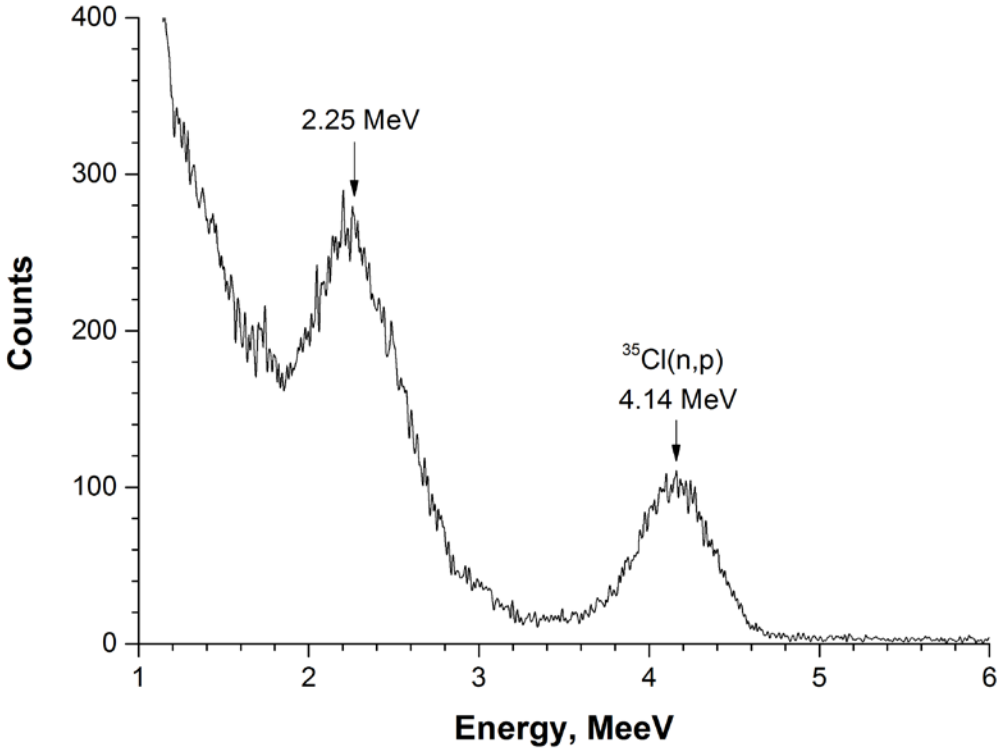

Figure 103: Measured response function of Cs_2LiYCl_6:Ce scintillator to 4 MeV neutrons

There is a difference in the theoretical and measured values of the sum of the incident neutron energy and Q-value, as previously mentioned in previous experiments, that increases linearly with neutron energy. This difference is due to the different light output from a proton in the crystal as opposed to electron. As the abscissa in the response functions represents the energy equivalent to the deposited energy by electrons, the energy deposited by protons is different due to quenching. Since protons are greater in mass than electrons, they lose more energy in a shorter distance, and therefore have a greater *dE/dX*.

It is important to notice that in all experiments, there are two main features; the first one is that the proton peak is linearly shifting towards higher energy as a function of incident neutron energy, and the second feature is that the energy difference between the two peaks is not constant but increases with the neutron energy. This an indication of the relationship between the value of the second peak and the excitation energy of the compound nucleus formed after the neutron

absorption. In other words, for any compound nucleus in its excited state, several different types of nuclear reactions are energetically possible. The probability of each reaction depends on the excitation energy in which the compound nucleus is in, as well as on the location of its nuclear levels. Thus, in this case, ^{35}Cl absorbs a neutron to form a compound nucleus ^{36}Cl, and depending on the incident neutron energy, the excitation energy of the ^{36}Cl compound nucleus takes different values. Consequently, there are many possible output reactions with different probabilities. The emission of a proton is only one channel among the energetically possible output reactions. When the proton is emitted, the recoil nucleus, ^{35}S, is either in its ground state, where in this case, mono-energetic protons are emitted and nothing else; or there are more than one group of protons emitted leaving the recoil nucleus in different excited states for a later gamma emission. The second peak appearing in the spectra therefore may correspond to one the excited states of the product nucleus.

All four experiments carried out with mono-energetic neutrons are summarized in Fig. 104. In this figure, it is clear to see that the peak due to fast neutrons reacting with ^{35}Cl, referred to as peak 1, is increasing by linearly shifting to the right on the spectra. The second peak, referred to as peak 2, is also present from 2.67 MeV onwards. This peak also shifts with increasing neutron energy. This indicates that both reactions are indeed induced by fast neutrons.

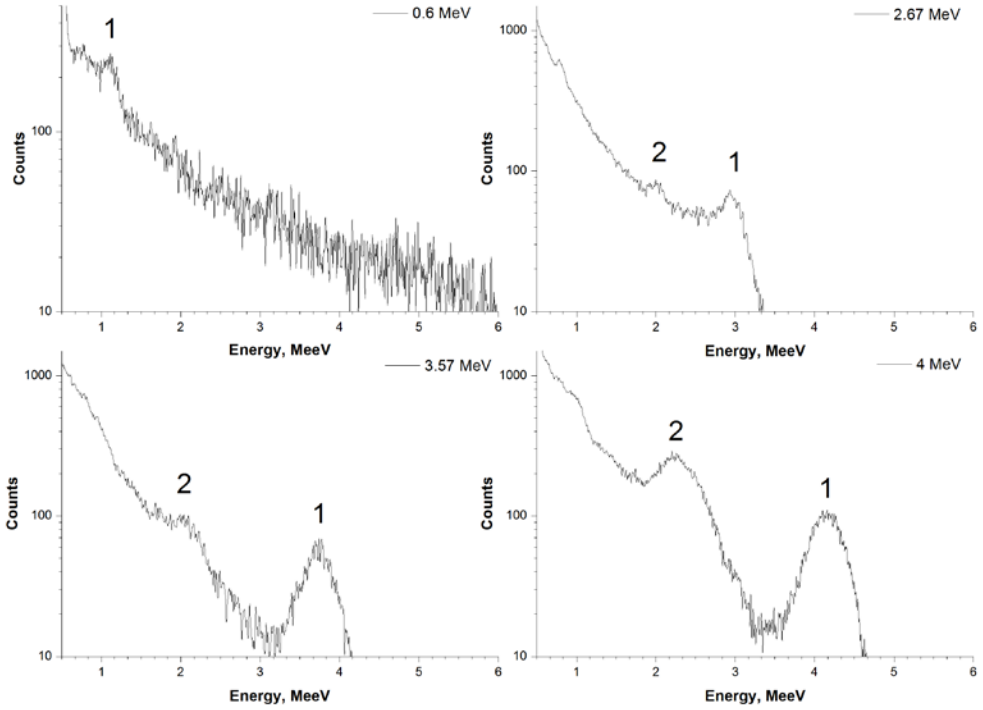

Figure 104: Comparison of measured response functions of Cs_2LiYCl_6:Ce scintillator to 0.6, 2.67, 3.57, and 4 MeV neutrons

In terms of neutron-gamma discrimination, seemingly the proton peak from neutron energies lower than 400 keV would be difficult to observe, as they lie within the range of pulses from around 1 MeV gamma-ray interactions on the spectra. The second proton peak only started appearing around 600 keV neutrons which indicated its relationship with the excited states of the compound nucleus of ^{36}Cl. As the neutron energy increases, this peak became more defined i.e. the probability of the emission of this proton group increases since the cross section of this output channel increases with the incident neutron energy. Taking into consideration the presence of the second peak and with a good calibration, one can use the CLYC crystal for fast neutron detection applications in the energy range from 0.6 MeV to at least 4 MeV.

A summary comparing the four response functions to fast neutrons is given in Fig. 105. In this figure, the points indicate the position of the proton peak form of $^{35}Cl(n,p)$ reaction with a given

neutron energy. This plot shows that the energy deposited by the proton in the reaction increases linearly with incident neutron energy.

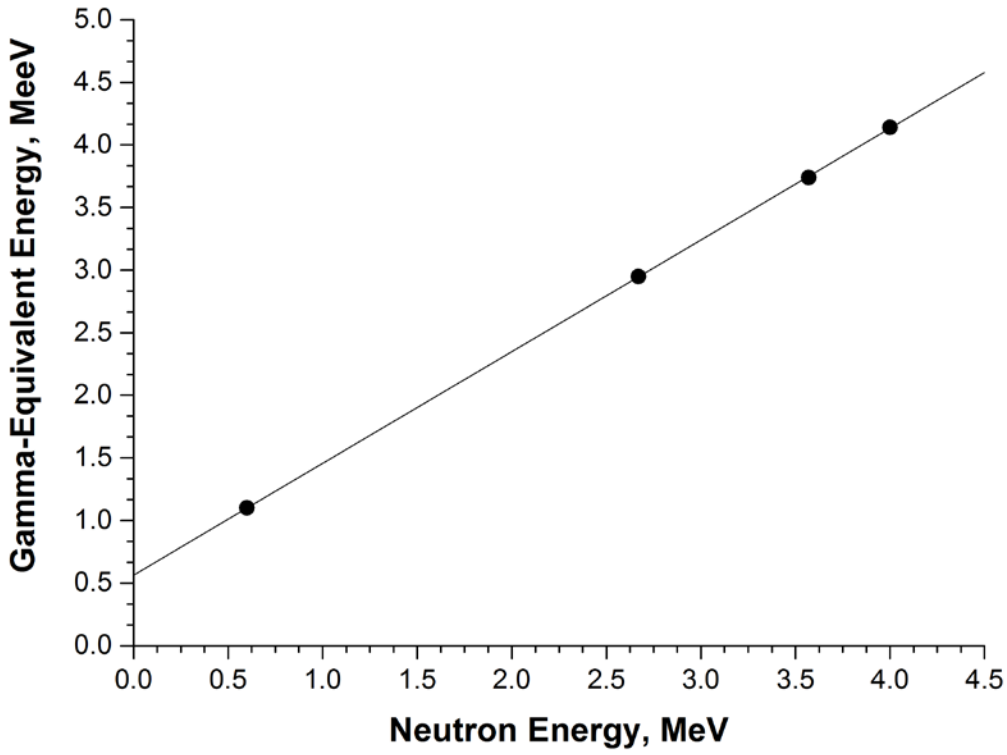

Figure 105: Gamma-equivalent energy from ^{35}Cl(n,p) reactions vs. neutron energy

The linearity of this scintillator's response to fast neutrons is a promising feature for fast neutron spectrometry. With well-defined peaks, the energy spectrum from a fast neutron source within tolerable limits can be deduced from the response function using this light output curve. It should be noted that the shift of the experimental value of the proton peak from its theoretical value is around 10% for all investigated energies. For instance, with a neutron energy of 2.67 MeV, the experimental value of the proton peak is at 2.95 MeV, instead of the theoretical value of 3.285 MeV.

Since this study aims to investigate the possibility to use CLYC for fast neutron detection, the resolution of the detector has been evaluated as a function of neutron energy. A Gaussian function was used to fit the fast neutron peaks. With the exception of 0.6 MeV, the energy

resolution is given in Table 6. At 0.6 MeV, the peak did not evolve enough to obtain a proper fit of it.

Table 6: Energy resolution of neutron energies of Cs_2LiYCl_6:Ce scintillator

Energy (MeV)	Energy Resolution, %
2.67	5.4
3.57	10.6
4	11.0

As the neutron energy increases, the resolution becomes worst. The increasing width of the peaks can be due to several reasons. The neutron energy produced is related to the target thickness and angle at which the detector is placed. The neutrons were generated using a charged particle accelerator, either by accelerating protons or deuterons, and therefore the neutron beam at a defined angle can be broader than a single group of mono-energetic neutrons. In addition, there are various effects related to photon emission statistics of the crystal which is an intrinsic propriety of the scintillator. Finally, the large background around the crystal in the experimental room has a significant impact on the peak shape.

4.3 Comparison and Discussion of Simulation and Experimental Results

In this section, the simulated and measured results of the detectors are plotted side by side for comparison. The first two detectors were analyzed for their response to thermal neutrons and the last detector for its response to fast neutrons. The comparison has been done by qualitatively looking at the responses and examining the reactions taking place in each set of results. The boron-loaded plastic scintillator is not included in this comparison due to the lack of any photo-peak on the pulse height spectra to be used for calibration.

4.3.1 LiI:Eu Scintillator

In Fig. 106, the thermal peak due to the $^{6}Li(n,\alpha)$ reaction can be seen in both response functions. The simulated response's x-axis represents the energy deposited by the alpha particle and triton, while the measured response's x-axis represents the energy deposited in MeeV.

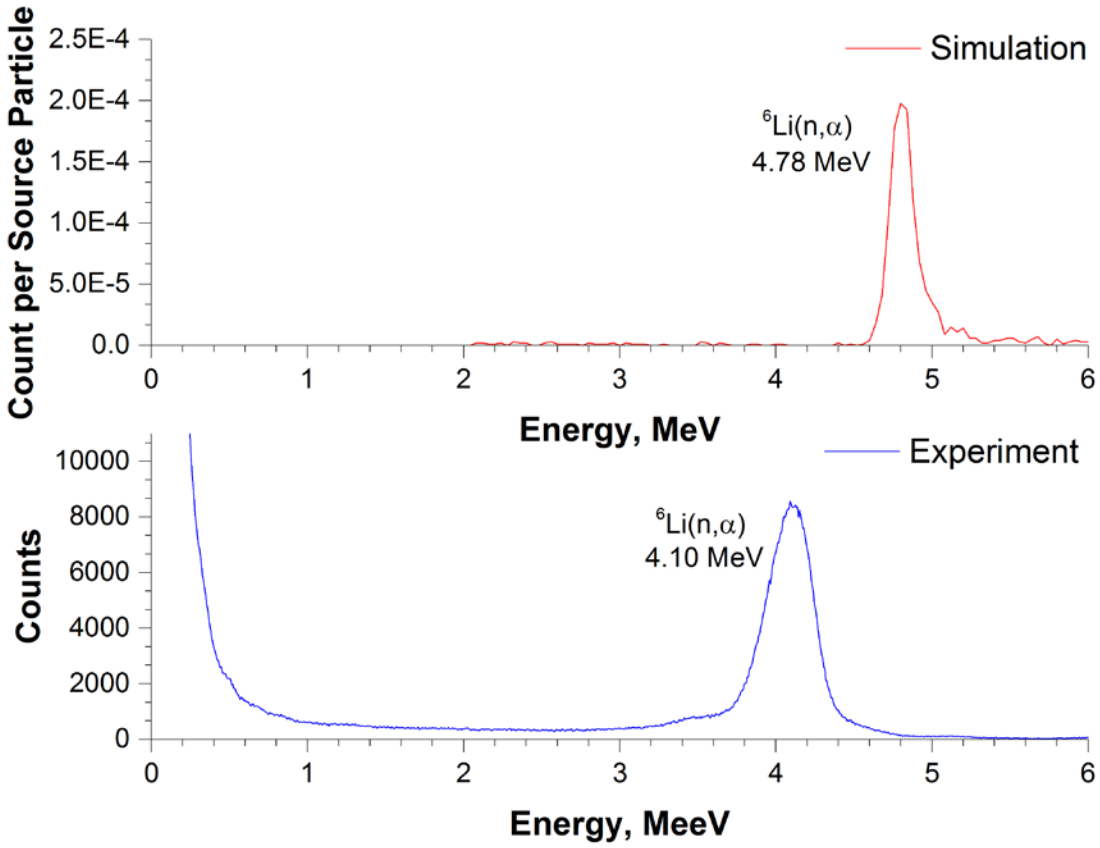

Figure 106: Comparison of the simulated and measured response functions of LiI:Eu scintillator to moderated AmBe neutron source

The shift in deposited energy value is observed from the simulated response as compared to the experimental response due to the light output of different charged particles. A large gap is observed from the background radiation in the experiment that would entail that both neutron and gamma-ray induced events can be easily separated.

4.3.2 ^{6}Li-enriched Cs_2LiYCl_6:Ce Scintillator

A summary of results from both simulation and experiments are presented in Fig. 107 ,when the detector has been irradiated with thermal neutrons. The thermal peak due to the ^{6}Li(n,α) reaction and photo-peak from ^{137}Cs is seen in both response functions.

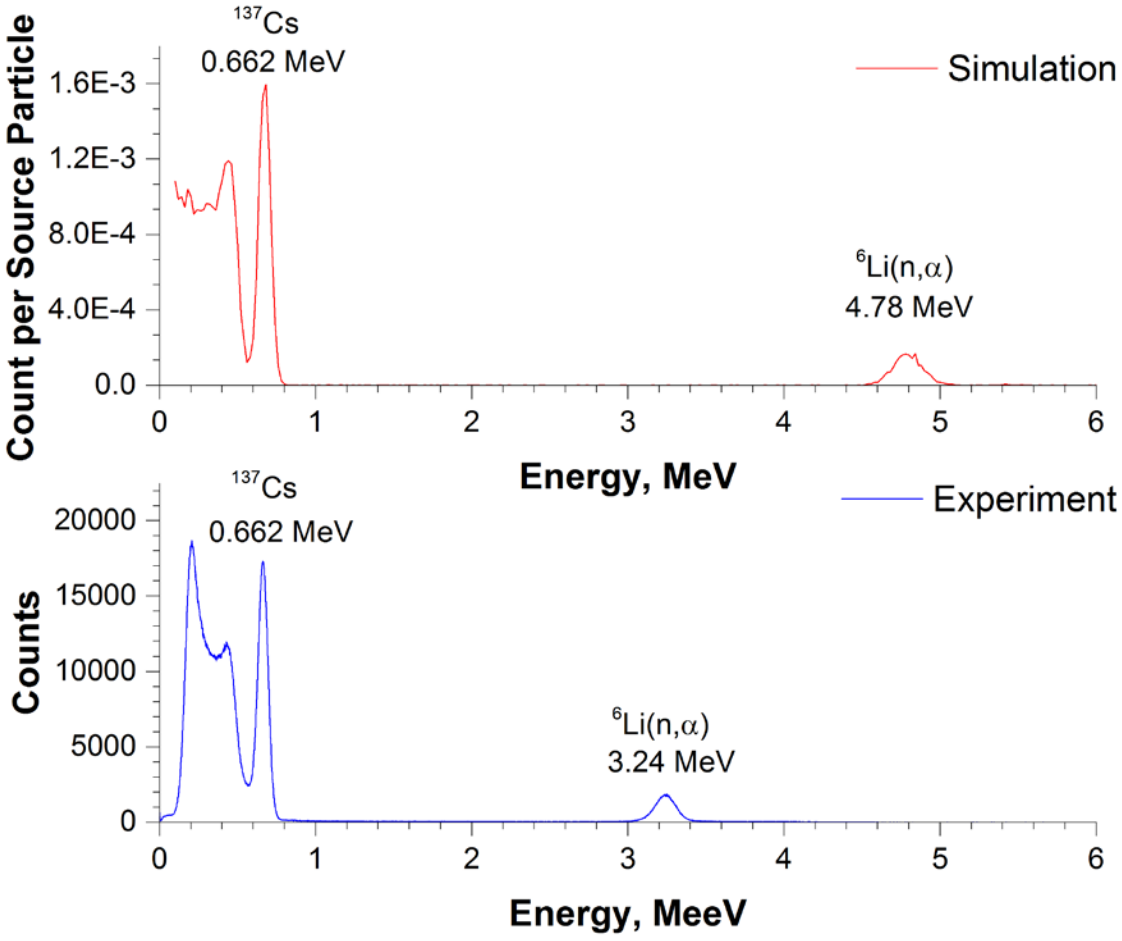

Figure 107: Comparison of the simulated and measured response functions of Cs_2LiYCl_6:Ce scintillator to moderated AmBe neutron source and ^{137}Cs source

Similar to the LiI:Eu scintillator, a shift in deposited energy value from the simulated response to the experimental response is observed. However, this shift is larger in this crystal than when compared to LiI:Eu, which would mean that LiI:Eu is more luminescent than CLYC for thermal neutrons. The ^{137}Cs photo-peak is observed at the same full energy value for both responses. The gap between the ^{137}Cs photo-peak and thermal neutron peak shows the crystal's ability to discriminate gamma-rays and neutrons using pulse height discrimination.

4.3.3 ^{7}Li-enriched Cs_2LiYCl_6:Ce Scintillator

The simulation and experimental data has been also compared for fast neutrons. The two plots are shown side by side in Figure 108 for 4 MeV neutrons. The comparison for 2.67 MeV and 3.57 MeV neutrons is given in Appendix C.

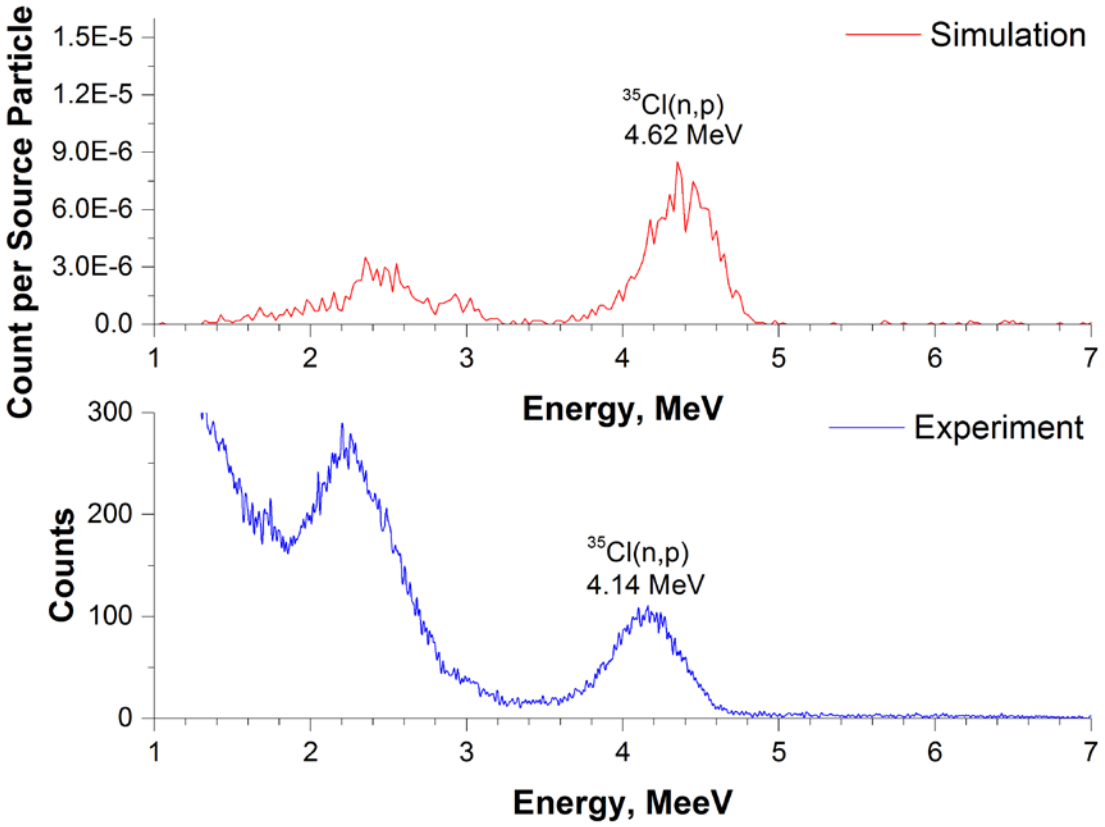

Figure 108: Comparison of the simulated and measured response functions of Cs_2LiYCl_6:Ce scintillator to 4 MeV neutrons

In Fig. 108, two peaks are seen in both response functions. A peak at 4.62 MeV in the simulation data and at 4.14 MeeV in the experiment are observed. This peak is due to the ^{35}Cl(n,p) reaction. The other peak is seen at 2.48 MeV in the simulation data and 2.22 MeeV in the experiment. In the simulations, this peak was solely due to protons. The cause of this peak was investigated through many simulations, and no absorption reaction can be identified with this peak. However, it is clear that the two peaks in each spectrum correspond to each other. A shift is also observed with both peaks from the simulated response to the experimental response. Depending on the

nature of the unknown peak, neutron-gamma discrimination using pulse height discrimination may be challenging since it overlaps with pulses from the lower end of the spectrum.

4.4 Detector Inter-Comparison

The four detectors were chosen and studied for their potential use in a neutron spectrometry. To evaluate their detection capabilities and properties, from previous discussions, Table 7 and Table 8 give a comparison of their detection and optical properties. For thermal neutron detection, LiI:Eu and ^{6}Li-enriched Cs_2LiYCl_6:Ce detectors are excellent candidates due to their high detection efficiency and ability to discriminate between neutron and gamma radiation. However, for the boron-loaded plastic scintillator, due to its light element content, does not meet the criteria of n-γ discrimination, and is therefore a poor candidate. However, for fast neutron detection, only the ^{7}Li-enriched Cs_2LiYCl_6:Ce detector demonstrates the ability to identify distinct proton peaks when bombarded with different neutron energies, at least in the range of a few hundred keVs to 4 MeV.

Table 7: Detection Capabilities

Detector	Gamma-rays	Thermal Neutrons	Fast Neutrons
LiI:Eu	Satisfactory	Good	Poor
^{6}Li-enriched Cs_2LiYCl_6:Ce	Good	Excellent	Poor
Boron-loaded plastic	Poor	Satisfactory	Poor
^{7}Li-enriched Cs_2LiYCl_6:Ce	Good	Satisfactory	Good

All detectors with the exception of the boron-loaded plastic scintillator can serve as gamma detectors with acceptable resolution to identify many of the isotopes encountered in industry. In terms of gamma spectrometry, the first version of Cs_2LiYCl_6:Ce scintillator (^{6}Li-enriched) had

the best resolution at most energies, and would thus be most suitable. The second version of Cs_2LiYCl_6:Ce (^{7}Li-enriched) and LiI:Eu have comparable energy resolution.

All detectors have the capability to detect thermal neutrons. The second version of CLYC would be the least suitable, since its ^{6}Li isotopic concentration is insignificant. While ^{10}B has a very high neutron cross section at thermal energies, it was challenging to resolve the peak in the spectrum, and would therefore not be the most suitable either. The first version of CLYC had the most resolved thermal peak, followed by LiI:Eu.

The second version of CLYC was the only suitable detector for fast neutrons. Distinct proton peaks were clearly observed using this scintillator. The first version of CLYC and the boron-loaded plastic scintillator have no ability to detect fast neutrons.

Table 8 gives a comparison of the detector properties.

Table 8: Detector Properties and Capabilities

Detector	Light Output	Energy Resolution	n-γ Discrimination	Decay Time
LiI:Eu	Good	Good	Excellent	Slow
^{6}Li-enriched Cs_2LiYCl_6:Ce	Excellent	Good	Good	Fast
Boron-loaded plastic	Satisfactory	Poor	Poor	Fast
^{7}Li-enriched Cs_2LiYCl_6:Ce	Excellent	Good	Good	Fast

The light output for inorganic scintillators is much better than organic scintillators. The boron-loaded plastic scintillator has the worst light output of 7500 ph/MeV. The LiI:Eu scintillator has a light output of 11,000 ph/MeV. The first CLYC scintillator has a light output of 20,000 ph/MeV and the second is comparable. Thus, the CLYC scintillators clearly have the best light output per MeV by a good margin.

The energy resolution of the neutron induced peaks is comparable. The first CLYC had the best resolution for the thermal neutron peak at 3.3%. The boron-loaded plastic scintillator closely followed with a resolution of 3.4%, then the LiI:Eu scintillator's resolution at 8%, and the second CLYC at 9.1%. For fast neutron peaks, there is no comparison since only the second CLYC scintillator could sufficiently detect them.

The method used for neutron-gamma discrimination is pulse height discrimination. The detector with the largest gap on the response function from neutron induced pulses to gamma induced pulses is LiI:Eu, since the GEE of its thermal peak was at 4.1 MeeV. The second CLYC follows with its thermal peak at 3.4 MeeV, then the first CLYC at 3.24 MeeV. The boron-loaded plastic scintillator could not be compared in this respect since its peak was not calibrated to a MeeV value. For fast neutrons, the second CLYC seemed to have the ability to discriminate at neutron energies higher than 0.6 MeV.

The time response of a scintillator is given by its decay time. Organic scintillators are generally much faster than inorganic scintillators. Hence, the boron-loaded plastic scintillator has the quickest response and is best suited for high counting rates. It has a decay time of 2.2 ns. For inorganic scintillators, the CLYC scintillators are fairly fast also, with decay times in the nanosecond range of 1 ns, 50 ns, and 1000 ns. The LiI:Eu scintillator is the slowest with a decay time of 1.4 μs.

Conclusions

This thesis has investigated four possible detectors that can be used in neutron spectrometry. All four detectors were essentially tested for their response to neutron and gamma radiation. On the thermal energy side, three detectors have been studied and explored. These detectors include a LiI:Eu, boron-loaded plastic, and ^{6}Li-enriched Cs_2LiYCl_6:Ce scintillators. The neutron capture reactions of ^{6}Li(n,α) and ^{10}B(n,α) were used for thermal neutron detection. On the fast energy side, a new approach has been taken with a recent Cs_2LiYCl_6:Ce scintillator. This approach does not rely on current methods that involve complex unfolding techniques to extract the energy spectra but it takes on a new methodology of using a neutron capture reaction with ^{35}Cl that produces a proton whose energy is proportional to the incident neutron energy. By using peaks that are well-resolved in the response function, fast spectrometry can be achieved. Thus, neutron spectrometry has been carried out by using two nuclear reactions, (n,α) and (n,p) on different elements for thermal and fast neutrons, respectively.

The methodology followed an empirical approach. The response functions of the four detectors were obtained through simulations and experiments. Numerous calculations were carried out using MCNPX code. Various experiments were conducted using an AmBe neutron source and neutron generator at UOIT, and a KN Van De Graaff accelerator at McMaster University. Response functions were generated for different gamma sources, thermal neutrons, and fast poly-energetic and mono-energetic neutron sources. Their responses and spectrometric properties were compared and analyzed to determine their applicability in neutron spectrometry.

In terms of thermal neutron detection, the first version of Cs_2LiYCl_6:Ce scintillator that was isotopically enriched with ^{6}Li had the best potential. This scintillator has excellent scintillation properties for thermal neutron detection. This includes exhibiting exceptional energy resolution and the ability to achieve neutron-gamma discrimination. Additionally, it has potential to serve as a gamma spectrometer, and can therefore be used for dual thermal neutron-gamma detection.

In terms of fast neutron detection, in the second version of Cs_2LiYCl_6:Ce scintillator, the concentration of ^{7}Li isotope was increased and the scintillator proved to be a unique and promising candidate to carry out fast neutron spectrometry. This was demonstrated by the use of the ^{35}Cl(n,p) reaction that produced well-defined proton peaks which provided direct energy

information about the incident neutron. The obtained light output curve varies linearly with neutron energy in the range from 0.4 MeV to 4 MeV. Similar to the other Cs_2LiYCl_6:Ce scintillator, the sensor can also serve as a multi-mode radiation detector. This depends on the isotope content and the ability to discriminate the pulses due to protons and alphas/tritons. The $^{35}Cl(n,p)$ reaction can provide the energy spectra for fast neutrons, and the $^{6}Li(n,\alpha)$ can provide the intensity information for low energy neutrons that are naturally present in the background. The use of the scintillator to cover these areas will in turn lead to a much simpler system. Further investigation is required.

Recommendations

The approach presented in this Ph.D. thesis can be further explored and delved into. Focusing on fast neutron spectrometry using the (n,p) reaction with ^{35}Cl, to enhance the efficiency of detection, a crystal with different isotope concentration can be developed and tested for its properties and response to neutron and gamma radiation. Its scintillation properties and detection capabilities can be studied and compared to the current CLYC scintillator.

Using the CLYC scintillators that were studied in this thesis, a neutron detector can be developed to detect thermal as well as fast neutrons. Focusing on the electronics side, more advanced hardware and software can be implemented to enhance the signal processing and improve the resolution of the detection system. These include the photomultiplier tube, multi-channel analyzer, and software used to obtain and process the output data. This would essentially improve the entire unit overall.

Further calculations with MCNPX can be used to determine the nature of different features of the pulse height spectra with fast neutrons.

Contribution to Knowledge

Journal Publications:

1. Khan, N., & Machrafi, R. (2014). Response Functions of a Cs_2LiYCl_6:Ce Scintillator in Mixed Neutron-Gamma Fields. *Annals of Nuclear Energy* (submitted).

2. Machrafi, R., & Khan, N. (2014). Fast Neutron spectrometry with Li depleted Cs_2LiYCl_6:Ce Scintillator. *Annals of Nuclear Energy* (submitted).

3. Khan, N., & Machrafi, R. (2014) Neutron and Gamma-ray Detection using a Cs_2LiYCl_6 Scintillator. *European Physical Journal*, Vol. 66, pp.11018-1-4.

Conference Papers (Refereed):

4. Khan, N., Machrafi, R., & Kovaltchouk, V. (2013). Response Functions of a Cs_2LiYCl_6 Scintillator to Neutron and Gamma Radiation. *Proceedings of the 21st International Conference on Nuclear Engineering*, Chengdu, China (pp.387-393).

5. Khan, N., & Machrafi, R. (2013). Neutron and Gamma-ray Detection using a Cs_2LiYCl_6 Scintillator. *Proceedings of the 25th International Nuclear Physics Conference*, Firenze, Italy, (pp.11018-1-4).

6. Khan, N., Ali, M., Hosny, A., & Machrafi, R. (2012). Response Functions of a Boron-Loaded Plastic Scintillator to Neutron and Gamma Radiation. *Proceedings of the 20th International Conference on Nuclear Engineering*, Anaheim, California, USA (pp.387-393).

7. Ali, M., Khan, N., Hosny, A., & Machrafi, R. (2012). Modelling and Experimental Study of Inorganic Crystal Response Function for Gamma Spectroscopy and Dosimetry. *Proceedings of the 20th International Conference on Nuclear Engineering*, Anaheim, California, USA (pp.603-607).

8. Kovaltchouk, V., Hosny, A., Machrafi, R., Ali, M., & Khan, N. (2012). Neutron Facility Based on High Intensity DT Neutron Generator. *Proceedings of the 20th International Conference on Nuclear Engineering*, Anaheim, California, USA (pp.759-765).

9. Machrafi, R., Fariad, A., Khan, N., & Kovaltchouk, V. (2011). Dual Detector for Online Neutron Gamma Detection. *Proceedings of the 2nd International Conference on Physics and Technology of Reactors and Applications*, Fez, Morocco (pp.)

Conference Presentations:

10. Khan, N., & Machrafi, R. (2013). Study of the Response Functions of a Cs_2LiYCl_6 Scintillator to Neutron and Gamma Radiation. *Presented at the 37th Annual Canadian Nuclear Society/Canadian Nuclear Association Student Conference*, Toronto, Ontario, Canada.

11. Khan, N., & Machrafi, R. (2012). Experimental and Simulation Study of the Response of a Boron-Loaded Plastic Scintillator to Neutrons and Gamma-rays. *Presented at the 36th Annual Canadian Nuclear Society/Canadian Nuclear Association Student Conference,* Saskatoon, Saskatchewan, Canada.

12. Khan, N. (2012). Experimental and Simulation Study of the Response of a Boron-Loaded Plastic Scintillator to Neutrons and Gamma-rays. *Presented at the UOIT 3rd Annual Graduate Student Research Conference,* Oshawa, Canada.

References

1) Hirning, C. R., & Waker, A. J. (1997). Needs and Performance Requirements for Neutron Monitoring in the Nuclear Power Industry. *Radiation Protection Dosimetry*, Vol. 70, No. 1-4, pp. 67-72.

2) Rannou, A., Clech, A., Devita, A., Dollo, R., & Pescayre, G. (1997). Evaluation of Individual Neutron Dosimetry by a Working Group in the French Nuclear Industry. *Radiation Protection Dosimetry*, Vol. 70, No. 1-4, pp. 181-186.

3) Luszik-Bhadra, M. (2004). Electronic Personal Dosemeters: The Solution to Problems of Individual Monitoring in Mixed Neutron/Photon Fields?. *Radiation Protection Dosimetry*, Vol. 110, No. 1-4, pp.747-752.

4) Barthe, J., Bordy, J. M., & Lahaye, T. (1997). Electronic Neutron Dosemeters: History and State of the Art. *Radiation Protection Dosimetry*, Vol. 70, No. 1-4, pp.59-66.

5) Vareille, J. C., Barelaud, B., Barthe, J., Bordy, J. M., Curzio, G., d'Errico, F., Decossas, J. L., Fernandez-Moreno, F., Lahaye, T., Luguera, E., Saupsonidis, O., Savvidis, E., & Zamani-Valassiadou, M. (1997). Advanced Detectors for Active Neutron Dosemeters. *Radiation Protection Dosimetry*, Vol. 70, No. 1-4, pp.79-82.

6) Bartlett, D. T., Tanner, R. J., & Thomas, D. J. (1999). Active Neutron Personal Dosemeters – A Review of Current Status. *Radiation Protection Dosimetry*, Vol. 86, No. 2, pp.107-122.

7) Alberts, W. G., Alexandre, P., Arend, E., d'Errico, F., Fiechtner, A., Roos, H., Schuhmacher, H., Wernli, C., & Wimmer, S. (2001). Development of Electronic Personal Neutron Dosemeters: A European Cooperation. *Radiation Protection Dosimetry*, Vol. 96, No. 1-3, pp.251-254.

8) Knoll, G. (2010). *Radiation Detection and Measurement* (4th ed.). New York: John Wiley & Sons Inc.

9) Cherry Jr., R. N. (1998). Introduction. In *Encyclopaedia of Occupational Health and Safety* 4th Ed (48.2). Geneva: International Labour Organization.

10) Podgorsak, E. B. (2005). *Radiation Oncology Physics: A Handbook for Teachers and Students*. Vienna: International Atomic Energy Agency.

11) Kase, K. R., Bjarngard, B., & Attix, F. H. (1987). *The Dosimetry of Ionizing Radiation Vol. II*. Orlando: Academic Press Inc.

12) Sims, C. S., & Killough, G. G. (1983). Neutron Fluence-To-Dose Equivalent Conversion Factors: A Comparison of Data Sets and Interpolation Methods. *Radiation Protection Dosimetry*, Vol. 5, No. 1, pp.45-48.

13) Bartlett, D. T., Chartier, J. L., Matzke, M., Rimpler, A., & Thomas, D. J. (2003). Concepts and Quantities in Spectrometry and Radiation Protection. *Radiation Protection Dosimetry*, Vol. 107, No. 1-3, pp.23-25.

14) Bernstein, W., & Schardt, A. W. (1952). Activation of LiI Crystals Phosphors. *Phys.Rev.*, Vol. 85, Issue 5, pp.919-920.

15) Nicholson, K. P., & Snelling, G. F. (1955). Some Lithium Iodide Phosphors for Slow Neutron Detection. *British Journal of Applied Physics*, Vol. 6, No. 3, pp.104-106.

16) Karpov, I. K., & Mikhal'chenko, G. A. (1965). Luminescent Properties of Lithium Iodide. *Journal of Applied Spectroscopy*, Vol. 3, No. 2, pp.130-133.

17) Schenck, J. (1953). Activation of Lithium Iodide by Europium. *Nature*, Vol. 171, pp.518-519.

18) Ophel, T. R. (1958). Response Curves of Alkali Halide Scintillators with Special Reference to the $Li^6(n,\alpha)$ Reaction in Lithium Iodide. *Nuclear Instruments*, Vol. 3, Issue 1, pp.45-48.

19) Swoboda, M., Arlt, R., Gostilo, V., Lupilov, A., Majorov, M., Moszynski, M., & Synfeld, A. (2005). Spectral Gamma Detectors for Hand-Held Radioisotope Identification Devices (RIDs) for Nuclear Safety Applications. *IEEE Transactions on Nuclear Science*, Vol. 52, No. 6, pp.3111-3118.

20) Syntfeld, A., Moszynski, M., Arlt, R., Balcerzyk, M., Kapusta, M., Majorov, M., Marcinkowski, R., Schotanus, P., Swoboda, M., & Wolski, D. (2005). ^{6}LiI(Eu) in Neutron and γ-ray Spectrometry – A High Sensitive Thermal Neutron Detector. *IEEE Transactions on Nuclear Science*, Vol. 52, No. 6, pp.3151-3156.

21) Mukhopadhyay, S., & McHugh, H., R. (2004). Portable Gamma and Thermal Neutron Detector using ^{6}LiI(Eu) Crystals. *Proceedings of Hard X-Ray and Gamma-Ray Detector Physics V*. San Diego, USA.

22) Aryaeinejad, R., Dardenne, Y. X., Cole, J. D., & Caffrey, A. J. (1996). Palm-Size Low-Level Neutron Sensor for Radiation Monitoring. *IEEE Transactions on Nuclear Science*, Vol. 43, No. 3, pp.1539-1543.

23) Engels, R., Reinartz, R., Schelten, J., & Czirr, B. (2000). Thermal Neutron Detection with the Lithium Borated Scintillator. *IEEE Transactions on Nuclear Science*, Vol. 47, Issue 3, pp.948-951.

24) Yanagida, T., Kawaguchi, N., Fujimoto, Y., Yokota, Y., Yamazaki, A., Watanabe, K., Kamada, K., & Yoshikawa, A.(2010). Evaluations of Scintillation Properties of $LiSrAlF_6$ Scintillator for Thermal Neutron Detection. *Proceedings of IEEE Nuclear Science Symposium Conference* (pp.182-184). Knoxville, USA.

25) Yamazaki, A., Watanabe, K., Uritani, A., Iguchi, T., Kawaguchi, N., Yanagida, T., Fujimoto, Y., Yokota, Y., Kamada, K., Fukuda, K., Suyama, T., & Yoshikawa A. (2011). Neutron–gamma Discrimination Based on Pulse Shape Discrimination in a Ce:$LiCaAlF_6$ Scintillator. *Nuclear Instruments and Methods in Physics Research Section A*, Vol. 652, Issue 1, pp.435-438.

26) Knitel, M. J., Dorenbos, P., de Haas, J. T. M., & van Eijk, C. W. E. (1996). $LiBaF_3$, A Thermal Neutron Scintillator with Optimal n-γ Discrimination. *Nuclear Instruments and Methods in Physics Research Section A: Accelerators, Spectrometers, Detectors and Associated Equipment*, Vol. 374, Issue 2, pp.197-201.

27) Reeder, P. L., & Bowyer, S. M. (2001). Neutron/gamma discrimination in $LiBaF_3$ Scintillator. *Journal of Radioanalytical and Nuclear Chemistry*, Vol. 248, No. 3, pp.707-711.

28) Reeder, P. L., & Bowyer, S. M. (2001). Fast Neutron and Alpha Detection Using $LiBaF_3$ Scintillator. *IEEE Transactions on Nuclear Science*, Vol. 48, No. 3, pp.351-355.

29) Bessiere, A., Dorenbos, P., van Eijk, C. W. E., Krämer, K. W., & Güdel, H. U. (2004). Luminescence and Scintillation Properties of $Cs_2LiYCl_6:Ce^{3+}$ for γ and Neutron Detection. *Nuclear Instruments and Methods in Physics Research Section A*,Vol. 537, Issue 1-2, pp.242-246.

30) Bessiere, A., Dorenbos, P., van Eijk, C. W. E., Krämer, K. W., & Güdel, H. U. (2004). *IEEE Transactions on Nuclear Science*, Vol. 51, Issue 5, pp.2970-2972.

31) Mukhopadhyay, S., Glodo, J., Hawrami, R., Shirwadkar, U., van Loef, E., Higgins, W. M., Churilov, A. V., & Shah, K. S. (2010). Detection of Nuclear Material with Dual Neutron-Gamma Detector. *Proceedings of IEEE International Conference on Technologies for Homeland Security* (pp.404-409).

32) van Eijk, C. W. E., de Haas, J. T. M., Dorenbos, P., Krämer, K. W., & Güdel, H. U. (2005). Development of Elpasolite and Monoclinic Thermal Neutron Scintillators. *Proceedings of IEEE Nuclear Science Symposium Conference* (pp.239-243).

33) Birowosuto, M. D., Dorenbos, P., de Haas, J. T. M., van Eijk, C. W. E., Krämer, K. W., & Güdel, H. U. (2008). Li-Based Thermal Neutron Scintillator Research; $Rb_2LiYBr_6:Ce^{3+}$ and Other Elpasolites. *IEEE Transactions on Nuclear Science*, Vol. 55, No. 3, pp.1152-1155.

34) Murray, R. B. (1957). Use of Li^6I as a Scintillator Detector and Spectrometer for Fast Neutrons. *Nuclear Instruments*, Vol. 2, pp.237-248.

35) Drake, D. M., Feldman, W. C., & Hurlbut, C. (1986). New Electronically Black Neutron Detectors. *Nuclear Instruments and Methods in Physics Research A*, Vol. 247, Issue 3, pp.576-582.

36) Flaska, M., & Pozzi, S. A. (2009). Digital Pulse Analysis for the Capture-Gated Liquid Scintillator BC-523A. *Nuclear Instruments and Methods in Physics Research A*, Vol. 599, Issue 2-3, pp.221-225.

37) Fisher, B. M., Abdurashitov, J. N., Coakley, K. J., Gavrin, V. N., Gilliam, D. M., Nico, J. S., Shikhin, A. A., Thompson, A. K., Vecchia, D. F., & Yants,V. E. (2011). Fast Neutron Detection with ^{6}Li-loaded Liquid Scintillator. *Nuclear Instruments and Methods in Physics Research A*, Vol. 646, Issue 1, pp.126-134.

38) Garbrah, B. W., & Whitley, J. E. (1967). Determination of Boron by Thermal Neutron Capture Gamma-Ray Analysis. *Analytical Chemistry*, Vol. 39. No. 3, pp.345-349.

39) Chou, H. P., & Horng, C. Y. (1992). Integral Test of a Boron-10 Loaded Liquid Scintillator for Neutron Detection. *Nuclear Instruments and Methods in Physics Research A*, Vol. 328, Issue 3, pp.522-525.

40) Swiderski, L., Moszynski, M., Wolski, D., Batsch, T., Iwanowska, J., Nassalski, A., Syntfeld-Kazuch, A., Szczesniak, T., Kniest, F., Kusner, M. R., Pausch, G., Stein, J., Klamra, W., Schotanus, P., & Hurlbut, C. (2010). Further Study of Boron-10 Loaded Liquid Scintillators for Detection of Fast and Thermal Neutrons. *IEEE Transactions on Nuclear Science*, Vol. 57, No. 1, pp.375-380.

41) Flaska, M., Pozzi, S. A., Bogard, J. S., Smith, S. E., Raffo-Caiado, A. C. (2009). Measurements of Continuous-In-Energy Neutron Sources Using the BC-523A Capture-Gated

Liquid Scintillator. *Proceedings of IEEE Nuclear Science Symposium Conference*. Orlando, USA.

42) Normand, S., Mouanda, B., Haan, S., & Louvel, M. (2002). Study of a New Boron Loaded Plastic Scintillator (Revised). *IEEE Transactions on Nuclear Science*, Vol. 49, No. 4, pp.1603-1608.

43) Hu, R. J., Kim, J. H., Ahn, S. H., Hong, B., Ito, M., Kang, T. I., Kim, B. I., Kim, H. C., Lee, K. B., Lee, K. S., Park, S., Ryu, M. S., Sim, K. S., & Hong, S. J. (2007). Characteristics of Boron-Loaded Plastic Scintillators for Neutron Measurements. *Journal of Korean Physical Society*, Vol. 50, No. 5, pp.1482-1488.

44) Feldman, W. C., Auchampaugh, G. F., & Byrd, R. C. (1991). A Novel Fast-Neutron Detector for Space Applications. *Nuclear Instruments and Methods in Physics Research A*, Vol. 306, Issue 1-2, pp.350-365.

45) Miller, M. C., Byrd, R. C., Ensslin, N., Feldman, W. C., Krick, M. S., Prettyman, T. H., & Russo, P. A. (1997). *Applied Radiation and Isotopes*, Vol. 48, No. 10-12, pp.1549-1555.

46) Normand, S., Delacour, P., Passard, C., & Loridon, J. (2004). Boron Loaded Plastic Scintillator Applied to Active Neutron Measurements of Waste Drums. *Proceedings of IEEE Nuclear Science Symposium Conference*. France.

47) Batchelor, R., Aves, R., & Skyrme, T. H. R. (1955). Helium-3 Filled Proportional Counter for Neutron Spectroscopy. *Review of Scientific Instruments*, Vol. 26, No. 11, pp.1037-1047.

48) Mills Jr, W. R., Caldwell, R. L., & Morgan, I. L. (1962). Low Voltage He^3-Filled Proportional Counter for Efficient Detection of Thermal and Epithermal Neutrons. *Review of Scientific Instruments*, Vol. 33, pp.866-868.

49) Sayres, A. R., Jones, K. W., & Wu, C. S. (1961). Interaction of Neutrons with ^{3}He. *Physical Review*, Vol. 122, No. 6, pp.1853-1863.

50) Johnson, C. H., & Trail, C. C. (1956). Proton-Recoil Neutron Spectrometer. *Review of Scientific Instruments*, Vol. 27, No. 7, pp.468-474.

51) Manolopoulou, M., Fragopoulou, F., Stoulos, S., Vagena, E., Westmeier, W., & Zamani, M. (2011). *Proceedings of IEEE 2nd International Conference on Advancements in Nuclear Instrumentation Measurement Methods and their Applications*, pp. 1-6.

52) Sayres, A., & Coppola, M. (1964). ^{3}He Neutron Spectrometer Using Pulse Risetime Discrimination. *Review of Scientific Instruments*, Vol. 35, No. 4, pp.431-437.

53) Combes, C. M., Dorenbos, P., Van Eijk, C.W. E., Kramer, K. W., & Gudel, H. U. (1999). Optical and Scintillation Properties of Pure and Ce^{3+}-doped Cs_2LiYCl_6 and Li_3YCl_6: Ce^{3+} crystals. *Journal of Luminescence,* Vol. 82, pp.299-305.

54) Van Loef, E. V. D., Dorenbos, P., Van Eijk, C. W. E., Kramer, K. W., & Gudel, H. U. (2002). Scintillation and Spectroscopy of the pure and Ce^{3+}-doped elpasolites: Cs_2LiYX_6 (X = Cl, Br). *Journal of Physics: Condensed Matter*, Vol. 14, pp.8481-8496.

55) Bessiere, A., Dorenbos,P., Van Eijk, C.W. E., Kramer, K. W., & Gudel, H. U. (2005). Luminescence and Scintillation Properties of Cs_2LiYCl_6: Ce^{3+} for γ and Neutron Detection. *Nuclear Instruments & Methods in Physics Research A*, Vol. 537, pp.242-246.

56) Rodnyi, P. A., Mikhailik, V. B., Stryganyuk, G. B., Voloshinovskii, A. S., van Eijk, C. W. E, & Zimmerer, G. F. (2000). Luminescence Properties of Ce-doped $Cs_2LiLaCl_6$ Crystals. *Journal of Luminescence*, Vol. 86, Issue 2, pp.161-166.

57) Higgins, W. M., Glodo, J., Shirwadkar, U., Churilov, A., Van Loef, E., Hawrami, R., Ciampi, G., Hines, C., & Shah, K.S. (2010). Bridgman Growth of Cs_2LiYCl_6: Ce and ^{6}Li-enriched $Cs_2{}^{6}LiYCl_6$:Ce Crystals for High Resolution Gamma Ray and Neutron Spectrometers. *Journal of Crystal Growth,* Vol. 312, pp.1216-1220.

58) Van Eijk, C. W. E., de Haas, J. T. M., Dorenbos, P., Krämer, K. W., & Güdel, H. U. (2005). Development of Elpasolite and Monoclinic Thermal Neutron Scintillators. *Proceedings of IEEE Nuclear Science Symposium Conference* (pp.239-243).

59) Birowosuto, M. D., Dorenbos, P., de Haas, J. T. M., van Eijk, C. W. E., Krämer, K. W., & Güdel, H. U. (2008). Li-Based Thermal Neutron Scintillator Research; Rb_2LiYBr_6:Ce^{3+} and Other Elpasolites. *IEEE Transactions on Nuclear Science*, Vol. 55, No. 3, pp.1152-1155.

60) Glodo, J., Hawrami, R., van Loef, E., Higgins, W., Shirwadkar, U., & Shah, K. S. (2009). Dual Gamma Neutron Detection with $Cs_2LiLaCl_6$. *Proceedings of SPIE* (pp.74490E-1-74490E-7).

61) Glodo, J., Van Loef, E., Hawrami, R., Higgins, W. M., Churilov, A., Shirwadkar, U., & Shah, K. S. (2011). Selected Properties of Cs_2LiYCl_6, $Cs_2LiLaCl_6$, and $Cs_2LiLaBr_6$ Scintillators. *IEEE Transactions on Nuclear Science*, Vol. 58, No.1, pp.333-338.

62) Bessiere, A., Dorenbos,P., Van Eijk, C.W. E., Kramer, K. W., & Gudel, H. U. (2004). New Thermal Neutron Scintillators: Cs_2LiYCl_6: Ce^{3+} and Cs_2LiYBr_6: Ce^{3+}. *IEEE Transactions on Nuclear Science*, Vol. 51, No. 5, pp.2970-2972.

63) Glodo, J., Brys, W., Entine, G., Higgins, W. M., van Loef, E. V. D., Squillante, M. R., & Shah, K. S. (2007). Cs_2LiYCl_6:Ce Neutron Gamma Detection System. *Proceedings of IEEE Nuclear Science SymposiumConference* (pp.959-962).

64) Glodo, J., Higgins, W. M., van Loef, E. V. D., & Shah, K. S. (2008). Scintillation Properties of 1 Inch Cs_2LiYCl_6: Ce Crystals. *IEEE Transactions on Nuclear Science*, Vol. 55, No. 3, pp.1206-1209.

65) Glodo, J., Higgins, W. M., van Loef, E. V. D., & Shah, K. S. (2009). Cs_2LiYCl_6: Ce Scintillator for Nuclear Monitoring Applications. *IEEE Transactions on Nuclear Science*, Vol. 56, No. 3, pp.1257-1261.

66) Mukhopadhyay, S., Glodo, J., Hawrami, R., Shirwadkar, U., van Loef, E., Higgins, W. M., Churilov, A. V., & Shah, K. S. (2010). Detection of Nuclear Material with Dual Neutron-Gamma Detector. *Proceedings of IEEE International Conference on Technologies for Homeland Security* (pp.404-409).

67) Lee, D. W., Stonehill, L. C., Klimenko, A., Terry, J. R., & Tornga, S. R. (2012). Pulse-shape Analysis of Cs_2LiYCl_6: Ce Scintillator for Neutron and Gamma-ray Discrimination. *Nuclear Instruments & Methods in Physics Research A*, Vol. 664, Issue 1, pp.1-5.

68) Bramblett, R. L., Ewing, R. I., & Bonner, T. W. (1960). A New Type of Neutron Spectrometer. *Nuclear Instruments and Methods*, Vol. 9, Issue 1, pp.1-12.

69) Alevra, A. V., & Thomas, D. J. (2003). Neutron Spectrometry in Mixed Fields: Multisphere Spectrometers. *Radiation Protection Dosimetry*, Vol. 107, No. 1-3, pp.37-72.

70) Awschalom, M., & Sanna, R. S. (1985). Applications of Bonner Sphere Detectors in Neutron Field Dosimetry. *Radiation Protection Dosimetry*, Vol. 10, No. 1-4, pp.89-101.

71) Lacoste, V., Gressier, V., Pochat J. L., Fernandez, F., Bakali, M., & Bouassoule, T. (2004). Characterization of Bonner Sphere Systems at Monoenergetic and Thermal Neutron Fields. *Radiation Protection Dosimetry*, Vol. 110, No. 1-4, pp.529-532.

72) Kralik, M., Aroua, A., Grecescu, M., Mares, V., Novotny, T., Schraube, H., & Wiegel, B. (1997). Specification of Bonner Sphere Systems for Neutron Spectrometry. *Radiation Protection Dosimetry*, Vol. 70, No. 1-4, pp.279-284.

73) Ogata, T., Kudo, S., Watanabe, Y., Muramatsu, T., Yamamoto, H., Iwai, S., Takagi, S., Harano, H., Matsumoto, T., & Nishiyama, J. (2011). The Calibration of a Bonner Sphere Spectrometer. *Radiation Protection Dosimetry*, Vol. 146, No. 1-3, pp.107-110.

74) Thomas, D. J., Hawkes, N. P., Jones, L. N., Kolkowski, P., & Roberts, N. J. (2007). Characterization and Utilization of a Bonner Sphere Set Based on Gold Activation Foils. *Radiation Protection Dosimetry*, Vol. 126, No. 1-4, pp.229-233.

75) Burgett, E. A., Hertel, N. E., & Howell, R. M. (2009). Energy Response and Angular Dependence of a Bonner Sphere Extension. *IEEE Transactions on Nuclear Science*, Vol. 56, No. 3, pp.1325-1328.

76) Dubeau, J., Hakmana Witharana, S. S., Yonkeu, A., & Atanackovic, J. (2010, June). A New Type of Neutron Spectrometer using Nested Moderator. *Proceedings of the IEEE NPSS International Workshop on Real Time Measurement, Instrumentation & Control*. Oshawa.

77) Dubeau, J., Hakmana Witharana, S. S., Atanackovic, J. Yonkeu, A., & Archambault, J. P. (2011). A Neutron Spectrometer using Nested Moderators. *Radiation Protection Dosimetry*, pp.1-6.

78) Tagziria, H., & Hansen, W. (2003). Neutron Spectrometry in Mixed Fields: Proportional Counter Spectrometers. *Radiation Protection Dosimetry*, Vol. 107, No. 1-3, pp.73-93.

79) Ing, H., Clifford, T., McLean, T., Webb, W., Cousins, T., & Dhermain, J. (1997). ROSPEC – A Simple Reliable High Resolution Neutron Spectrometer. *Radiation Protection Dosimetry*, Vol. 70, No. 1-4, pp.273-278.

80) Heimbach, C. (2006). NIST Calibration of a Neutron Spectrometer ROSPEC. *Journal of Research of the National Institute of Standards and Technology*, Vol. 111, No. 6, pp.419-428.

81) Ing, H., Djeffal, S., Clifford, T., Li, L., Noulty, R., & Machrafi, R. (2007). Modification of ROSPEC to Cover Neutrons from Thermal to 18 MeV. *Radiation Protection Dosimetry*, Vol. 126, No. 1-4, pp.350-354.

82) Brooks, F. D. (1959). A Scintillation Counter with Neutron and Gamma-ray Discriminator. *Nuclear Instruments and Methods*, Vol. 4, pp.151–163.

83) Perkins, L. J., & Scott, M. C. (1979). The Application of Pulse Shape Discrimination in NE213 to Neutron Spectrometry. *Nuclear Instruments and Methods*, Vol. 166, pp.451–464.

84) Broek, H. W., & Anderson, C. E. (1960). The Stilbene Scintillation Crystal as a Spectrometer for Continuous Fast-Neutron Spectra. *Review of Scientific Instruments*, Vol. 31, pp.1063-1069.

85) Lee, S. K., Kang, B. H., Lee, W. G., Kim, J. K., Kim, Y. K., Galunov, N. Z., & Kim, G. D. (2009). Scintillation Properties of Large Area Composite Stilbene Scintillator for Neutron Detection. *Proceedings of the 2009 IEEE Nuclear Science Symposium Conference*. Orlando, USA.

86) Verbinski, V. V., Burrus, W. R., Love, T. A., Zobel, W. & Hill, N. W. (1968). Calibration of an Organic Scintillator for Neutron Spectrometry. *Nuclear Instruments and Methods*, Vol. 65, pp.8–25.

87) Klein, H. (2003). Neutron Spectrometry in Mixed Fields: NE213/BC501A Liquid Scintillation Spectrometers. *Radiation Protection Dosimetry*, Vol. 107, No. 1-3, pp.95-109.

88) Knauf, K., Alevra, A. V., Klein, H., & Wittstock, J. (1989). Neutronenspektrometrie im Strahlenschutz. *PTB-Mitteilungen*, Vol. 99, pp.101-106.

89) Aruoa, A., Boschung, M., Cartier, F., Gresescu, M., Prêtre, S., Valley, J. F., & Wernli, C. (1994). Characterization of a Mixed Neutron-Gamma Fields Inside the Swiss Nuclear Power Plants by Different Active Systems. *Radiation Protection Dosimetry*, Vol. 51, pp.17-25.

90) Thomas, D. J., Waker, A. J., Hunt, J. B., Bardell, A. G., & More, B. R. (1992). An Intercomparison of Neutron Field Dosimetry Systems. *Radiation Protection Dosimetry*, Vol. 44, No. 1-4, pp.219-222.

91) Grecescu, M., Aruoa, A., Boschung, M., Fiechtner, A., Gmur, K., Laedermann, J.-P., Valley, J.-F., & Wernli, C. (2002). Neutron Field Measurements at the 590 MeV Ring Cyclotron of the Paul Scherrer Institute. *Nuclear Instrument Methods A*, Vol. 476, pp.58-62.

92) Vanhavere, F., Vermeesch, F., Chartier, J. L., Itie, C., Rosenstock, W., Köble, T., & d'Errico, F. (2002). A Comparison of Different Neutron Spectrometry Systems at the Reactor Facility VENUS. *Nuclear Instrument Methods A*, Vol. 476, pp.395-399.

93) Schraube, H., Kneschaurek, P., Schraube, G., Wagner, F. M., & Weitzenegger, E. (2002). Neutron Spectra Around Medical Treatment Facilities. *Nuclear Instrument Methods A*, Vol. 476, pp.463-467.

94) Goldhagen, P., Reginatto, M., Kniss, T., Wilson, J. W., Singleterry, R. C., Jones, I. W., & Van Steveninck, W. (2002). Measurement of the Energy Spectrum of Cosmic-ray Induced Neutrons Aboard an ER-2 High-Altitude Airplane. *Nuclear Instrument Methods A*, Vol. 476, pp.42-51.

95) Pelowitz, D. B., ed. (2011). *MCNPX™ User's Manual Version 2.7.0 (LA-CP-11-00438)*. Los Alamos National Laboratory.

96) Schwarz, A. L., Schwarz, R. A., & Carter, L. L. (2011*). MCNP/MCNPX Visual Editor Computer Code Manual Version 24E*. Los Alamos National Laboratory.

97) ISO International Standards. (2001). *ISO 8529-1 Reference Neutron Radiations – Part 1: Characteristics and Methods of Production.*

98) Hamm, R. W., & Hamm, M. E. (2012). *Industrial Accelerators and Their Applications*. Singapore: World Scientific Publishing Co. Pte. Ltd.

99) Lee, C. L., & Zhou, X. -L. (1998). Thick Target Yields for the ^{7}Li(p,n)^{7}Be Reaction Near Threshold. *Nuclear Instruments and Methods in Physics Research B*, Vol. 152, pp.1-11.

100) Radiation Monitoring Devices Inc. (2012). *Application Note: General CLYC*. Watertown, http://rmdinc.com/.

101) Hamamatsu Photonics K. K. (1996). *Hamamatsu Photomultiplier Tube R3998-02*. Shizuoka, http://www.hamamatsu.com/.

102) Eljen Technology. *EJ-550 and EJ-552 Silicon Greases Data Sheet*. Sweetwater, http://www.eljentechnology.com/.

103) Bridgeport Instruments, LLC. (2009) *High Performance Embedded MCA with USB Interface: eMorpho-HP Version R2*. Austin, http://www.bridgeportinstruments.com/.

104) Canberra Industries Inc. (2010). *Basic Counting System*. Meriden, http://www.canberra.com/.

105) Bridgeport Instruments, LLC. (2009) *eMorphoBrief –U6*. Austin, http://www.bridgeportinstruments.com/.

106) ENDF/B-VII.1 Incident Neutron Data, National Nuclear Data Center, Brookhaven National Laboratory, http://www.nndc.bnl.gov/.

107) ENDF/B-VII.0 Incident Neutron Data, National Nuclear Data Center, Brookhaven National Laboratory, http://www.nndc.bnl.gov/.

108) Bridgeport Instruments, LLC. (2009). *eMorpho User Manual Version R1*. Austin, http://www.bridgeportinstruments.com/.

109) Wavemetrics. (2009). *Igor Pro User Manual 6.1.2.1*. Lake Oswego, http://www.wavemetrics.com/.

110) Cember, H. (1996). *Introduction to Health Physics* (3^{rd} ed.). USA: McGraw-Hill Medical.

111) Tsoulfanidis, N. (1995). *Measurement and Detection of Radiation* (2^{nd} ed.). USA: Taylor & Francis.

112) Ahmed, S. N. (2007). *Physics & Engineering of Radiation Detection*. UK:Academic Press Inc.

113) Birks, J. B. (1964). *The Theory and Practice of Scintillation Counting*. London: Pergamon.

114) Siegbahn, K. (1955). *Beta and Gamma-ray Spectroscopy*. New York: Interscience Publishers Inc.

115) Kovaltchouk, V., & Machrafi, R. (2011). Monte Carlo Simulations of Response Functions for Gas Filled and Scintillator Detectors with MCNPX Code. *Annals of Nuclear Energy*, Vol. 38, No. 4, pp. 788-793.

116) Kim, G. D., Woo, H. J., Hong, W., & Kim, Y. K. (2009). Mono-energetic Neutron Source Using the ^{7}Li(p,n)^{7}Be Reaction. *Journal of the Korean Physical Society*, Vol. 55, No. 4, pp.1404-1408.

117) Yang, F., & Hamilton, J. H. (2010). *Modern Atomic and Nuclear Physics: Revised Edition*. Singapore: World Scientific Publishing Co. Pte. Ltd.

118) International Commission on Radiological Protection. (1996). *Conversion Coefficients for use in Radiological Protection against External Radiation: ICRP Publication 74. Ann. ICRP 26 (3-4).*

Appendices

Appendix A: Neutron Cross Sections

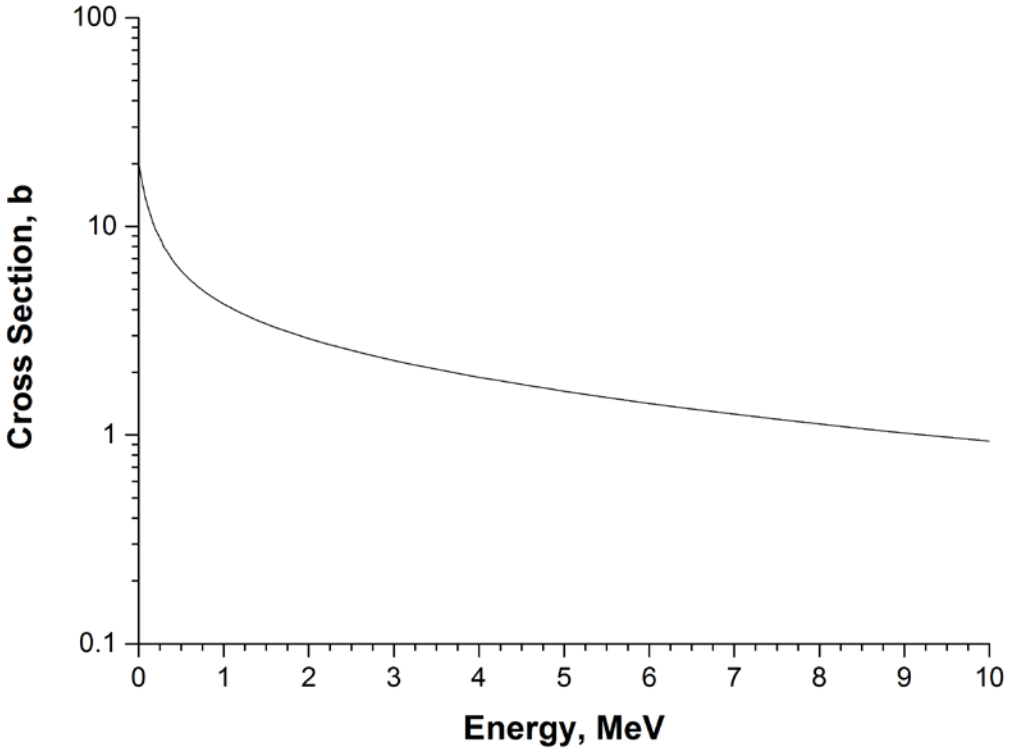

Figure A-1: ENDF/B-VII.1 Neutron elastic scattering cross section with ^{1}H [106]

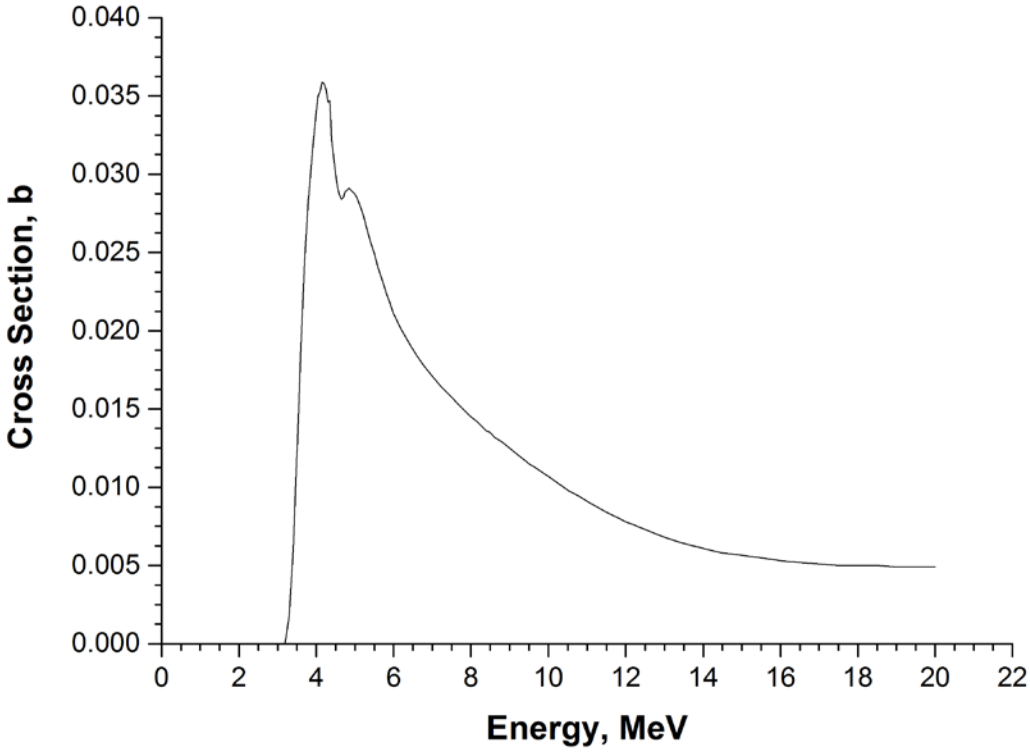

Figure A-2: ENDF/B-VII.0 neutron cross section for ^{6}Li(n,p) [107]

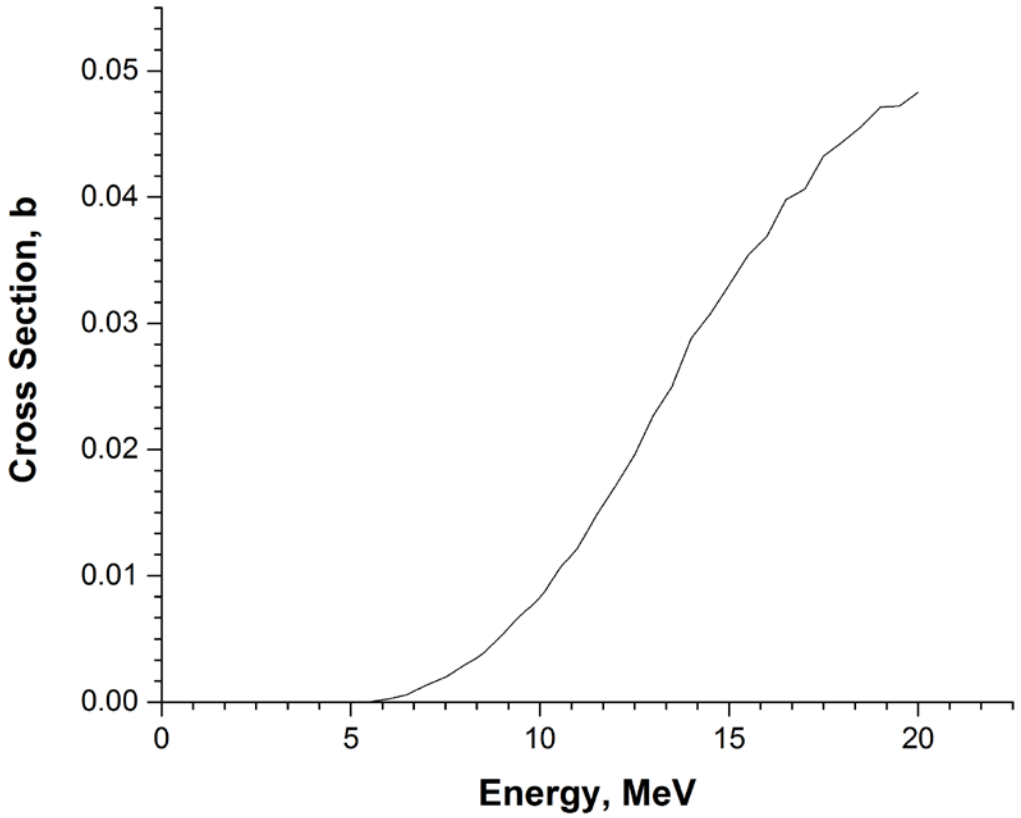

Figure A-3: ENDF/B-VII.0 neutron cross section for ^{35}Cl(n,d) [107]

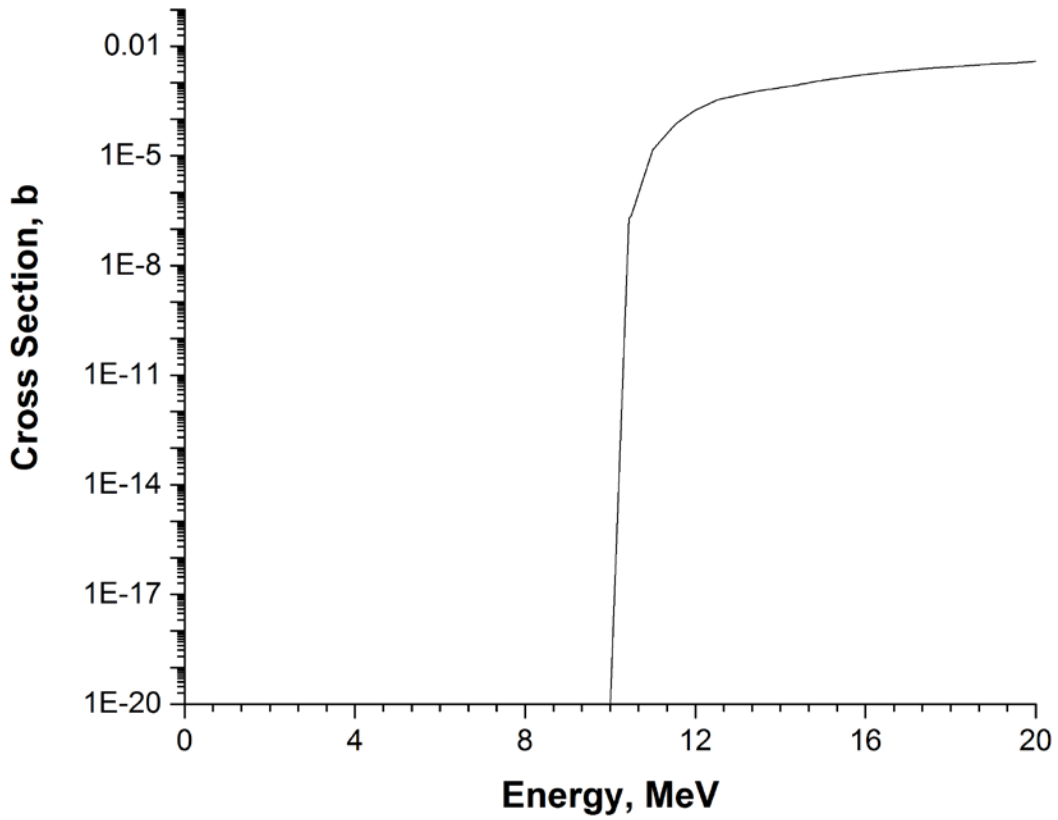

Figure A-4: ENDF/B-VII.0 neutron cross section for ^{35}Cl(n,t) [107]

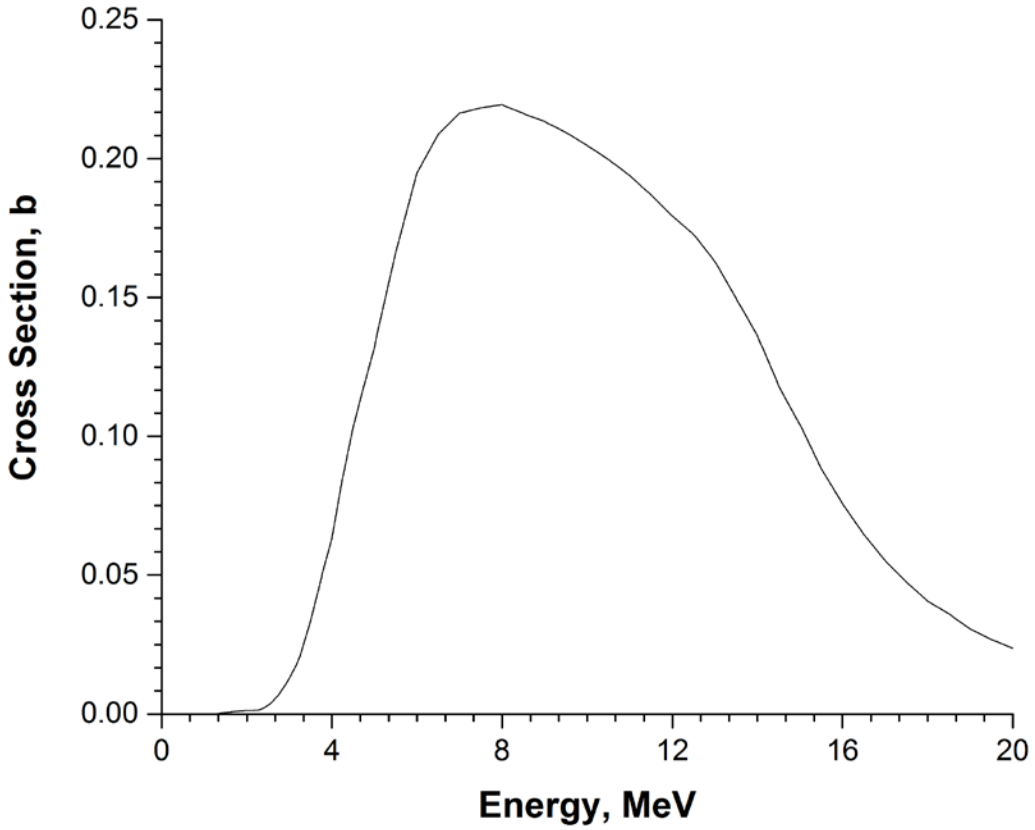

Figure A-5: ENDF/B-VII.0 neutron cross section for ^{35}Cl(n,α) [107]

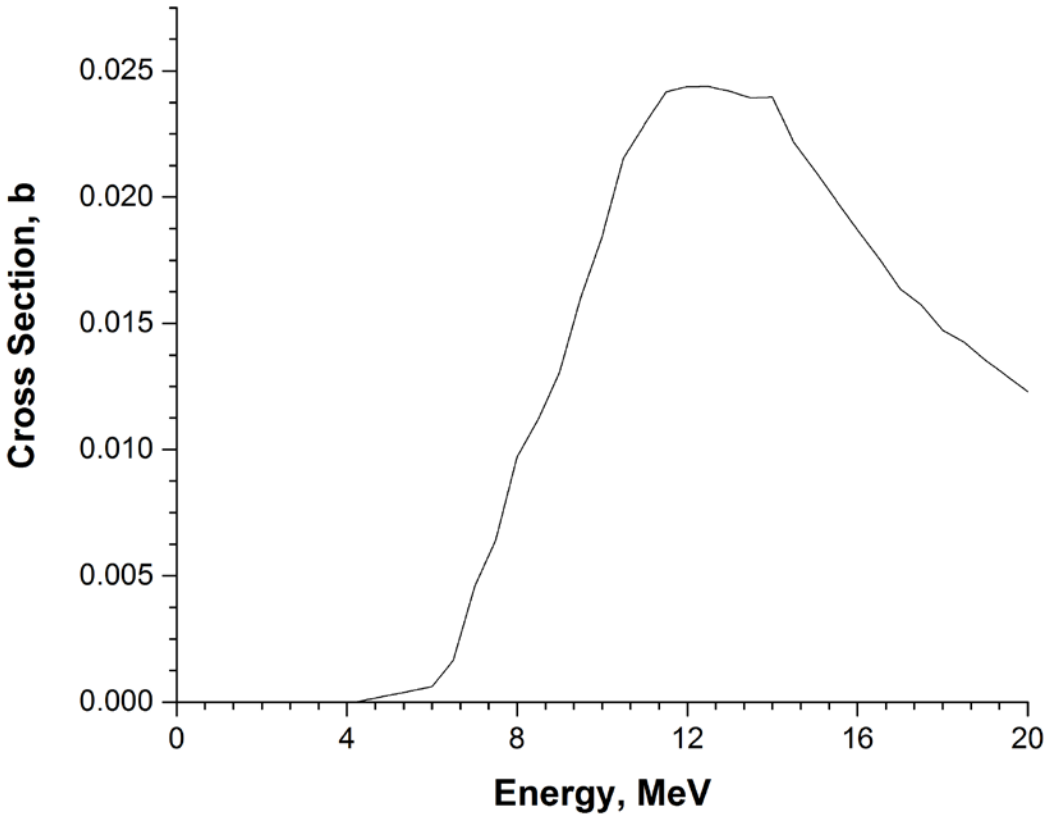

Figure A-6: ENDF/B-VII.0 neutron cross section for ^{37}Cl(n,p) [107]

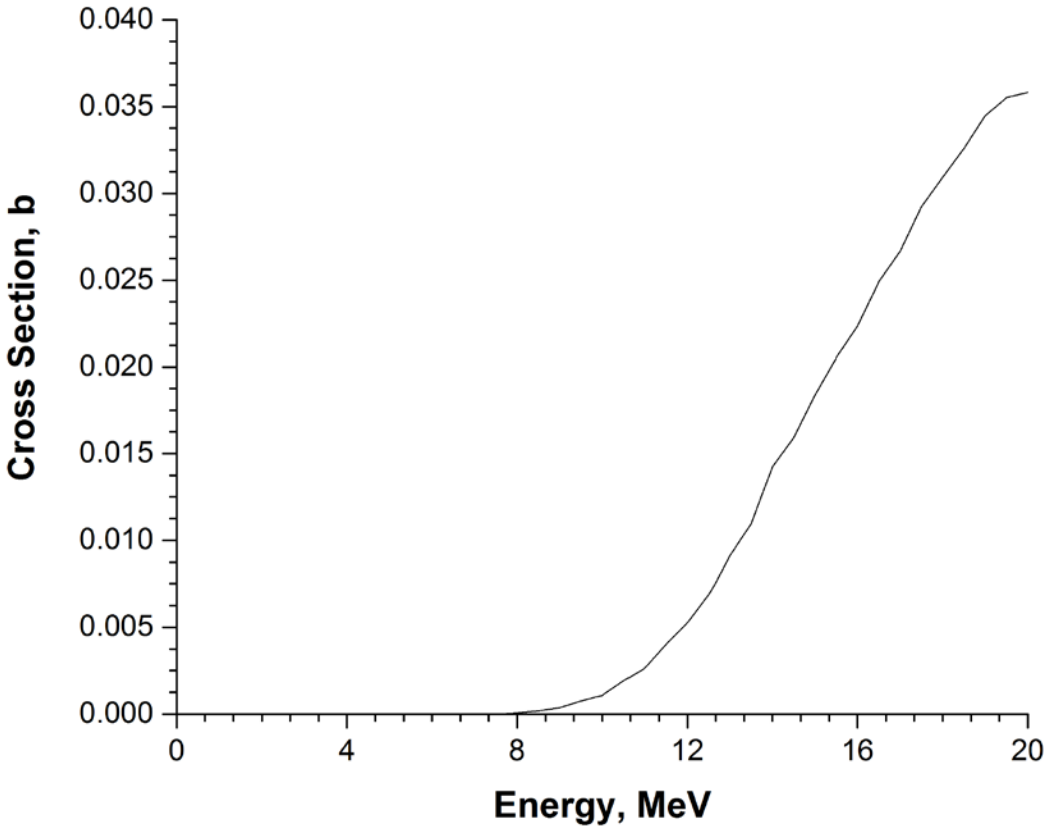

Figure A-7: ENDF/B-VII.0 neutron cross section for ^{37}Cl(n,d) [107]

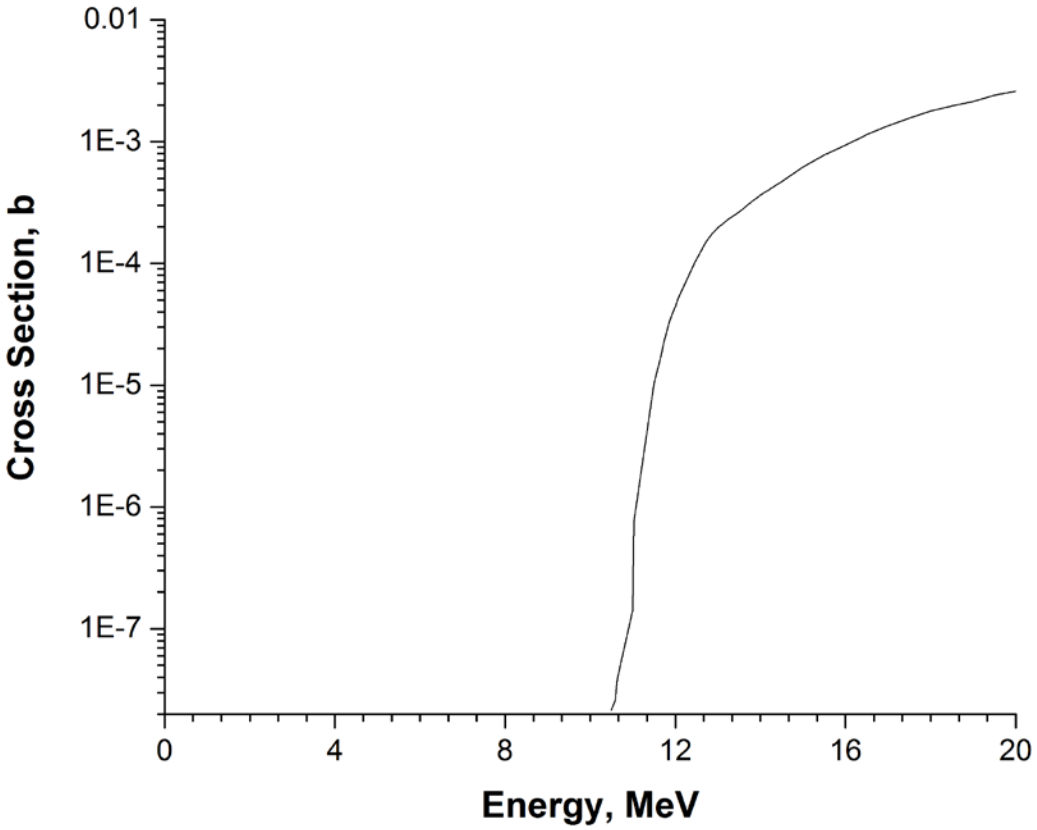

Figure A-8: ENDF/B-VII.0 neutron cross section for ^{37}Cl(n,t) [107]

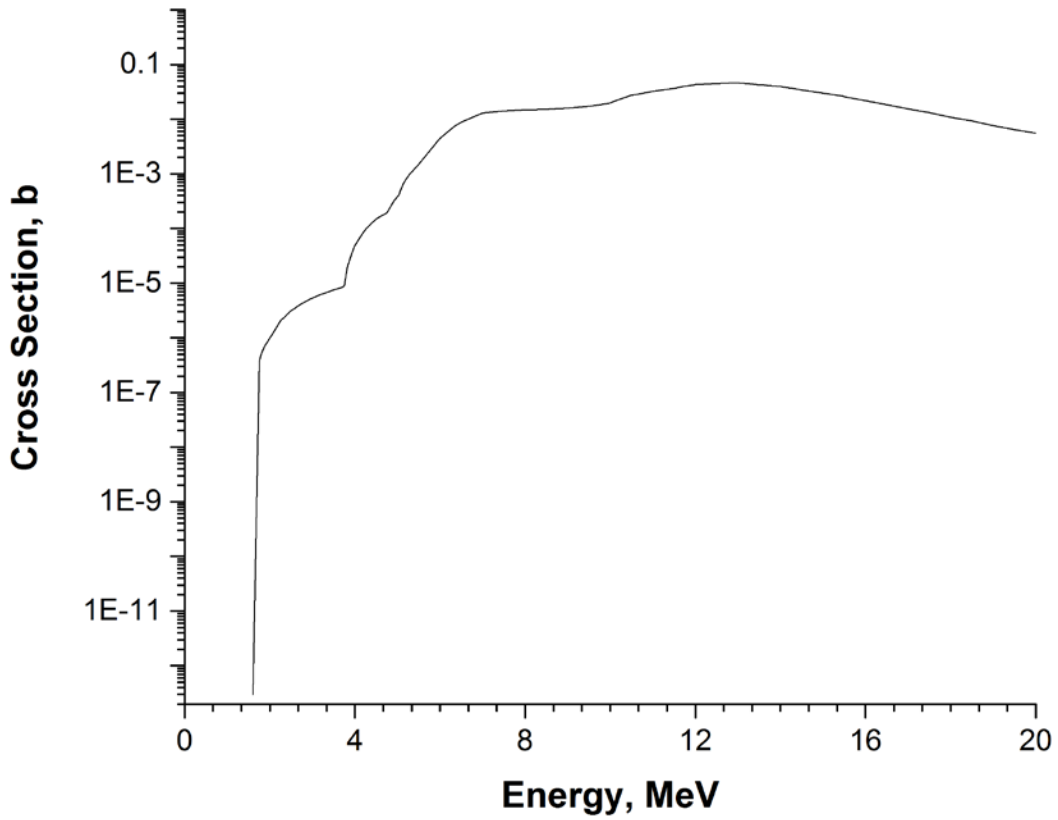

Figure A-9: ENDF/B-VII.0 neutron cross section for ^{37}Cl(n,α) [107]

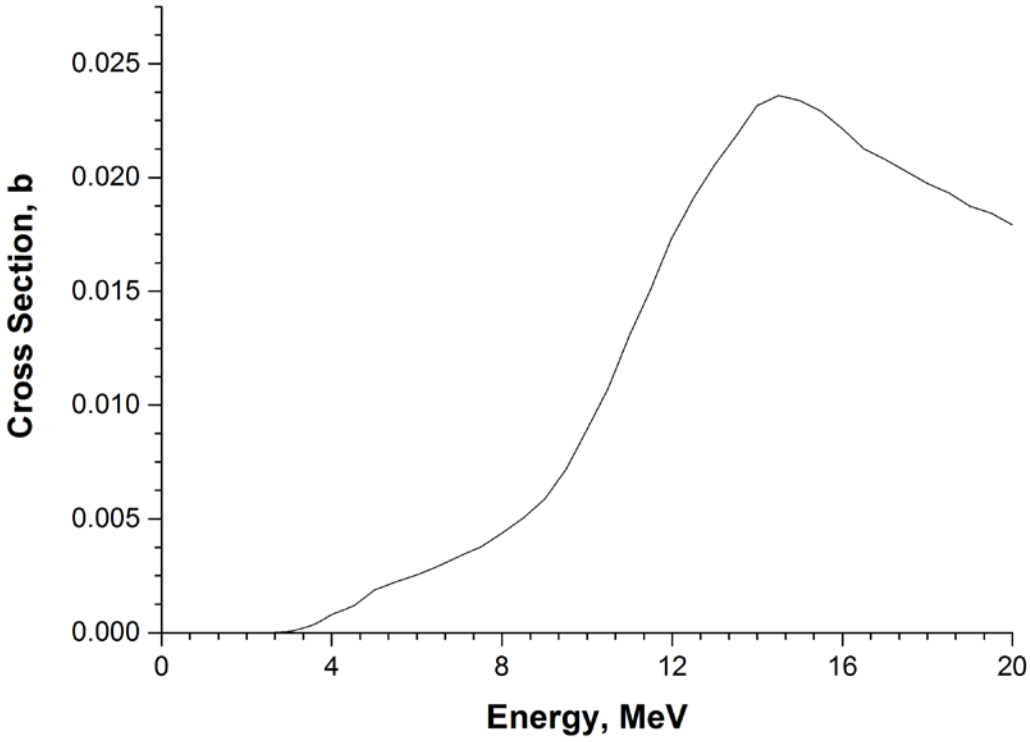

Figure A-10: ENDF/B-VII.0 neutron cross section for ^{89}Y(n,p) [107]

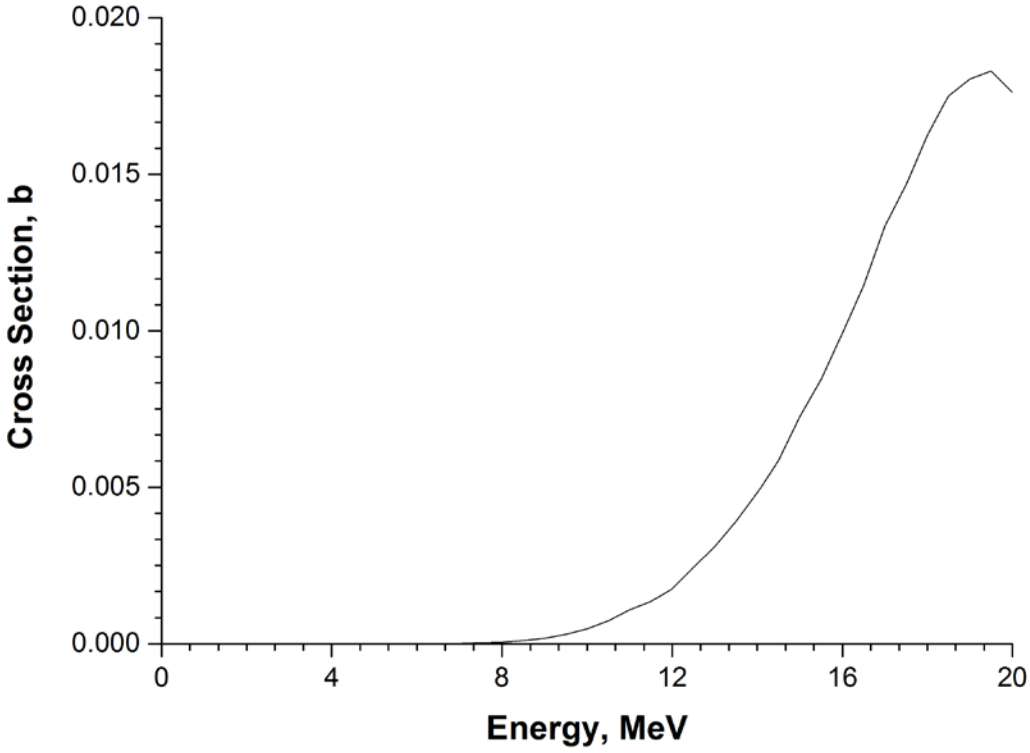

Figure A-11: ENDF/B-VII.0 neutron cross section for ^{89}Y(n,α) [107]

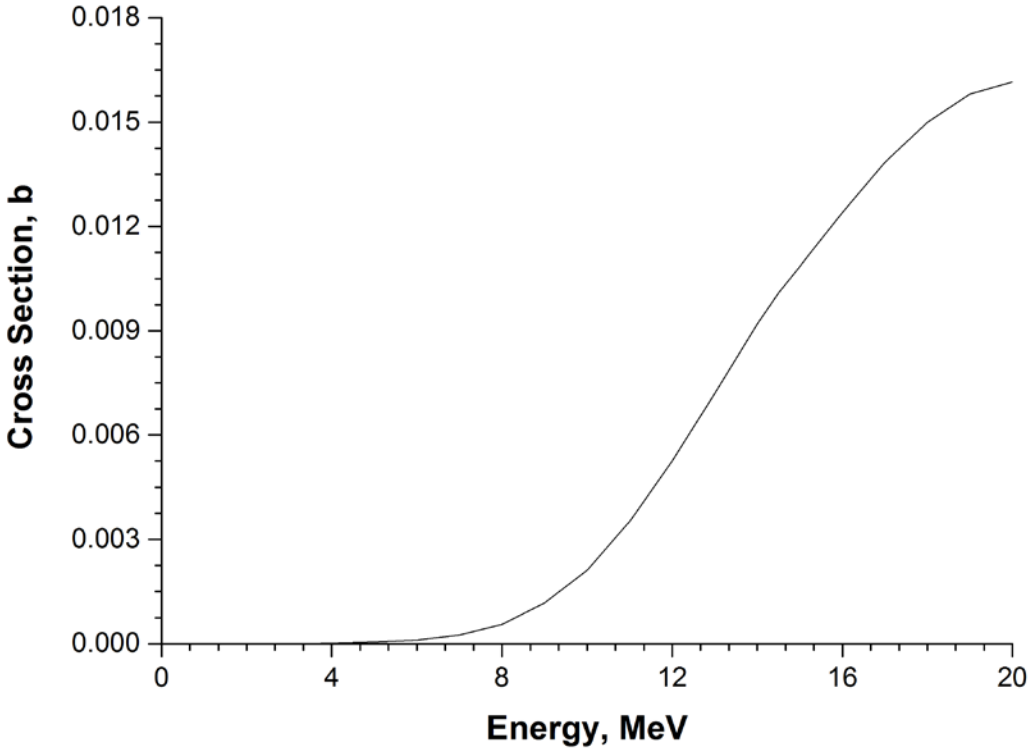

Figure A-12: ENDF/B-VII.0 neutron cross section for ^{133}Cs(n,p) [107]

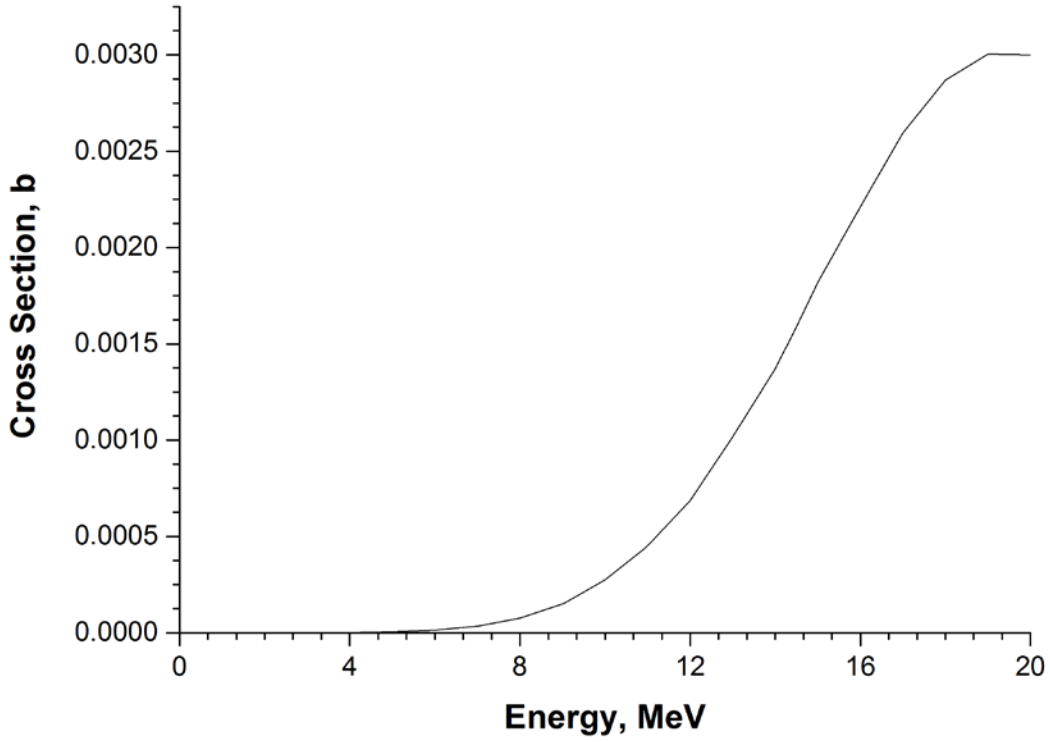

Figure A-13: ENDF/B-VII.0 neutron cross section for ^{133}Cs(n,α) [107]

Appendix B: Additional Simulations

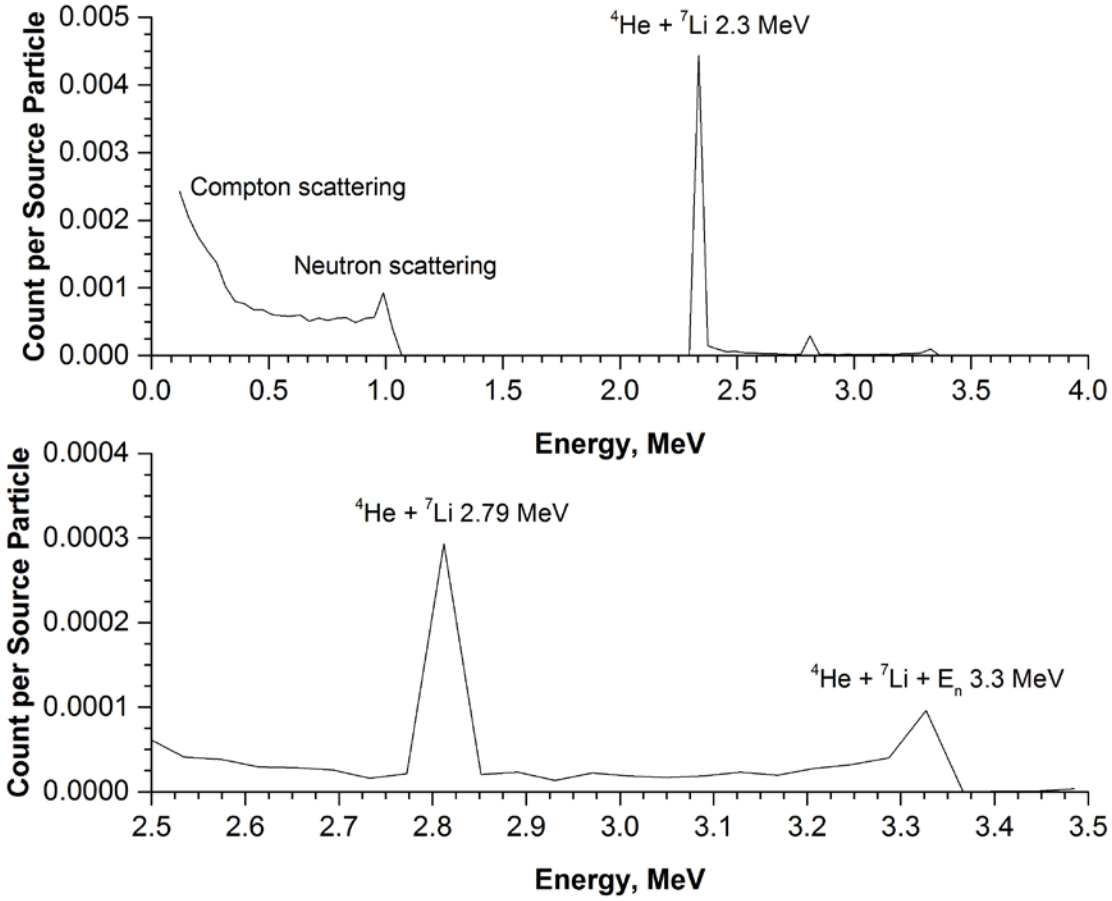

Figure B-1: Simulated response function of boron-loaded plastic scintillator to 1 MeV neutrons

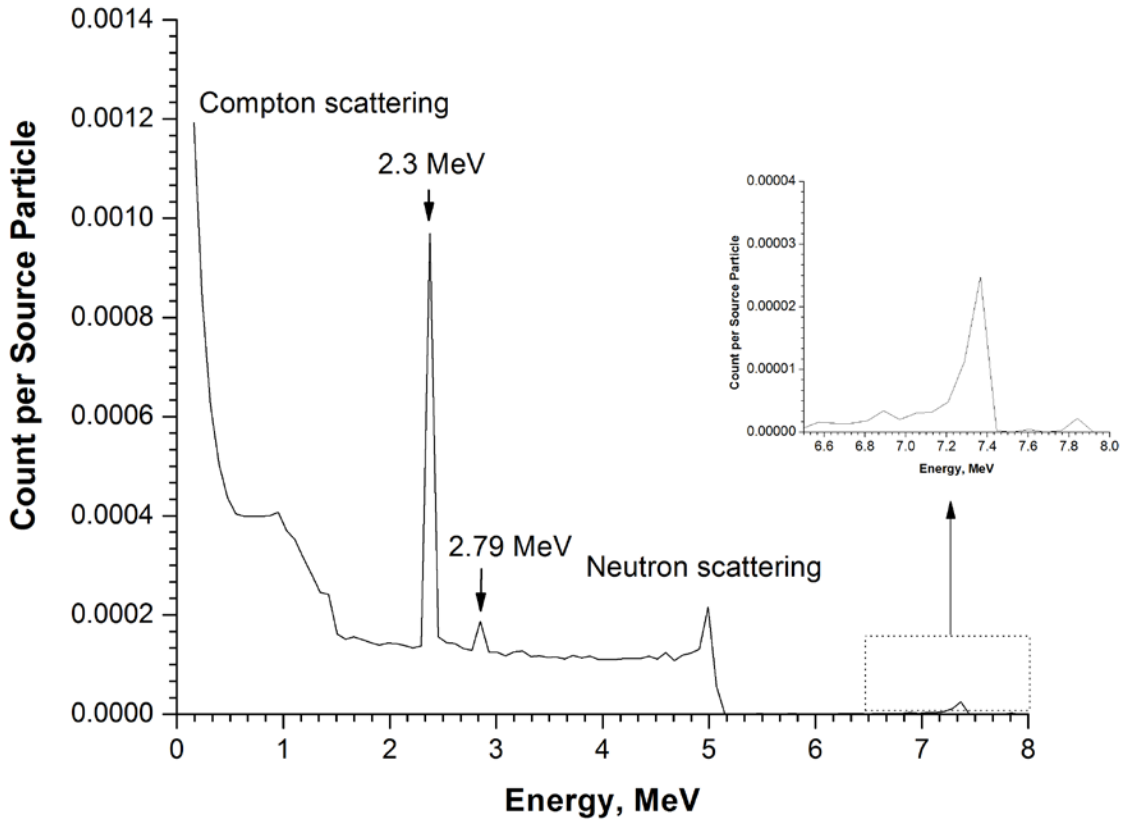

Figure B-2: Simulated response function of boron-loaded plastic scintillator to 5 MeV neutrons

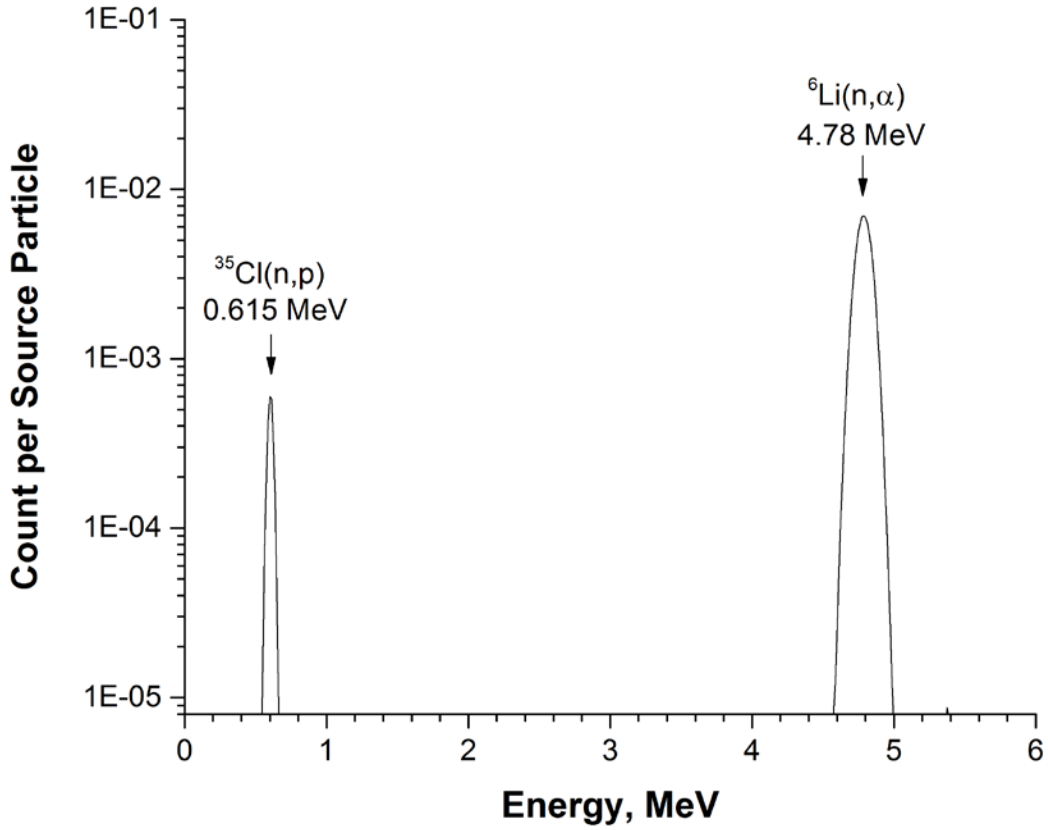

Figure B-3: Simulated response function of natural Li Cs_2LiYCl_6:Ce scintillator to thermal neutrons

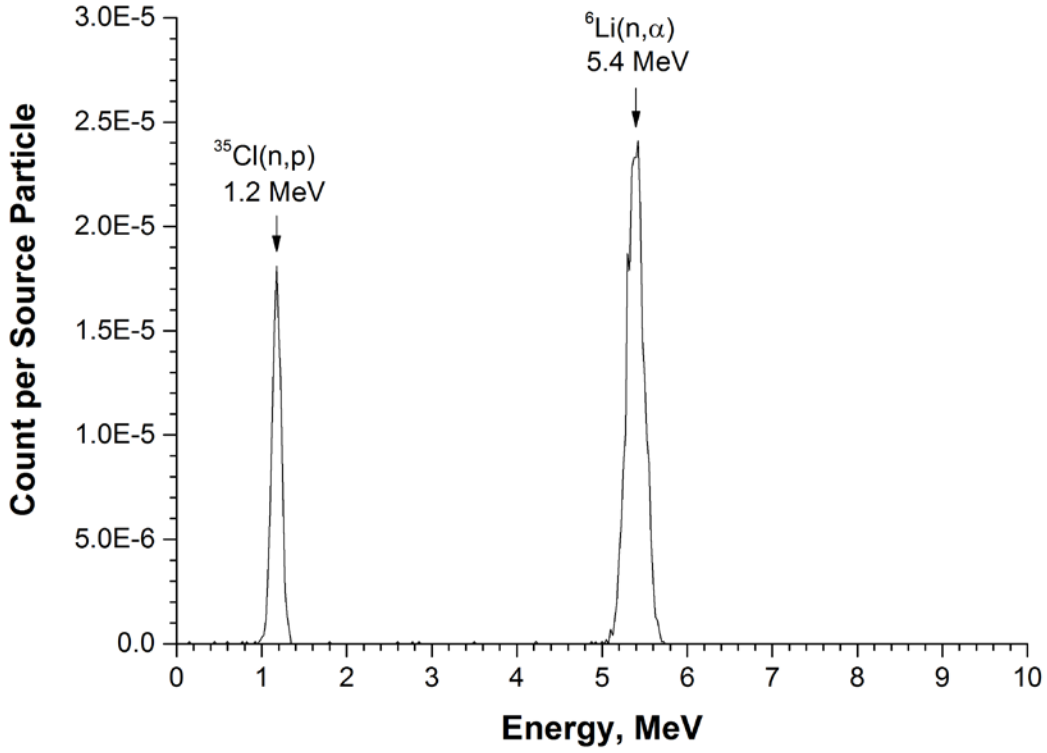

Figure B-4: Simulated response function of natural Li Cs_2LiYCl_6:Ce scintillator to 0.6 MeV neutrons

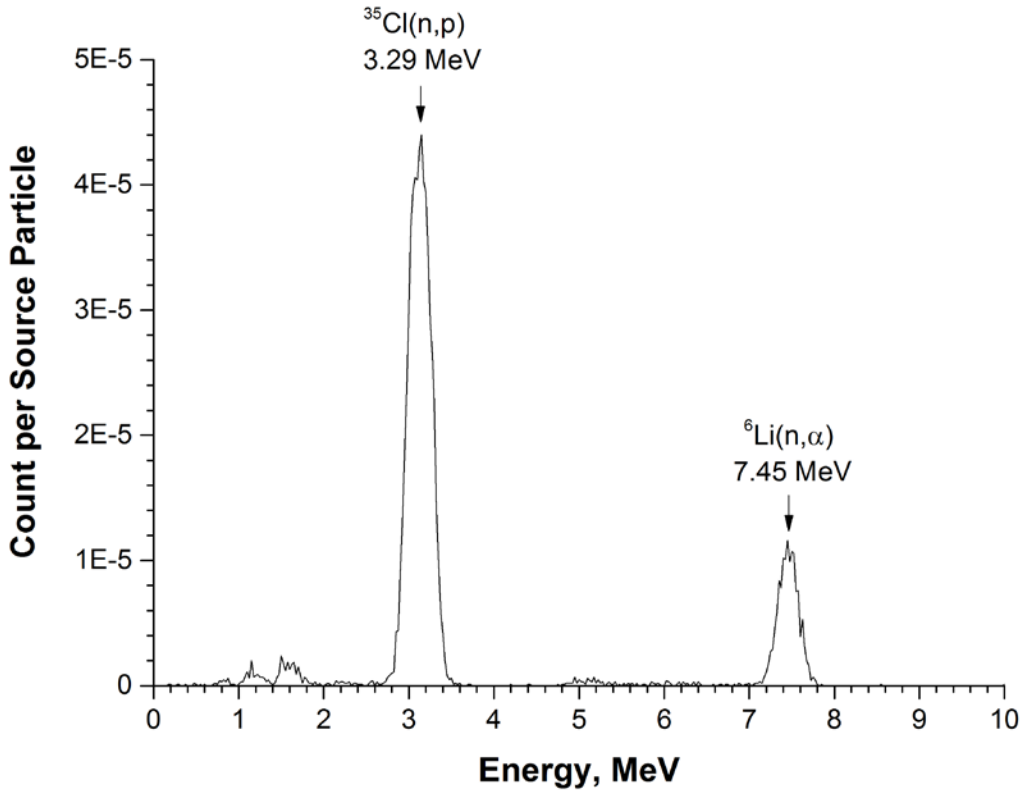

Figure B-5: Simulated response function of natural Li Cs_2LiYCl_6:Ce scintillator to 2.67 MeV neutrons

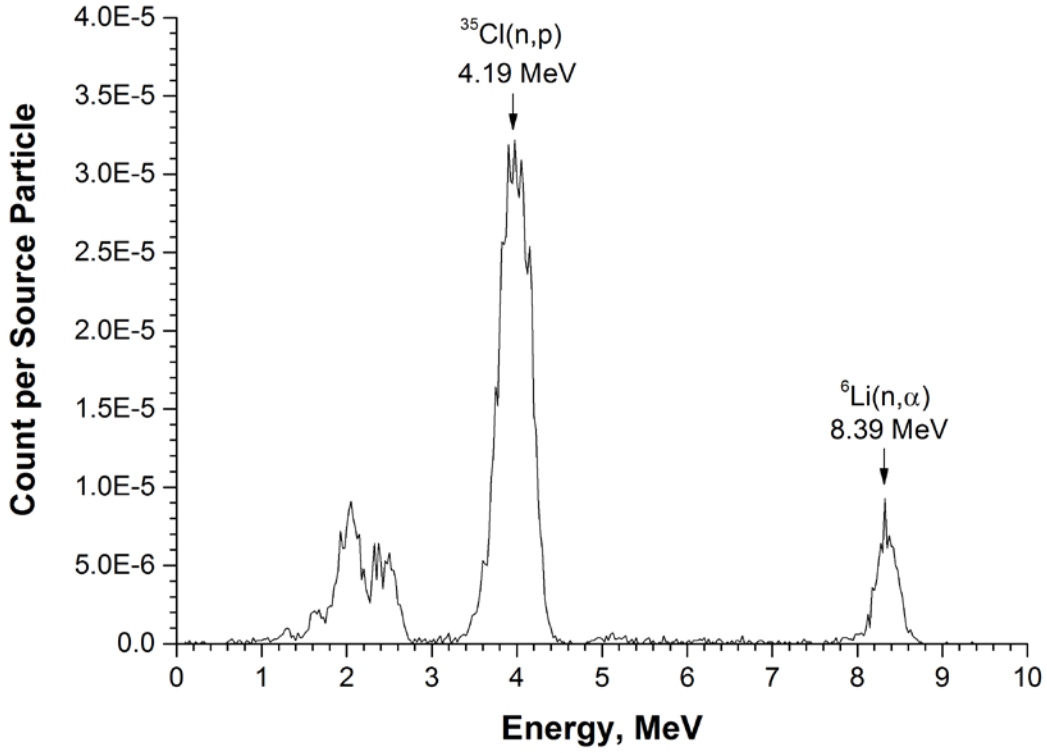

Figure B-6: Simulated response function of natural Li Cs_2LiYCl_6:Ce scintillator to 3.57 MeV neutrons

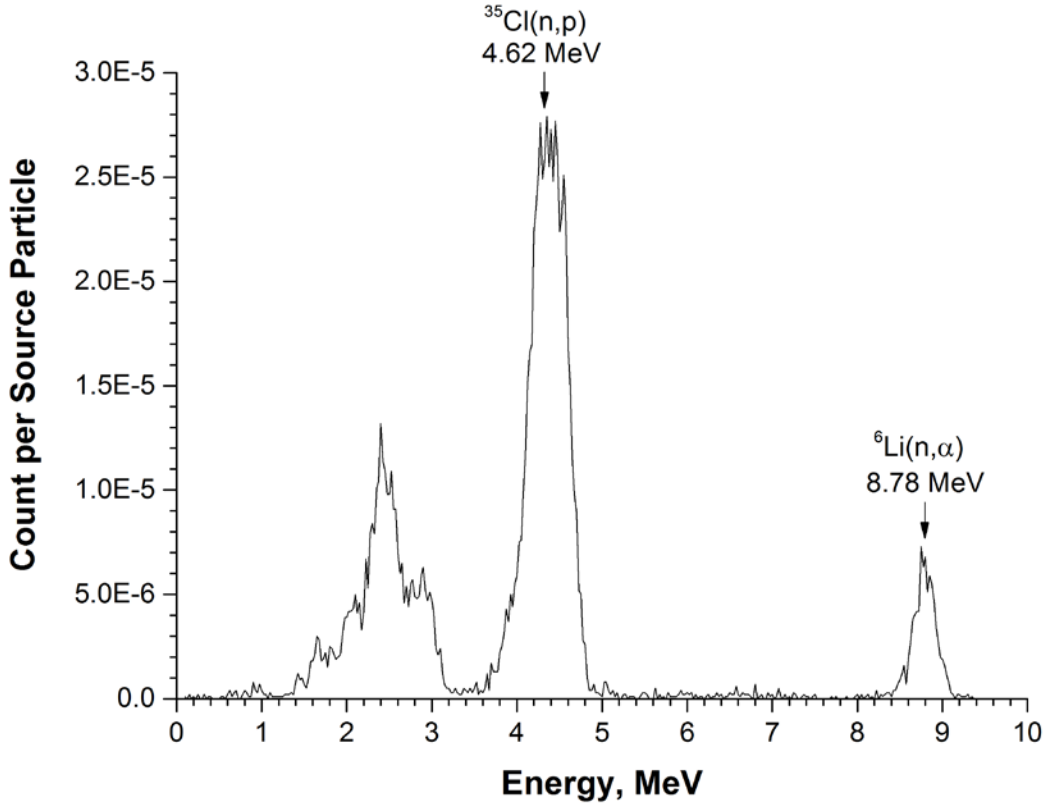

Figure B-7: Simulated response function of natural Li Cs_2LiYCl_6:Ce scintillator to 4 MeV neutrons

Appendix C: Additional Experiments

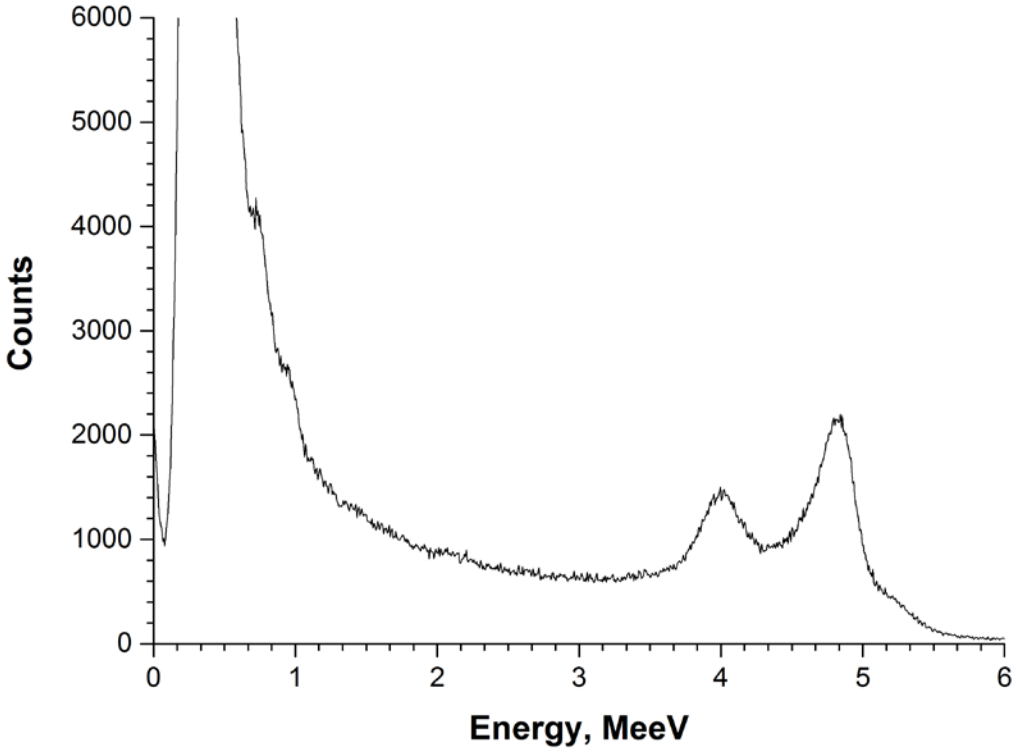

Figure C-1: Measured response function of LiI:Eu scintillator to AmBe neutron source

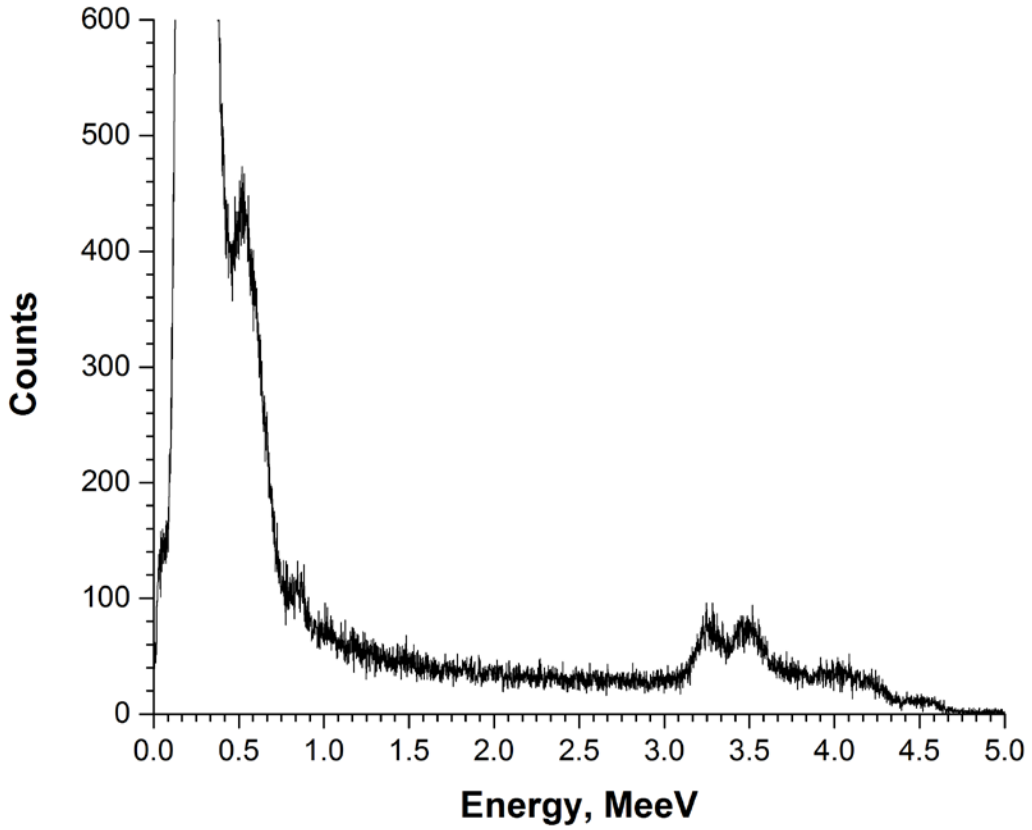

Figure C-2: Measured response function of ^{6}Li-enriched Cs_2LiYCl_6:Ce scintillator to AmBe neutron source

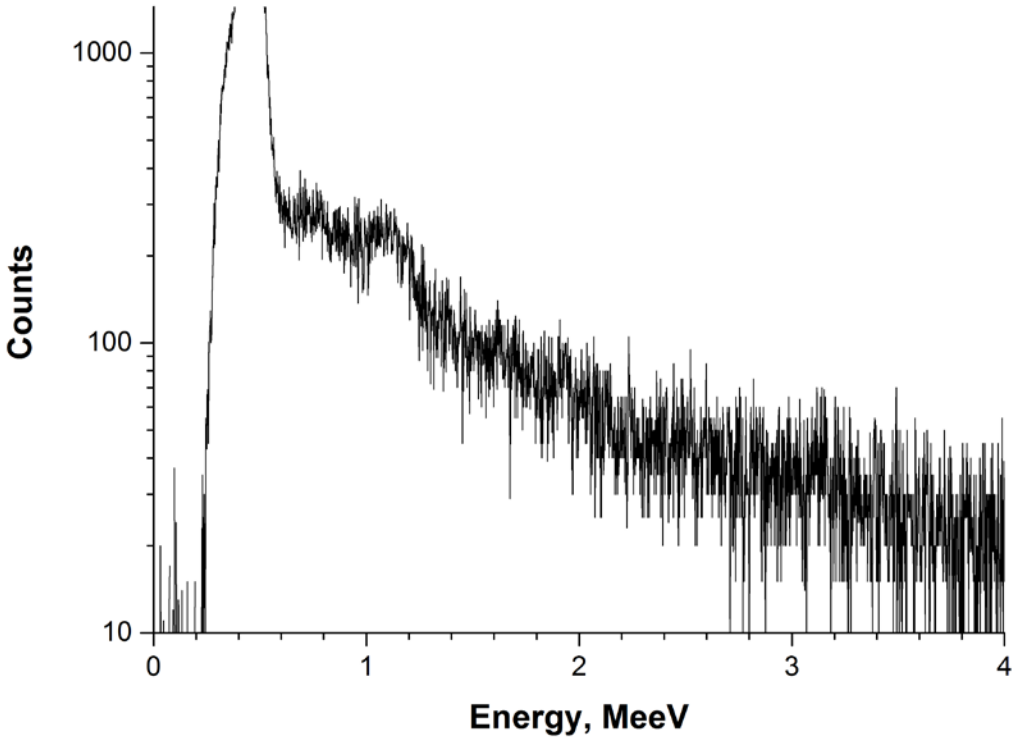

Figure C-3: Measured response function of ^{7}Li-enriched Cs_2LiYCl_6:Ce scintillator to 0.6 MeV neutrons

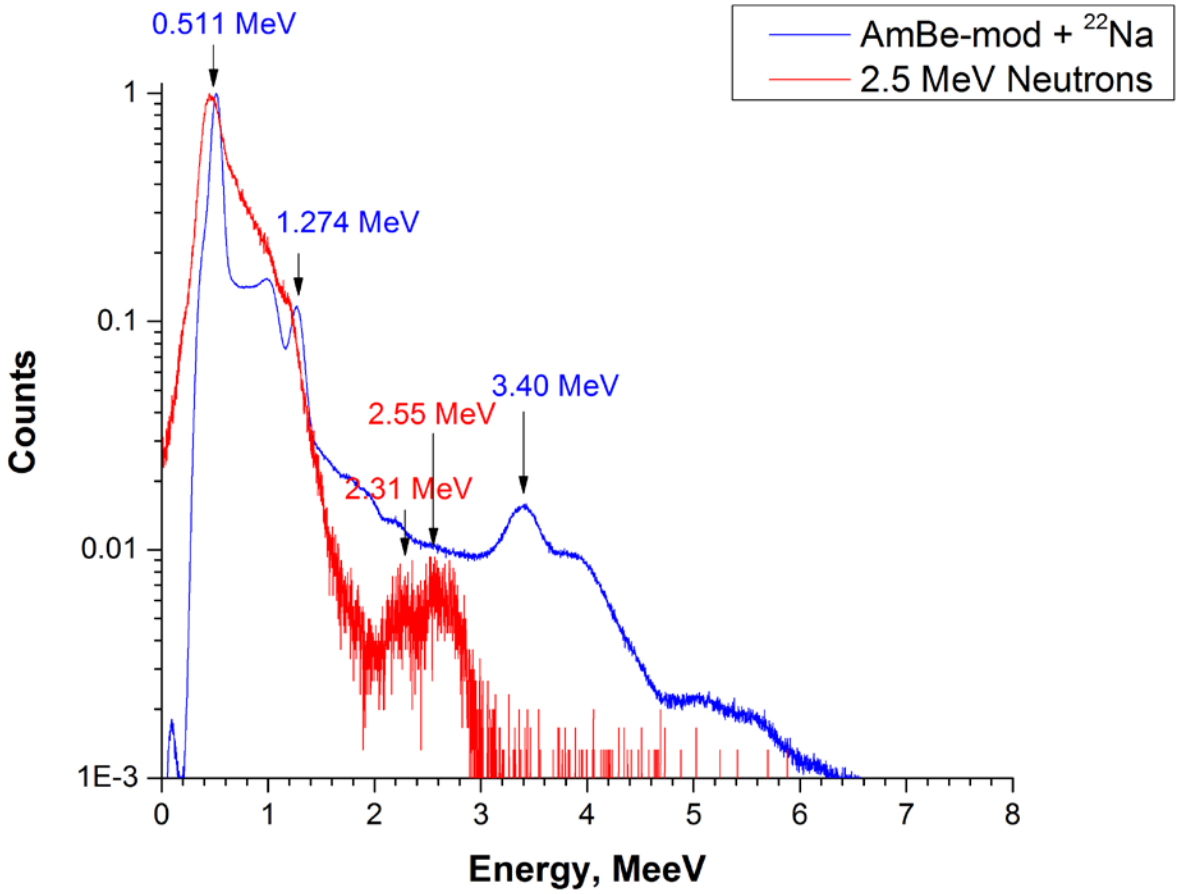

Figure C-4: Measured response function of ^{7}Li-enriched Cs_2LiYCl_6:Ce scintillator to ^{22}Na, moderated AmBe neutron sources, and 2.5 MeV neutrons

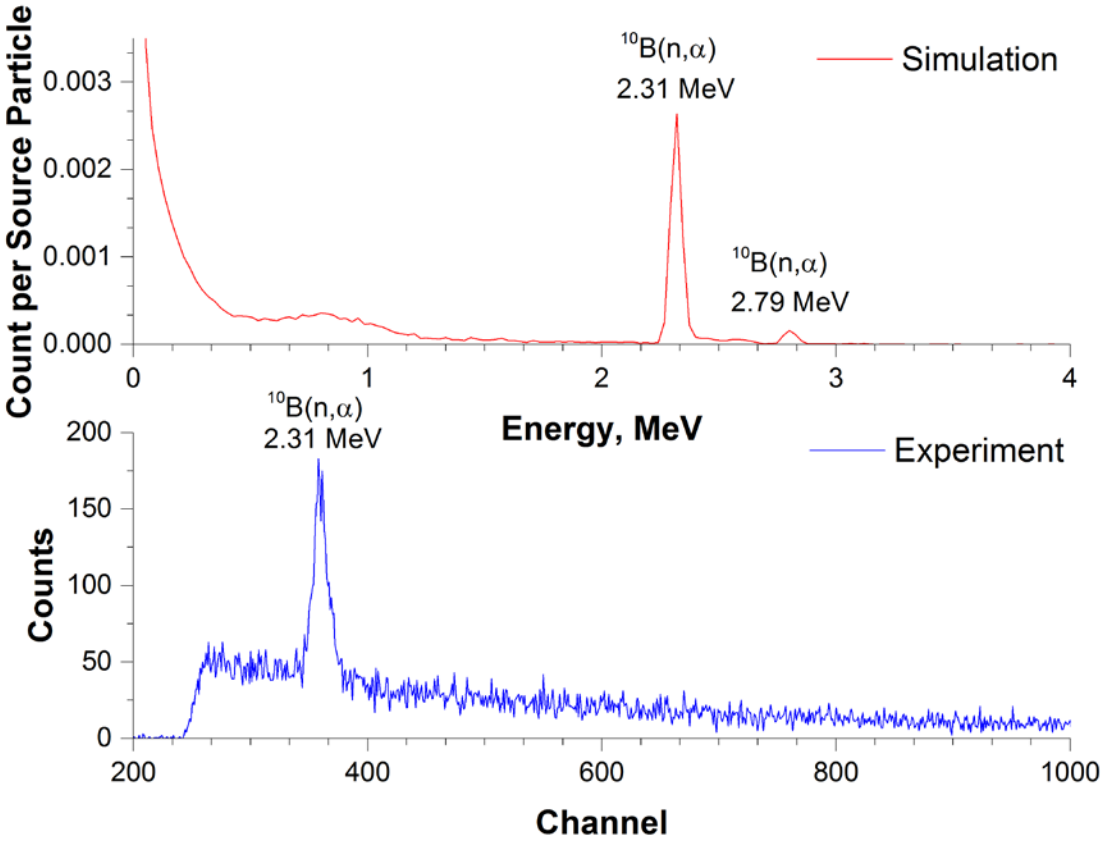

Figure C-5: Comparison of the simulated and measured response functions of boron-loaded plastic scintillator to moderated AmBe neutron source

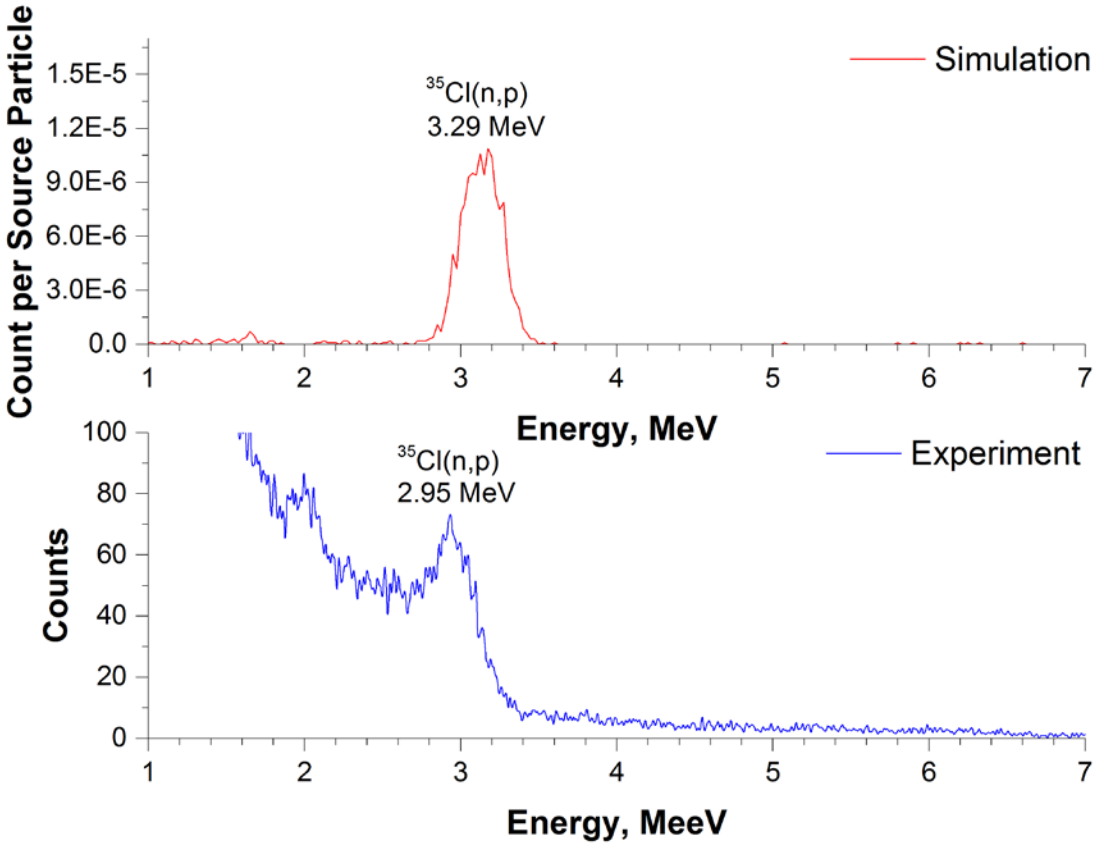

Figure C-6: Comparison of the simulated and measured response functions of the Cs_2LiYCl_6:Ce detector to 2.67 MeV neutrons

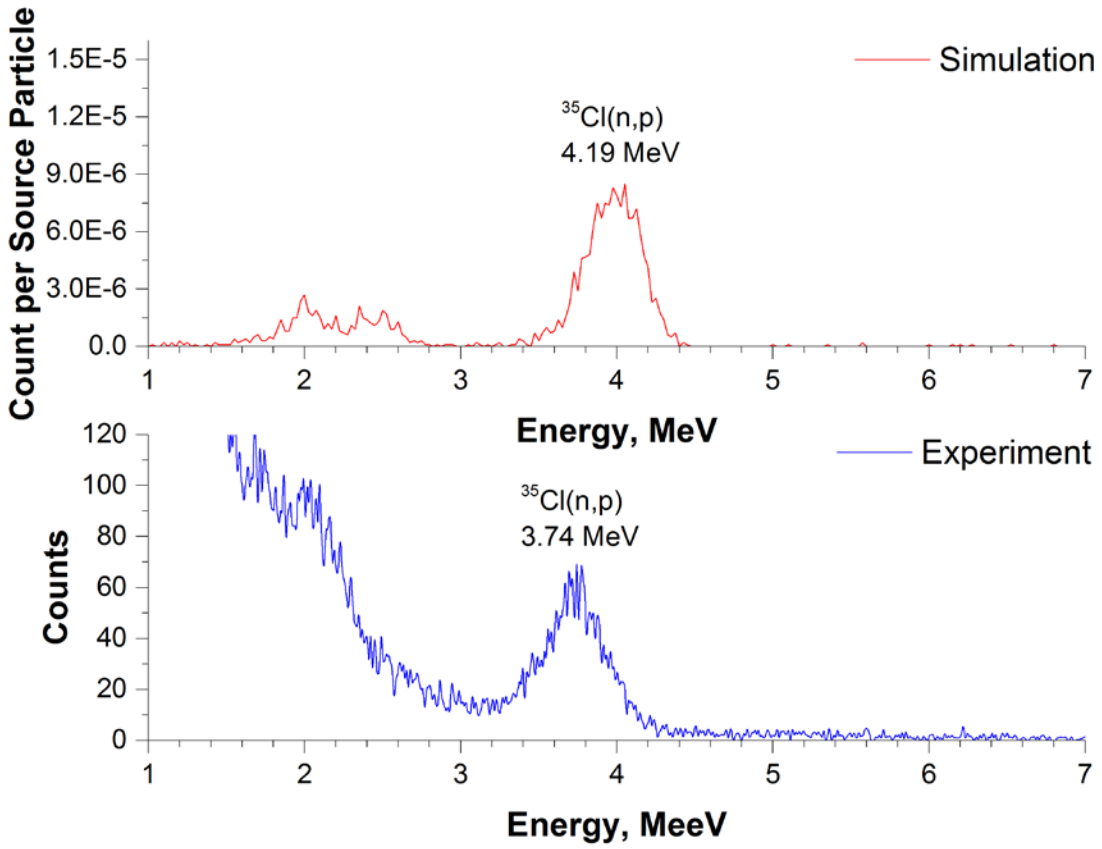

Figure C-7: Comparison of the simulated and measured response functions of the Cs_2LiYCl_6:Ce detector to 3.57 MeV neutrons